ENHANCEMENTS TO SYNTHETIC APERTURE RADAR CHIRP WAVEFORMS AND NON-COHERENT SAR CHANGE DETECTION FOLLOWING LARGE SCALE DISASTERS

A Thesis
Presented to
The Academic Faculty

by

Cihan Bayındır

In Partial Fulfillment
of the Requirements for the Degree
Doctor of Philosophy in the
School of Civil and Environmental Engineering

Georgia Institute of Technology
May 2013

ENHANCEMENTS TO SYNTHETIC APERTURE RADAR CHIRP WAVEFORMS AND NON-COHERENT SAR CHANGE DETECTION FOLLOWING LARGE SCALE DISASTERS

Approved by:

J. David Frost, Committee Chair,
Co-Advisor
School of Civil and Environmental
Engineering
Georgia Institute of Technology

Christopher F. Barnes, Co-Advisor
School of Electrical and Computer
Engineering
Georgia Institute of Technology

Yi-Chang James Tsai
School of Civil and Environmental
Engineering
Georgia Institute of Technology

Erik I. Verriest
School of Electrical and Computer
Engineering
Georgia Institute of Technology

Steven P. French
School of City and Regional Planning
School of Architecture
Georgia Institute of Technology

Date Approved: 27 February 2013

I dedicate this dissertation to my smart and beautiful sister Dilan Bayındır.

ACKNOWLEDGEMENTS

I would like to thank my co-advisors, Dr. James David Frost and Dr. Christopher Floyd Barnes, for their support and understanding with the technical and non-technical matters during last three years I spent at the Georgia Institute of Technology. Dr. James David Frost was very helpful both with the academic matters inside the civil and environmental engineering department and the disaster reconnaissance section of this dissertation.

SAR signal processing section of this dissertation would have never been possible without Dr. Christopher Floyd Barnes's competence and experience on the topic. It was an excellent opportunity for me to work with them. I thank them for their patience and persistant support.

I also thank dissertation committee members Dr. Erik I. Verriest, Dr. Yi-Chang James Tsai and Dr. Steven P. French for the review of this dissertation and critical comments.

Dr. Levent Değertekin was also very helpful with his guidance within Gatech, recommendation letters and his electro-acoustic transducers class. I thank him for all these.

I would also like to thank my former advisor, Dr. James Thornton Kirby, for his support during the two years I spent at the University of Delaware and for his recommendation letters. I have learned much of my hydrodynamics and spectral analysis from him.

Dr. Ali Farhadzadeh and his dear wife Mrs. Fahimeh Pouryani were extremely helpful and friendly throughout the years I spent in the U.S. During the worst times I had in U.S. Ali was with me and never hesitated to show his generous helps. I feel very fortunate to have met them and hope we keep in touch forever.

My dear friends, structural engineer Gökcan Karakuş and economist Hakan Bingöl, were always supportive with their regular phone calls and encouragement. I thank them all for making the long distances short.

Finally I want to thank my family, my father Ahmet Bayındır, my mother Göksel Bayındır and my sister Dilan Bayındır for their endless support and understanding. My

father is a great source of inspiration for me since the early days in the primary school. With his great expertise and talent in arts, law, history of science and arts, Ottoman language and proficiency in Persian he made very remarkable effects in the development of my career by introducing me the critical men and concepts of science, art, philosophy and language. I could have never been able to learn about those great things even with decades of studies under the university professors of these distinct areas. Also during my studies in the U.S. he accompanied me with few caricatures of outstanding quality. I feel extremely proud and lucky to have such a father and I thank him.

My mother, after retiring from her art and teaching activities, dedicated herself to my and my sister's development into a useful citizen and human. She is the figure that ties our family members to each other so tightly. It is not really possible for anyone to thank his/her mother but for the years I spent in the U.S. I thank her for putting up with this situation, for excellent Turkish food cooking instructions and for teaching us how to be happy and thankful with the small things.

I am particularly grateful for the understanding and support given by my smart and beautiful sister, Dilan Bayındır. She is the first of the few persons that gives me motivation to go on. At the last stages of writing, she made me extremely happy by getting perfect grades from the successive examinations in a very busy schedule. While she was busy with her professional guidance, counseling, adult and early childhood education activities as well as her doctoral studies, she created the possibility of seeing my family through web talks. I thank her for all these and for being my sister.

I wish I am a son good enough that this family deserves. Their love is the most valuable thing I ever had. I hope this dissertation accounts for the missing three years in our lives which we lived far from each other.

This research is supported by Georgia Institute of Technology under research assistantship funds. The satellite imagery used in this research is provided by Japanese Space Agency's Advanced Land Observation Satellite (ALOS) through NASA's Alaska SAR Facility (ASF), at the University of Alaska, Fairbanks, AK.

TABLE OF CONTENTS

LIST OF TABLES

LIST OF FIGURES

SUMMARY

Synthetic aperture radar (SAR) is one of the most versatile tools ever invented for imaging. Due to its better Rayleigh resolution SAR imaging provides the highest quality radar imagery. These imagery are used for many applications including but not limited to terestrial mapping, disaster reconnaissance, medical imaging and military applications. SAR images can be produced using different kinds of imaging geometries such as stripmap, spotlight, circular and elevation circular. There are also various image processing techniques used to reconstruct the images. Some of these methods are digital reconstruction via range stacking, digital reconstruction via time domain correlation and backprojection, polar format processing, Stolt format processing (digital reconstruction via spatial frequency interpolation) and range-Doppler imaging. Imaging techniques or geometries which can improve the resolution of the reconstructed imagery is always desired in the SAR imaging.

In this dissertation both the linear and nonlinear frequency modulated chirp signals are discussed. The most widely used frequency modulated chirp signal, linear frequency modulated chirp signal, and some of its properties such as spectrum, point spread function and matched filter are summarized. A new nonlinear frequency modulated chirp signal which has the form of $\exp(j\eta t^{1.75})$ and named as $t^{0.75}$ frequency modulated ($t^{0.75}$FM) chirp signal is introduced, which can be used to improve the image resolution. Compared to the generally used linear frequency modulated chirps, this chirp is shown to be capable of reducing the sidelobes of the point spread function without having an adverse effect on signal-to-noise ratio and mainlobe width of the point spread function. It is also shown that adopting a same bandwidth same slew rate approach, $t^{0.75}$FM chirp has a shorter pulse duration compared to linear frequency modulated chirp therefore is more efficient. It is also discussed that $t^{0.75}$FM can have some other potential uses such as when used in hybrid chirps it can help to improve the resolution.

In order to validate the new offered chirp signal, spotlight SAR imaging geometry together with 2D polar and Stolt format reconstruction algorithms are considered. The synthetic examples are generated using both chirps with polar and Stolt format processing and it is shown that $t^{0.75}$FM chirp can improve the resolution compared to the LFM chirp. Reconstructed imagery provides a synthetic data basis for testing the change detection methodology and algorithms.

A new change detection method which depends on the idea of generating two different final change maps of the initial and final images, is offered. First final change map is obtained by cumulatively adding the sequences of change maps in such a manner that common change areas are excluded and uncommon change areas are included in the successive change maps. The second final change map is obtained by comparing the first and the last images in the temporal sequence. This method requires at least three image sequence to be employed and can be generalized to longer temporal image sequences. The purpose of this approach is to provide a double check mechanism to the conventional approach and thus can reduce the probability of false alarm. The specific algorithms utilized for testing this method are the widely used correlation coefficient change statistic and the intensity ratio change statistic algorithms. Therefore these algorithms and the probabilistic selection of the threshold criteria is discussed as well.

This method together with the algorithms mentioned are first applied to synthetic data generated by Stolt format processing. It is shown that the method works on synthetic data. The method together with the algorithms mentioned are also applied to two case studies of real disasters, one is 2010 Gulf of Mexico oil spill and the second is 2008 China Sichuan earthquake. It is shown that two final change map method can reduce the false identifications of the changes. Also it is shown that intensity ratio change statistics is a better tool for identifying the changes due to oil contamination.

The data used in this study is acquired by Japanese Aerospace Agency's Advanced Land Observing Satellite (ALOS) through Alaska SAR Facility (ASF), at the University of Alaska, Fairbanks, AK.

CHAPTER I

INTRODUCTION

Synthetic aperture radar (SAR) is a radar system which provides high resolution maps used for imaging targets including but not limited to terrains, planets, civilian infrastructure and military operations. Airborne warning and control systems, surveillance target attack systems and NASA space shuttle systems are equipped with this radar system. This system is also used for medical imaging methods.

Generally SAR imaging is classified according to the imaging geometry . Some of these classes are stripmap, spotlight, circular and elevation circular SAR imaging.

Images of the targets are constructed using some special signal processing techniques. Some of these techniques are digital reconstruction via range stacking, digital reconstruction via time domain correlation and backprojection, polar format processing, Stolt format processing (digital reconstruction via spatial frequency interpolation) and range-Doppler imaging.

One of the most dominant techniques used to extract information from SAR images is called change detection (CD) technique. This technique relies on making comparison between the images taken at different times to detect the changes occured. While mainly used for disaster reconnaissance purposes, CD technique is also used for military reconnaissance.

SAR imaging, or more generally imaging discipline, is always open for new contributions which can lead to better quality images.

The contributions of this dissertation can be summarized by the flowchart given in the Figure (1) below.

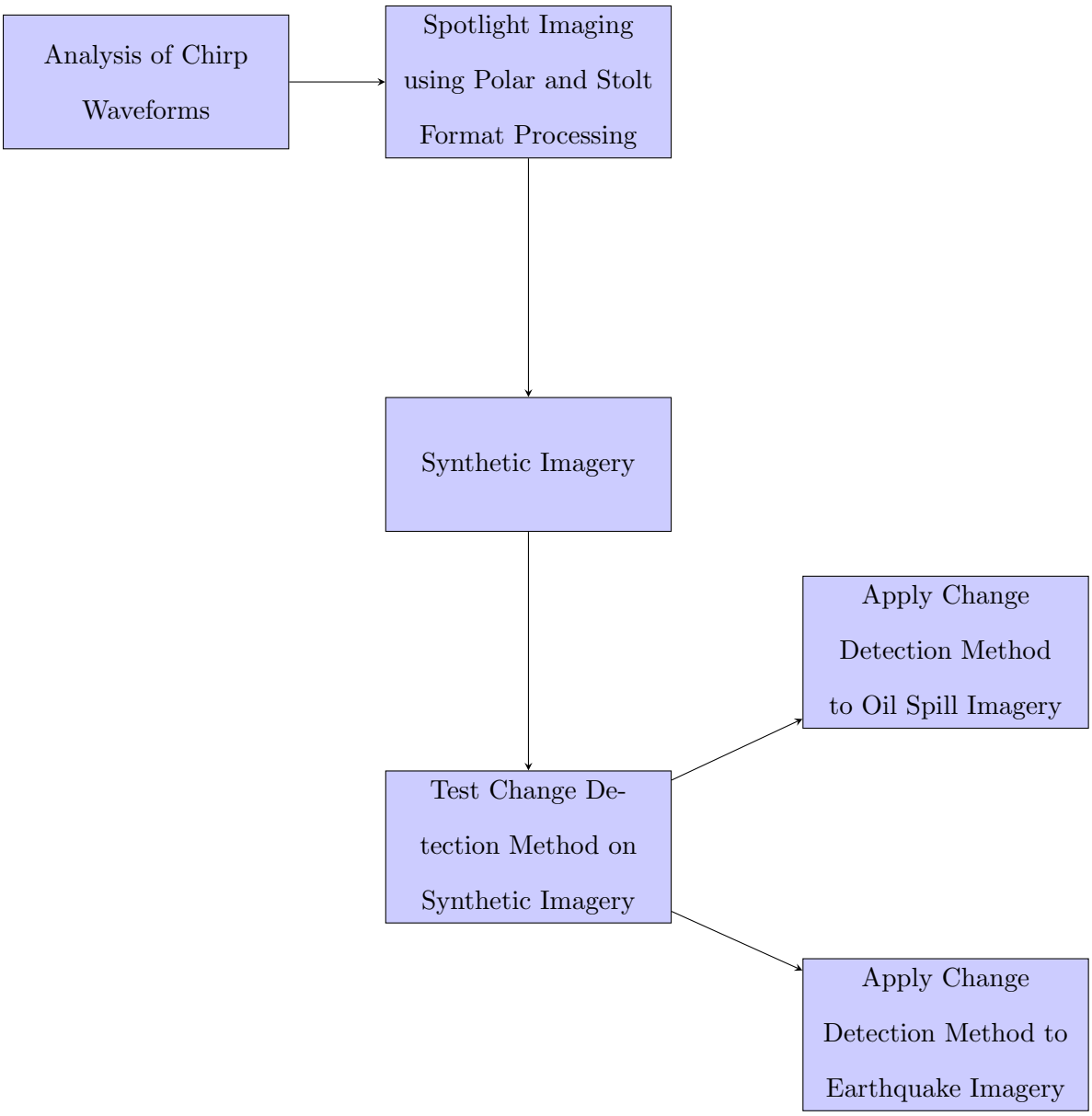

Figure 1: Flowchart of dissertation contributions.

More specifically; in chapter 2 of this dissertation a summary of the SAR imaging history, modalities and reconstruction methods are presented.

In chapter 3, the temporal and the spatial frequency modulated chirp signals are discussed. Most commonly used form of chirp signals is linear frequency modulated (LFM) signal. The detailed analysis of LFM signals, including some of its properties such as spectrum, point spread function and matched filter, is presented. Additionally a new nonlinear

frequency modulated chirp signal which has the form of $\exp(j\eta t^{1.75})$ and named as $t^{0.75}$ frequency modulated ($t^{0.75}$FM) chirp signal is introduced. Compared to the generally used linear frequency modulated chirps, this chirp is shown to be capable of reducing the sidelobes of the point spread function without having an adverse effect on signal-to-noise ratio and mainlobe width of the point spread function. It is also shown that adopting a same bandwidth, same slew rate approach $t^{0.75}$FM chirp has a shorter pulse duration compared to linear frequency modulated chirp therefore is more efficient. It is also discussed that $t^{0.75}$FM can have some other potential uses such as when used in hybrid chirps it can help to improve the resolution.

In chapter 4, the spotlight SAR imaging geometry, with a concentration on polar and Stolt format processing reconstruction methods, is discussed. Some examples of synthetic imagery are reconstructed using both processing techniques are presented. Additionally comparison of synthethic imagery reconstructed with LFM and $t^{0.75}$FM chirps are performed, for both of the processing techniques.

One of the most widely used family of techniques used to extract information from SAR images is called change detection algorithms. These techniques rely on making comparison between the images taken at different times to detect the changes occured. Although mainly used for disaster reconnaissance purposes, change detection technique is also used for military reconnaissance. In chapter 5, a new change detection method which depends on the idea of generating two different final change maps of the initial and final images, is offered. First final change map is obtained by cumulatively adding the sequences of change maps in such a manner that common change areas are excluded and uncommon change areas are included in the successive change maps. The second final change map is obtained by comparing the first and the last images in the temporal sequence. This method requires at least three image sequence to be employed and can be generalized to longer temporal image sequences. The purpose of this approach is to provide a double check mechanism to the conventional approach and thus can reduce the probability of false alarm. The specific algorithms utilized for testing this method are the widely used correlation coefficient

change statistic and the intensity ratio change statistic algorithms. Therefore these algorithms and the probabilistic selection of the threshold criteria are discussed as well. This two final change map method together with the algorithms mentioned are applied to synthetic data reconstructed by the Stolt format processing which provides higher resolution imagery compared to polar format processing and obeys the real imaging scenarios better.

In chapter 6, the two final change map method together with the algorithms mentioned are applied to real disaster data which is acquired by Japanese Aerospace Agency's Advanced Land Observing Satellite (ALOS). Technical properties of the ALOS system are presented. The two disasters considered are the 2010 Gulf of Mexico oil spill and the 2008 China Sichuan earthquake. A brief history of these disasters and use of SAR data in assessing those type of disasters are presented as well. While oil spill is an evolving type of disaster, the earthquake is an impulsive type. The correlation coefficient change statistic and the intensity ratio change statistic algorithms as well as the two final change map method are tested on these disaster imagery. It is shown that correlation coefficient change statistic has a better performance on assessing the changes occured in bright pixel areas whereas the intensity ratio change statistic is a better choice for the oil spill detection, especially in the vicinity of lands. The use of both statistics may be necessary to detect the changes in the bright or dark pixel regions. It is also shown that the number of false alarms can be significantly reduced using the double check mechanism introduced by two final change map method.

In chapter 7, conclusions and the recommendations for future work are presented.

CHAPTER II

SYNTHETIC APERTURE RADAR (SAR) IMAGING

Remote sensing techniques are fundamental ways of creating terrestrial maps therefore assessing natural hazards and disasters [34]. Some of these techniques are synthetic aperture radar (SAR), optical, multispectral, thermal, ultra-violet (UV) and digital elevation model (DEM) imaging techniques [34]. These techniques has some advantages and disadvantages compared to each other. For example SAR imaging provides high resolution and high precision data as well as it can be used in all weather conditions [34]. It can also be used during day or night. However its accuracy may depend on the acquisition geometry and wavelength [34]. SAR side-looking acquisition geometry creates distortion and shadowed regions in the image [34]. Coherent SAR imaging is also very sensitive to the scattering of electromagentics waves from the target therefore does not work well for vegetated areas [34]. Optical imaging provides high resolution data and for some case studies it is shown that optical imagery can perform better than SAR imagery in assessing the changes due to disasters [34] however optical imaging can only be performed during day time and generally areas covered are not as large as the areas covered by SAR imaging. Multispectral imaging technique provides spectral information about the scene however band-limited imaging may result in loss of the spatial resolution [34]. Thermal and UV techniques are well tested and widely used however they provide relatively low spatial resolution and they require very high temporal resolution to monitor the changes [34]. DEM technique gives very precisive elevation measurements therefore can be used in observing the volumetric changes due to disasters such as landslides [34]. However DEM data especially when acquired by light detection and ranging (LiDAR) sensors is expensive and takes considerable amount of time [34]. In this dissertation SAR remote sensing technique and imagery is considered however the enhancements to the incoherent SAR change detection offered can also be used in other remote sensing change detection studies.

SAR is a high quality imaging technique originally developed for airborne radar systems. The motivation behind SAR technique is to improve the cross range resolution of a radar imaging system. The cross-range (or lateral) Rayleigh resolution Δ_R of an antenna with diameter D is given by the relation

$$\Delta_R = \frac{R\lambda}{D} \tag{1}$$

where λ is the wavelength and R is the range [48]. The resolution can be improved by making D larger. However, antenna size is limited by practical limitations. The concept of a synthetic aperture was introduced in 1951 by Carl Wiley, an engineer employed at the Goodyear Aircraft Corporation [33]. By introducing a synthethic aperture the effective diameter of the antenna can be increased. Therefore the Rayleigh resolution given by equation (1) can be improved. Although he filed for a US patent for his invention, it was not until 1965 the patent was issued [33]. For his invention Wiley used the name Doppler beam sharpening instead of synthetic aperture radar .

L. J. Cutrona of the University of Michigan and C. W. Sherwin of the University of Illinois developed the same ideas from a spectral point of view [4]. Joint effort between these two universities was conducted in 1953 under the project name Project Wolverine. This project resulted in a high resolution combat surveillance radar system [4]. Due to lack of high performance computers and signal processing algorithms, early systems were made up of optical components such as lens performing Fourier transforms and holographic recording techniques. With the advance of digital computers and invention of efficient signal processing algorithms such as fast Fourier transforms, radar systems are revolutionized and today their hardware consists of digital components instead of optical analog components [14]. Currently SAR imaging has a wide range of applications including but not limited to terresterial topographic imaging, airborne and spaceborne reconnaissance, underground resource exploration, mine detection, missile tracking and medical imaging [48]. SAR imaging became one of the most critical inventions of the 20th century.

There are modalities of SAR imaging operations which are generally named after imaging geometry. Most commonly used mode is stripmap SAR imaging. In stripmap imaging, the radar platform flies in a linear path and ground strips are imaged without any beam steering.

This modality is used when large areas of terrain needs to be mapped [48].

Another widely used mode is spotlight SAR imaging. In spotlight SAR, the radar platform again flies in a linear path but by electronical or mechanical beem steering a ground spot is targeted at distinct times of the flight. This modality can provide better resolution imagery compared to stripmap SAR imaging modality [48].

There are also some imaging modalities where radar platform flies in a nonlinear orbit. Two of these methods are circular SAR imaging and elevation circular SAR imaging. In circular imaging radar platform flies in a circular orbit. The circular SAR is capable of producing acceptably good imagery with a partial or full rotation and also is capable of generating image slices along the vertical axis of the target function [47]. Another recently offered modality is elevation circular SAR imaging. In elevation circular SAR imaging the radar platform not only flies in a circular orbit but also changes elevation along the orbit [22].

In forward looking SAR imaging the radar platform illuminates a ground target located in the direction of flight instead of illuminating an area sidewards as sidescan SAR imaging scenarios discussed above. A detailed discussion of forward looking SAR used for runway imaging can be seen in [4] and [15].

Volumetric SAR (VolSAR) imaging is a recently emerging technique discussed in [4] which can be used to reconstruct the volumetric images of the target scene. VolSAR imaging can be applied to all known imaging geometries discussed above. VolSAR imaging heavily depends on 3D signal processing. A discussion of 3D signal processing can be seen in [8]. After image reconstruction process the resulting 3D VolSAR imagery consists of so called voxels instead of 2D imagery containing pixels. VolSAR imaging can be achieved for the all modalities listed above and can be named as stripmap VolSAR, spotlight VolSAR, circular VolSAR, elevation circular VolSAR and forward looking VolSAR [4]. A detailed discussion of the VolSAR imaging can be seen in [4].

There are also various image reconstruction methods used for the different types of the imaging scenarios discussed above. SAR signal processing techniques used for these image reconstruction methods can be classified as Fresnel (truncated Taylor series), Fraunhofer

(plane wave) approximations or Huygens-Fresnel approximation-free method [4]. Depending on the basics of the underlying ideas reconstruction algorithms are given special names. For example, stripmap SAR image reconstruction can be performed by Stolt format (also known as digital reconstruction via spatial frequency interpolation), range stacking, time domain correlation or backprojection algorithms [48]. Spotlight SAR image reconstruction can be performed by polar format, Stolt format, reconstruction in squint spatial coordinates, digital reconstruction via range stacking, time domain correlation or backprojection algorithms as discussed in [48]. Circular SAR image reconstruction can be performed by Stolt format and digital reconstruction via range stacking and via time domain correlation and backprojection algorithms [48]. Elevation circular SAR image reconstruction can be achieved by time domain correlation, plane wave approximation or wavefront reconstruction techniques [22]. Forward looking SAR can be performed via any of the reconstruction methods mentioned above depending on the illuminated geometry.

SAR imaging heavily depends on Fourier analysis whose discussion can be seen in [12]. More detailed discussions of the SAR imaging algorithms can be seen in [48], [23], [30], [4], [17] and [14].

CHAPTER III

CHIRP SIGNALS

The range resolution due a pulse is given by $\Delta_R = \frac{cT_p}{2}$ where c is the speed of light and T_p is the pulse duration [36]. Resolution can be improved by using a shorter pulse but in order to satisfy an average power limit, T_p can not be infinitely small [14]. Modern radar systems can overcome this difficulty by transmitting phase-coded long pulses [14]. Compression of these signals is performed with signal processing operations after reception [14]. Some of these phase-codings are linear frequency modulated codes, Barker codes, chirp-like phase codes, Golomb's codes, Huffman codes and asymptotically perfect codes as given in [36].

The most popular choice for an analog phase-coded waveform is linear frequency-modulated (LFM) waveform [14]. LFM waveforms are popular because of the ease of signal generation and processing [14]. Another name used for this waveform is *chirp* because an audio signal of changing frequency over time is similar to a bird's chirp [14]. The LFM chirp signals are not only used in SAR systems but also in conventional radar systems [14]. SAR phase histories usually contains both temporal and spatial chirp elements [4].

In this section both the temporal and spatial chirp waveforms are discussed. The analysis for the linear frequency modulated waveforms is presented. A similar discussion can be seen in [30]. Additionally a new type of chirp signal, whose phase function is of the form $t^{1.75}$, is offered and its properties are summarized in the following sections. This new chirp signal is named as $t^{0.75}$ frequency modulated ($t^{0.75}$FM) chirp waveform.

3.1 Temporal Chirp Signals

In this section chirp signals which are frequency modulated in the time domain are discussed. The analysis for the linear frequency modulated waveforms are presented as well as a new type of chirp signal, which is named as $t^{0.75}$ frequency modulated waveform, which has certain advantages over the linear frequency modulated waveform, is offered.

3.1.1 Linear Frequency Modulated Chirp Signals

The most commonly used form of the chirp signal in radar signal processing is the linear chirp signal which is also known as linear frequency modulated (LFM) chirp signal. The LFM chirp can be written as

$$p(t)^{LFM} = \exp(j\alpha t^2) \tag{2}$$

where j is the imaginary number with $j^2 = -1$ and α is called the slew rate. In the Figure (2) a plot of LFM chirp given in equation (2) can be seen for $\alpha = 100$.

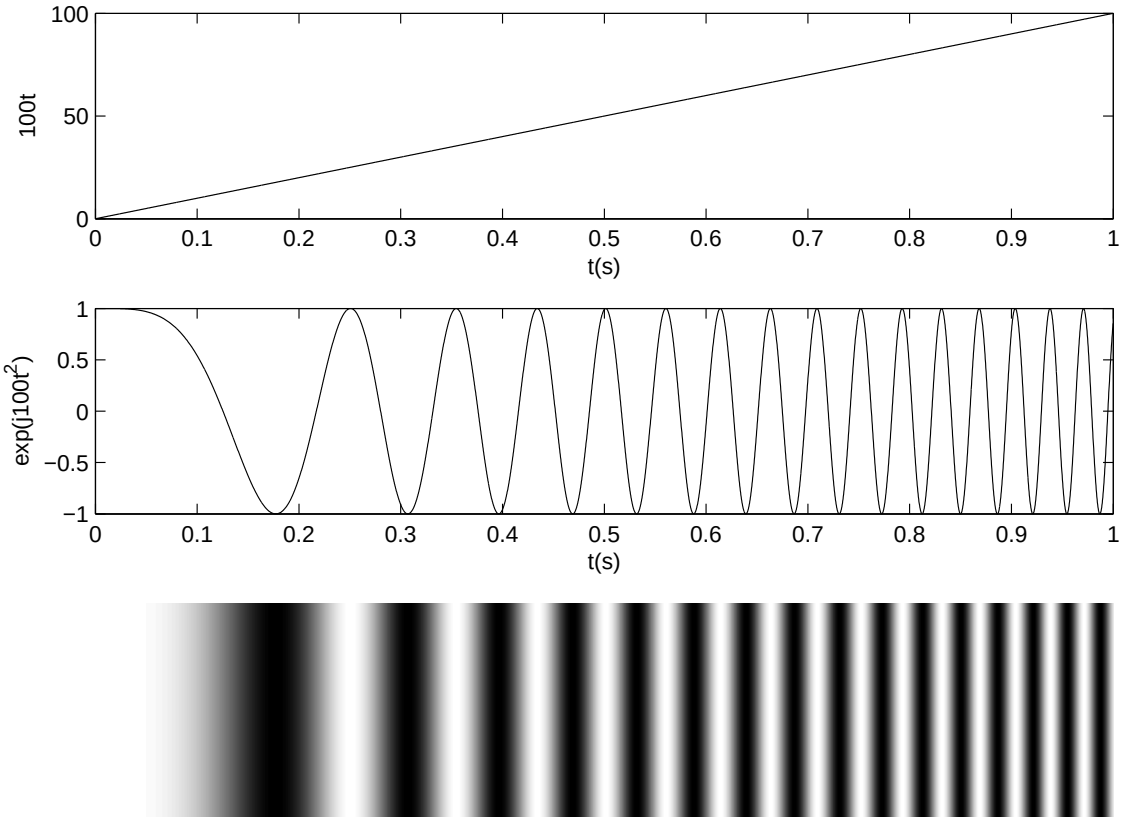

Figure 2: LFM chirp signal phase map.

As it can be seen in the Figure (2) the LFM chirps exhibit a linearly varying phase modulating function. Therefore it is called linear frequency modulated chirp. Linearly increasing or decreasing LFM chirps are used in SAR signal processing [4]. In this section only linearly increasing LFM chirps are considered.

Spectrum of LFM Chirps For image reconstruction process it may be necessary to use the spectrum of the LFM chirps depending on the reconstruction methodology. The Fourier transform of the LFM signal given by equation (2) can be written as

$$\begin{aligned} P(\omega)^{LFM} &= FT_{1D}^{t}\left\{p(t)^{LFM}\right\} \\ &= \int_{-\infty}^{\infty} \exp(j\alpha t^2)\exp(-j\omega t)dt \\ &= \int_{-\infty}^{\infty} \exp\left[j\alpha\left(t^2 - t\frac{\omega}{\alpha}\right)\right]dt \end{aligned} \tag{3}$$

By completing the argument of the integrand to a square one can rewrite the equation (3) as follows

$$P(\omega)^{LFM} = \exp\left[-j\frac{\omega^2}{4\alpha}\right]\int_{-\infty}^{\infty}\exp\left[j\alpha\left(t-\frac{\omega}{2\alpha}\right)^2\right]dt \tag{4}$$

Setting

$$x = \sqrt{\alpha}\left(t-\frac{\omega}{2\alpha}\right), \qquad dx = \sqrt{\alpha}dt \tag{5}$$

the integral in the equation (4) becomes

$$\int_{-\infty}^{\infty}\exp\left[j\alpha\left(t-\frac{\omega}{2\alpha}\right)^2\right]dt = \frac{1}{\sqrt{\alpha}}\int_{-\infty}^{\infty}\exp\left(jx^2\right)dx \tag{6}$$

Using Euler's identity

$$\exp\left(jx^2\right) = \cos\left(x^2\right) + j\sin\left(x^2\right) \tag{7}$$

and using the following tabulated values of the Fresnel integrals given in [3],

$$\int_{-\infty}^{\infty}\cos\left(x^2\right)dx = \int_{-\infty}^{\infty}\sin\left(x^2\right)dx = \sqrt{\frac{\pi}{2}} \tag{8}$$

one can obtain

$$\begin{aligned} \frac{1}{\sqrt{\alpha}}\int_{-\infty}^{\infty}\exp\left(jx^2\right)dx &= \frac{1}{\sqrt{\alpha}}\left(\sqrt{\frac{\pi}{2}} + j\sqrt{\frac{\pi}{2}}\right) \\ &= \sqrt{\frac{\pi}{\alpha}}e^{j\frac{\pi}{4}} \end{aligned} \tag{9}$$

so that equation (4) becomes

$$P(\omega)^{LFM} = \sqrt{\frac{\pi}{\alpha}}e^{j\frac{\pi}{4}}\exp\left(j\frac{\omega^2}{4\alpha}\right) \tag{10}$$

which is the spectrum of the LFM chirp given by the equation (2). It is useful to note that an LFM chirp in time domain has a spectrum which is an LFM chirp in the frequency domain.

Pulse LFM Chirps In radar signal processing the LFM chirps are used with a windowing function since it is only possible to generate a finite duration waveform. The pulse LFM chirps can be written as

$$p_{\Pi_{(T_p)}}(t)^{LFM} = \Pi_{(T_p)}(t)\exp(j\alpha t^2) \tag{11}$$

where T_p is the pulse duration and

$$\Pi_{(T_p)}(t) = \begin{cases} 1 & \text{if } -T_p/2 \le t \le T_p/2 \\ 0 & \text{if otherwise} \end{cases} \tag{12}$$

is the windowing function. The plot of the pulsed LFM chirp given in equation (11) is essentially the same plot given in Figure (2) with the windowing function mentioned above.

Spectrum of Pulse LFM Chirps For image reconstruction process it may be necessary to use the spectrum of the pulse LFM chirps depending on the reconstruction methodology. The Fourier transform of the pulse LFM chirp can be written as

$$P_{\Pi_{(2\alpha T_p)}}(\omega)^{LFM} = FT^t_{1D}\left\{p_{\Pi_{(T_p)}}(t)^{LFM}\right\} \tag{13}$$

which leads to

$$\begin{aligned} P_{\Pi_{(2\alpha T_p)}}(\omega)^{LFM} &= \int_{-\infty}^{\infty} \Pi_{(T_p)}(t)\exp(j\alpha t^2)\exp(-j\omega t)dt \\ &= \int_{-T_p/2}^{T_p/2} \exp\left[j\alpha\left(t^2 - t\frac{\omega}{\alpha}\right)\right]dt \end{aligned} \tag{14}$$

By completing the argument of the integrand to a square one can rewrite the equation (14) as follows

$$P_{\Pi_{(2\alpha T_p)}}(\omega)^{LFM} = \exp\left[-j\frac{\omega^2}{4\alpha}\right]\int_{-T_p/2}^{T_p/2}\exp\left[j\alpha\left(t - \frac{\omega}{2\alpha}\right)^2\right]dt \tag{15}$$

Setting

$$x = \sqrt{\alpha}\left(t - \frac{\omega}{2\alpha}\right), \qquad dx = \sqrt{\alpha}dt \tag{16}$$

one obtains

$$P_{\Pi_{(2\alpha T_p)}}(\omega)^{LFM} = \frac{1}{\sqrt{\alpha}}\exp\left[-j\frac{\omega^2}{4\alpha}\right]\int_{\sqrt{\alpha}(-T_p/2-\omega/2\alpha)}^{\sqrt{\alpha}(T_p/2-\omega/2\alpha)}\exp\left(jx^2\right)dx \tag{17}$$

which can be rewritten as

$$P_{\Pi_{(2\alpha T_p)}}(\omega)^{LFM} = \frac{1}{\sqrt{\alpha}} \exp\left[-j\frac{\omega^2}{4\alpha}\right] \times \left(-\int_0^{\sqrt{\alpha}\left(\frac{-T_p}{2}-\frac{\omega}{2\alpha}\right)} \exp\left(jx^2\right) dx + \int_0^{\sqrt{\alpha}\left(\frac{T_p}{2}-\frac{\omega}{2\alpha}\right)} \exp\left(jx^2\right) dx \right) \tag{18}$$

As given in [3], the definite Fresnel integral is defined as

$$F(\omega) = [C(\omega) + jS(\omega)] \tag{19}$$

where

$$C(\omega) = \sqrt{\frac{2}{\pi}} \int_0^{\omega} \cos\left(x^2\right) dx \tag{20}$$

$$S(\omega) = \sqrt{\frac{2}{\pi}} \int_0^{\omega} \sin\left(x^2\right) dx \tag{21}$$

A plot of $C(\omega)$ and $S(\omega)$ can be seen in the Figure (3) below.

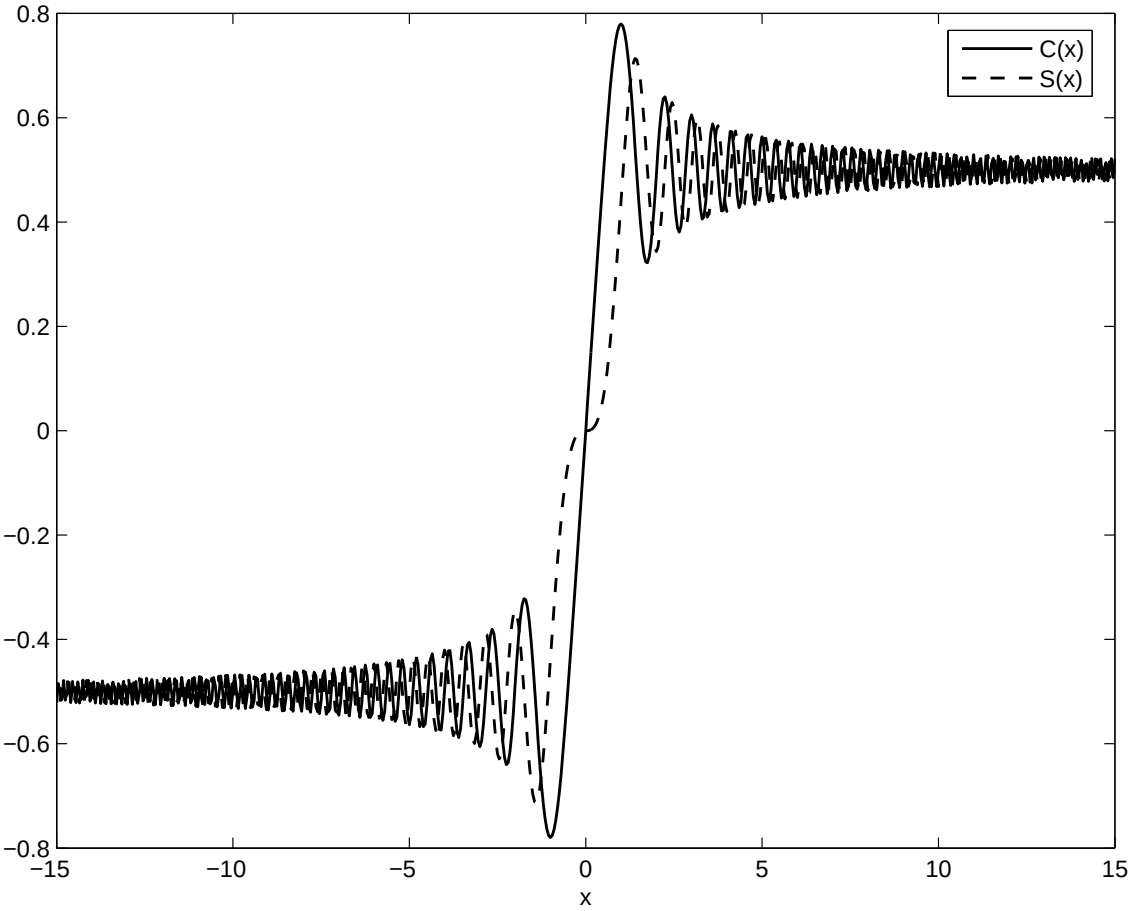

Figure 3: The real and imaginary parts of Fresnel integral.

Using the fact that Fresnel integral is an odd function, that is, $F(-\omega) = -F(\omega)$, one obtains

$$P_{\Pi_{(2\alpha T_p)}}(\omega)^{LFM} = \sqrt{\frac{\pi}{2\alpha}} \exp\left[-j\frac{\omega^2}{4\alpha}\right] \times \sqrt{\frac{2}{\pi}} \left(\int_0^{\frac{1}{2\sqrt{\alpha}}(\omega+\alpha T_p)} \exp\left(jx^2\right) dx - \int_0^{\frac{1}{2\sqrt{\alpha}}(\omega-\alpha T_p)} \exp\left(jx^2\right) dx \right) \tag{22}$$

which can be rewritten as

$$P_{\Pi_{(2\alpha T_p)}}(\omega)^{LFM} = \sqrt{\frac{\pi}{2\alpha}} \exp\left(-j\frac{\omega^2}{4\alpha}\right) \left[F\left(\frac{\omega+\alpha T_p}{2\sqrt{\alpha}}\right) - F\left(\frac{\omega-\alpha T_p}{2\sqrt{\alpha}}\right) \right] \tag{23}$$

The plot of the equation (23) which is the Fourier transform of the pulse LFM chirp given by equation (11) can be seen in the Figure (4) for $\alpha = 2$.

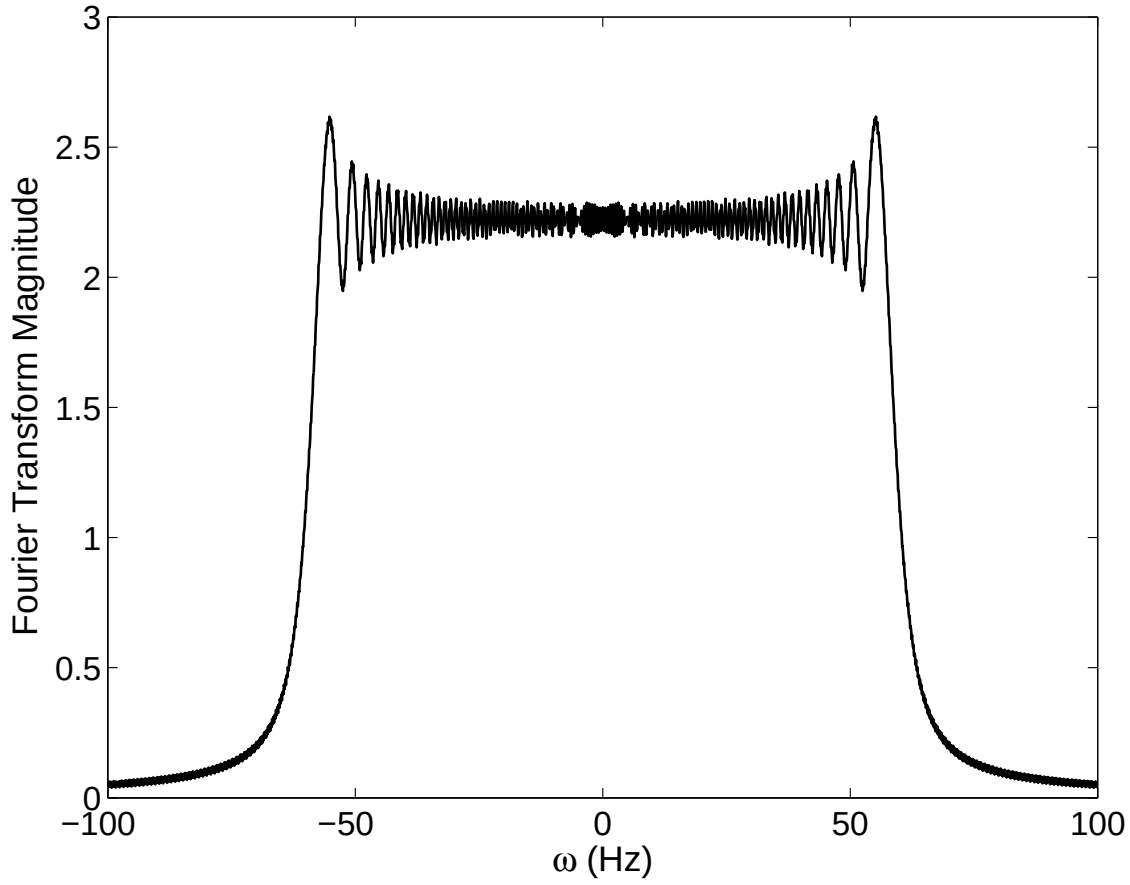

Figure 4: Fourier transform of the pulse LFM chirp signal.

Matched Filtering for LFM Chirp Signals Matched filtering is the primary method used to detect the presence of a known signal, or template, in an unknown signal. It

can be performed by correlating the known signal with the unknown signal. Matched filtering can be performed in time or frequency domains by using Fourier transforms and convolutions. Matched filtering is extensively used in radar and sonar signal processing, telecommunications and some other branches of signal processing.

Considering a received 1D signal model given by

$$\begin{aligned} s(t) &= \sum_n s_n(t) \\ &= \sum_n \sigma_n p\left(t - \frac{2x_n}{c}\right), \quad \text{where} \quad n = 1, 2, ... \end{aligned} \tag{24}$$

where p is the known signal. The Fourier transform of the equation (24) is

$$S(\omega) = P(\omega) \sum_n \sigma_n \exp\left(-j\omega \frac{2x_n}{c}\right) \tag{25}$$

If the bandwidth is infinite, that is if $P(\omega)$ nonzero, then the range imaging can be performed by an operation called source deconvolution. But in practice it is not possible to use a signal with infinite bandwidth. Therefore for this purpose we are using the matched filtering. Matched filtering is also used to remove additive white noise when the signal is corrupted [36],[48]. Performing matched filtering in the frequency domain

$$\begin{aligned} s_M(t) &= IFT_{1D}^{\omega}\left[S(\omega)P^*(\omega)\right] \\ &= IFT_{1D}^{\omega}\left[\sum_n \sigma_n \left|P(\omega)\right|^2 \exp\left(-j\omega \frac{2x_n}{c}\right)\right] \\ &= \sum_n \sigma_n \mathsf{psf}_t\left(t - \frac{2x_n}{c}\right) \end{aligned} \tag{26}$$

where $P^*(\omega)$ is the complex conjugate of $P(\omega)$ and IFT_{1D}^{ω} denotes 1D inverse Fourier transform operation and

$$\begin{aligned} \mathsf{psf}_t(t) &= IFT_{1D}^{\omega}\left[\left|P(\omega)\right|^2\right] \\ &= \frac{1}{2\pi}\int_{-\infty}^{\infty} \left|P(\omega)\right|^2 e^{j\omega t} d\omega \end{aligned} \tag{27}$$

is the point spread function. Matched filtered signal can also be written as

$$\begin{aligned} s_M(t) &= s(t) \otimes p^*(-t) \\ &= f_0\left(\frac{ct}{2}\right) \otimes \mathsf{psf}_t(t) \end{aligned} \tag{28}$$

where $\otimes$ is the time domain convolution. Inverse Fourier transform of $P^*(\omega)$ is $p^*(-t)$ which is the time domain matched filter. For instance if the radar bandwith is $\omega \in [\omega_c - \omega_o, \omega_c + \omega_o]$ and $|P(\omega)| = 1$ for these ω values that point spread function becomes

$$\mathsf{psf}_t(t) = \frac{\omega_o}{\pi} \exp(j\omega_c t)\mathrm{sinc}(\omega_o t) \tag{29}$$

where sinc function is defined by

$$\mathrm{sinc}(x) = \frac{\sin(x)}{x} \tag{30}$$

Some researchers use the normalized version of the equation (29) such as [48]. Then the target function can be formed by

$$f(x) = s_M(t) = \sum_n \sigma_n \mathsf{psf}_t \left[\frac{2}{c}(x - x_n)\right] \tag{31}$$

where

$$x = \frac{c}{2}t \tag{32}$$

Considering the Fourier transform of the LFM chirp signal given in the equation (10) one can perform its matched filtering as follows

$$\mathsf{psf}_t^{LFM}(t) = IFT_{1D}^{\omega}\left[\left|P(\omega)^{LFM}\right|^2\right] = IFT_{1D}^{\omega}\left[\frac{2\pi}{\alpha}\right] \tag{33}$$

which leads to

$$\mathsf{psf}_t^{LFM}(t) = \frac{2\omega_o}{\alpha} \exp(j\omega_c t)\mathrm{sinc}(\omega_o t) \tag{34}$$

so that

$$\begin{aligned} s_M^{LFM}(t) &= \sum_n \sigma_n \mathsf{psf}_t^{LFM}\left[\frac{2}{c}(x - x_n)\right] \\ &= \sum_n \sigma_n \frac{2\omega_o}{\alpha} \exp\left(j\omega_c \frac{2}{c}(x - x_n)\right) \mathrm{sinc}\left(\frac{\omega_o 2(x - x_n)}{c}\right) \end{aligned} \tag{35}$$

which gives the target scattering function $f(x)$.

3.1.2 $t^{0.75}$ Frequency Modulated Chirp Signals

Besides the typical LFM chirp signals discussed in the previous section there are other types of chirp signals called nonlinear frequency modulated (NLFM) chirps. A summary of existing NLFM chirps can be seen in [18]. The motivation behind offering a new chirp is

to improve the image resolution as well as to achieve a form which can be implemented in the hardware optimally. There are various ways to check if the offered chirp is improving the resolution or not. Most commonly used method is to evaluate autocorrelation or point spread function of the chirps in comparison and to check if the sidelobes are reduced as well as to look at the mainlobe width. As a tradeoff sidelobe reduction causes the mainlobe width to be increased which is an undesired effect, therefore it is desired to be limited.

Sidelobes of the autocorrelation functions of a chirp signal can be reduced to any level by applying a nonuniform amplitude function however this method results in reduced SNR, hard to implement and causes an increase in the mainlobe width [16]. Therefore, there are various forms of NFLM chirps offered in the literature which do not rely on this method. In this section a new NLFM chirp signal is offered which is named as $t^{0.75}$ frequency modulated ($t^{0.75}$FM) chirp signal. As discussed in the coming sections this chirp can achieve a reduction in the sidelobes of the autocorrelation function without having an adverse effect on the mainlobe width and SNR. Also this chirp can reach the same bandwidth of the LFM with the same slew rate using a shorter pulse duration, or reversely the same bandwidth of the LFM with the same pulse duration using a smaller slew rate. Therefore it more effective for hardware.

$t^{0.75}$FM chirp signal given in the following form

$$p(t) = \exp(j\eta t^{1.75}) \tag{36}$$

where η is the slew rate. In Figure (5) a plot of $t^{0.75}$FM chirp given in equation (36) can be seen for $\eta = 100$.

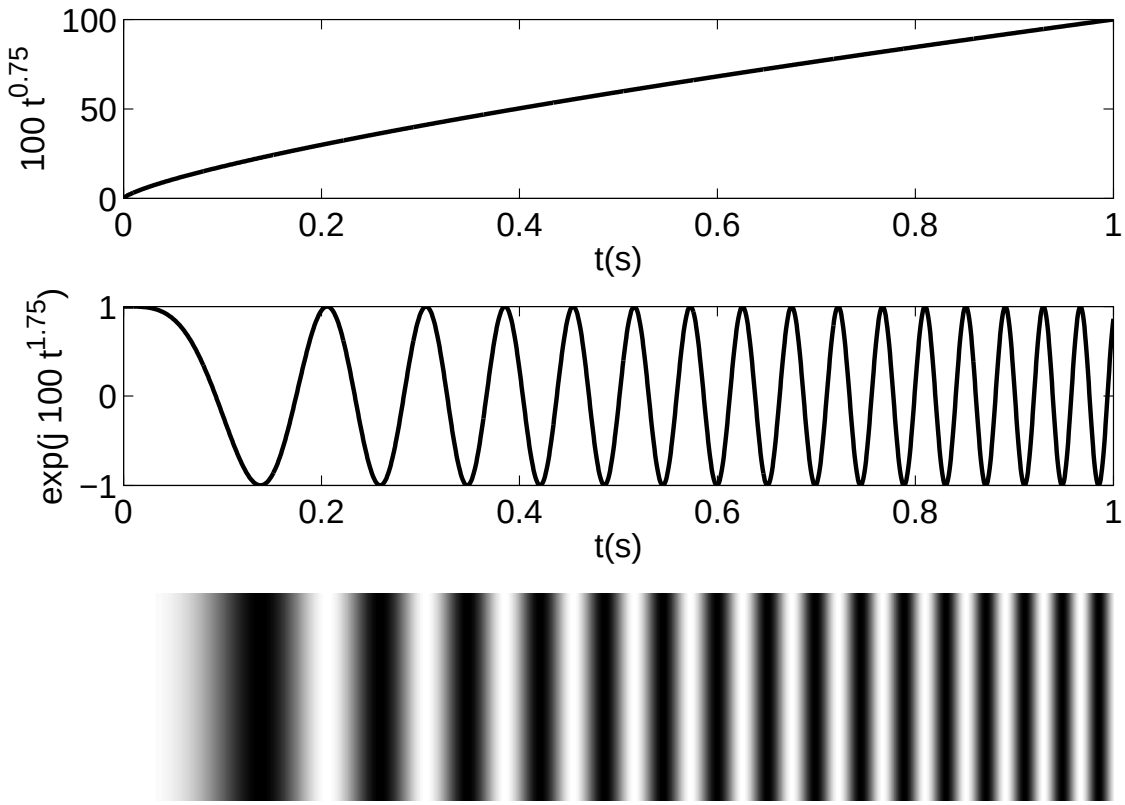

Figure 5: $t^{0.75}$FM chirp signal phase map.

The chirps, which have phase functions of the form t^p, where p is a noninteger such that $1.5 < p < 2$ show the similar tradeoffs in sidelobe reduction and mainlobe width increase of their point spread functions as will be discussed in the coming sections. Therefore $p = 1.75$ is selected as the mean value of this interval.

In order to calculate the bandwidth of the $t^{0.75}$FM chirp signal it is necessary to write the time derivative of the phase function as

$$\dot{\phi}(t) = 1.75\eta t^{0.75} \tag{37}$$

For a pulse with $T_s = 0,\ T_f = T_p$ the bandwidth of the $t^{0.75}$FM chirp signal becomes

$$B = 1.75\eta T_p^{0.75} \tag{38}$$

In order to perform a fair comparison between chirps generally same bandwidth approach is used. Taking the same chirp rates, that is $\eta = \alpha$, same bandwidth requirement leads to

$$2\alpha T_{p_{LFM}} = 1.75\eta T_{p_{t^{0.75}FM}}^{0.75} \tag{39}$$

which leads to

$$T_{p_{t^{0.75}FM}} \approx 1.19 T_{p_{LFM}}^{4/3} \tag{40}$$

Since the values of $T_{p_{LFM}}$ in radar imaging problems is generally on the order of microseconds, this relation states that same bandwidth can be achieved using a shorter pulse of $t^{0.75}$FM chirp compared to the pulse of the LFM chirp. Therefore the $t^{0.75}$FM chirp is more efficient.

Spectrum of $t^{0.75}$FM Chirp Signals The Fourier transform of the $t^{0.75}$FM chirp signal given by equation (36) can be expressed as

$$\begin{aligned} P(\omega) &= FT_{1D}^{t}\left\{p(t)\right\} \\ &= \int_{-\infty}^{\infty} \exp(j\eta t^{1.75}) \exp(-j\omega t) dt \end{aligned} \tag{41}$$

Asymptotic methods provide good approximations to the integrals which can not be evaluated analytically such as the integral given in the equation (41). One of the most powerful asymptotic methods is the method of stationary phases [7]. A discussion of the method of stationary phases is provided in the Appendix B. Implementing the method of stationary phases given in Appendix B one can write the phase function of the integral given in the equation (41) as

$$\Lambda(t) = \eta t^{1.75} - \omega t \tag{42}$$

First derivative of the phase function can be written as

$$\dot{\Lambda}(t) = 1.75\eta t^{0.75} - \omega \tag{43}$$

and the second derivative of the phase function can be written as

$$\ddot{\Lambda}(t) \approx \frac{1.31\eta}{t^{0.25}} \tag{44}$$

Stationary point, t_s, can be found by setting

$$\dot{\Lambda}(t_s) = 1.75\eta t_s^{0.75} - \omega = 0 \tag{45}$$

which leads to $t_s \approx \omega^{4/3}/2.11\eta^{4/3}$. The phase function, Λ, and the second derivative of the phase function, $\ddot{\Lambda}$, can be evaluated at the stationary point, t_s, as

$$\Lambda(t_s) \approx \frac{-0.20\omega^{7/3}}{\eta^{4/3}} \tag{46}$$

and

$$\ddot{\Lambda}(t_s) \approx \frac{1.58\eta^{4/3}}{\omega^{1/3}} \tag{47}$$

Following the method of stationary phases analysis given in the Appendix B the approximation of the integral given in the equation (41) can be obtained as

$$P(\omega) \sim 1.99\frac{\omega^{1/6}}{\eta^{2/3}} e^{j(\pi/4 - 0.20\omega^{7/3}/\eta^{4/3})} \tag{48}$$

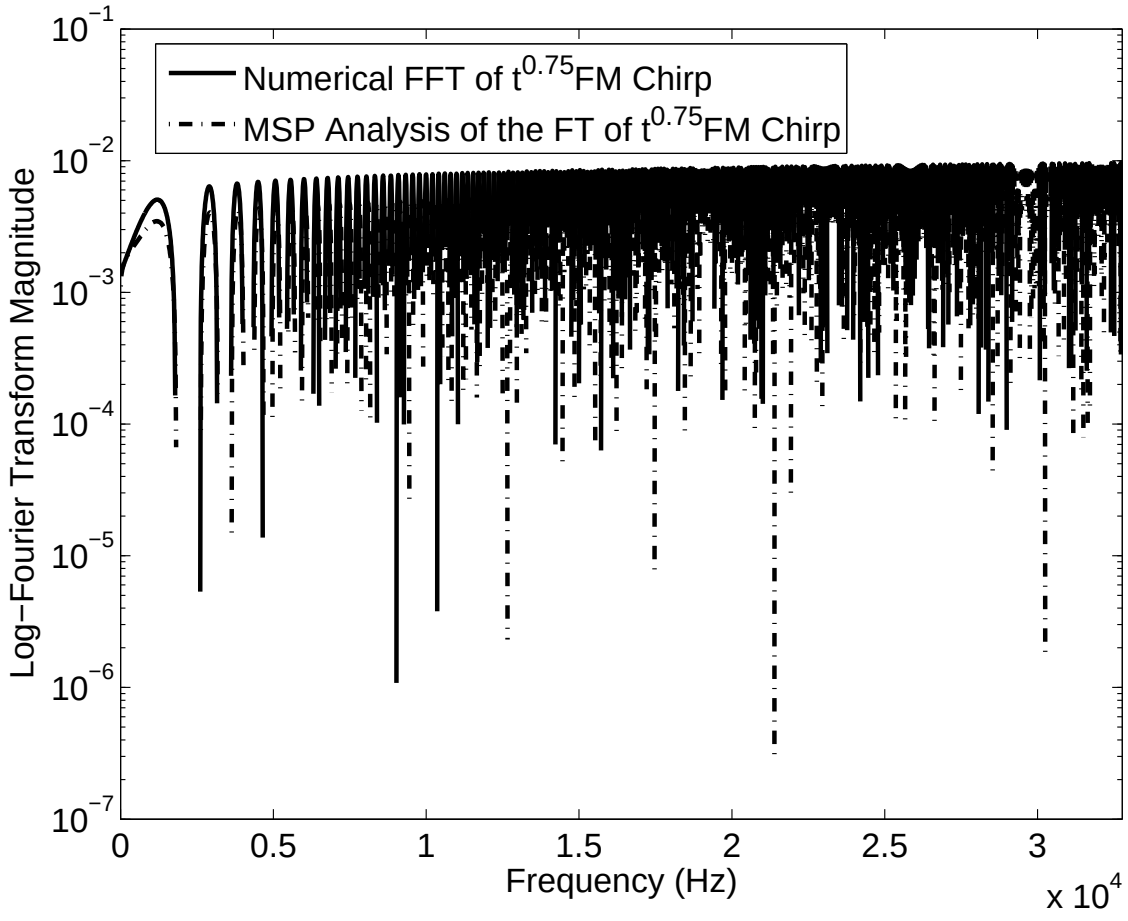

Figure 6: Comparison of the numerical and asymptotic Fourier transforms of the $t^{0.75}$FM chirp signal.

In the Figure (6) a comparison of the numerical and method of stationary phases evaluation of the one sided Fourier transform of the $t^{0.75}$FM chirp signal is presented for $\alpha = 2\times10^6$ and pulse duration window $[0, 0.1]$.

Pulse $t^{0.75}$FM Chirp Signals In radar signal processing the $t^{0.75}$FM chirps can be used with a windowing function since it is only possible to generate a finite duration waveform. The pulse $t^{0.75}$FM chirp can be written as

$$p_{\Pi_{(T_p)}}(t) = \Pi_{(T_p)}(t) \exp(j\eta t^{1.75}) \tag{49}$$

where T_p is the pulse duration and

$$\Pi_{(T_p)}(t) = \begin{cases} 1 & \text{if } 0 \leq t \leq T_p \\ 0 & \text{if otherwise} \end{cases} \tag{50}$$

is the windowing function. The plot of the pulsed $t^{0.75}$FM chirp given in the equation (49) is essentially the same plot given in the Figure (5) with the windowing function mentioned above.

Spectrum of Pulse $t^{0.75}$FM Chirp Signals The Fourier transform of the pulse $t^{0.75}$FM chirp signal given by the equation (49) can be expressed as

$$\begin{aligned} P(\omega) = FT^t_{1D}\left\{p(t)\right\} &= \int_{-\infty}^{\infty} \Pi_{(T_p)}(t) \exp(j\eta t^{1.75}) \exp(-j\omega t) dt \\ &= \int_0^{T_p} \exp(j\eta t^{1.75}) \exp(-j\omega t) dt \end{aligned} \tag{51}$$

which can be evaluated as

$$P(\omega) \sim \begin{cases} 1.99 \frac{\omega^{1/6}}{\eta^{2/3}} e^{j(\pi/4 - 0.20\omega^{7/3}/\eta^{4/3})} & \text{if } t_s \approx \omega^{4/3}/2.11\eta^{4/3} \in [0, T_p] \\ 0 & \text{if otherwise} \end{cases} \tag{52}$$

The expression in upper branch of the equation (51) is derived previously for the $t^{0.75}$FM chirp signals and the expression in the lower branch of the equation (51) is guaranteed by the Riemann-Lebesgue lemma discussed in the Appendix B.

Matched Filtering for $t^{0.75}$FM Chirp Signals The matched filter for the $t^{0.75}$FM chirp signal can be obtained by following the process given in equations (24) to (32). Considering the Fourier transform of the $t^{0.75}$FM chirp signal its point spread function can be calculated as

$$\mathsf{psf}_t(t) = IFT^{\omega}_{1D}\left[|P(\omega)|^2\right] \tag{53}$$

Calculating this function numerically a comparison of the point spread functions of the LFM and $t^{0.75}$FM chirps presented in the Figure (7) below for a bandwidth of 100 MHz and a time window of $[0, 100 \times 10^{-6}]$ s for both chirps which have different chirp rates.

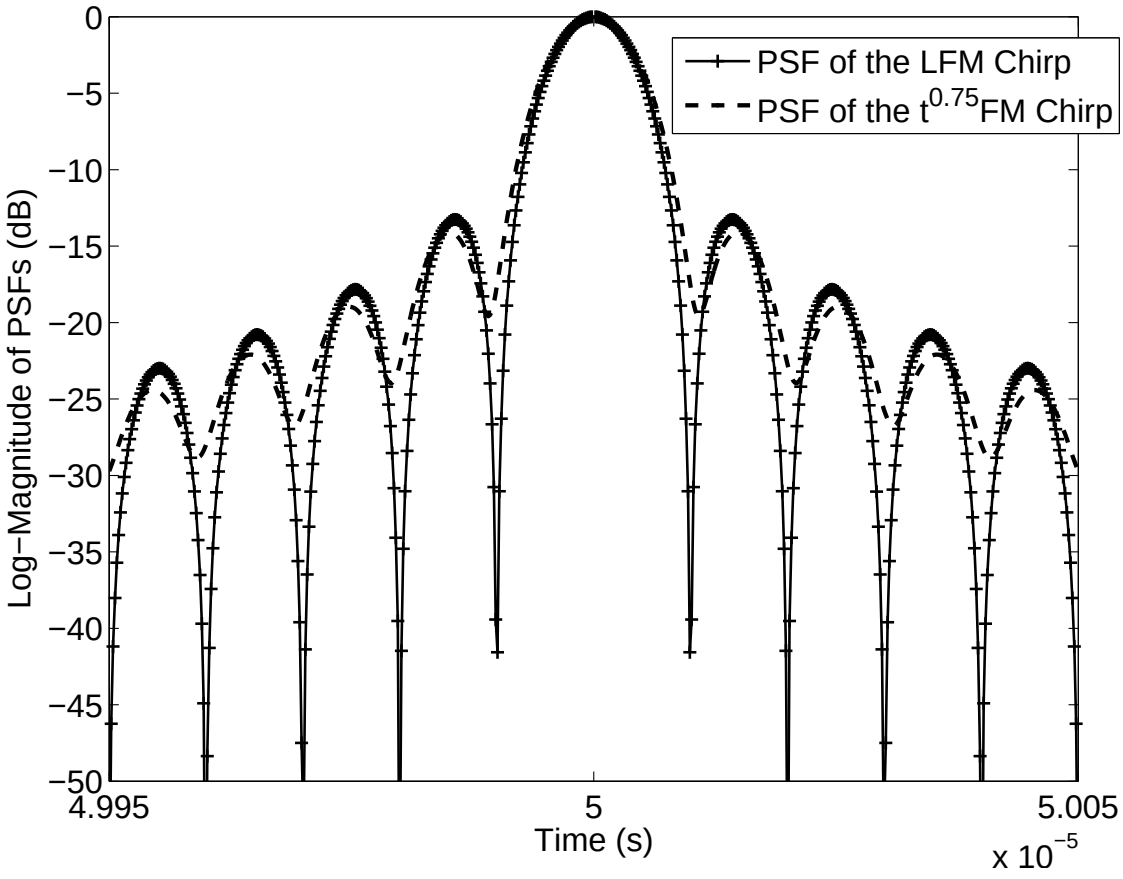

Figure 7: Comparison of the point spread functions of the LFM and $t^{0.75}$FM chirp signals-1.

For the given parameters the comparison of the point spread functions of the LFM and $t^{0.75}$FM chirps suggest that -3 dB mainlobe width of LFM chirp is around 8.77×10^{-9}s where as $t^{0.75}$FM chirp has a -3 dB mainlobe width of approximately 9.53×10^{-9}s. The ratio of these two parameters yield to a value of approximately 1.08 which suggests that the mainlobe of the point spread function of the $t^{0.75}$FM chirps is slightly larger than that of the LFM chirp, almost unrecognizable. Also reading of peak sibelobe values approximately lead to -13.25 dB for LFM chirp and -14.15 dB for the $t^{0.75}$FM chirp. Therefore a reduction of 0.90 dB can be achieved using the $t^{0.75}$FM chirp without having an adverse effect on the mainlobe width of the point spread function, therefore image quality can be improved.

Repeating the same analysis for a bandwidth of 60 MHz and a time window of $[0, 1 \times 10^{-6}]$s for both chirps which have different chirp rates, one can obtain the Figure (8) presented below.

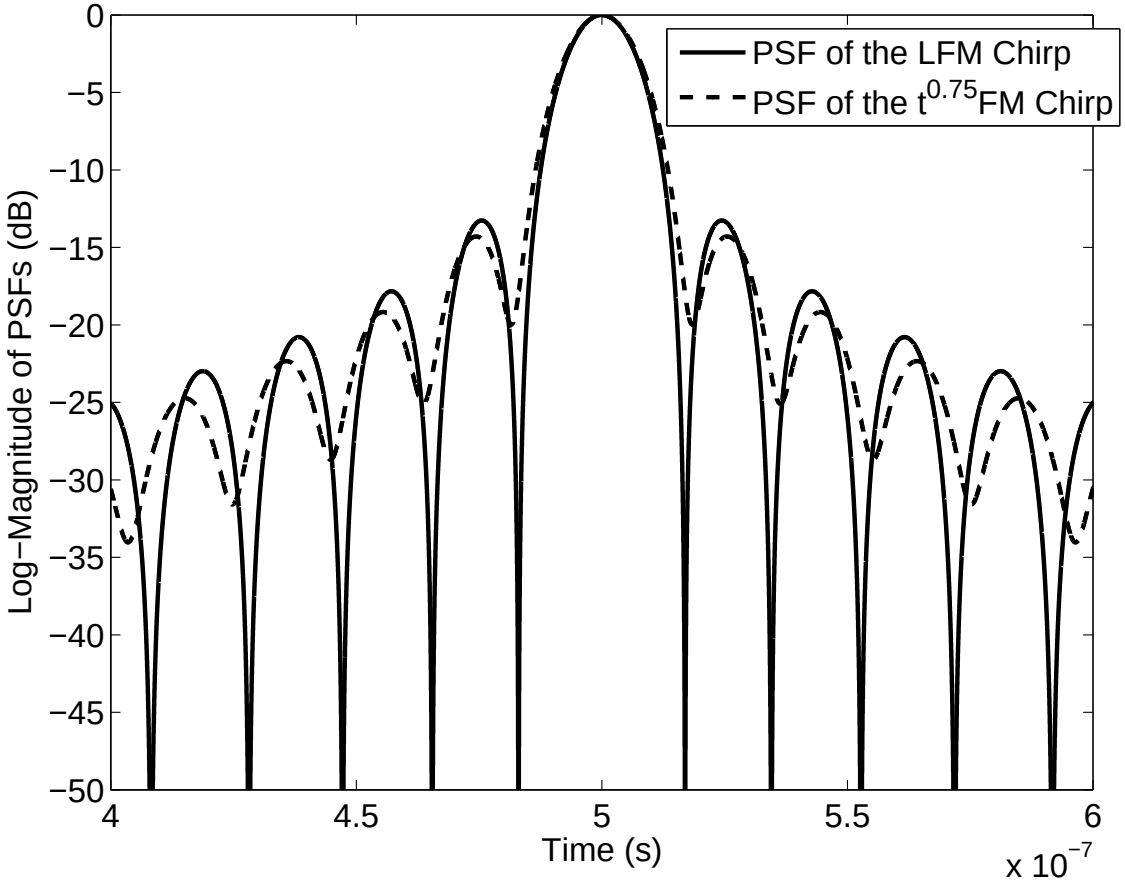

Figure 8: Comparison of the point spread functions of the LFM and $t^{0.75}$FM chirp signals-2.

For the given parameters the comparison of the point spread functions of the LFM and $t^{0.75}$FM chirps suggest that -3 dB mainlobe width of LFM chirp is around 1.48×10^{-8}s where as $t^{0.75}$FM chirp has a -3 dB mainlobe width of approximately 1.56×10^{-8}s. The ratio of these two parameters yield to a value of approximately 1.05 which suggests that the mainlobe of the point spread function of the $t^{0.75}$FM chirps is slightly larger than that of the LFM chirp, almost unrecognizable. Also reading of peak sibelobe values approximately lead to -13.25 dB for LFM chirp and -14.30 dB for the $t^{0.75}$FM chirp. Therefore a reduction of 1.05 dB can be achieved using the $t^{0.75}$FM chirp without having an adverse effect on the

mainlobe width of the point spread function, therefore image quality can be improved.

Finally using the point spread functions, the matched filter for $t^{0.75}$FM chirp can be written as

$$s_M(t) \sim \sum_n \sigma_n \mathsf{psf}_t \left[\frac{2}{c}(x - x_n)\right] \tag{54}$$

which gives the target scattering function $f(x)$.

Other Possible uses of the $t^{0.75}$FM Chirp Signal As it can be seen in [18] and [16], researchers are mainly interested in reducing the sidelobes of the point spread functions of the LFM either by applying nonuniform windowing or by offering new type of nonlinear frequency modulated waveforms. As mentioned before, although applying nonuniform windowing can reduce the sidelobe levels to any level desired, this method causes a loss in the signal-to-noise ratio [16]. Therefore there are some different forms of nonlinear frequency modulated chirps offered in the literature to reduce the sidelobe levels of the point spread functions.

A widely used chirp is a hybrid chirp which has the derivative of the phase function of the form of tan-LFM [16]. For a positive time interval of $[0, T_p]$ it can be written as

$$p_{_{hyb_1}}(t) = \exp(j\phi_{_{hyb_1}}(t)) \tag{55}$$

with a derivative of the phase function

$$\phi^{'}_{_{hyb_1}}(t) = \pi B \left[\frac{2\beta \tan(t\gamma/T_p)}{\tan(\gamma)} + \frac{2(1-\beta)t}{T_p}\right] \tag{56}$$

and therefore the phase function, $\phi_{_{hyb_1}}(t)$, becomes

$$\phi_{_{hyb_1}}(t) = \pi B \left[-\frac{2T_p\beta}{\gamma \tan(\gamma)} \ln|\cos(t\gamma/T_p)| + \frac{(1-\beta)t^2}{T_p}\right] \tag{57}$$

where β, γ are two parameters generally selected as $\beta = 0.5$, $\gamma = 1.4$ and where B is the bandwidth [16]. It is useful to mention that for $\beta = 0$ the hybrid chirp reduces to the LFM chirp and for $\beta = 1$ the hybrid chirp reduces to a chirp with tan-frequency modulation.

Replacing the LFM part of the hybrid with the $t^{0.75}$FM chirp another hybrid chirp (tan-$t^{0.75}$FM) is defined

$$p_{_{hyb_2}}(t) = \exp(j\phi_{_{hyb_2}}(t)) \tag{58}$$

with a derivative of the phase function

$$\phi'_{_{hyb_2}}(t) = \pi B \left[\frac{2\beta \tan(t\gamma/T_p)}{\tan(\gamma)} + \frac{2(1-\beta)t^{0.75}}{T_p^{0.75}} \right] \tag{59}$$

and therefore the phase function, $\phi_{_{hyb_2}}(t)$, becomes

$$\phi_{_{hyb_2}}(t) = \pi B \left[-\frac{2T_p\beta}{\gamma \tan(\gamma)} \ln|\cos(t\gamma/T_p)| + \frac{8(1-\beta)t^{1.75}}{7T_p^{0.75}} \right] \tag{60}$$

again where the β, γ are two parameters which can be selected as $\beta = 0.5$, $\gamma = 1.4$ and where B is the bandwidth. Following the necessary steps mentioned for the calculation of the point spread functions one can obtain the results presented below.

For a bandwidth of 100 MHz and a time window of $[0, 100 \times 10^{-6}]$ s for both hybrid chirps and the LFM chirp, one can obtain the following point spread functions presented in the Figure (9).

For the given parameters the comparison of the point spread functions of the LFM, tan-LFM and tan-$t^{0.75}$FM chirps suggest that -3 dB mainlobe width of LFM chirp is around 8.77×10^{-9}s where as tan-LFM and $t^{0.75}$FM chirps have -3 dB mainlobe widths of approximately 10.68×10^{-9}s and 11.06×10^{-9}s, respectively. The ratio of the mainlobe widths of the hybrid chirps to the mainlobe width of LFM chirp yield to approximately 1.21 and 1.26 which suggests that the mainlobe width of the point spread function of the hybrid chirps are larger than that of the LFM chirp. Also reading of peak sibelobe values approximately lead to -13.25 dB for LFM, -18.52 dB for the tan-LFM and -22.14 dB for the tan-$t^{0.75}$FM chirps. Therefore a reduction of 5.27 dB can be achieved using the tan-LFM instead of LFM and a further reduction of 3.62 dB can be obtained by using tan-$t^{0.75}$FM instead of tan-LFM, thus a total reduction of 8.89 dB. Therefore image quality can be improved using $t^{0.75}$FM chirp in the hybrid form as well.

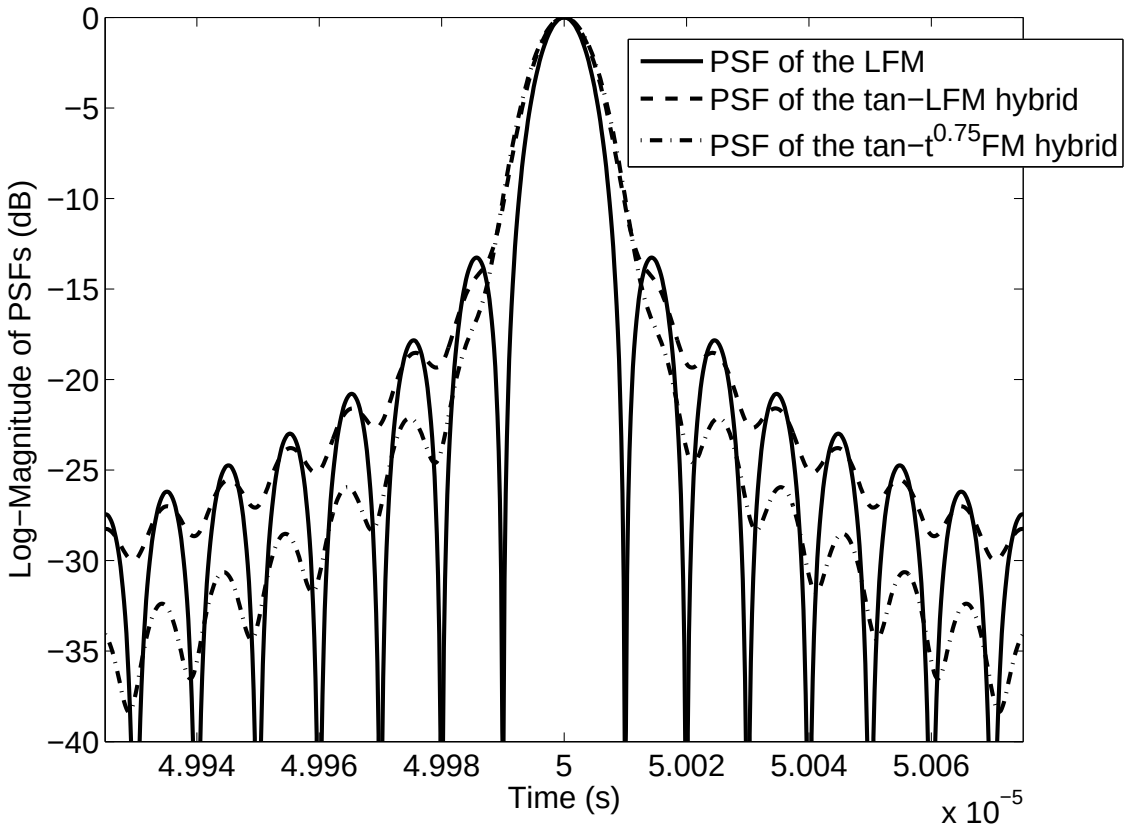

Figure 9: Comparison of the point spread functions of the LFM and hybrid chirp signals-1.

Repeating the same analysis for a bandwidth of 60 MHz and a time window of $[0, 1 \times 10^{-6}]$s for all chirps which have different chirp rates, one can obtain the Figure (10) presented below.

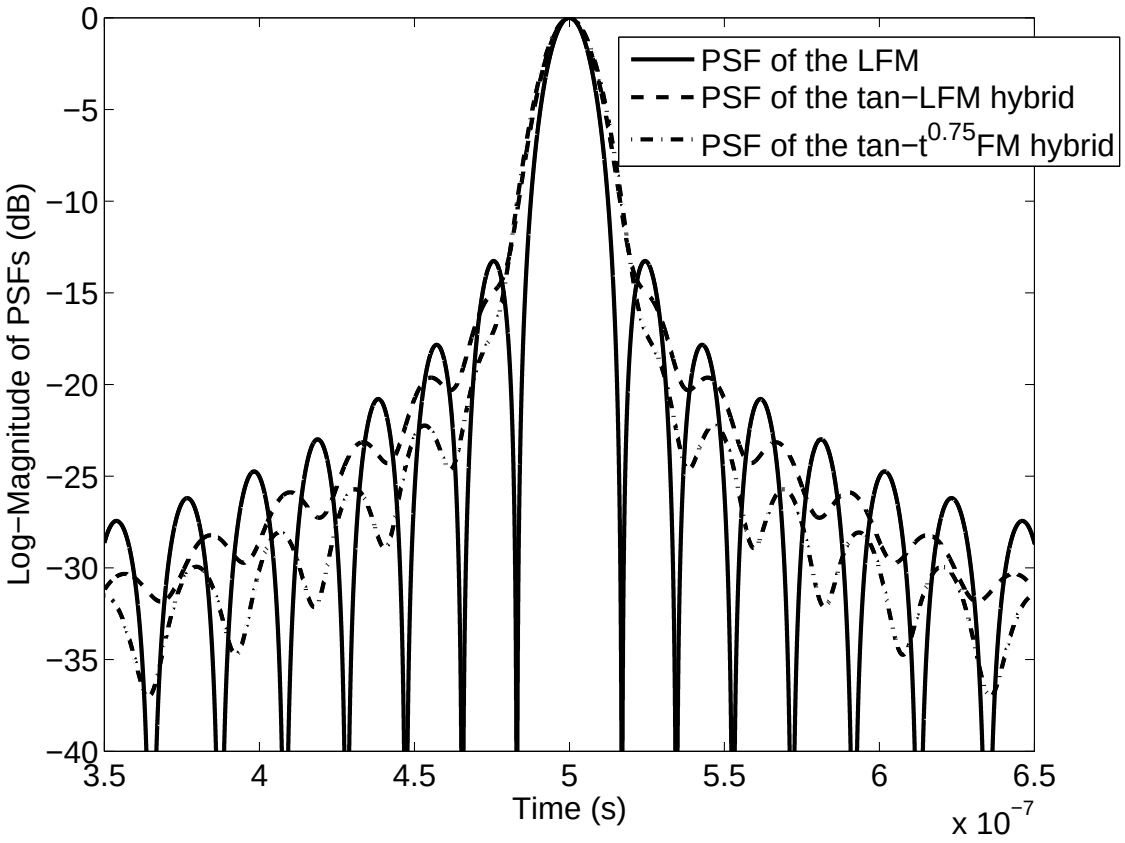

Figure 10: Comparison of the point spread functions of the LFM and hybrid chirp signals-2.

For the given parameters the comparison of the point spread functions of the LFM, tan-LFM and tan-$t^{0.75}$FM chirps suggest that -3 dB mainlobe width of LFM chirp is around 1.48×10^{-9}s where as tan-LFM and $t^{0.75}$FM chirps have -3 dB mainlobe widths of approximately 1.76×10^{-8}s and 1.84×10^{-8}s, respectively. The ratio of the mainlobe widths of the hybrid chirps to the mainlobe width of LFM chirp yield to approximately 1.18 and 1.24 which suggests that the mainlobe width of the point spread function of the hybrid chirps are larger than that of the LFM chirp. Also reading of peak sibelobe values approximately lead to -13.25 dB for LFM, -19.62 dB for the tan-LFM and -22.23 dB for the tan-$t^{0.75}$FM chirps. Therefore a reduction of 6.37 dB can be achieved using the tan-LFM instead of LFM and a further reduction of 2.61 dB can be obtained by using tan-$t^{0.75}$FM instead of tan-LFM, thus a total reduction of 8.98 dB. Therefore image quality can be improved using $t^{0.75}$FM chirp in the hybrid form as well.

3.2 Spatial Chirp Signals

In this section chirp signals which are wavenumber-modulated in the spatial domain are discussed. The commonly used slow-time chirp signal in linear aperture SAR is the slow-time hyperbolic phase modulation

$$p(u) = \exp(-j2k_\omega r_n(u)) \tag{61}$$

where $r_n(u)$ is the sensor-to-scatterer distance as a function of aperture u. Using $r_n(u) = \sqrt{x_n^2 + (u - y_n)^2}$ slow-time hyperbolic phase signal becomes

$$p(u) = \exp\left[-j2k_\omega \sqrt{x_n^2 + (u - y_n)^2}\right] \tag{62}$$

Using the Taylor series expansion the Fresnel formula for r_n becomes

$$r_n(u) \approx x_n + \frac{(u - y_n)^2}{2x_n} + ... \tag{63}$$

A comparison of the r_n and its Fresnel approximation given in the equation (63) can be seen in the figure (11) where $y_n = 0$ is assumed.

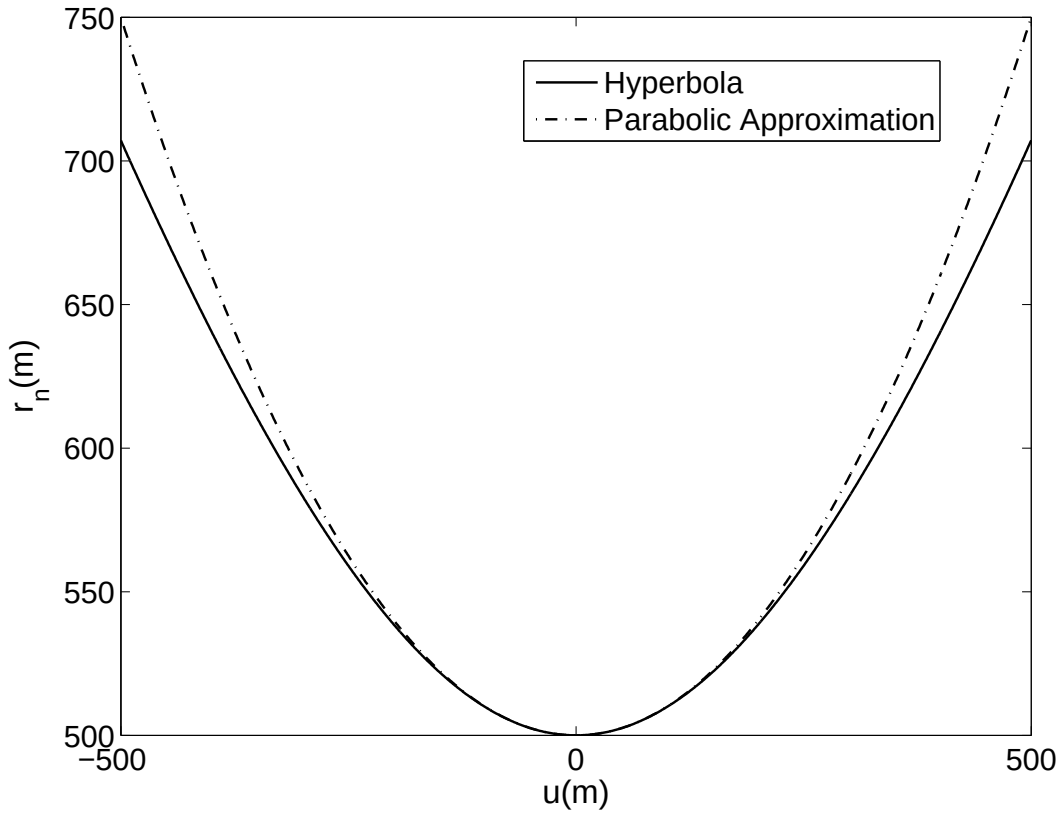

Figure 11: Hyperbolic and parabolic phase functions.

Using the Fresnel approximation given by the equation (63) one can rewrite the chirp given in equation (62) as

$$p(u) = \exp(-j2k_\omega r_n(u)) \approx \exp(-j2k_\omega x_n) \exp\left[-jk_\omega \frac{u^2}{x_n}\right] \tag{64}$$

which is an approximately LFM chirp signal modulated in the aperture domain.

Spectrum of Spatial Chirp Signals Consider the expression given in equation (62). Following the analysis given in [26] one can calculate the Fourier Transform of this signal as follows

$$P(k_u) = \int_{-\infty}^{\infty} \exp\left[-j2k_\omega \sqrt{x_n^2 + (u - y_n)^2}\right] \exp(-jk_u u) du \tag{65}$$

Using the method of stationary phases given in Appendix B one can write the phase function as

$$\Lambda(u) = -2k_\omega \sqrt{x_n^2 + (u - y_n)^2} - k_u u \tag{66}$$

The first derivative of the phase function can be written as

$$\dot{\Lambda}(u) = \frac{2k_\omega(y_n - u)}{\sqrt{x_n^2 + (u - y_n)^2}} - k_u \tag{67}$$

The second derivative of the phase function can be written as

$$\ddot{\Lambda}(u) = -\frac{2k_\omega x_n^2}{(x_n^2 + (u - y_n)^2)^{3/2}} \tag{68}$$

The stationary point, u^s, can be found by setting

$$\dot{\Lambda}(u^s) = \frac{2k_\omega(y_n - u^s)}{\sqrt{x_n^2 + (u^s - y_n)^2}} - k_u = 0 \tag{69}$$

which leads to $u^s = y_n - \frac{k_u x_n}{\sqrt{4k_\omega^2 - k_u^2}}$. Evaluating the phase function and its second derivative at this stationary point one obtains

$$\Lambda(u^s) = -\sqrt{4k_\omega^2 - k_u^2}x_n - k_u y_n \tag{70}$$

and

$$\ddot{\Lambda}(u^s) = -\frac{(4k_\omega^2 - k_u^2)^{3/2}}{4k_\omega^2 x_n} \tag{71}$$

Using equation (159) one obtain the asymptotic value of the integral given in equation (65) as

$$P(k_u) \approx \sqrt{\frac{8\pi k_\omega^2 x_n}{j(4k_\omega^2 - k_u^2)^{3/2}}} \exp\left(-j\sqrt{4k_\omega^2 - k_u^2}x_n\right) \exp(-jk_u y_n) \tag{72}$$

Finite Aperture Spatial Chirp Signals In radar signal processing the spatial chirps are used with a windowing function since it is only possible to generate a finite duration waveform. The spatial chirp can be written as

$$p_{\Pi_{(2L)}}(u) = \Pi_{(2L)}(u) \exp(-j2k_{\omega_c} r_n(u)) \tag{73}$$

where $2L$ is the synthetic aperture length and

$$\Pi_{(2L)}(u) = \begin{cases} 1 & \text{if } -L \leq u \leq L \\ 0 & \text{if otherwise} \end{cases} \tag{74}$$

is the windowing function.

Spectrum of Finite Aperture Spatial Chirp Signals The Fourier transform of the finite aperture spatial chirp signal given by the equation (73) can be expressed as

$$P(k_u) = FT^u_{1D}\left\{\Pi_{(2L)}(u)\exp(-j2k_{\omega_c}r_n(u))\right\} \tag{75}$$

which can be evaluated as

$$P(k_u) \sim \begin{cases} \exp\left(-j\sqrt{4k_\omega^2 - k_u^2}x_n\right)\exp(-jk_u y_n) & \text{if } u^s = y_n - \frac{k_u x_n}{\sqrt{4k_\omega^2 - k_u^2}} \in [-L, L] \\ 0 & \text{if otherwise} \end{cases} \tag{76}$$

where the coefficient $\sqrt{\frac{8\pi k_\omega^2 x_n}{j(4k_\omega^2 - k_u^2)^{3/2}}}$ is suppressed in the first branch. The expression in upper branch of the equation (76) is derived previously for the spatial chirp signals and the expression in the lower branch of the equation (76) is guaranteed by the Riemann-Lebesgue lemma discussed in the Appendix B.

CHAPTER IV

SPOTLIGHT SYNTHETIC APERTURE RADAR IMAGING

Early stripmap SAR systems were developed beginning in the 1950s, but spotlight SAR systems needed to wait until about 1980s. In the early 1960s a group of scientists of the Willow Run Laboratories, sponsored by the Air Force to study the identification of the spaceborne objects, were working on fine resolution imaging of the rotating objects [14]. Although the first experiments performed on a platform with a small size later experiments are performed over large areas of terrain using airborne SAR sensors [14]. This work can be viewed as the earliest work in spotlight SAR imaging. The data collected during experiments are recorded using analog optical techniques. Until 1969 the scientist were trying to record the data in the rectangular format which deteriorated the fine resolution. After then they started to record the data in polar format which made the fine resolution spotlight imagery possible [14]. This technique is now widely accepted as the polar format processing technique in the radar imaging. With the maturation of the digital computers in 1970s the analog systems are replaced with digital systems. Today digital SAR processor heavily based on digital memories and FPGA technologies are able to perform real time image reconstruction, both for spotlight imaging and other SAR modalities.

Spotlight SAR image reconstruction can be achieved by few different methods. Some of these are polar format processing, Stolt format processing and range-Doppler imaging. In this chapter a comparison of the polar format processing and the Stolt format processing algorithms using both the LFM and $t^{0.75}$FM chirp signals is presented. Polar format processing is a valid approximation for the unmanned aerial vehicle (UAV) SAR systems with long range small spot size imaging situations. Stolt format processing is also used in satellite SAR systems and it can also be implemented for stripmap imaging modality. The synthetic examples reconstructed in this chapter provides a basis for assessing the change detection methods presented in the chapter 5 of this dissertation.

A more detailed and complete discussion of the spotlight SAR imaging can be seen in [14], [48], [46], [23], [4].

4.1 Spotlight SAR Imaging Geometry

Two dimensional imaging geometry for spotlight SAR can be seen in the Figure (12) below which is valid for ground plane imaging. The slant plane imaging can also be treated similarly.

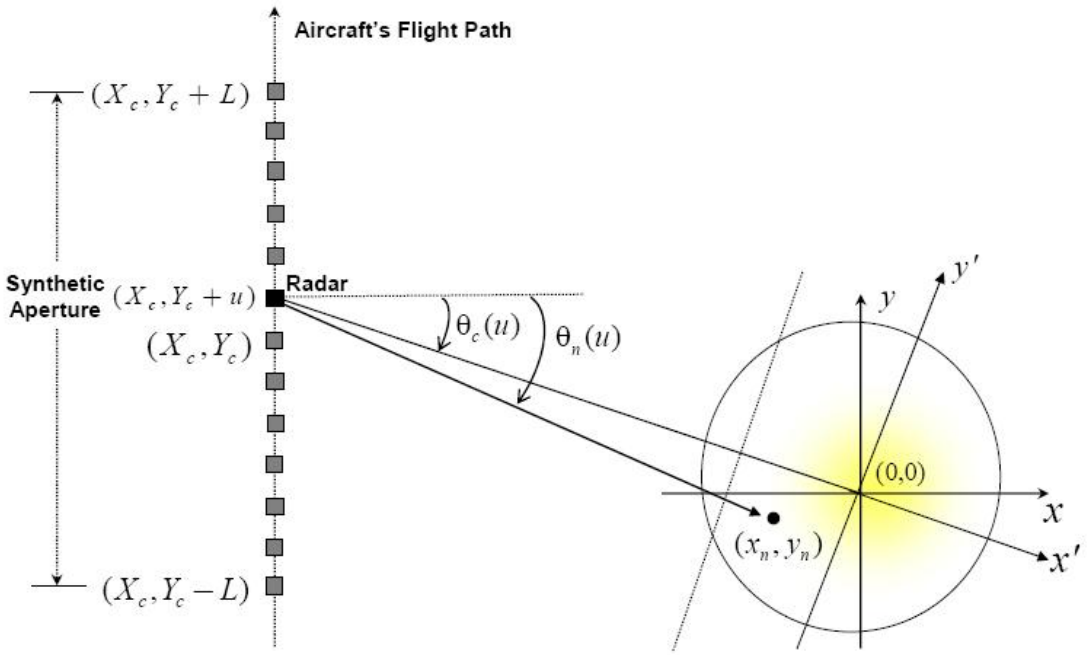

Figure 12: Spotlight imaging geometry for polar format processing.

The x and y coordinates denote the range and cross-range distances. These are also called fast time and slow time distances. The transmitting and receiveing radar moves along a linear path given by $x = X_c$. The synthetic aperture is denoted by u, where $u \in [-L, L]$. The illuminated region is a disk of radius X_o which is also called the spotlighted region. The radar hardware generates a time-dependent pulsed signal $p(t)$ which can be LFM or $t^{0.75}$FM chirps discussed in Chapter 3. Since the aircraft speed is much slower than the speed of light it is a valid approximation to accept the receive and transmit mode coordinates to be

the same.

In reality flight geometry deviates from the straight path, therefore motion compensation algorithms and hardware are widely used. The idealized flight motion case are considered throughout this dissertation.

4.2 Spotlight SAR via Polar Format Processing

Polar format reconstruction can be achieved using two different approximations as given in [48]. The first approximation is plane wave approximation and the second approximation is narrow bandwith narrow beamwidth approximation. In this dissertation polar format reconstruction via plane wave approximation is considered. The derivations followed in this chapter is given by [46].

Polar format processing for SAR image formation is based on the far field Fraunhofer approximation of wave field theory. A detailed discussion of the Fraunhofer approximation can be seen in [25]. The imaging geometry of polar format applications is constrained to ensure the Fraunhofer approximation is accurate.

Continuous Model Considering the SAR imaging geometry presented in figure (12) total recorded signal with amplitude functions ignored becomes [46]

$$ss(t,u) = \int\int ff(x,y)p\left[t - \frac{2\sqrt{(X_c - x)^2 + (Y_c + u - y)^2}}{c}\right] dxdy \tag{77}$$

where $ff(x,y)$ is the target area's scattering function, u is the synthetic aperture, t is time, c is the propagation speed of the electromagnetic wave which is the speed of light and integration is carried out over points (x,y) which rests in disk of radius X_o. Taking the fast-time Fourier Transform and performing baseband conversion one obtains [46]

$$Ss(\omega,u) = P(\omega)\int\int ff(x,y)\exp\left[-j2k_\omega\sqrt{(X_c - x)^2 + (Y_c + u - y)^2}\right] dxdy \tag{78}$$

For simplicity defining $Ss(\omega,u)/P(\omega)$ or its matched filtered form that is $Ss(\omega,u)P^*(\omega)$ by $Ss(\omega,u)$ [46]

$$Ss(\omega,u) = \int\int ff(x,y)\exp\left[-j2k_\omega\sqrt{(X_c - x)^2 + (Y_c + u - y)^2}\right] dxdy \tag{79}$$

Defining

$$\theta_c = \arctan\left(\frac{Y_c + u}{X_c}\right) \tag{80}$$

Transforming variables from (x, y) coordinate system to (x', y') coordinate system as given in the Figure (12), the equation (79) becomes [46]

$$Ss(\omega, u) = \int_{x'}\int_{y'} ff'(x', y') \exp\left[j2k_\omega \sqrt{\left(\sqrt{X_c^2 + (Y_c + u)^2} - x'\right)^2 + y'^2}\right] dx'dy' \tag{81}$$

Making the following plane wave approximation [46]

$$2k_\omega \sqrt{\left(\sqrt{X_c^2 + (Y_c + u)^2} - x'\right)^2 + y'^2} \approx 2k_\omega \left(\sqrt{X_c^2 + (Y_c + u)^2} - x'\right) \tag{82}$$

the equation (81) becomes [46]

$$\begin{aligned} Ss(\omega, u) &\approx \int_{x'}\int_{y'} ff'(x', y') \exp\left[j2k_\omega \left(\sqrt{X_c^2 + (Y_c + u)^2} - x'\right)\right] dx'dy' \\ &= \exp\left[j2k_\omega \left(\sqrt{X_c^2 + (Y_c + u)^2}\right)\right] \int_{x'}\int_{y'} f'(x', y') \exp\left(-j2k_\omega x'\right) dx'dy' \end{aligned} \tag{83}$$

This can be written as [46]

$$Ss(\omega, u) \approx \exp\left[j2k_\omega \left(\sqrt{X_c^2 + (Y_c + u)^2}\right)\right] FF'(k_{x'}, k_{y'}) \tag{84}$$

where

$$k_{x'} = 2k_\omega \quad \text{and} \quad k_{y'} = 0 \tag{85}$$

Making the transformation from $(k_{x'}, k_{y'})$ to (k_x, k_y) wavenumber system and using the analysis given in Appendix B one obtains [46]

$$Ss(\omega, u) \approx \exp\left[j2k_\omega \left(\sqrt{X_c^2 + (Y_c + u)^2}\right)\right] FF(k_x, k_y) \tag{86}$$

This expression leads to [46]

$$FF(k_x, k_y) \approx \exp\left[-j2k_\omega \left(\sqrt{X_c^2 + (Y_c + u)^2}\right)\right] Ss(\omega, u) \tag{87}$$

where

$$k_x = 2k_\omega \cos(\theta_c) = 2k_\omega \frac{X_c}{\sqrt{X_c^2 + (Y_c + u)^2}} \tag{88}$$

and

$$k_y = 2k_\omega \sin(\theta_c) = 2k_\omega \frac{Y_c + u}{\sqrt{X_c^2 + (Y_c + u)^2}} \tag{89}$$

The inverse 2D Fourier transform can be used to construct the target reflectivity function $ff(x, y)$ using $FF(k_x, k_y)$ given in the equation (87). This completes the all necessary steps for polar format processing algorithm for spotlight SAR. In the Figure (58) the polar format processing algorithm flowchart is presented.

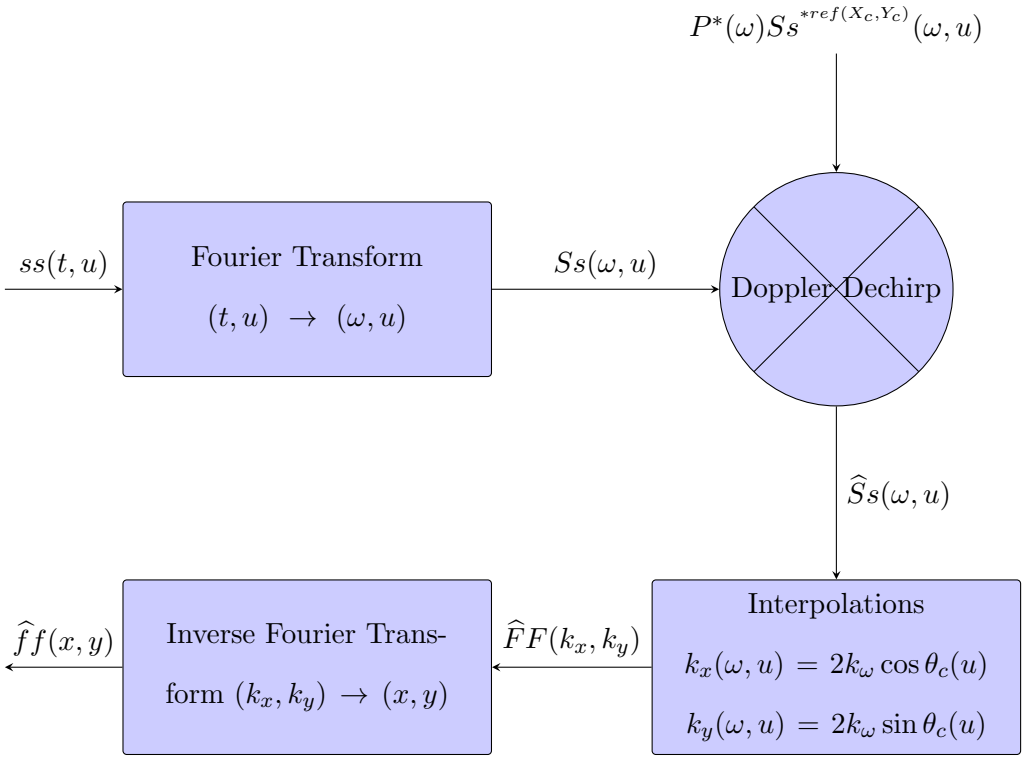

Figure 13: Polar format processing algorithm flowchart.

Discrete Model If the number of scatterers in the spotlight region is finite then one can use a discrete model. The discrete model for polar format processing of spotlight SAR imaging can be summarized as follows. For finite number of scatterers the equation (77) becomes

$$ss(t,u) = \sum_n ff_n(x_n, y_n) p\left[t - \frac{2\sqrt{(X_c - x_n)^2 + (Y_c + u - y_n)^2}}{c}\right] \tag{90}$$

which is the recorded signal by the radar hardware. In equation (90) n is the number of scatterers in the scene and $ff_n(x_n, y_n)$ is the scattering function of a scatterer located at x_n, y_n which rests inside a disk of radius X_o. Taking the fast-time Fourier Transform and

performing matched filtering one obtains

$$Ss(\omega,u)=\sum_n ff_n(x_n,y_n)\exp\left[-j2k_\omega\sqrt{(X_c-x_n)^2+(Y_c+u-y_n)^2}\right] \tag{91}$$

Defining

$$\theta_c=\arctan\left(\frac{Y_c+u}{X_c}\right) \tag{92}$$

Transforming variables from (x_n,y_n) to (x'_n,y'_n) where

$$\begin{bmatrix}x'_n\\y'_n\end{bmatrix}=\begin{bmatrix}\cos(\theta_c) & \sin(\theta_c)\\-\sin(\theta_c) & \cos(\theta_c)\end{bmatrix}\begin{bmatrix}x_n\\y_n\end{bmatrix} \tag{93}$$

the equation (91) becomes

$$Ss(\omega,u)=\sum_n ff'_n(x'_n,y'_n)\exp\left[j2k_\omega\sqrt{\left(\sqrt{X_c^2+(Y_c+u)^2}-x'_n\right)^2+{y'_n}^2}\right] \tag{94}$$

Making the following plane wave approximation

$$2k_\omega\sqrt{\left(\sqrt{X_c^2+(Y_c+u)^2}-x'_n\right)^2+{y'_n}^2}\approx 2k_\omega\left(\sqrt{X_c^2+(Y_c+u)^2}-x'_n\right) \tag{95}$$

the equation (94) becomes

$$\begin{aligned}Ss(\omega,u)&\approx\sum_n ff'_n(x'_n,y'_n)\exp\left[j2k_\omega\left(\sqrt{X_c^2+(Y_c+u)^2}-x'_n\right)\right]\\&=\exp\left[j2k_\omega\left(\sqrt{X_c^2+(Y_c+u)^2}\right)\right]\sum_n ff'_n(x'_n,y'_n)\exp\left(-j2k_\omega x'_n\right)\end{aligned} \tag{96}$$

This can be written as

$$Ss(\omega,u)\approx\exp\left[j2k_\omega\left(\sqrt{X_c^2+(Y_c+u)^2}\right)\right]FF'(k_{x'},k_{y'}) \tag{97}$$

where

$$k_{x'}=2k_\omega\ \text{ and }\ k_{y'}=0 \tag{98}$$

Making the transformation from $(k_{x'},k_{y'})$ to (k_x,k_y) wavenumber system and using the analysis given in appendix B one obtains

$$Ss(\omega,u)\approx\exp\left[j2k_\omega\left(\sqrt{X_c^2+(Y_c+u)^2}\right)\right]FF(k_x,k_y) \tag{99}$$

This expression leads to

$$FF(k_x,k_y)\approx\exp\left[-j2k_\omega\left(\sqrt{X_c^2+(Y_c+u)^2}\right)\right]Ss(\omega,u) \tag{100}$$

where

$$k_x = 2k_\omega \cos(\theta_c) = 2k_\omega \frac{X_c}{\sqrt{X_c^2 + (Y_c + u)^2}} \tag{101}$$

and

$$k_y = 2k_\omega \sin(\theta_c) = 2k_\omega \frac{Y_c + u}{\sqrt{X_c^2 + (Y_c + u)^2}} \tag{102}$$

The inverse 2D Fourier transform can be used to construct the target scattering function $\sum_n ff_n(x_n, y_n)$ using $FF(k_x, k_y)$ given in the equation (100). This completes the all necessary steps for polar format processing algorithm for spotlight SAR with finite number of scatterers in the scene.

Constraints for Validity In this section the constraints for validity of the polar format processing algorithm considering only the broadside case, that is, $Y_c = 0$ is discussed. Plane wave approximation in the equation (82) introduces an error [46]

$$\frac{k_\omega(x^2 \sin^2 \theta_c + y^2 \cos^2 \theta_c + xy \sin 2\theta_c)}{X_c} \tag{103}$$

where only significant terms are considered. For a small target spot with a disk of radius X_o, that is, $2\theta_c$ is small, the maximum phase error due to equation (103) can be written as [46]

$$\frac{k_\omega X_c^2(1 + \sin 2\theta_c)}{X_c} \approx \frac{k_\omega X_o^2}{X_c} \tag{104}$$

A weaker approximation can be obtained rewriting equation (103) as [46]

$$\frac{k_\omega(x^2 \sin^2 \theta_c - y^2 \sin^2 \theta_c + xy \sin 2\theta_c)}{X_c} + \frac{k_\omega y^2}{X_c} \tag{105}$$

The last term in the equation (105), $k_\omega y^2 / X_c$, is independent of the radar position u. Associating this term with the scattering function a new target scattering function can be written as follows [46]

$$f(x, y) \exp(j \frac{k_\omega y^2}{X_c}) \tag{106}$$

For narrow bandwidth radar signal the frequencies can be approximated by center frequency so that expression (106) can be written as [46]

$$f(x, y) \exp(j \frac{k_\omega y^2}{X_c}) \approx f(x, y) \exp(j \frac{k_{\omega_c} y^2}{X_c}) \tag{107}$$

where k_{ω_c} is the center frequency of the radar signal. The first phase term in the equation (105) has to be much less than one for a valid inversion so that [46]

$$\frac{k_\omega X_o^2 \sin 2\theta_c}{X_c} \ll 1 \tag{108}$$

The wavelengths of the radar signal is on the interval $[k_{\omega_{min}}, k_{\omega_{max}}]$. Thus the central wavenumber can be written as [46]

$$k_{\omega_c} = \frac{k_{\omega_{min}} + k_{\omega_{max}}}{2} \tag{109}$$

Therefore equation (107) is a good approximation only if [46]

$$\frac{(k_{\omega_{max}} - k_{\omega_{min}})X_o^2}{2X_c} \ll 1 \tag{110}$$

Following [46], the range resolution, Δ_x, for spotlight SAR imaging geometry can be written as [46]

$$\Delta_x = \frac{2\pi}{2(k_{\omega_{max}} - k_{\omega_{min}})} \tag{111}$$

Using the equation (110) in the equation (111) one obtains [46]

$$\frac{\pi X_o^2}{2\Delta_x X_c} \ll 1 \tag{112}$$

which implies

$$\Delta_x \gg \frac{\pi X_o^2}{2X_c} \tag{113}$$

The constraint given in the equation (113) is the requirement for the plane wave approximation to be acceptable and polar format processing inversion to be valid.

4.2.1 Polar Format Processing using LFM Signals

In this section 9 examples of spotlight imaging using polar format processing with LFM chirp signals are presented. Therefore for the $p(t)$ in the equation (90) the expression given in the equation (2) and its corresponding matched filter is used.

The first example is for a single scatterer located at $x = 0\text{m}, y = 0\text{m}$ with the parameters $X_c = 1500\text{m}, Y_c = 0\text{m}, X_o = 100\text{m}, L = 150\text{m}$. In the Figure (14) the recorded SAR signal as a function of u and t is presented.

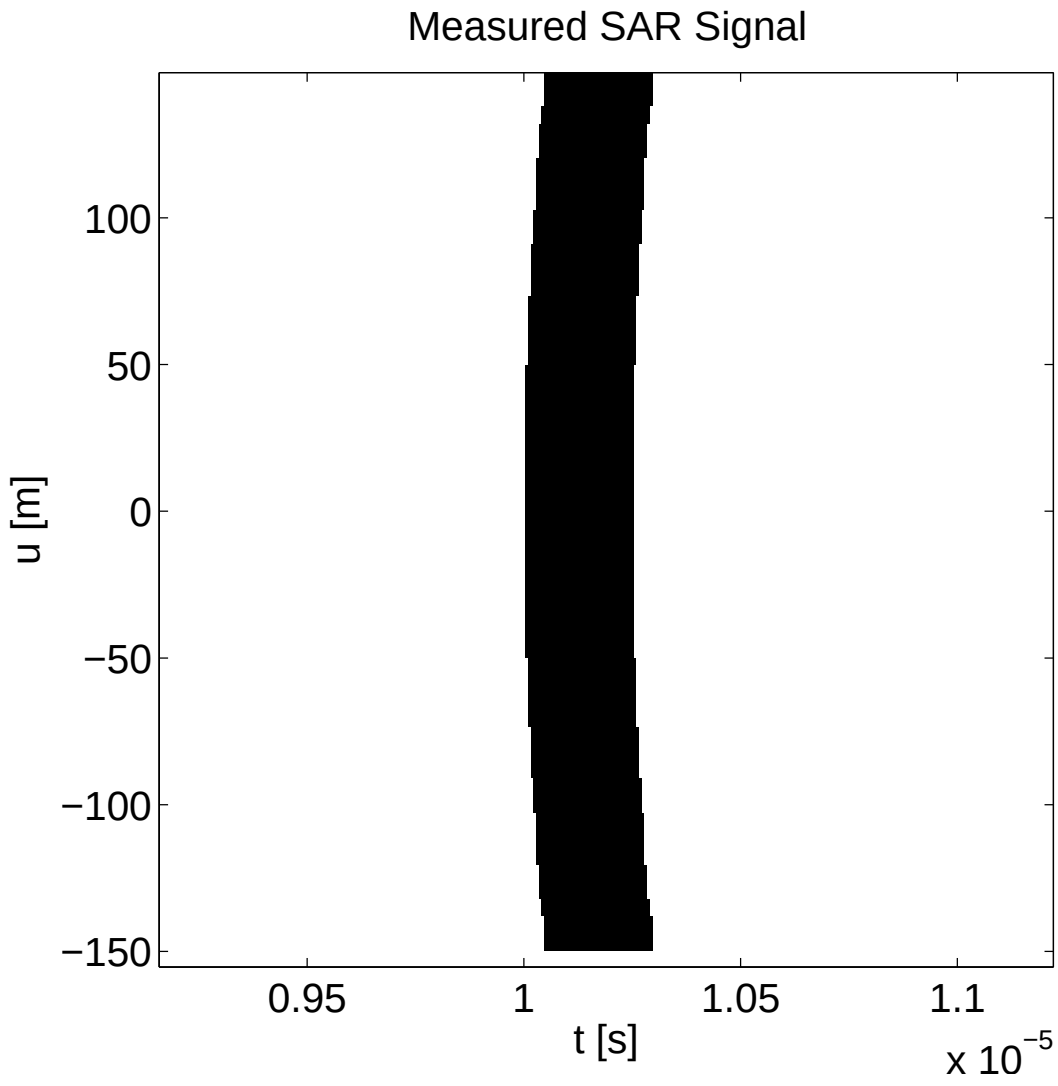

Figure 14: Measured SAR signal of a single scatterer at $x = 0\text{m}, y = 0\text{m}$-broadside mode.

Applying the matched filtering operation along t axis to the signal given in the Figure (14) one obtains the signal given in the Figure (15).

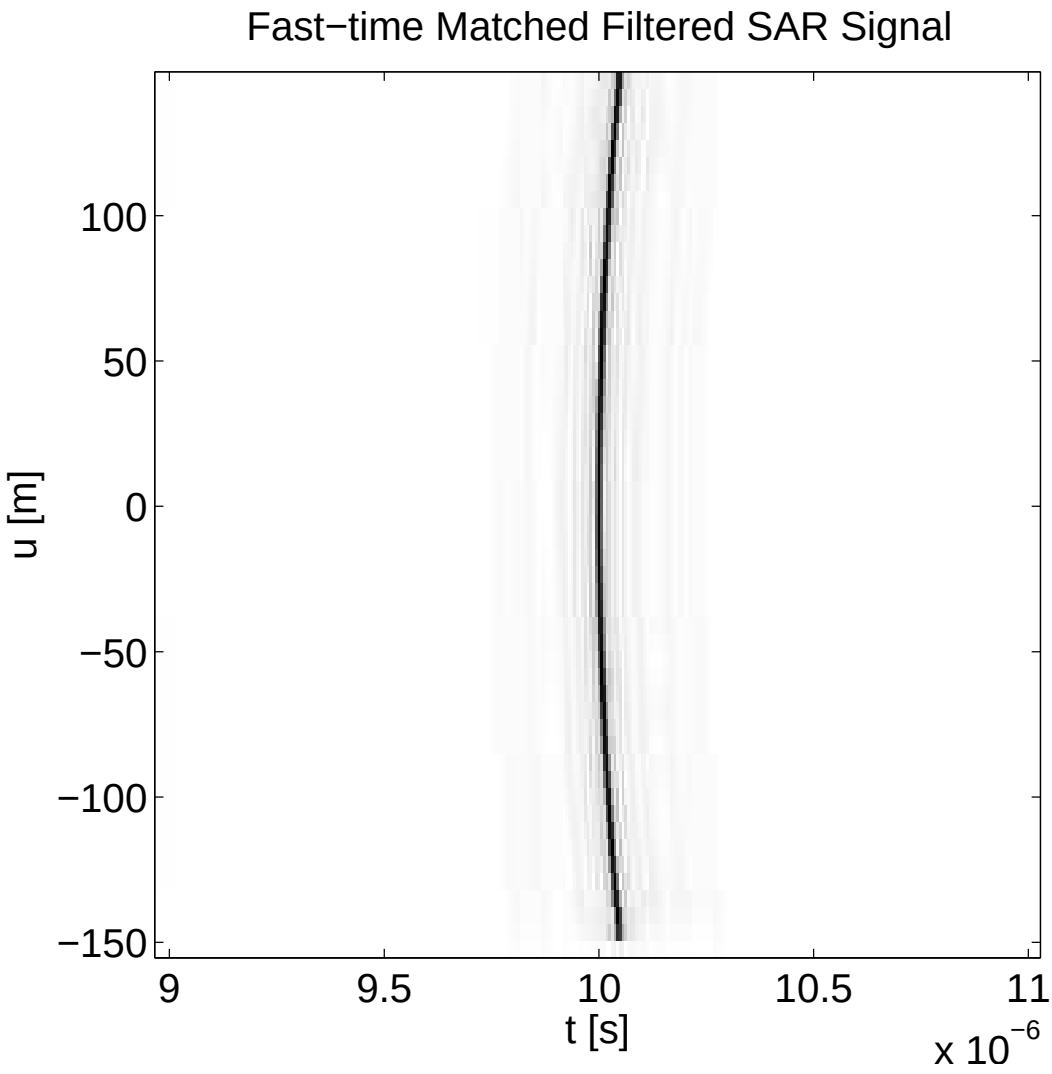

Figure 15: Fast-time matched filtered SAR signal of a single scatterer at $x = 0\text{m}, y = 0\text{m}$-broadside mode.

After 2D Fourier transforming and matched filtering in the u domain one obtains the scene spectrum given in the Figure (16).

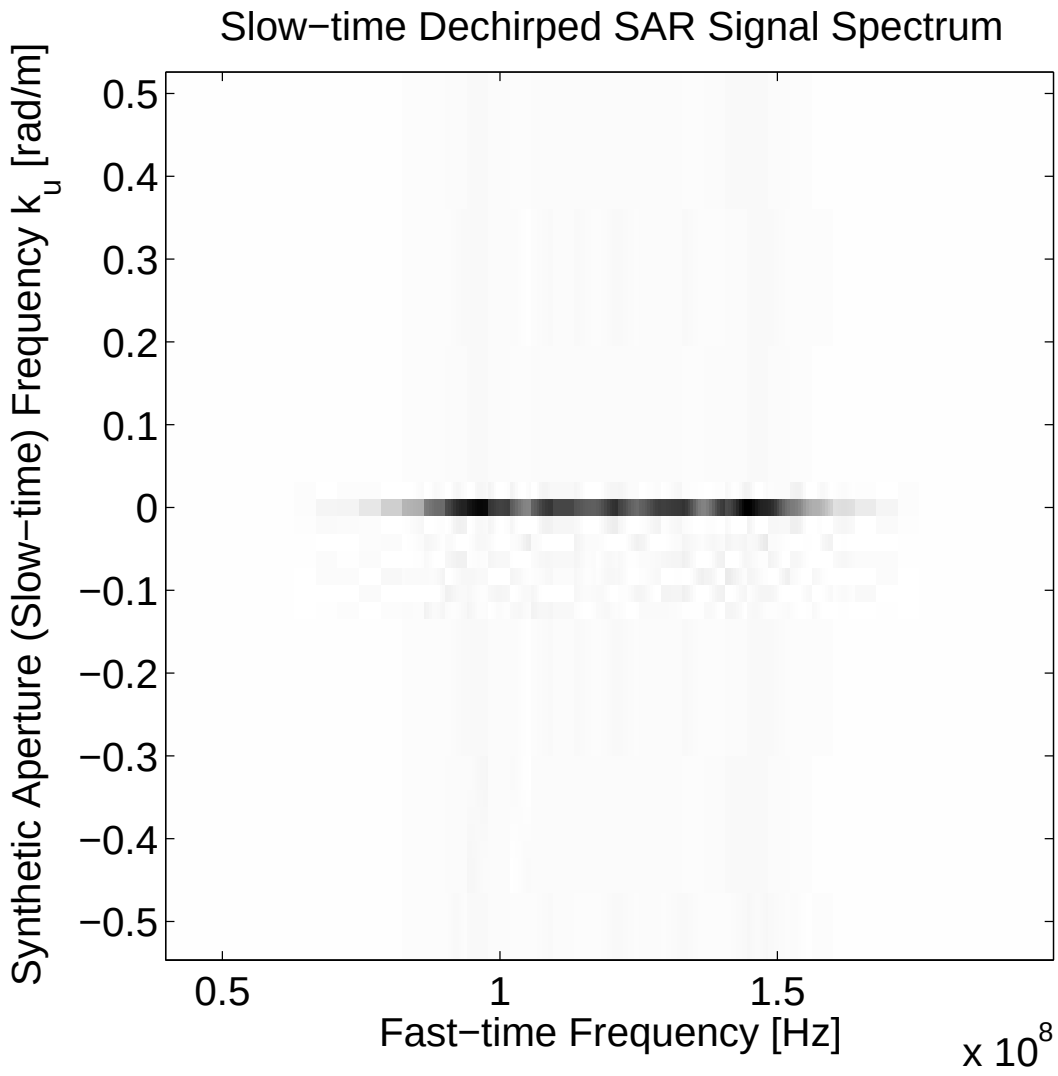

Figure 16: Compressed SAR signal spectrum of a single scatterer at $x = 0\text{m}, y = 0\text{m}$-broadside mode.

Performing the PFA wavenumber interpolations and using 2D inverse Fourier transform operation one obtains the scene scattering function which is presented in the Figure (17).

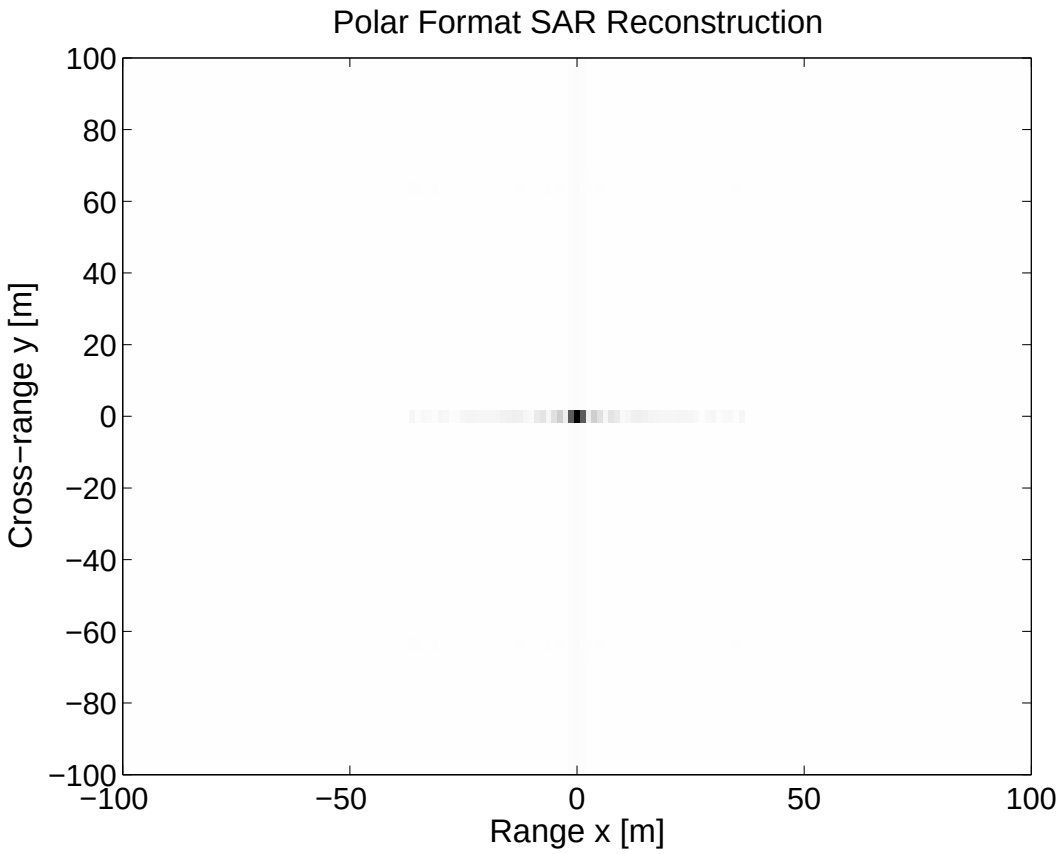

Figure 17: Polar format SAR reconstruction of a single scatterer at $x = 0\text{m}, y = 0\text{m}$-broadside mode.

The second example is for a single scatterer located at $x = 0\text{m}, y = 0\text{m}$ with the parameters $X_c = 1500\text{m}, Y_c = 500\text{m}, X_o = 100\text{m}, L = 150\text{m}$. In the Figure (18) the recorded SAR signal as a function of u and t is presented.

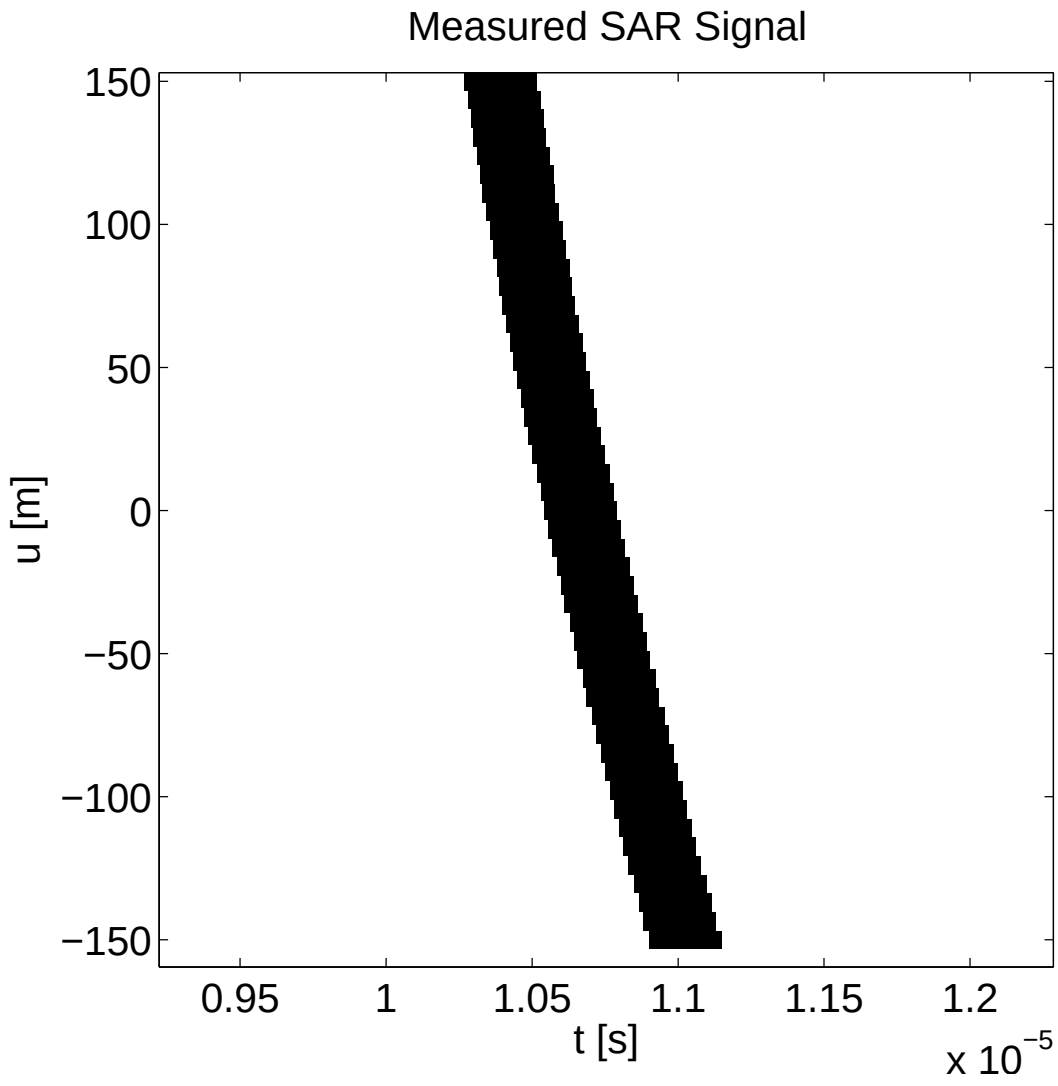

Figure 18: Measured SAR signal of a single scatterer at $x = 0\text{m}, y = 0\text{m}$-squinted mode.

Applying the matched filtering operation along t axis to the signal given in the Figure (18) one obtains the signal given in the Figure (19).

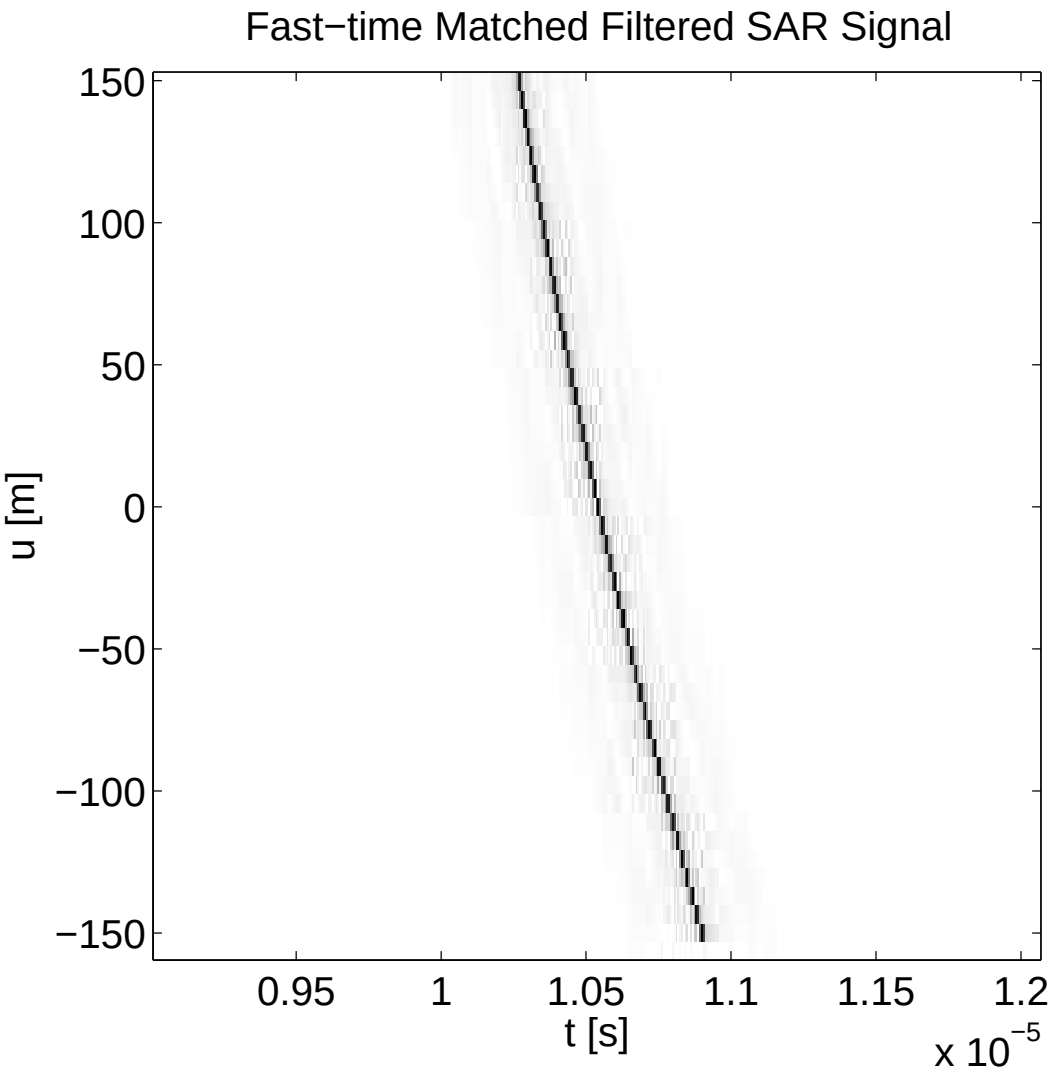

Figure 19: Fast-time matched filtered SAR signal of a single scatterer at $x = 0\text{m}, y = 0\text{m}$-squinted mode.

After 2D Fourier transforming and matched filtering in the u domain one obtains the scene spectrum given in the Figure (20).

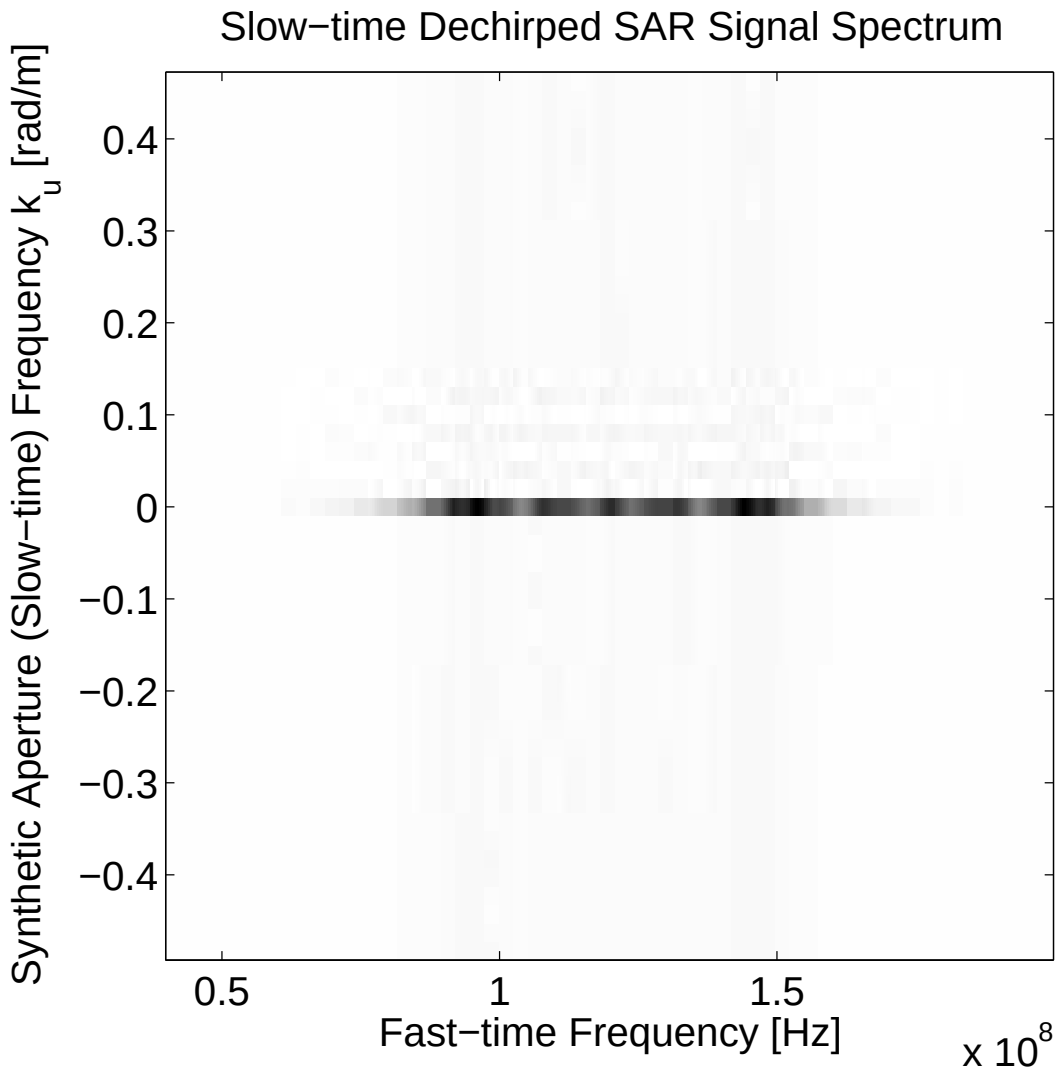

Figure 20: Compressed SAR signal spectrum of a single scatterer at $x = 0\text{m}, y = 0\text{m}$-squinted mode.

Performing the PFA wavenumber interpolations and using 2D inverse Fourier transform operation ones obtain the scene scattering function which is presented in the Figure (21).

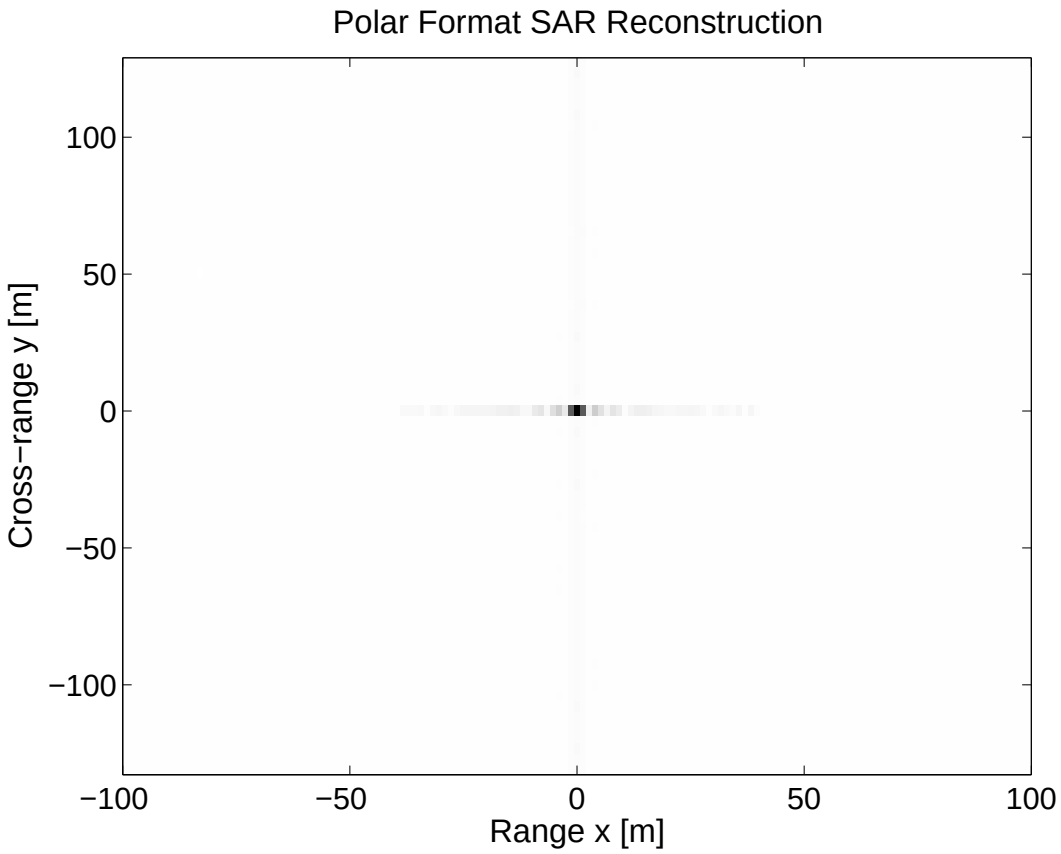

Figure 21: Polar format SAR reconstruction of a single scatterer at $x = 0\text{m}, y = 0\text{m}$-squinted mode.

The third example is for a single scatterer located at $x = 20\text{m}, y = 20\text{m}$ with the parameters $X_c = 1500\text{m}, Y_c = 0\text{m}, X_o = 100\text{m}, L = 150\text{m}$. In the Figure (22) the recorded SAR signal as a function of u and t is presented.

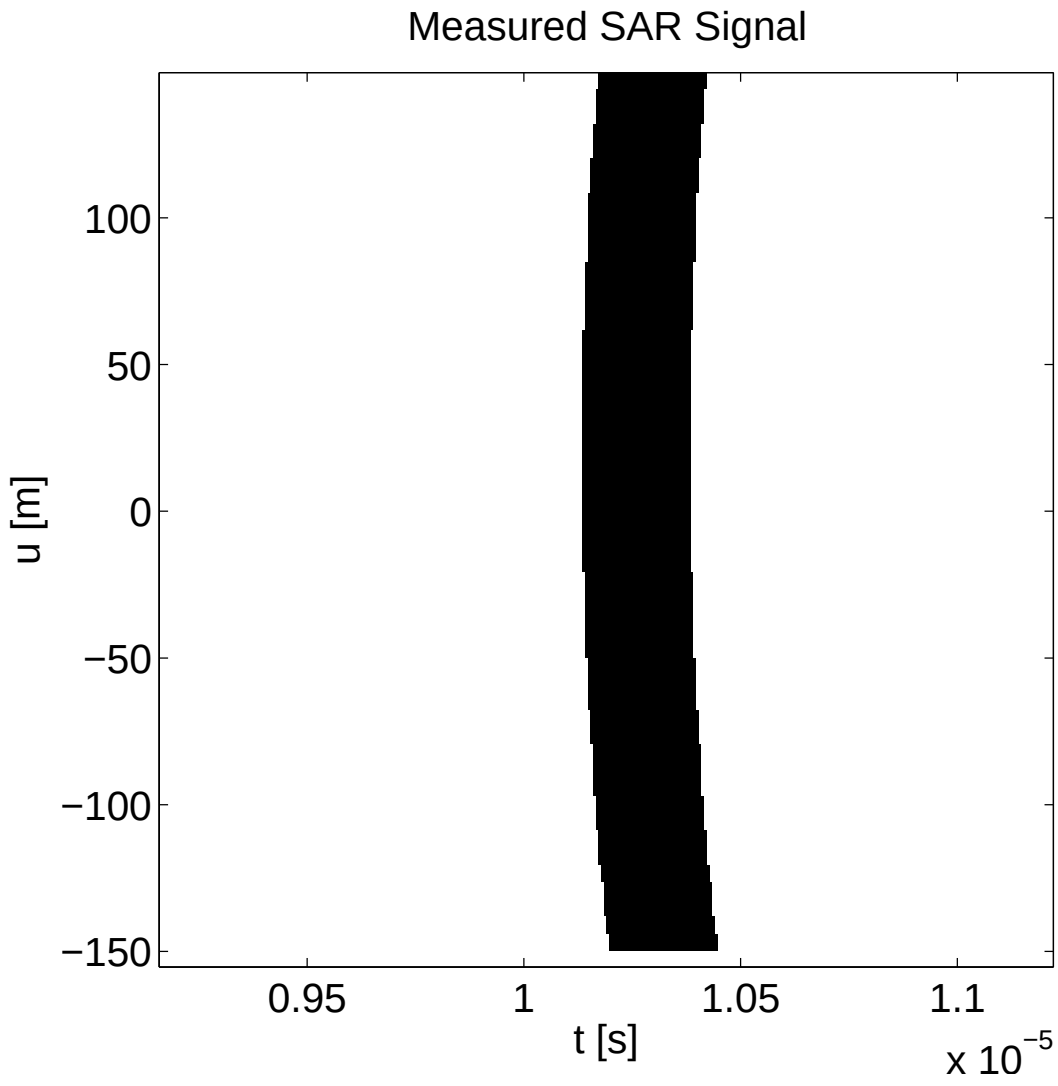

Figure 22: Measured SAR signal of a single scatterer at $x = 20\text{m}, y = 20\text{m}$-broadside mode.

Applying the matched filtering operation along t axis to the signal given in the Figure (22) one obtains the signal given in the Figure (23).

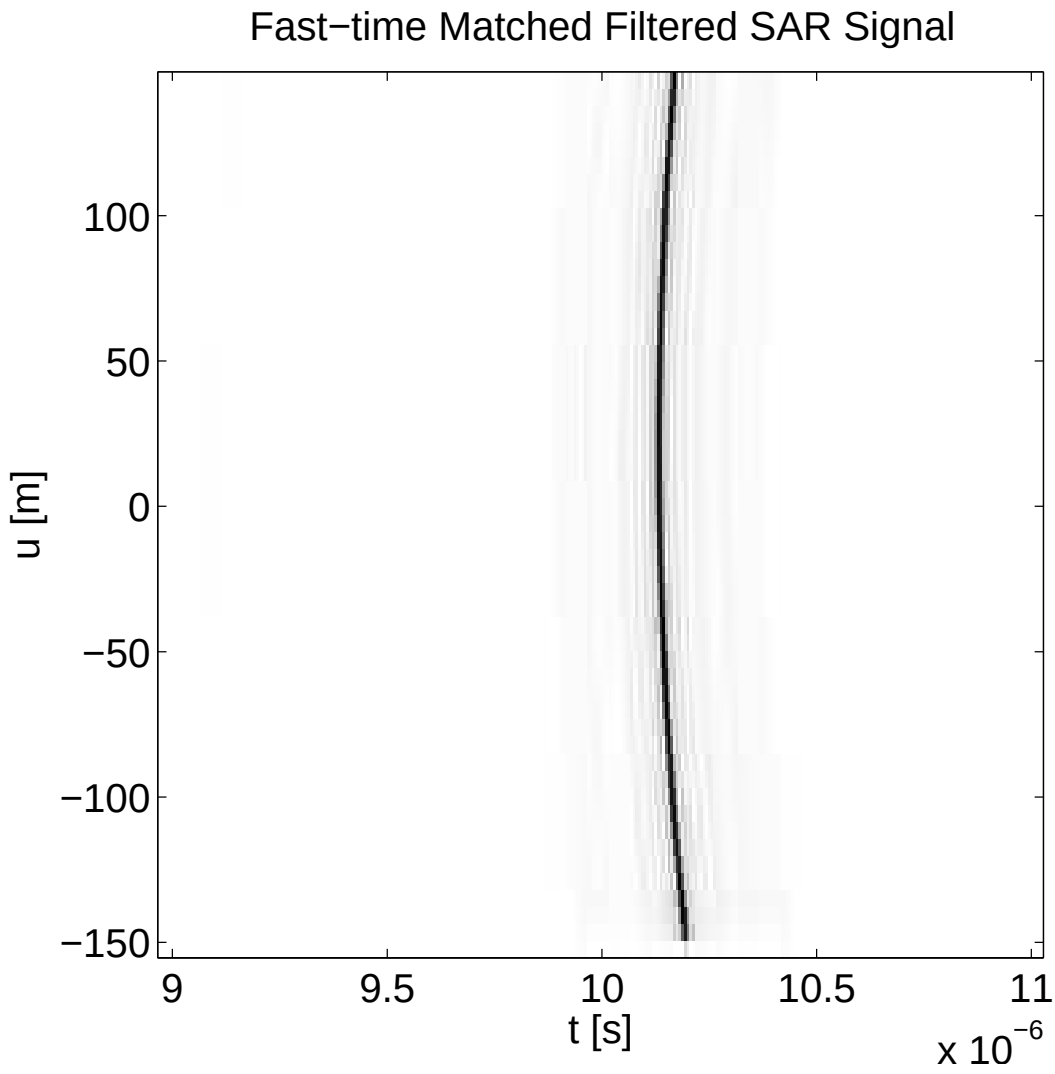

Figure 23: Fast-time matched filtered SAR signal of a single scatterer at $x = 20\text{m}, y = 20\text{m}$-broadside mode.

After 2D Fourier transforming and matched filtering in the u domain one obtains the scene spectrum given in the Figure (24).

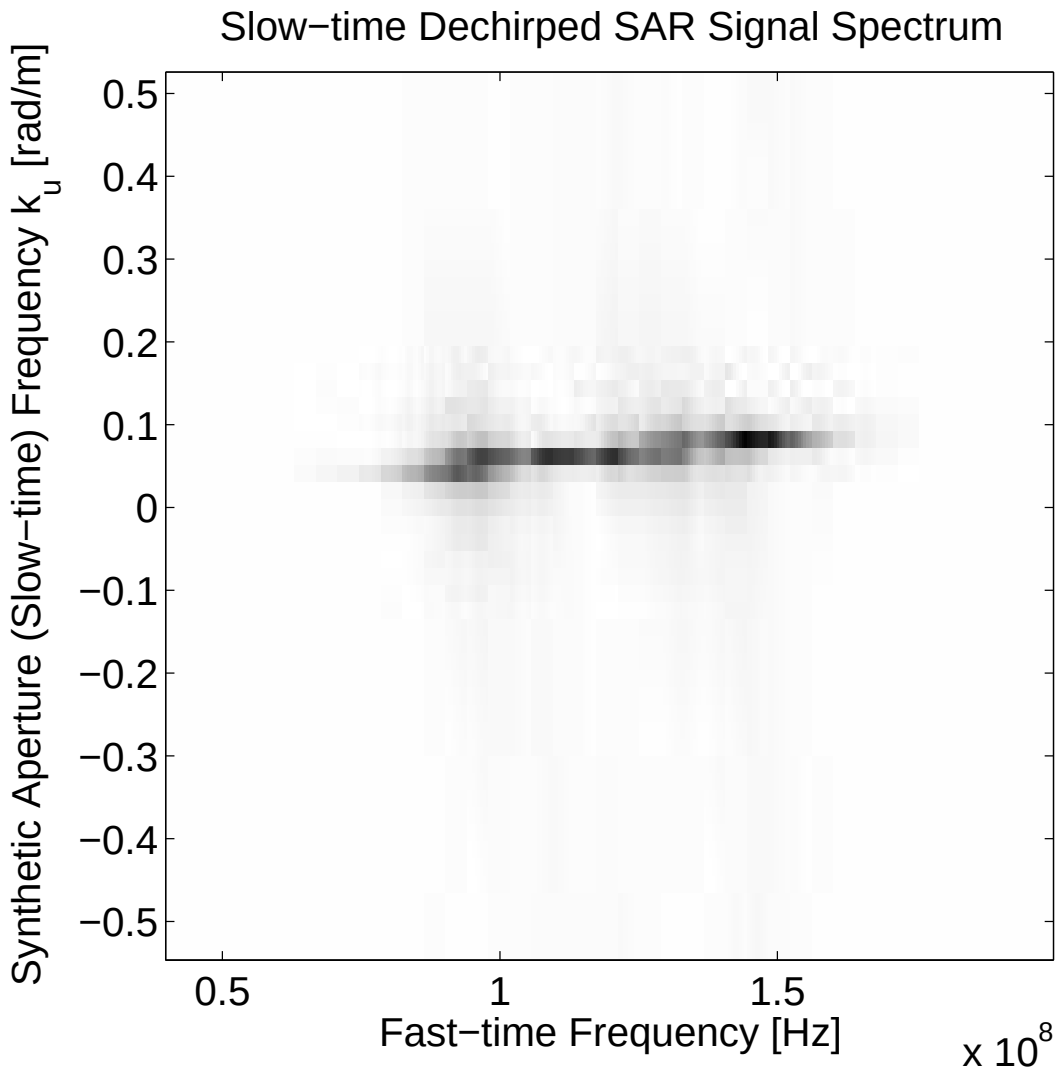

Figure 24: Compressed SAR signal spectrum of a single scatterer at $x = 20\text{m}, y = 20\text{m}$-broadside mode.

Performing the PFA wavenumber interpolations and using 2D inverse Fourier transform operation one obtains the scene scattering function which is presented in the Figure (25).

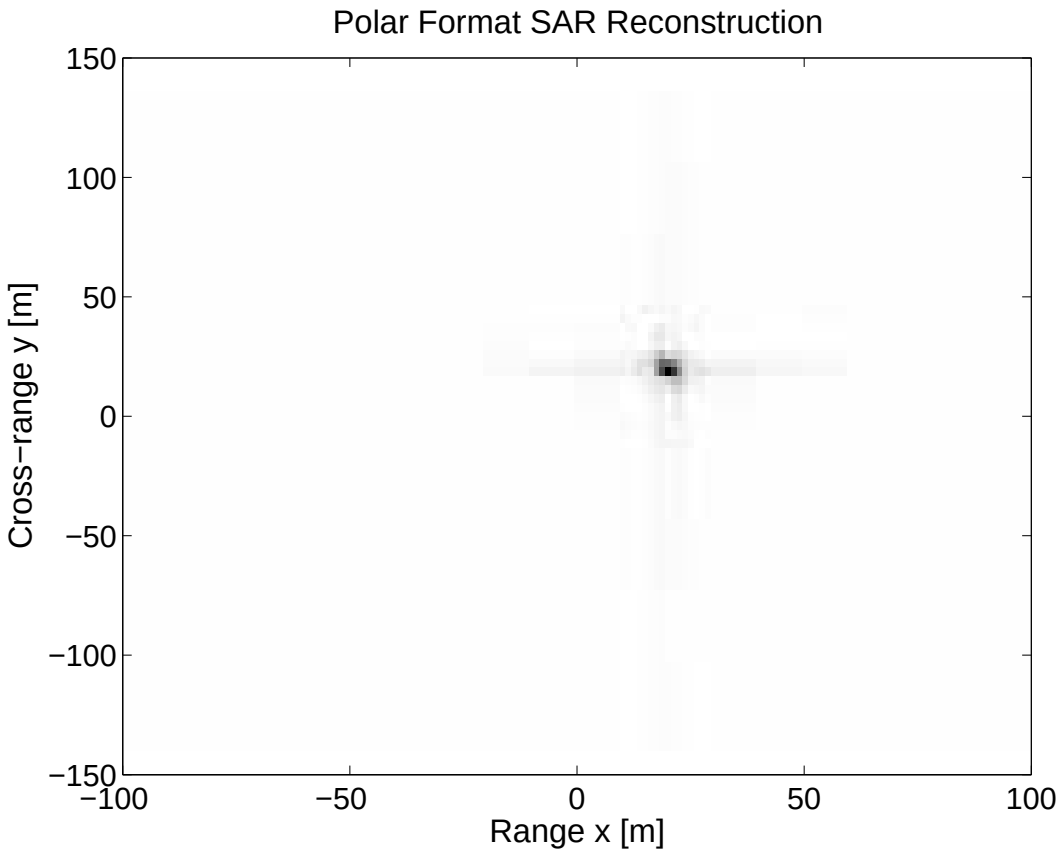

Figure 25: Polar format SAR reconstruction of a single scatterer at $x = 20\text{m}, y = 20\text{m}$-broadside mode.

The fourth example is for a single scatterer located at $x = 20\text{m}, y = 20\text{m}$ with the parameters $X_c = 1500\text{m}, Y_c = 500\text{m}, X_o = 100\text{m}, L = 150\text{m}$. In the Figure (26) the recorded SAR signal as a function of u and t is presented.

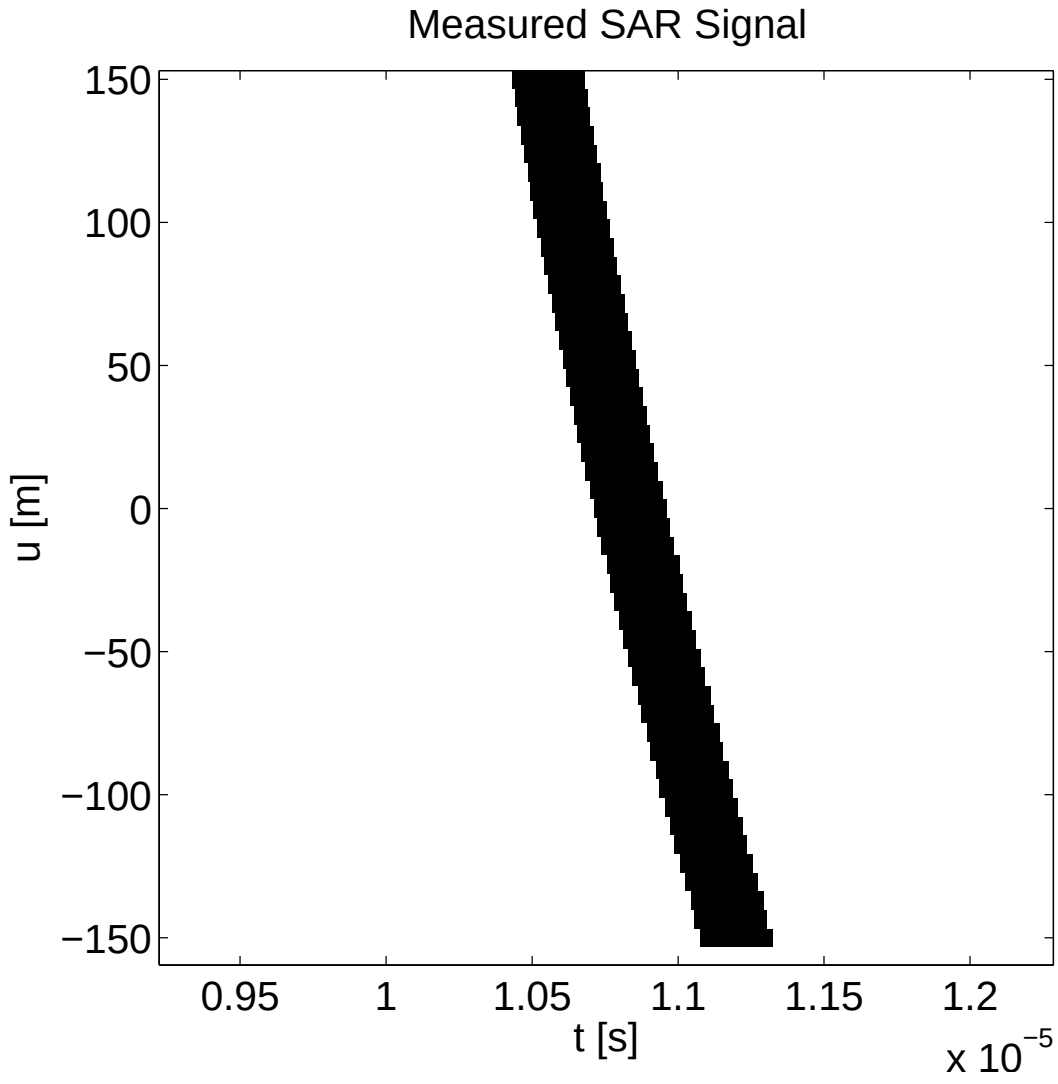

Figure 26: Measured SAR signal of a single scatterer at $x = 20\text{m}, y = 20\text{m}$-squinted mode.

Applying the matched filtering operation along t axis to the signal given in the Figure (26) one obtains the signal given in the Figure (27).

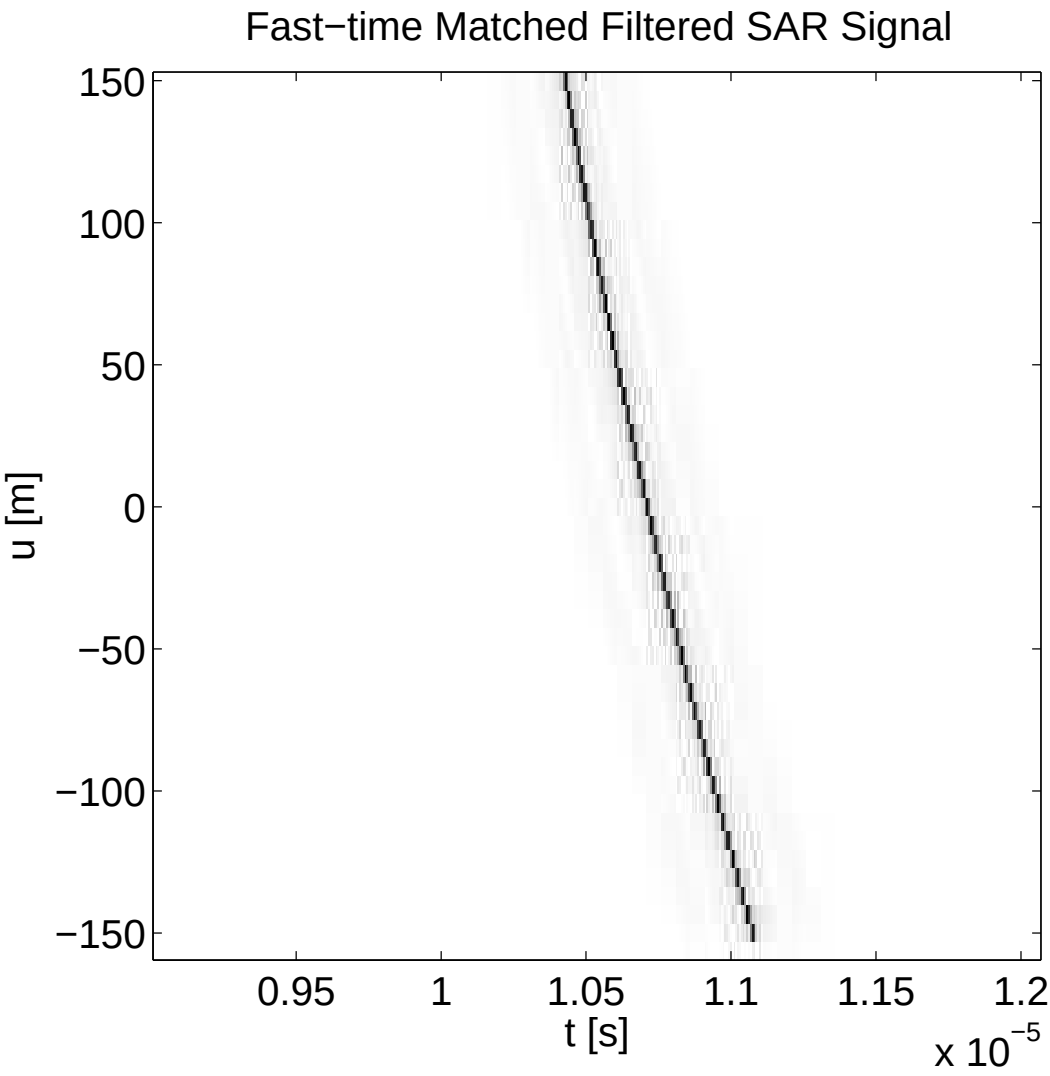

Figure 27: Fast-time matched filtered SAR signal of a single scatterer at $x = 20\text{m}, y = 20\text{m}$-squinted mode.

After 2D Fourier transforming and matched filtering in the u domain one obtains the scene spectrum given in the Figure (28).

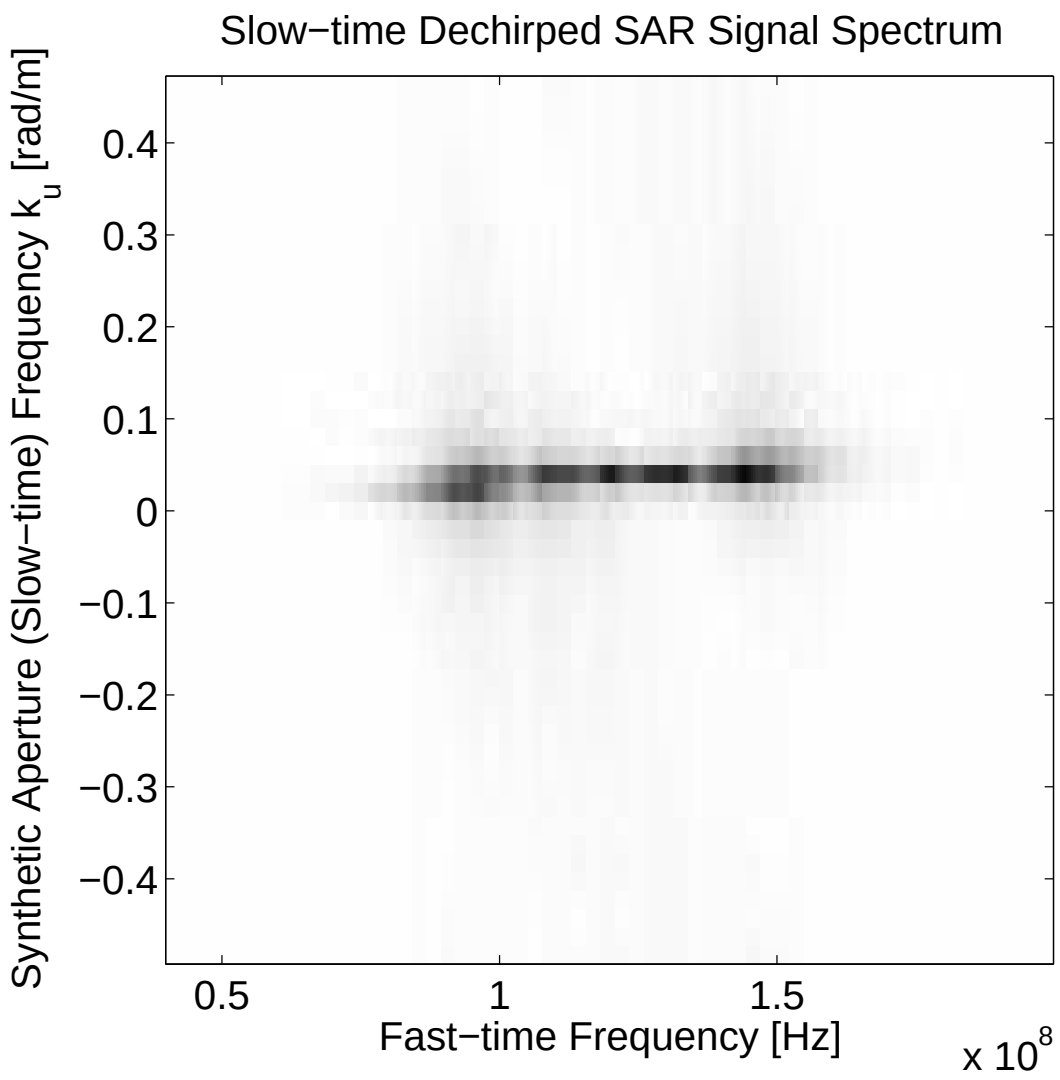

Figure 28: Compressed SAR signal spectrum of a single scatterer at $x = 20\text{m}, y = 20\text{m}$-squinted mode.

Performing the PFA wavenumber interpolations and using 2D inverse Fourier transform operation one obtains the scene scattering function which is presented in the Figure (29).

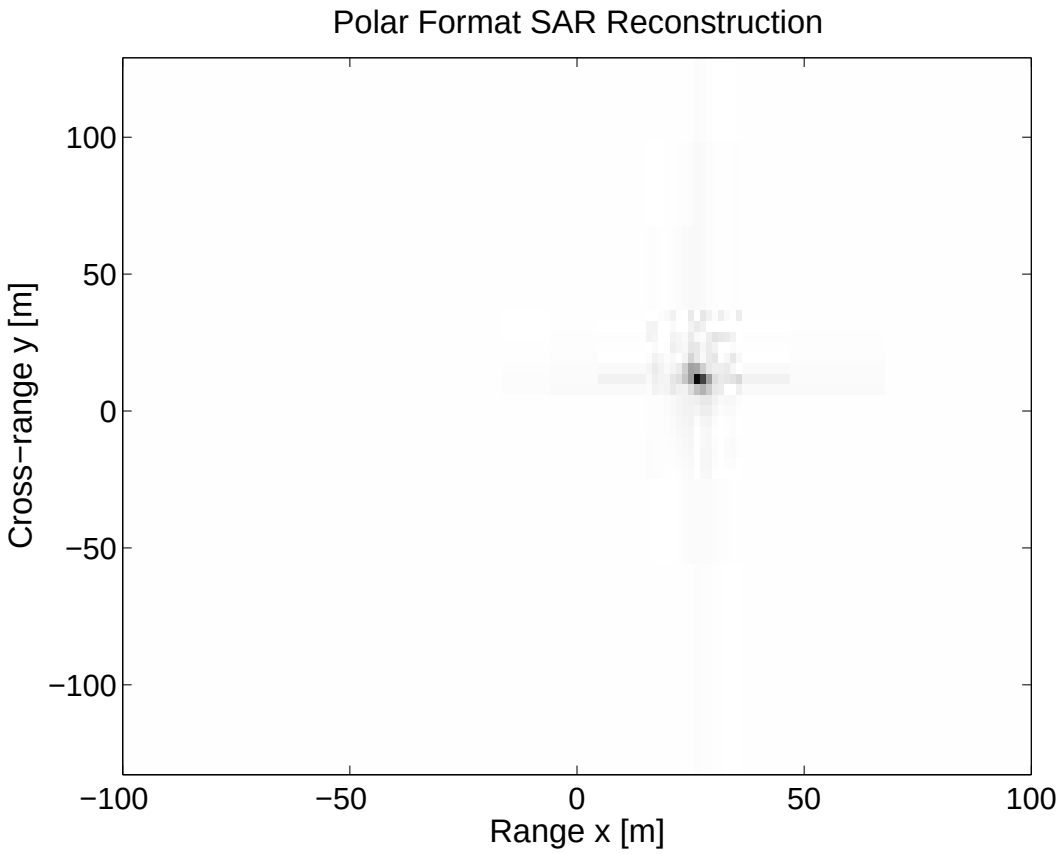

Figure 29: Polar format SAR reconstruction of a single scatterer at $x = 20\text{m}, y = 20\text{m}$-squinted mode.

The fifth example is for 5 scatterers located at $x_1 = 0\text{m}, y_1 = 0\text{m}$, $x_2 = 70\text{m}, y_2 = -60\text{m}$, $x_3 = -70\text{m}, y_3 = 60\text{m}$, $x_4 = -60\text{m}, y_4 = 75\text{m}$, $x_5 = 60\text{m}, y_5 = -75\text{m}$ with the parameters $X_c = 1500\text{m}, Y_c = 0\text{m}, X_o = 100\text{m}, L = 100\text{m}$. In the Figure (30) the recorded SAR signal as a function of u and t is presented.

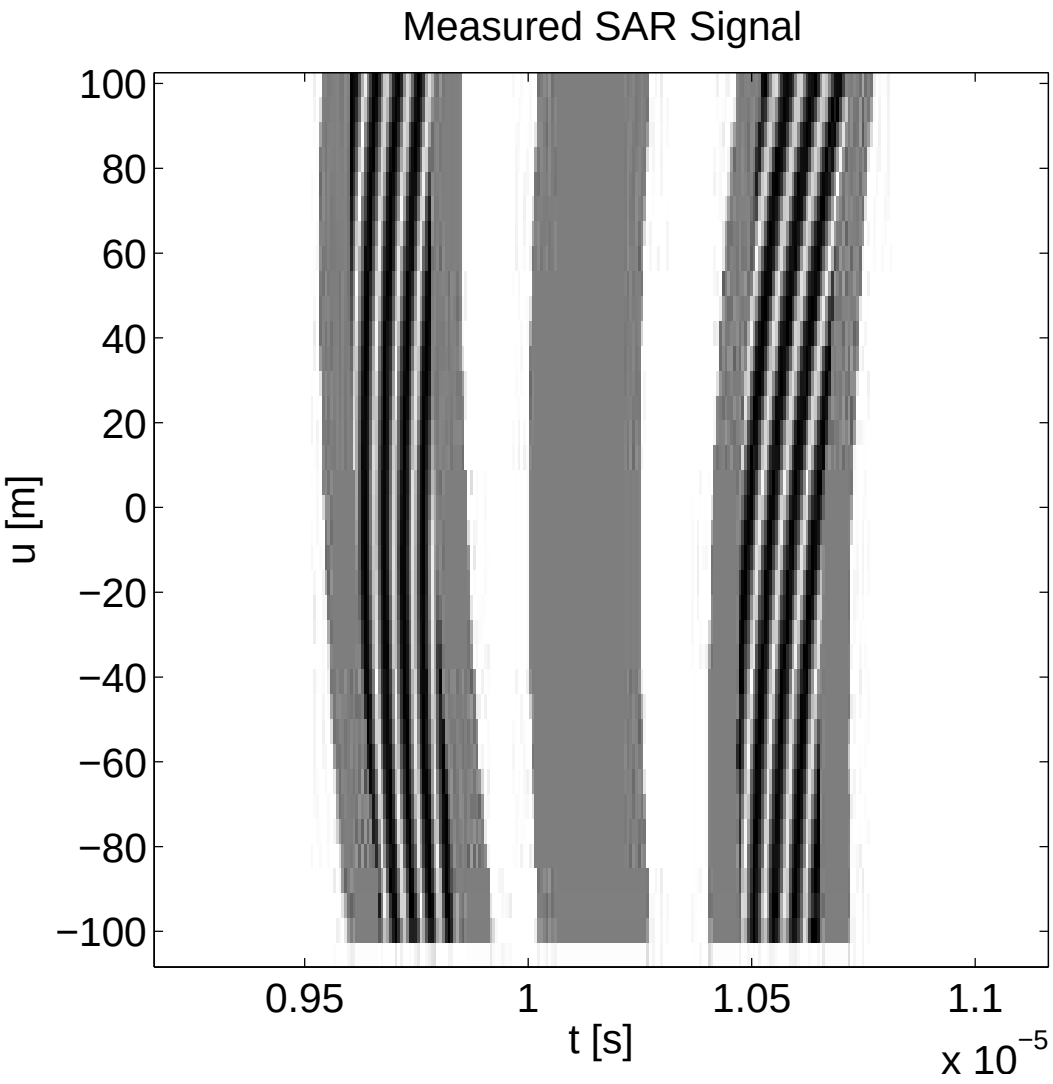

Figure 30: Measured SAR signal of 5 scatterers-broadside mode.

Applying the matched filtering operation along t axis to the signal given in the Figure (30) one obtains the signal given in the Figure (31).

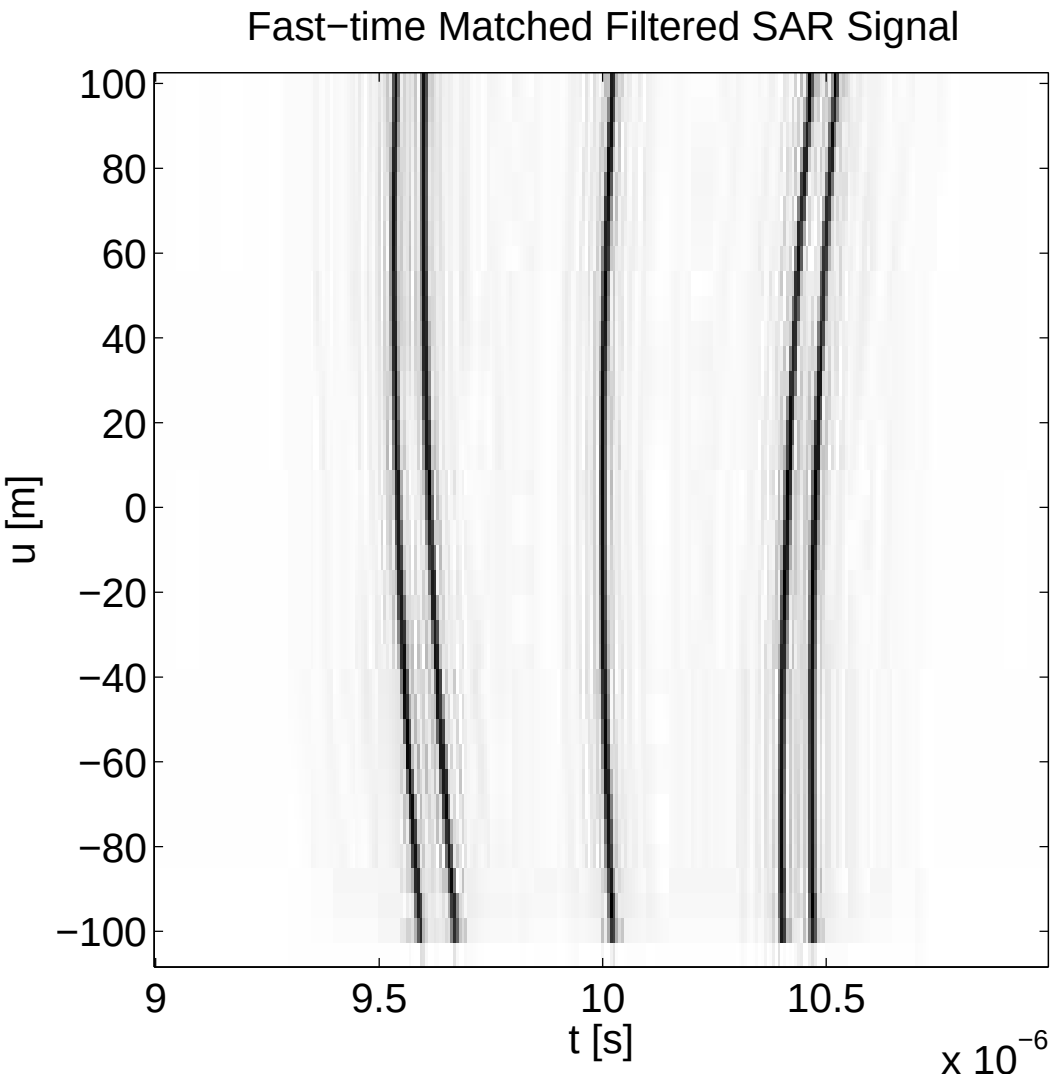

Figure 31: Fast-time matched filtered SAR signal of 5 scatterers-broadside mode.

After 2D Fourier transforming and matched filtering in the u domain one obtains the scene spectrum given in the Figure (32).

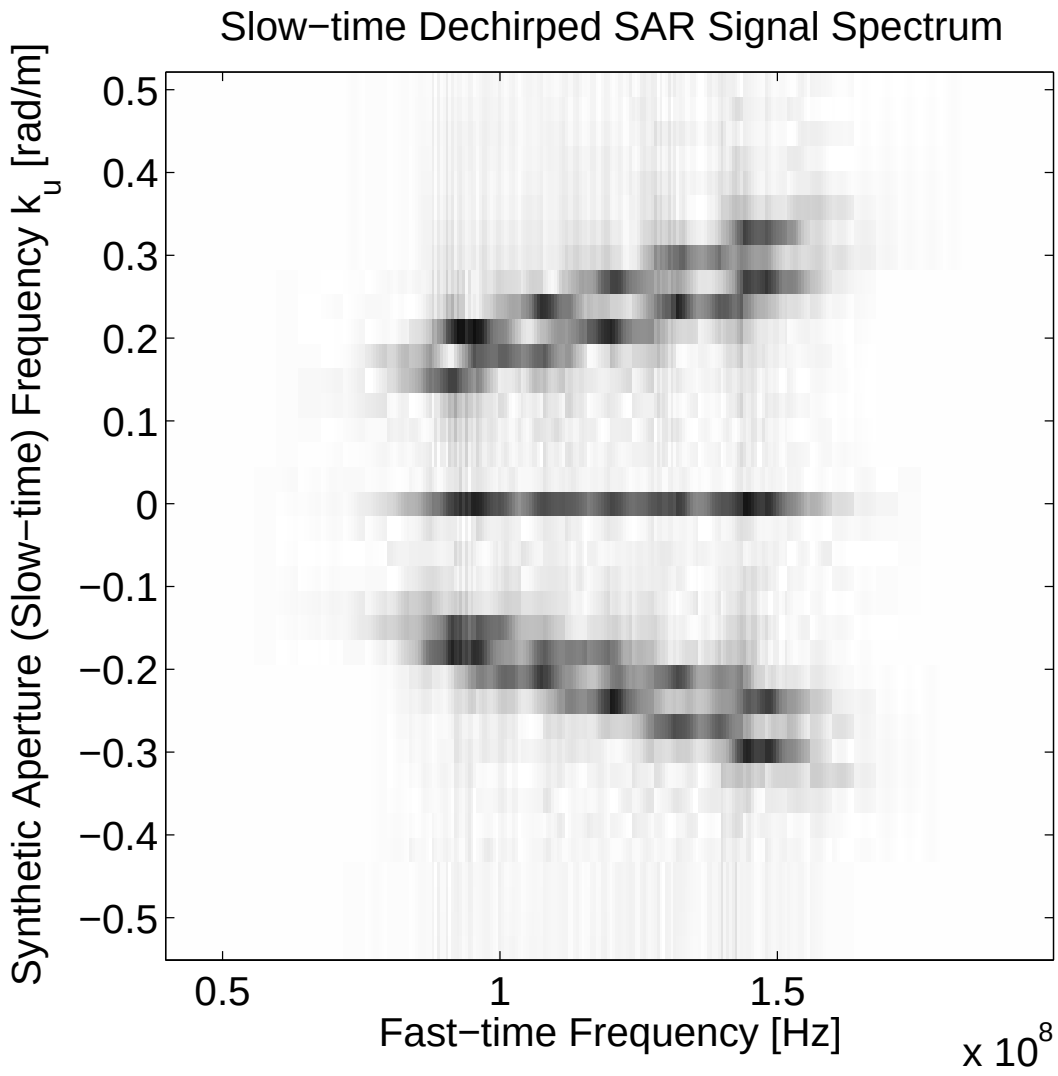

Figure 32: Compressed SAR signal spectrum of 5 scatterers-broadside mode.

Performing the PFA wavenumber interpolations and using 2D inverse Fourier transform operation one obtains the scene scattering function which is presented in the Figure (33).

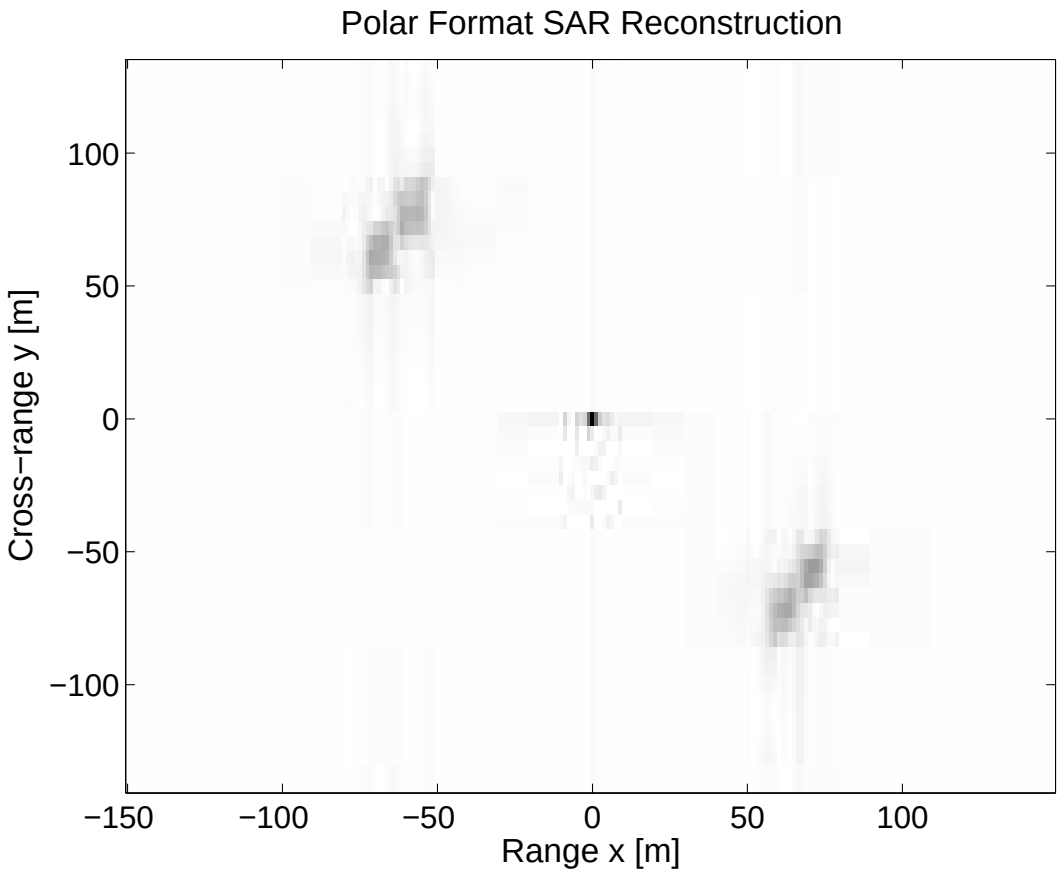

Figure 33: Polar format SAR reconstruction of 5 scatterers-broadside mode.

The sixth example is for 5 scatterers located at $x_1 = 0\text{m}, y_1 = 0\text{m}$, $x_2 = 70\text{m}, y_2 = -60\text{m}$, $x_3 = -70\text{m}, y_3 = 60\text{m}$, $x_4 = -60\text{m}, y_4 = 75\text{m}$, $x_5 = 60\text{m}, y_5 = -75\text{m}$ with the parameters $X_c = 1500\text{m}, Y_c = 500\text{m}, X_o = 100\text{m}, L = 100\text{m}$. In the Figure (34) the recorded SAR signal as a function of u and t is presented.

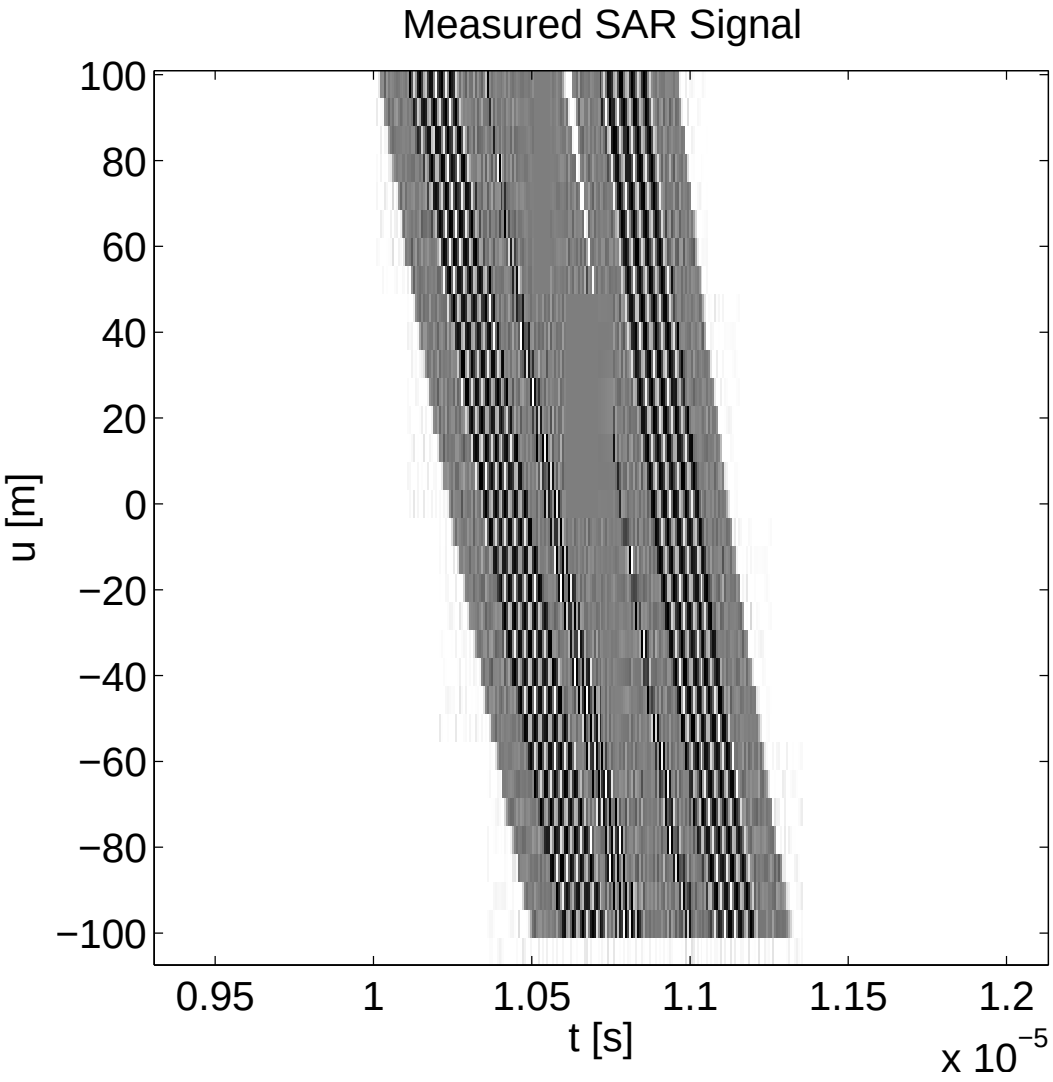

Figure 34: Measured SAR signal of 5 scatterers-squinted mode.

Applying the matched filtering operation along t axis to the signal given in the Figure (34) one obtains the signal given in the Figure (35).

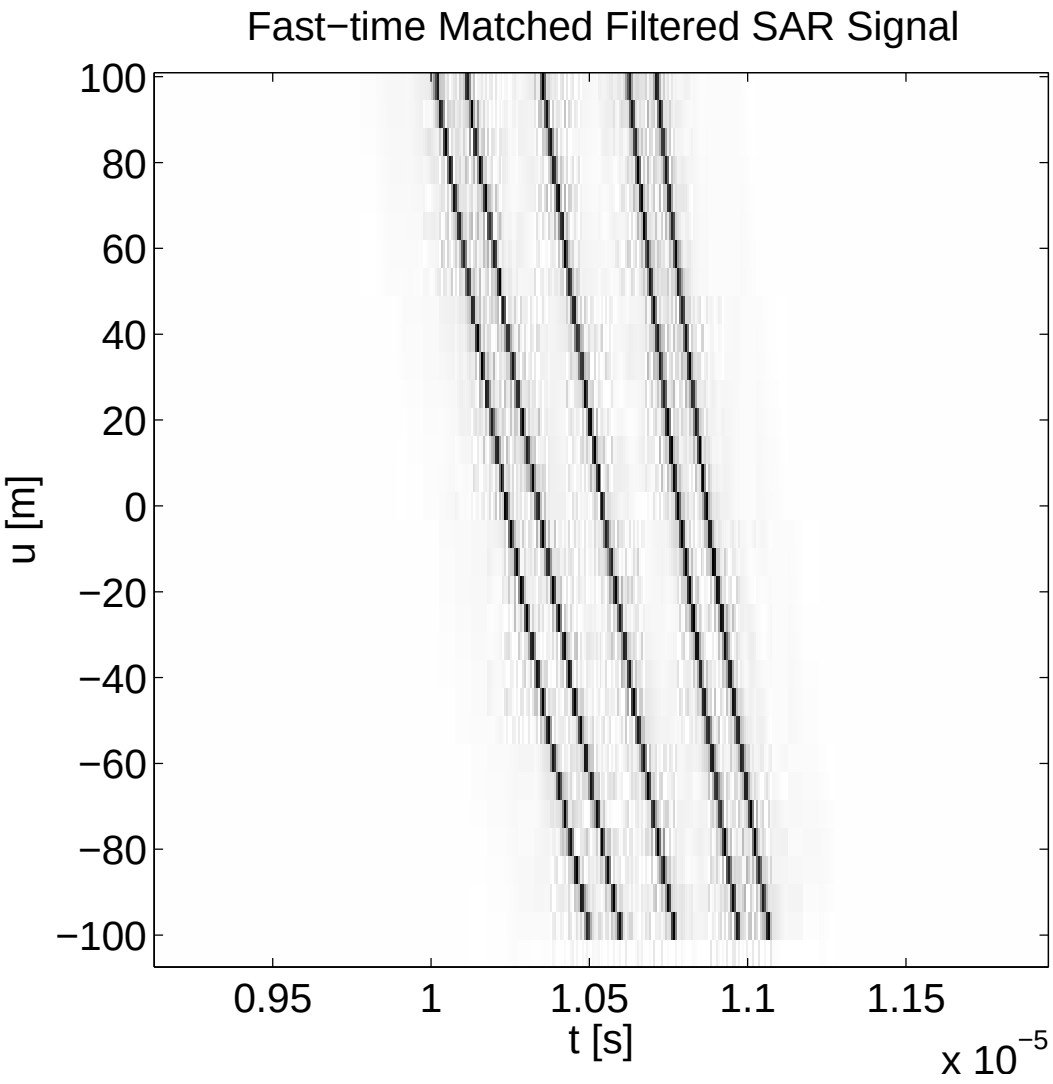

Figure 35: Fast-time matched filtered SAR signal of 5 scatterers-squinted mode.

After 2D Fourier transforming and matched filtering in the u domain one obtains the scene spectrum given in the Figure (36).

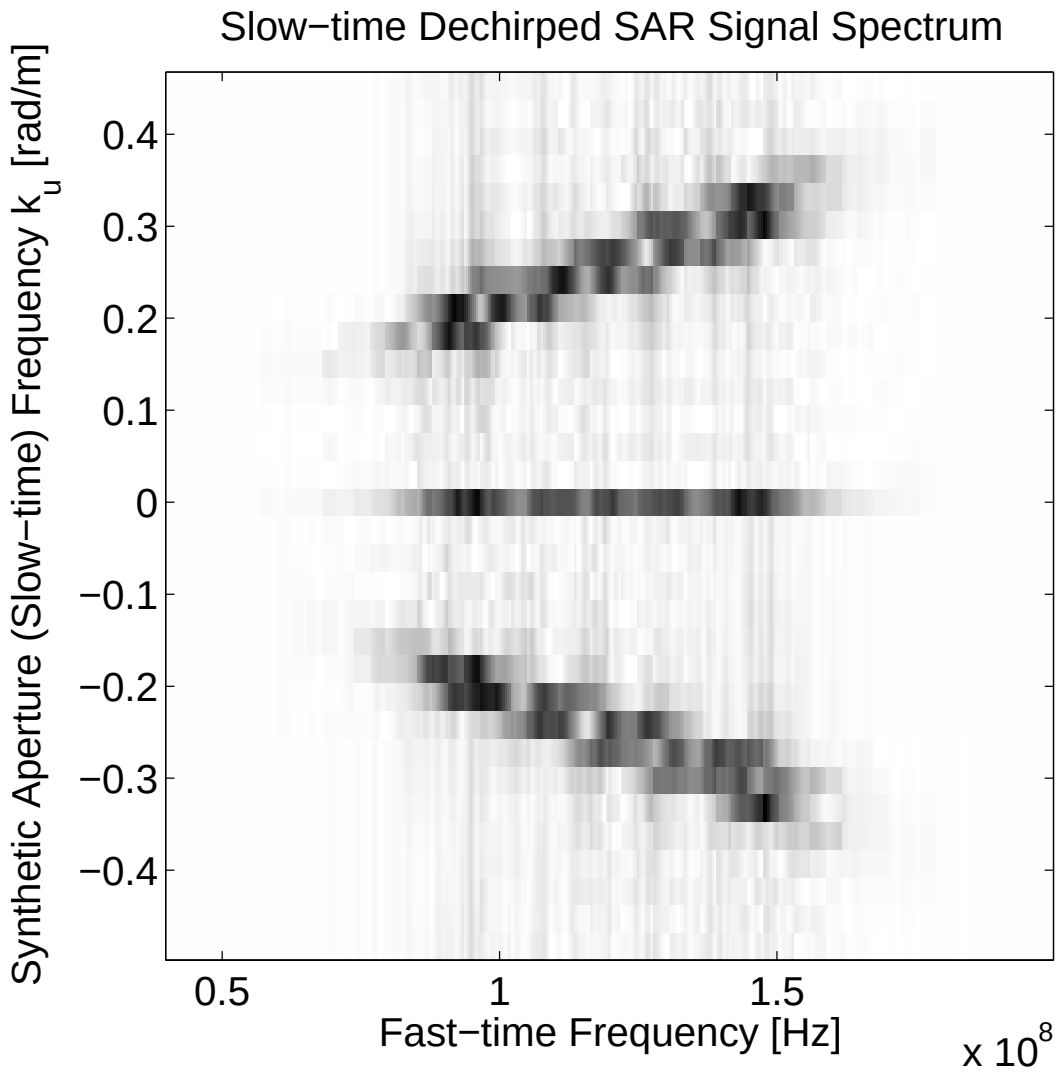

Figure 36: Compressed SAR signal spectrum of 5 scatterers-squinted mode.

Performing the PFA wavenumber interpolations and using 2D inverse Fourier transform operation one obtains the scene scattering function which is presented in the Figure (37).

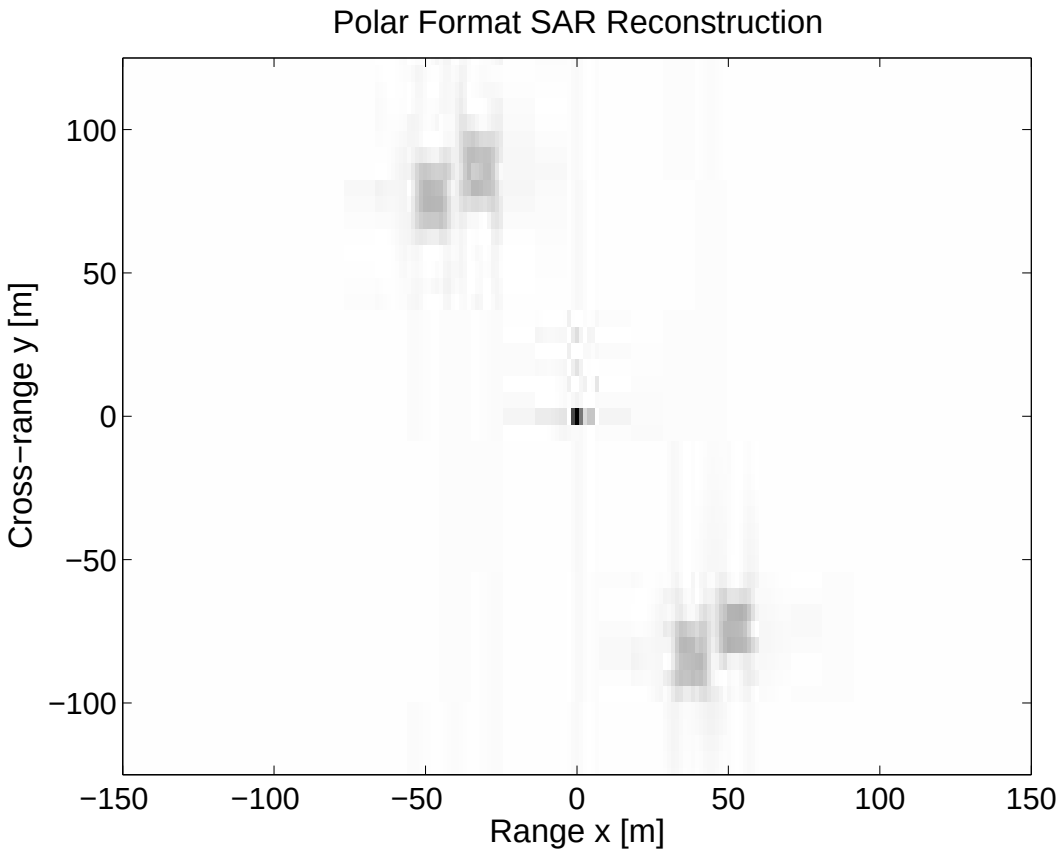

Figure 37: Polar format SAR reconstruction of 5 scatterers-squinted mode.

The seventh example is for 25 scatterers uniformly distributed inside a square with coordinates $(-50\text{m}, -50\text{m})$, $(-50\text{m}, 50\text{m})$, $(50\text{m}, 50\text{m})$, $(50\text{m}, -50\text{m})$ with the parameters $X_c = 1500\text{m}, Y_c = 0\text{m}, X_o = 100\text{m}, L = 100\text{m}$. In the Figure (38) the recorded SAR signal as a function of u and t is presented.

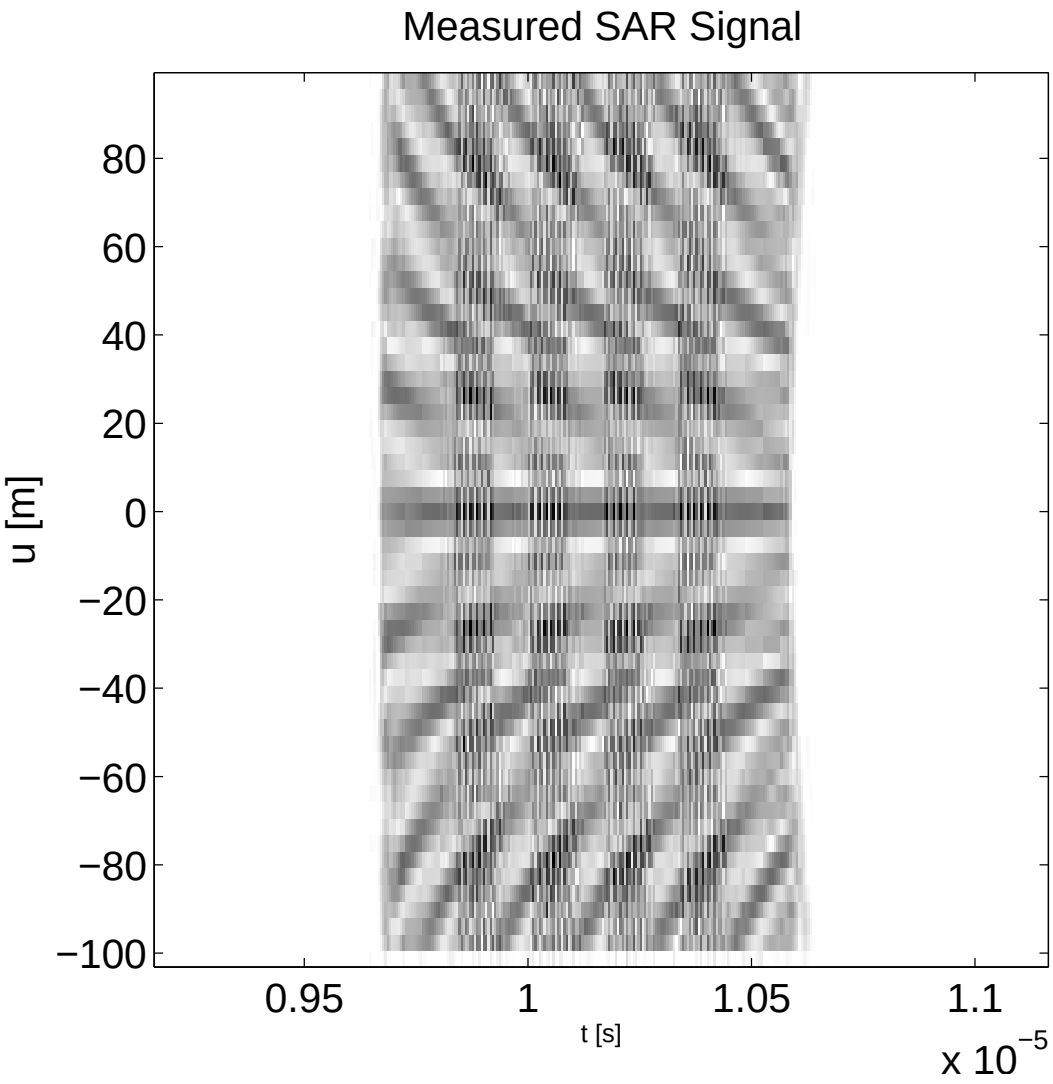

Figure 38: Measured SAR signal of 25 scatterers-broadside mode.

Applying the matched filtering operation along t axis to the signal given in the Figure (38) one obtains the signal given in the Figure (39).

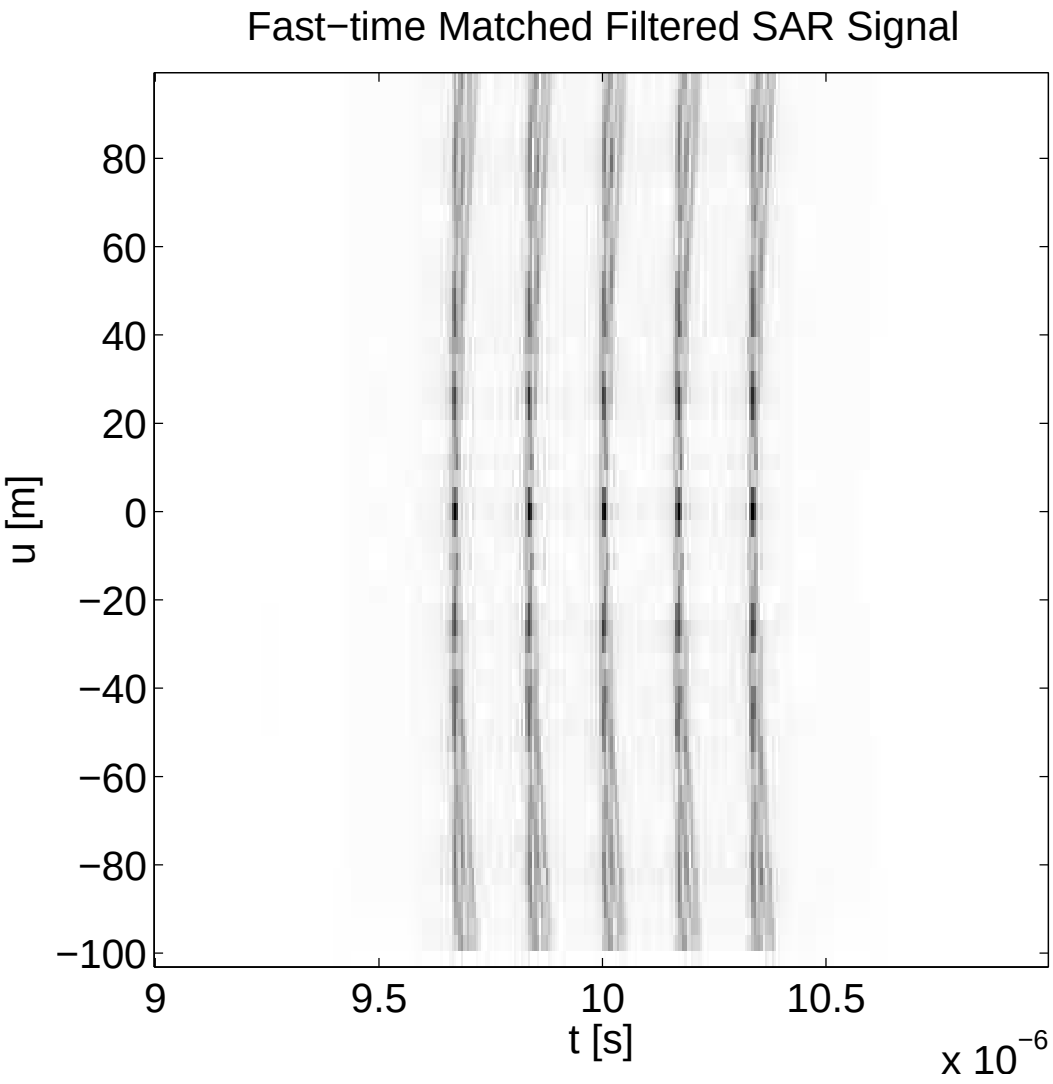

Figure 39: Fast-time matched filtered SAR signal of 25 scatterers-broadside mode.

After 2D Fourier transforming and matched filtering in the u domain one obtains the scene spectrum given in the Figure (40).

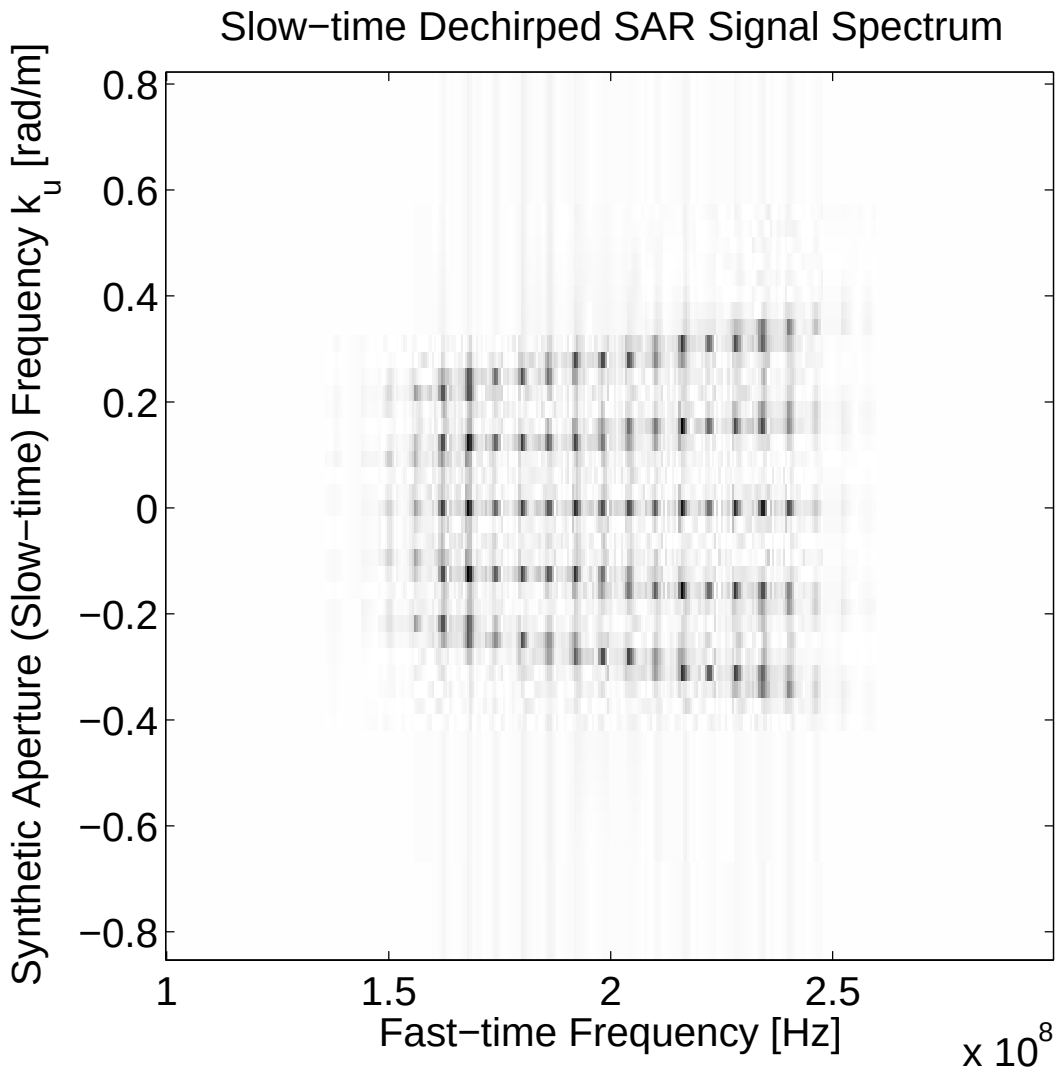

Figure 40: Compressed SAR signal spectrum of 25 scatterers-broadside mode.

Performing the PFA wavenumber interpolations and using 2D inverse Fourier transform operation one obtains the scene scattering function which is presented in the Figure (41).

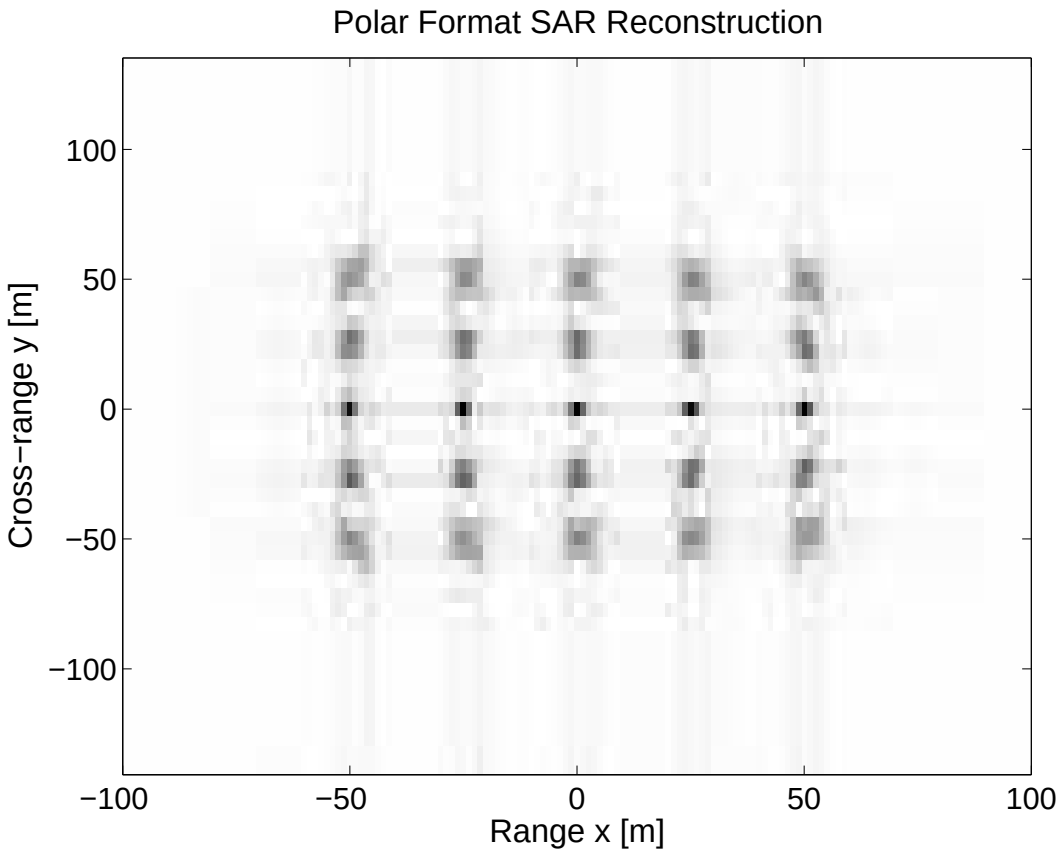

Figure 41: Polar format SAR reconstruction of 25 scatterers-broadside mode.

The eighth example is for 25 scatterers uniformly distributed inside a square with coordinates $(-50\text{m}, -50\text{m})$, $(-50\text{m}, 50\text{m})$, $(50\text{m}, 50\text{m})$, $(50\text{m}, -50\text{m})$ with the parameters $X_c = 1500\text{m}, Y_c = 500\text{m}, X_o = 100\text{m}, L = 100\text{m}$. In the Figure (42) the recorded SAR signal as a function of u and t is presented.

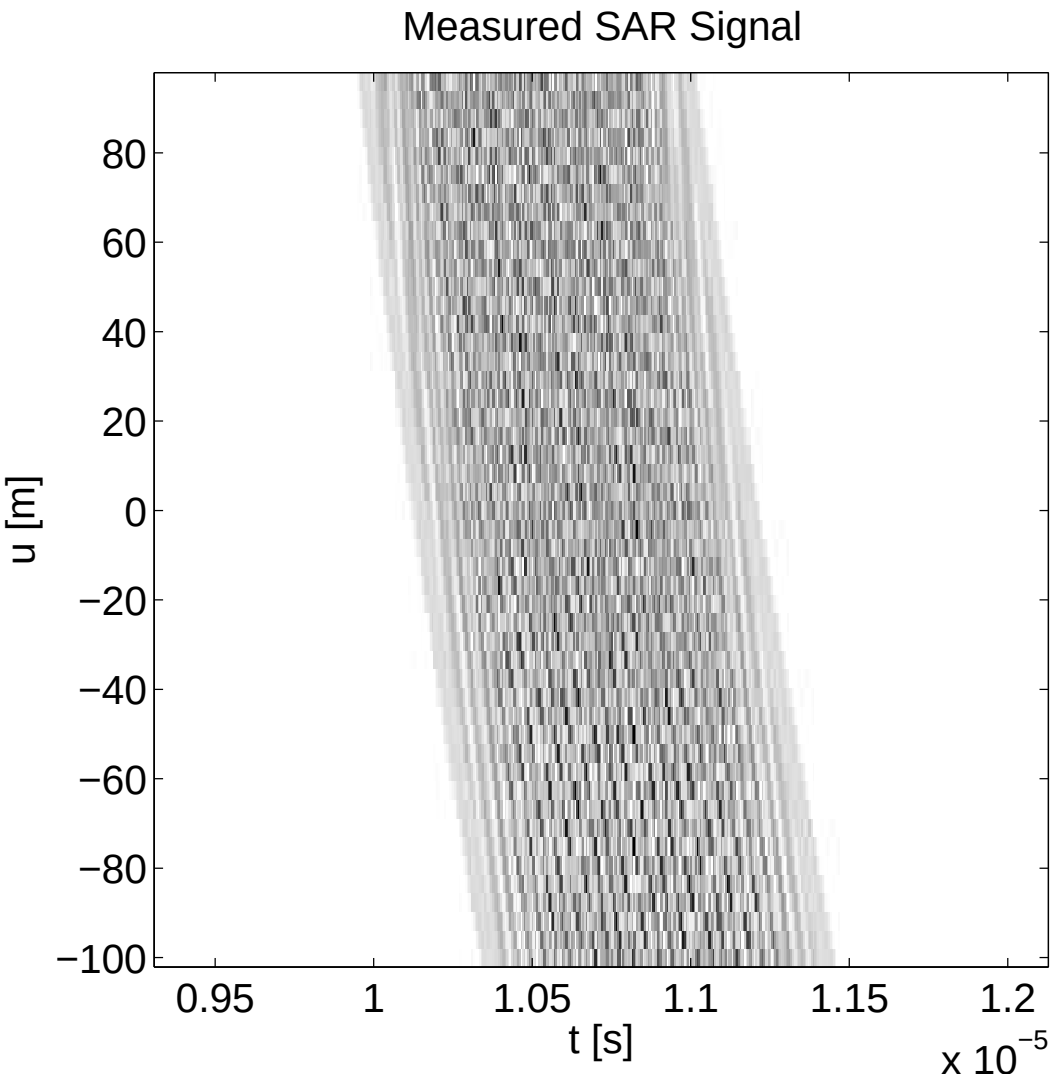

Figure 42: Measured SAR signal of 25 scatterers-squinted mode.

Applying the matched filtering operation along t axis to the signal given in the Figure (42) one obtains the signal given in the Figure (43).

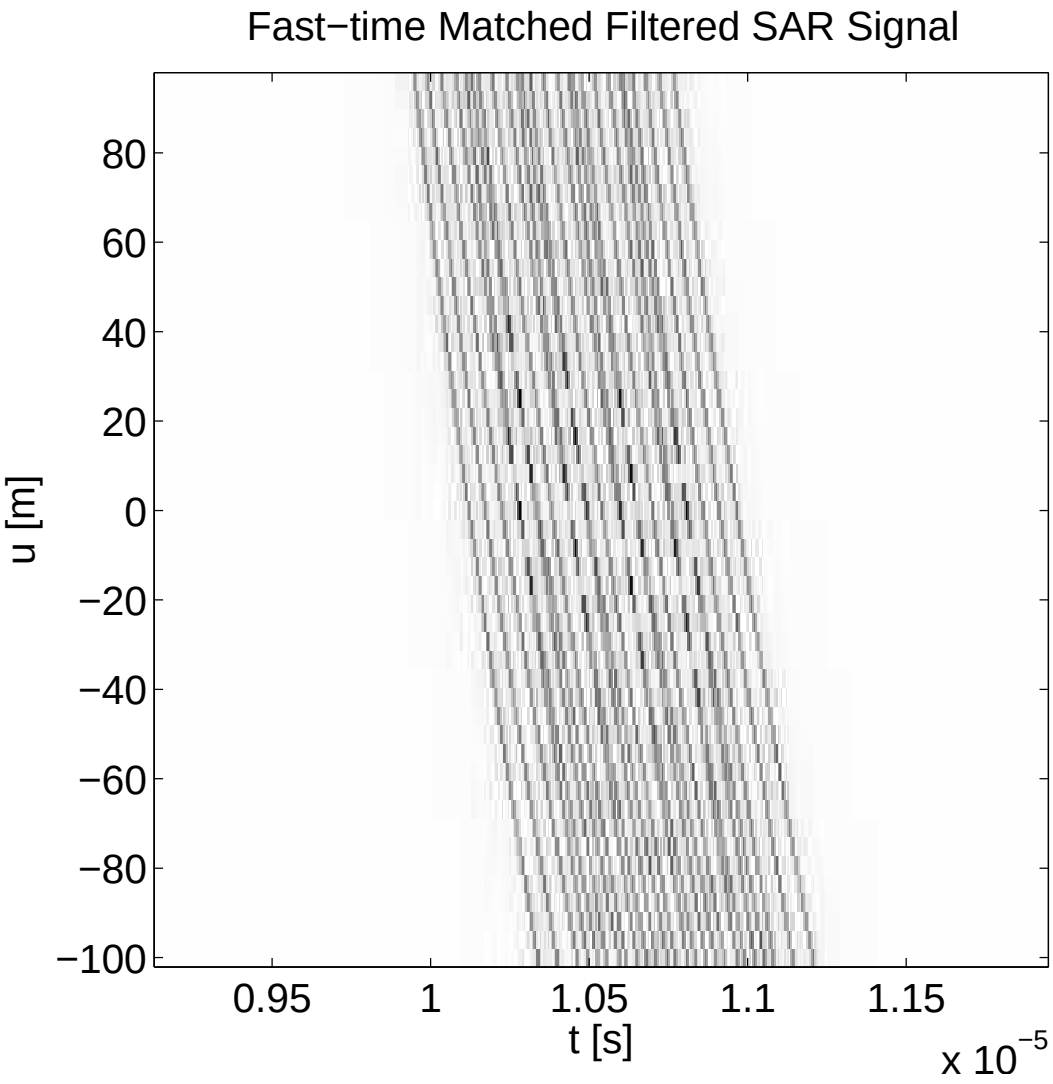

Figure 43: Fast-time matched filtered SAR signal of 25 scatterers-squinted mode.

After 2D Fourier transforming and matched filtering in the u domain one obtains the scene spectrum given in the Figure (44).

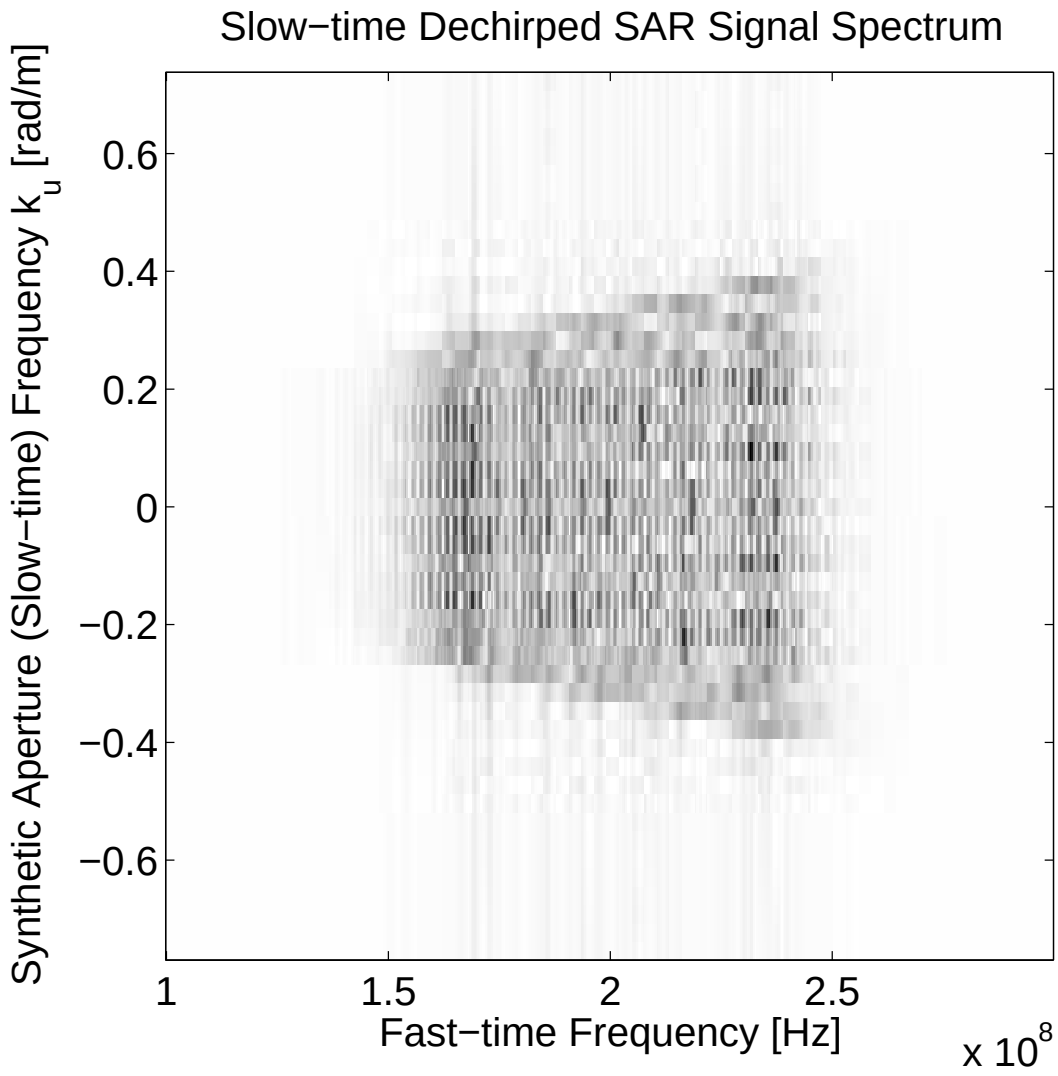

Figure 44: Compressed SAR signal spectrum of 25 scatterers-squinted mode.

Performing the PFA wavenumber interpolations and using 2D inverse Fourier transform operation one obtains the scene scattering function which is presented in the Figure (45).

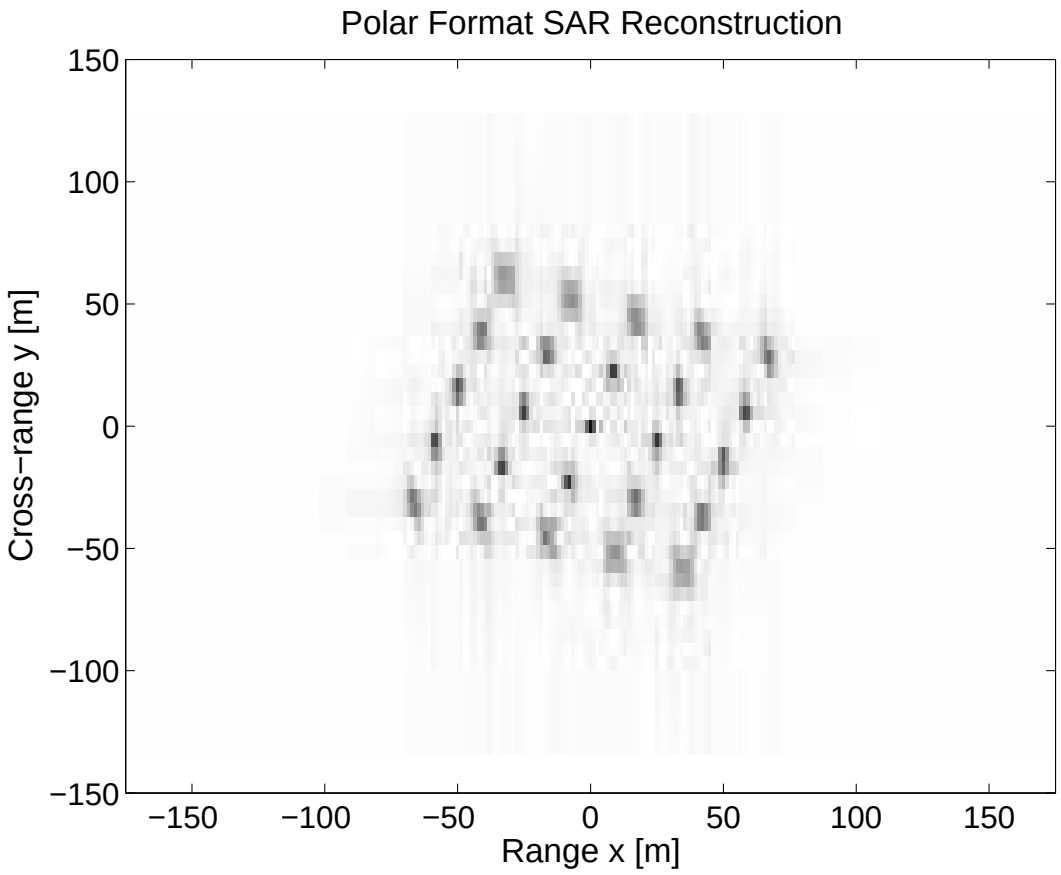

Figure 45: Polar format SAR reconstruction of 25 scatterers-squinted mode.

The ninth example is for 25 scatterers uniformly distributed inside a square with coordinates $(-50\text{m}, -50\text{m})$, $(-50\text{m}, 50\text{m})$, $(50\text{m}, 50\text{m})$, $(50\text{m}, -50\text{m})$ with the parameters $X_c = 10000\text{m}, Y_c = 0\text{m}, X_o = 100\text{m}, L = 300\text{m}$. In the Figure (46) the recorded SAR signal as a function of u and t is presented.

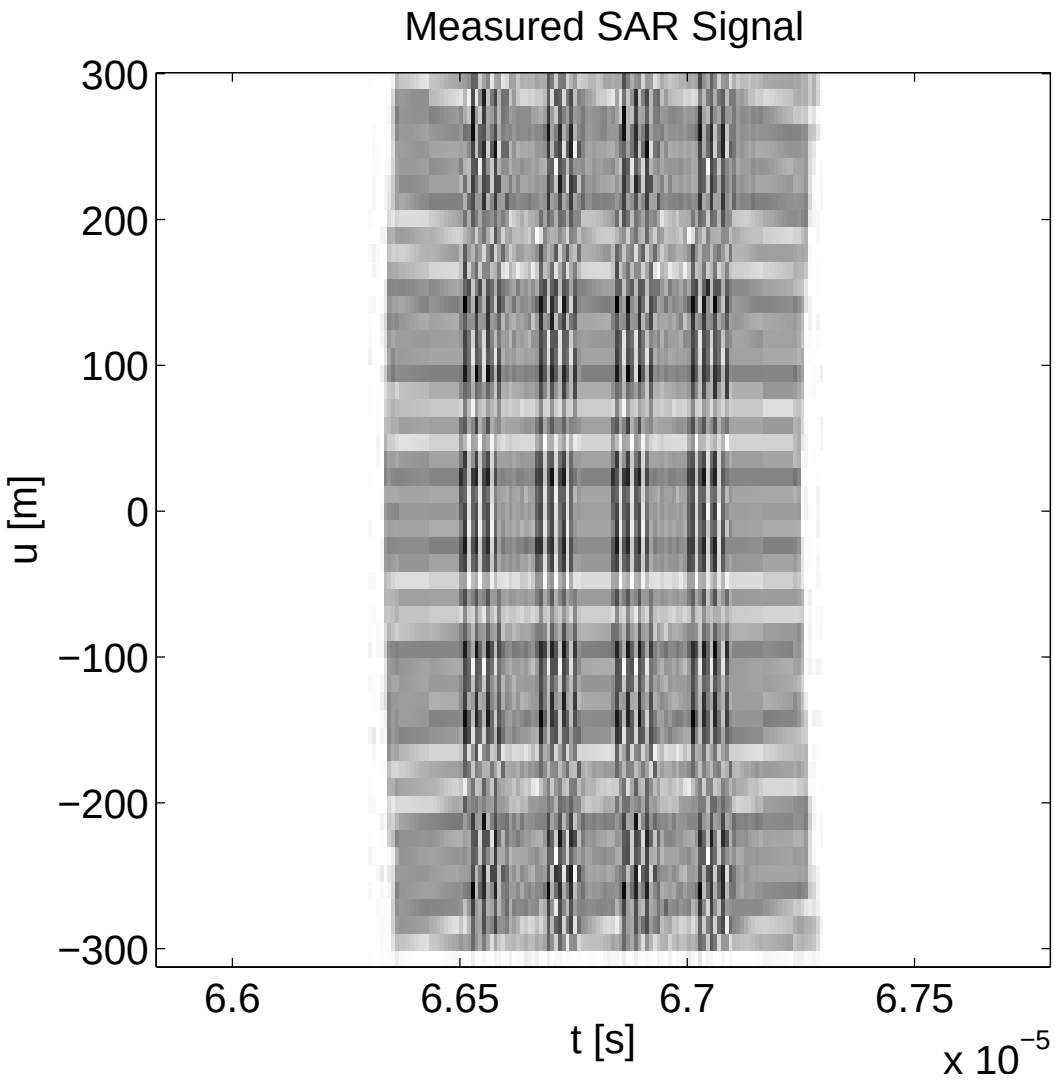

Figure 46: Measured SAR signal of 25 scatterers-far field broadside mode.

Applying the matched filtering operation along t axis to the signal given in the Figure (46) one obtains the signal given in the Figure (47).

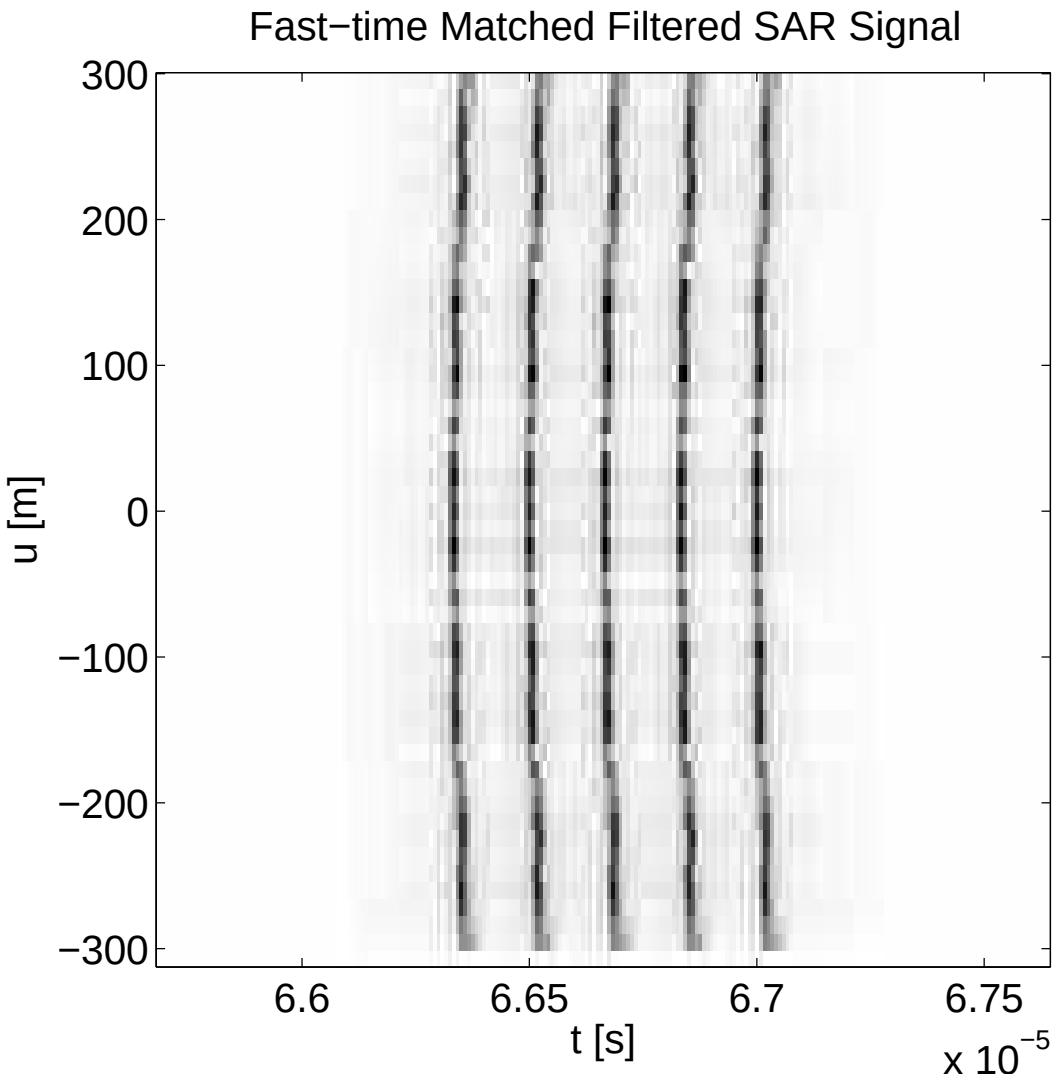

Figure 47: Fast-time matched filtered SAR signal of 25 scatterers-far field broadside mode.

After 2D Fourier transforming and matched filtering in the u domain one obtains the scene spectrum given in the Figure (48).

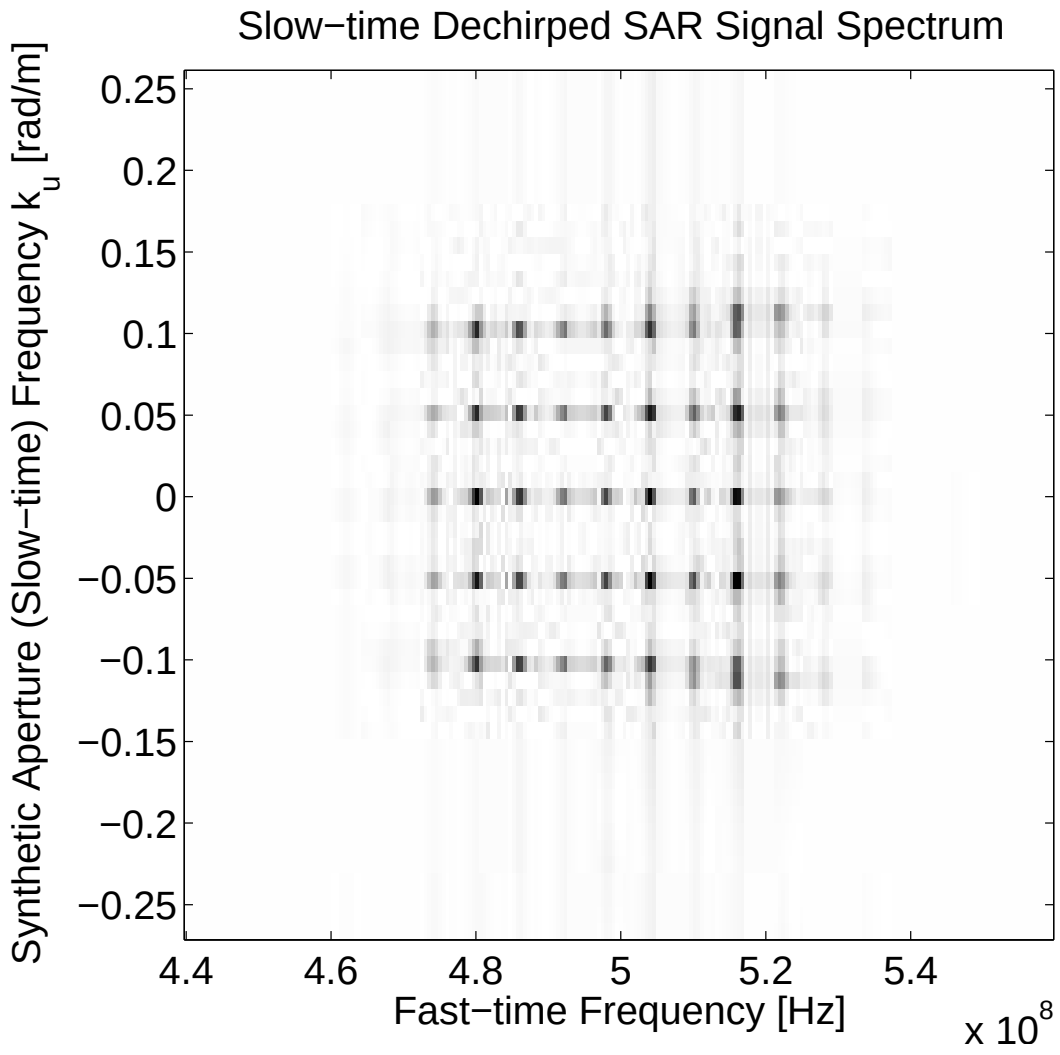

Figure 48: Compressed SAR signal spectrum of 25 scatterers-far field broadside mode.

Performing the PFA wavenumber interpolations and using 2D inverse Fourier transform operation one obtains the scene scattering function which is presented in the Figure (49).

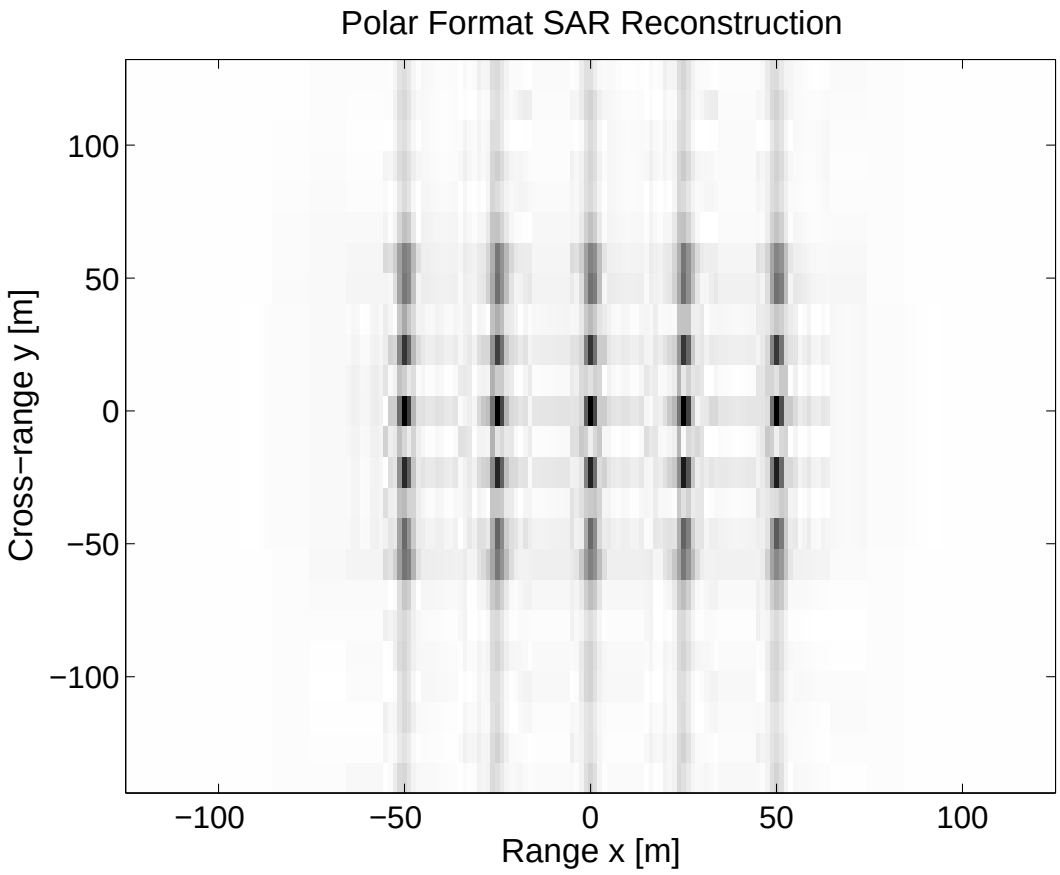

Figure 49: Polar format SAR reconstruction of 25 scatterers-far field broadside mode.

4.2.2 Polar Format Processing using $t^{0.75}$FM Signals

In this section the imagery reconstructed by LFM and $t^{0.75}$FM chirps using polar format processing are compared. 3 example images which are reconstructed by polar format processing for spotlight imaging geometry are presented. Therefore for the $p(t)$ in the equation (90), the expression given in the equation (2) for LFM chirp and the expression given in the equation (36) for $t^{0.75}$FM chirp are used.

The first example is for a single scatterer located at $x = 0\text{m}, y = 0\text{m}$ with the parameters $X_c = 1500\text{m}, Y_c = 500\text{m}, X_o = 100\text{m}, L = 100\text{m}$ with signal parameters $T_p = 1 \times 10^{-6}\text{s}$, $f_c = 200 \times 10^6$ Hz, $f_o = 10 \times 10^6$ Hz. In the Figure (50) the image reconstructed by PFA with LFM chirp signal is presented. The chirp rate for these parameters is $\alpha \approx 6.28 \times 10^{13}$.

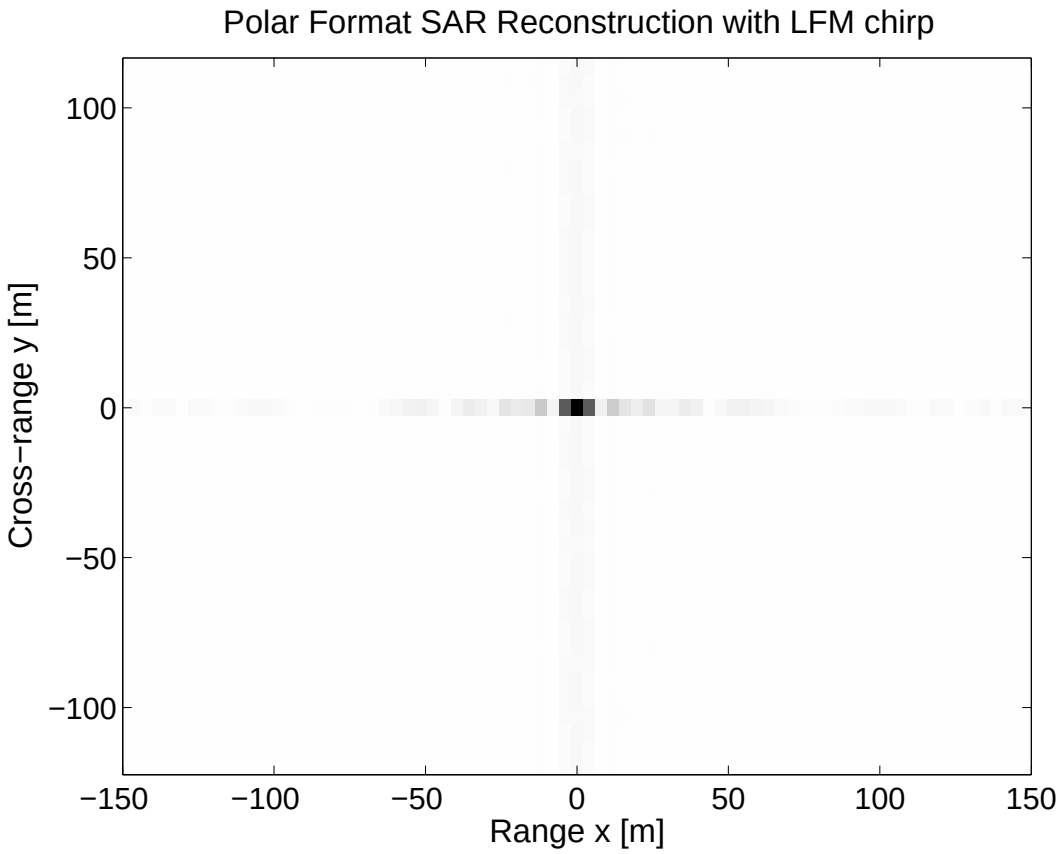

Figure 50: Polar format SAR reconstruction of a single scatterer at $x = 0\text{m}, y = 0\text{m}$-squinted mode-using LFM chirp.

The image reconstructed by PFA with $t^{0.75}$FM chirp signal, which can be seen in the Figure (51), is almost identical to image reconstructed by LFM chirp with reduced sidelobes and has a lower chirp rate which is $\eta \approx 2.27 \times 10^{12}$.

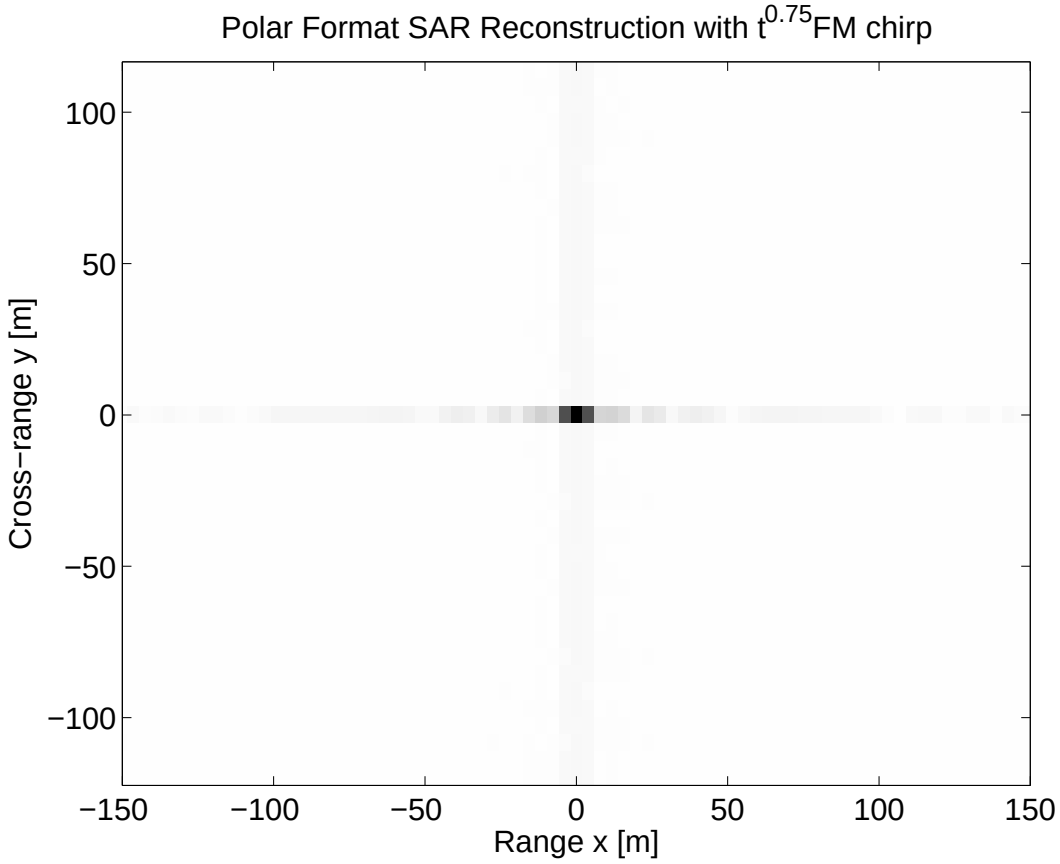

Figure 51: Polar format SAR reconstruction of a single scatterer at $x = 0\text{m}, y = 0\text{m}$-squinted mode-using $t^{0.75}$FM chirp.

The second example is for 5 scatterers located at $x_1 = 0\text{m}, y_1 = 0\text{m}$, $x_2 = 14\text{m}, y_2 = -12\text{m}$, $x_3 = -14\text{m}, y_3 = 12\text{m}$, $x_4 = -12\text{m}, y_4 = 15\text{m}$, $x_5 = 12\text{m}, y_5 = -15\text{m}$ with the parameters $X_c = 1500\text{m}, Y_c = 0\text{m}, X_o = 100\text{m}, L = 150\text{m}$ with signal parameters $T_p = 10 \times 10^{-6}\text{s}$, $f_c = 200 \times 10^6$ Hz, $f_o = 15 \times 10^6$ Hz. In the Figure (52) the image reconstructed by PFA with LFM chirp signal is presented. The chirp rate for these parameters is $\alpha \approx 9.42 \times 10^{12}$.

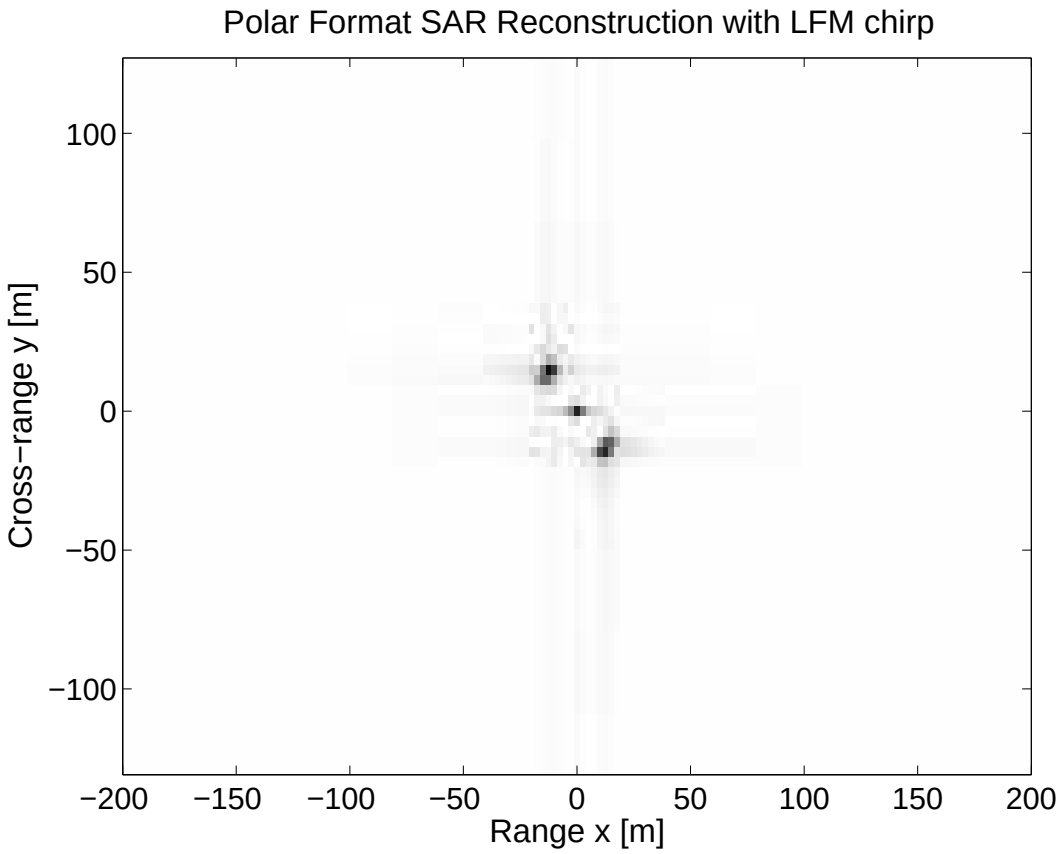

Figure 52: Polar format SAR reconstruction of 5 scatterers-broadside mode-using LFM chirp.

The image reconstructed by PFA with $t^{0.75}$FM chirp signal, which can be seen in the Figure (53), is almost identical to image reconstructed by LFM chirp with reduced sidelobes and has a lower chirp rate which is $\eta \approx 6.05 \times 10^{11}$.

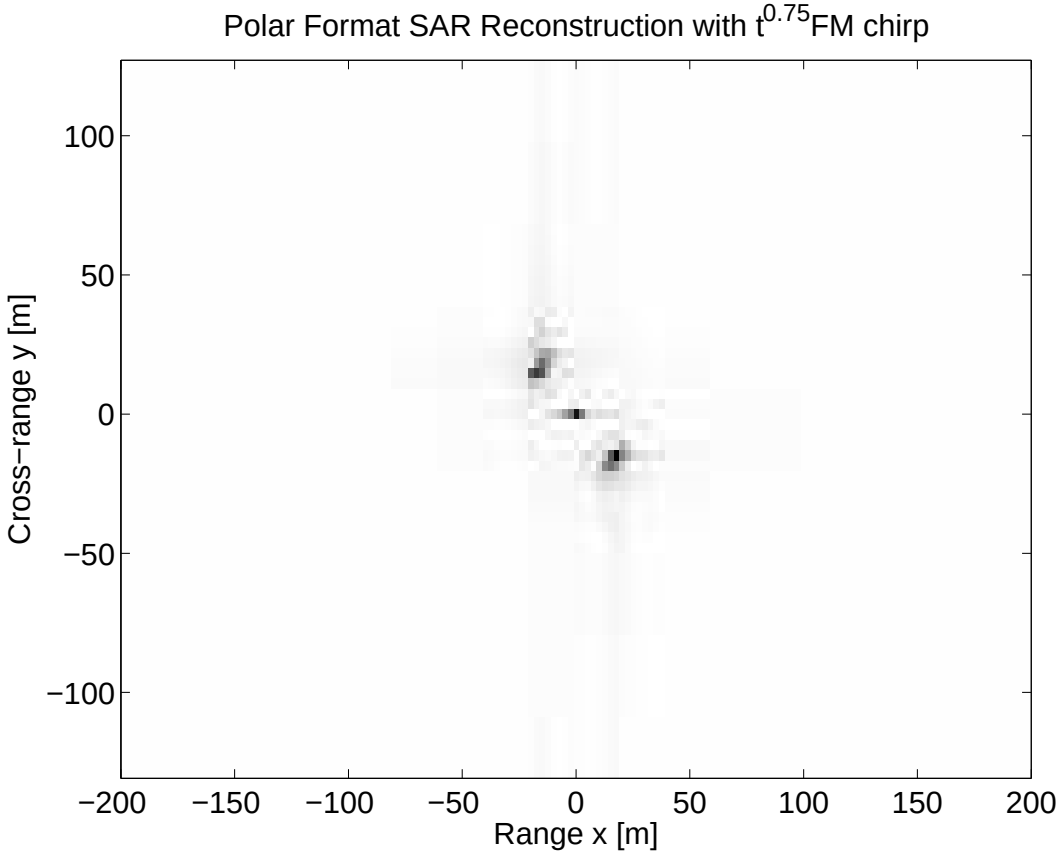

Figure 53: Polar format SAR reconstruction of 5 scatterers-broadside mode-using $t^{0.75}$FM chirp.

The third example is for 25 scatterers uniformly distributed inside a square with coordinates $(-25\text{m}, -25\text{m})$, $(-25\text{m}, 25\text{m})$, $(25\text{m}, 25\text{m})$, $(25\text{m}, -25\text{m})$ with the parameters $X_c = 1500\text{m}, Y_c = 0\text{m}, X_o = 100\text{m}, L = 100\text{m}$ with signal parameters $T_p = 5 \times 10^{-6}\text{s}$, $f_c = 200 \times 10^6$ Hz, $f_o = 12 \times 10^6$ Hz. In the Figure (54) the image reconstructed by PFA with LFM chirp signal is presented. The chirp rate for these parameters is $\alpha \approx 1.50 \times 10^{13}$.

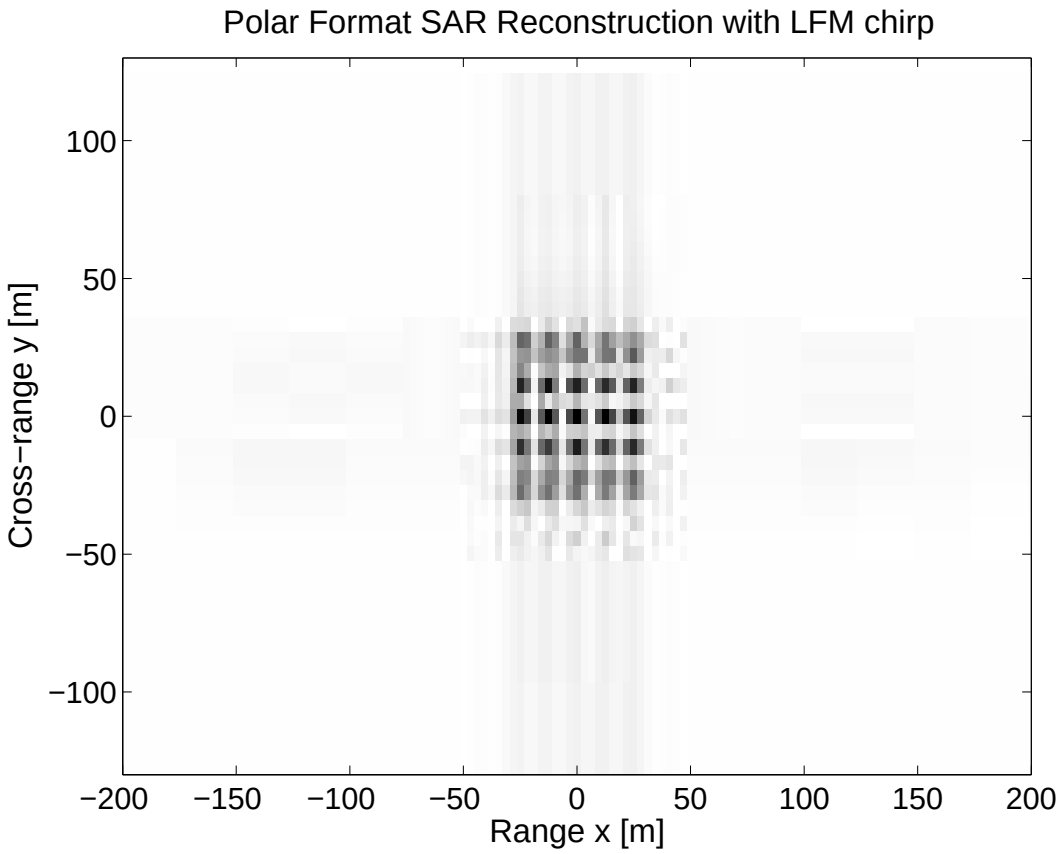

Figure 54: Polar format SAR reconstruction of 25 scatterers-broadside mode-using LFM chirp.

The image reconstructed by PFA with $t^{0.75}$FM chirp signal, which can be seen in the Figure (55), is almost identical to image reconstructed by LFM chirp with reduced sidelobes and has a lower chirp rate which is $\eta \approx 8.14 \times 10^{11}$.

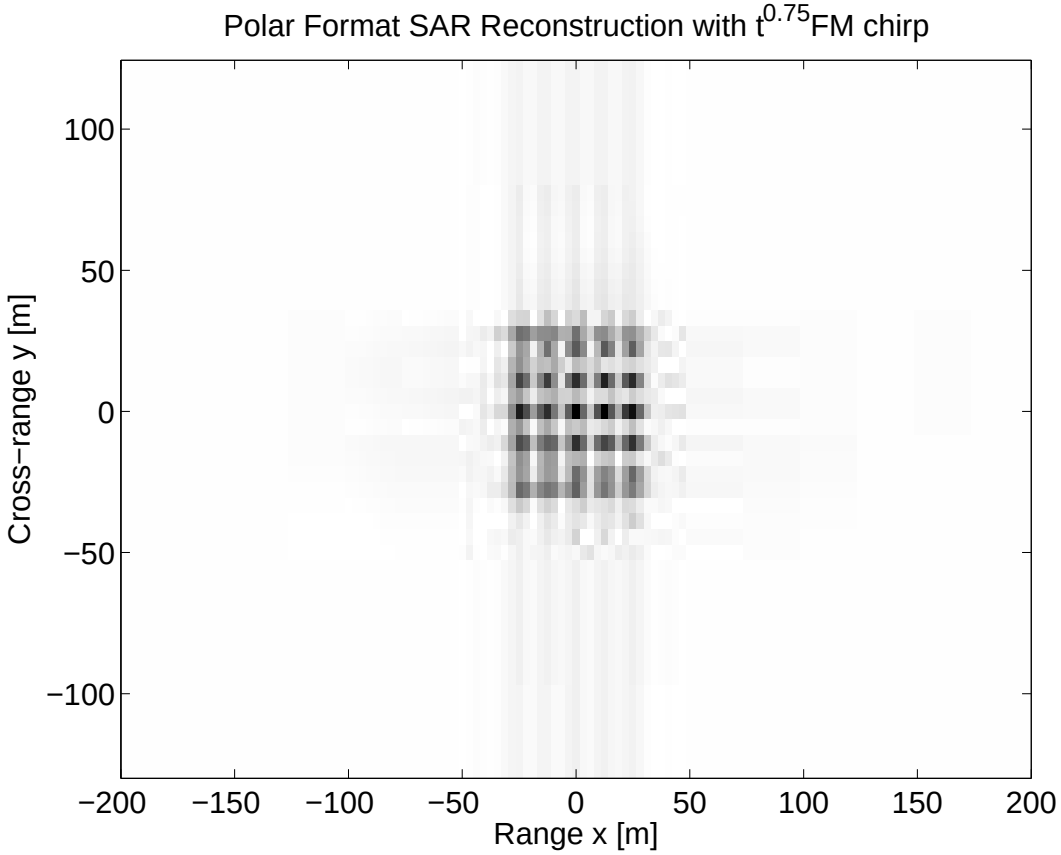

Figure 55: Polar format SAR reconstruction of 25 scatterers-broadside mode-using $t^{0.75}$FM chirp.

4.3 Spotlight SAR via Stolt Format Processing

In this section the Stolt format processing algorithm used to construct the images of spotlighted region is discussed. In some of the literature, as in [48], the term digital reconstruction via spatial frequency interpolation instead of Stolt format processing is used. Based on the analysis given for migration by Fourier Transform scheme in [49] it is preferred to use the term Stolt format processing eventhough the same idea is originally developed for seismic imaging (see [9] and [50]). In this section the derivations given in [48] are followed. Spotlight SAR imaging geometry for Stolt format processing can be seen in the Figure (56) below

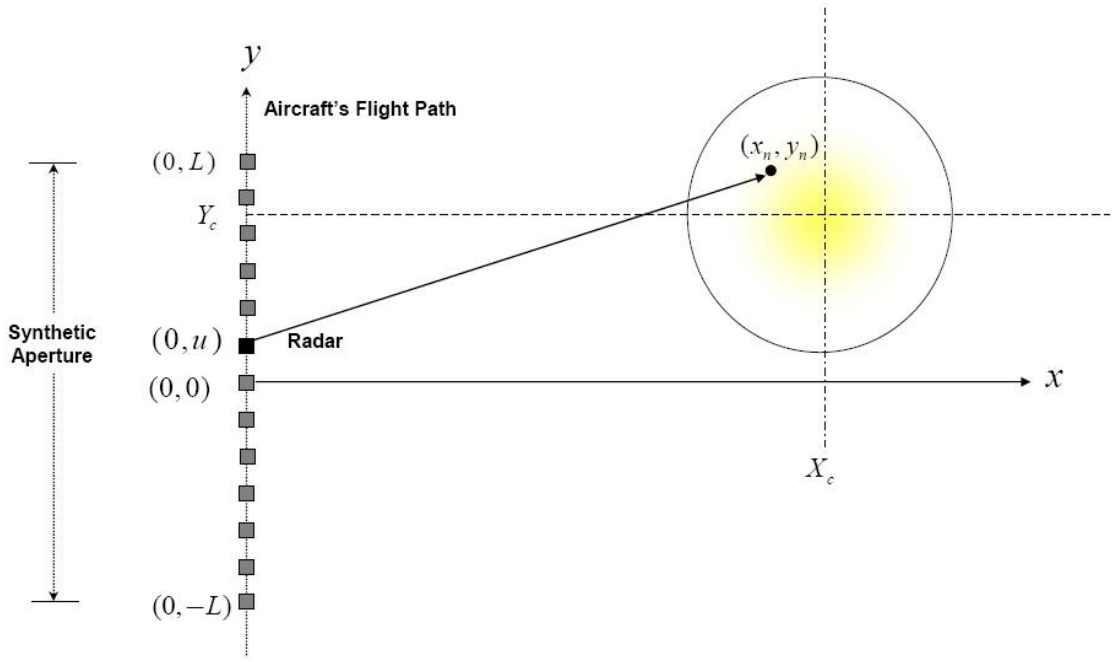

Figure 56: Spotlight imaging geometry for Stolt format processing.

It is useful to note that Stolt format processing is performed in the aperture coordinate system and no switching to the scene or rotated scene coordinate system is necessary. Considering the spotlight SAR imaging geometry presented in figure (56) total recorded signal becomes [48]

$$ss(t,u) = \sum_n \sigma_n p\left[t - \frac{2\sqrt{(x_n)^2 + (y_n - u)^2}}{c}\right] \tag{114}$$

where σ_n is the radar cross section of the n^{th} scatterer, x_n and y_n are its coordinates, u is the synthetic aperture and c is the speed of electromagnetic wave, which is the speed of light. The fast time Fourier transform of the signal given in equation (114) can be written as [48]

$$Ss(\omega,u) = P(\omega)\sum_n \sigma_n \exp\left[-j2k_\omega\sqrt{(x_n)^2 + (y_n - u)^2}\right] \tag{115}$$

where $k_\omega = \omega/c$ is the wavenumber. Applying the slow-time Fourier transform relation given by equation (72) to the equation (115) and suppressing amplitude factors one obtains

[48]

$$SS(\omega, k_u) = P(\omega) \sum_n \sigma_n \exp\left(-j\sqrt{4k_\omega^2 - k_u^2}x_n - jk_u y_n\right) \tag{116}$$

Defining two new functions as [48]

$$k_x(\omega, k_u) = \sqrt{4k_\omega^2 - k_u^2} \quad \text{and} \quad k_y(\omega, k_u) = k_u \tag{117}$$

one can rewrite equation (116) as [48]

$$SS(\omega, k_u) = P(\omega) \sum_n \sigma_n \exp\left(-jk_x(\omega, k_u)x_n - jk_y(\omega, k_u)y_n\right) \tag{118}$$

An ideal target function can be defined by [48]

$$ff_o(x, y) = \sum_n \sigma_n \delta(x - x_n, y - y_n) \tag{119}$$

which has the 2D Fourier Transform [48]

$$FF_o(k_x, k_y) = \sum_n \sigma_n \exp(-jk_x x_n - jk_y y_n) \tag{120}$$

Using the equation (120) one can rewrite the equation (118) as [48]

$$SS(\omega, k_u) = P(\omega) FF_o\left[k_x(\omega, k_u), k_y(\omega, k_u)\right] \tag{121}$$

which leads to [48]

$$FF_o\left[k_x(\omega, k_u), k_y(\omega, k_u)\right] = \frac{SS(\omega, k_u)}{P(\omega)} \tag{122}$$

As pointed out in the matched filtering sections of LFM and $t^{0.75}$FM chirp signals, for a bandlimited signal, for the reconstruction it is not possible to use the the equation (122). Therefore the construction via fast time matched filtering is performed so that for the recorded SAR signal $FF(k_x, k_y)$ spectrum becomes [48]

$$FF\left[k_x(\omega, k_u), k_y(\omega, k_u)\right] = P*(\omega) SS(\omega, k_u) = |P(\omega)|^2 \sum_n \sigma_n \exp(-jk_x x_n - jk_y y_n) \tag{123}$$

where $k_u \in [-2k_\omega, 2k_\omega]$ and $\omega \in [\omega_c - \omega_o, \omega_c + \omega_o]$. The sample spacing in the slow time wavenumber domain is given by [48]

$$\Delta_{k_u} = \frac{2\pi}{N_u \Delta_u} \tag{124}$$

where N_u is the number of synthetic aperture samples of the SAR signal given in the equation (115) and Δ_u is the sample spacing in u domain. Since $k_y = k_u$ the mapping into k_y domain is evenly spaced but for k_x we use the relation [48]

$$k_x = \sqrt{4k^2 - k_u^2} \tag{125}$$

Discretizing the equation for k_y we obtain [48]

$${}_{ab}k_y = {}_{a}k_u = a\Delta_{k_u} \tag{126}$$

where $a = 1, 2, ..., N_u$, $b = 1, 2, ..., N_\omega$ and N_ω is the number of samples in the fast time frequency, ω, domain. Discretizing the equation for k_x one obtains [48]

$${}_{ab}k_x = \sqrt{4\ {}_{b}k_\omega^2 - {}_{a}k_u} \tag{127}$$

where

$${}_{b}k_\omega = b\Delta_k = b\frac{\Delta_\omega}{c} \tag{128}$$

are the evenly spaced collocation points in the $k_\omega = \omega/c$ domain and Δ_ω is the sample spacing of the fast time frequency ω. Therefore the sampled fast time frequency collocation points become $\omega_b = c_b k_\omega$. A graphical representation of this interpolation process can be seen in the Figure (57) below

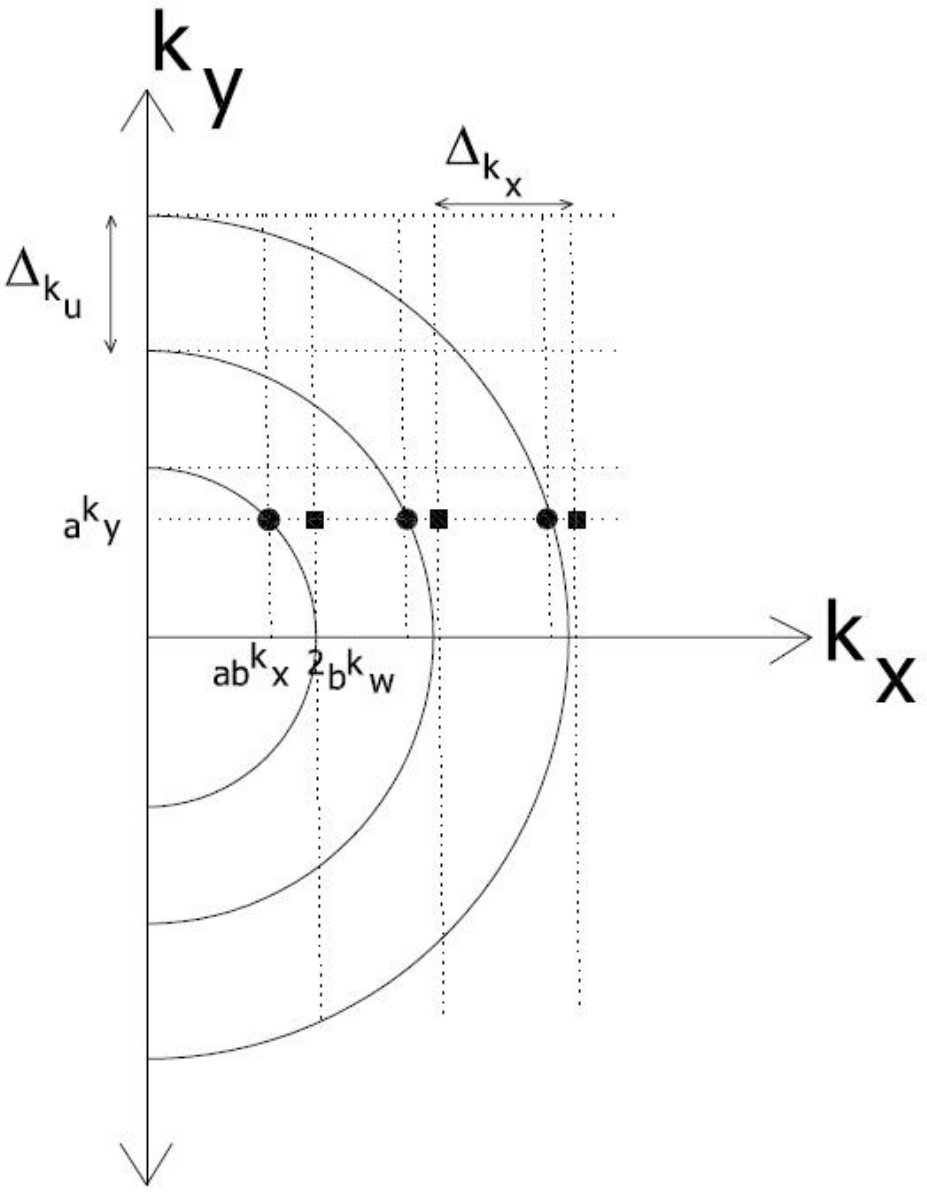

Figure 57: Spatial frequency mapping for discrete wavenumber data.

In the case of long range spotlight or stripmap SAR imaging the slow time wavenumber, k_u, is much smaller than the wavenumber, k_ω, that is, $|k_u| \ll k_\omega$. When the conditions $|k_u| \ll k_\omega$ and $2\omega_o \ll \omega_c$ are satisfied the interpolation problem can be avoided by using the approximation [48]

$$k_x \approx 2k_\omega \tag{129}$$

This approximation in the wavenumber data assignment causes slight degradations in the reconstructed images, but results in severe degradation when used in the phase function given below [48]

$$\exp\left[-jk_x(\omega, k_u)x_n\right] \tag{130}$$

Since in majority of imaging situations the target area is not located at the center of synthetic aperture, that is $Y_c \neq 0$, so that baseband conversion of the target area is necessary. For these squinted SAR systems baseband conversion can be obtained by

$$FF_b(k_x, k_y) = FF(k_x, k_y)\exp\left(jk_xX_c + jk_yY_c\right) \tag{131}$$

where FF_b denotes the baseband spectrum of the target's scattering function. Using the equation (117) in the equation (131) one obtains [48]

$$\begin{aligned} FF_b\left[k_x(\omega, k_u), k_y(\omega, k_u)\right] &= P^*(\omega)SS(\omega, k_u)\exp\left[jk_x(\omega, k_u)X_c + jk_y(\omega, k_u)Y_c\right] \\ &= P^*(\omega)\exp\left(j\sqrt{4k_\omega^2 - k_u^2}X_c + jk_uY_c\right)SS(\omega, k_u) \end{aligned} \tag{132}$$

The squinted mode reconstruction can also be accomplished by 2D matched filtering. Considering the radar signal scattered from a single reflector located at the center of the target area [48]

$$ss_o(t, u) = p\left[t - \frac{2\sqrt{X_c^2 + (Y_c - u)^2}}{c}\right] \tag{133}$$

one can obtain its 2D Fourier Transform as [48]

$$SS_o(\omega, k_u) = P(\omega)\exp\left(-j\sqrt{4k_\omega^2 - k_u^2}X_c - jk_uY_c\right) \tag{134}$$

Therefore the baseband reconstruction can also be achieved by 2D matched filtering as follows [48]

$$FF_b\left[k_x(\omega, k_u), k_y(\omega, k_u)\right] = SS(\omega, k_u)SS_o^*(\omega, k_u) \tag{135}$$

In the case $Y_c = 0$, SAR mode is known to be broadside mode. The whole analysis given for squinted mode can be followe for broadside mode as well, with $Y_c = 0$. In the Figure (58) one can see the Stolt format processing algorithm steps given above in a flowchart format.

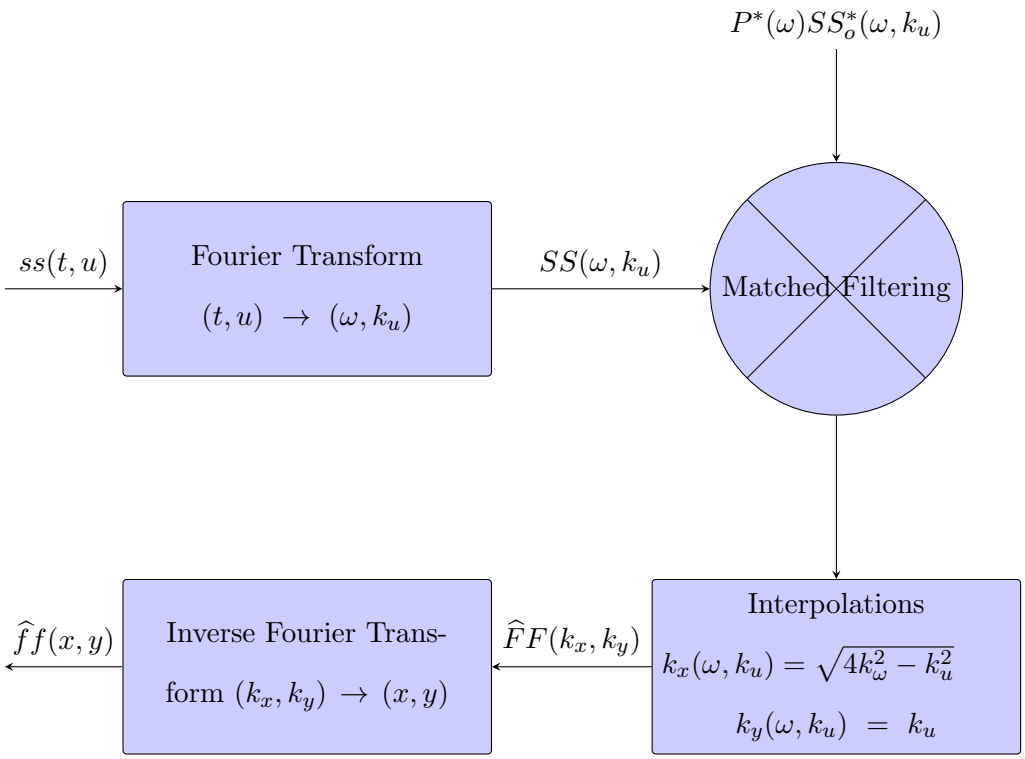

Figure 58: Stolt format processing algorithm flowchart.

From this point forward FF instead of FF_b, the baseband Fourier Transform of the target's scattering function, is used. Using evenly spaced data, $k_x = b\Delta_{k_x}$, one can perform the interpolation as follows [48]

$$FF(k_x,\ {}_{ab}k_y) = \sum_b F(b\Delta_{k_x},\ {}_{ab}k_y) z(k_x - b\Delta_{k_x}) \tag{136}$$

where

$$z(k_x) = \text{sinc}\left(\frac{k_x}{\Delta_{k_x}}\right) \tag{137}$$

is the sinc interpolating function. To achieve computational efficiency one can use a windowing function so that [48]

$$FF(k_x,\ {}_{ab}k_y) = \sum_{|k_x - b\Delta_{k_x}| \leq N_s \Delta_{k_x}} F(b\Delta_{k_x},\ {}_{ab}k_y) z_v(k_x - b\Delta_{k_x}) \tag{138}$$

where

$$z_v(k_x) = \begin{cases} z(k_x)v(k_x) & \text{for } |k_x| \leq N_s\Delta_{k_x} \\ 0 & \text{otherwise} \end{cases} \tag{139}$$

is the windowing function. The signal $v(k_x)$ can be any window. Selecting the Hamming window as given below [48]

$$v(k_x) = \begin{cases} 0.54 + 0.46\cos(\frac{\pi k_x}{N_s \Delta_{k_x}}) & \text{for } |k_x| \leq N_s \Delta_{k_x} \\ 0 & \text{otherwise} \end{cases} \tag{140}$$

In Figure (59) the Hamming window for $N_s = 128$ is presented.

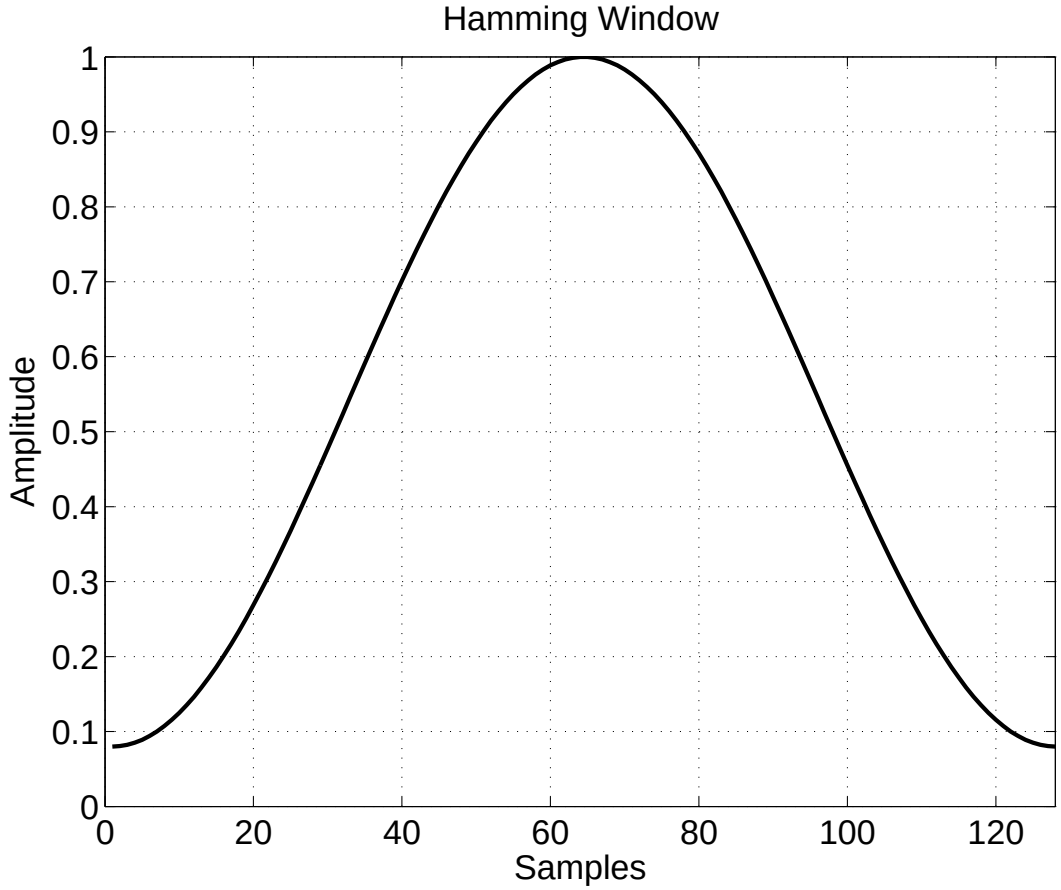

Figure 59: Hamming window.

In the simulations which are presented in the subsections 4.3.1 and 4.3.2 interpolation from evenly spaced data is used. The process of interpolation from unevenly spaced data can be seen in [48].

4.3.1 Stolt Format Processing using LFM Signals

In this section 9 examples of spotlight imaging, using Stolt format processing with LFM chirp signals, is presented. Therefore for the $p(t)$ in the equation (114) the expression given in the equation (2) and its corresponding matched filter is used.

The first example is for a single scatterer located at $x = 0\text{m}, y = 0\text{m}$ with the parameters $X_c = 1500\text{m}, Y_c = 0\text{m}, X_o = 100\text{m}, L = 150\text{m}$. This is the same scene illustrated in example 1 of the section 4.2.1. In the Figure (60) the wavenumber coverage for Stolt format processing is presented.

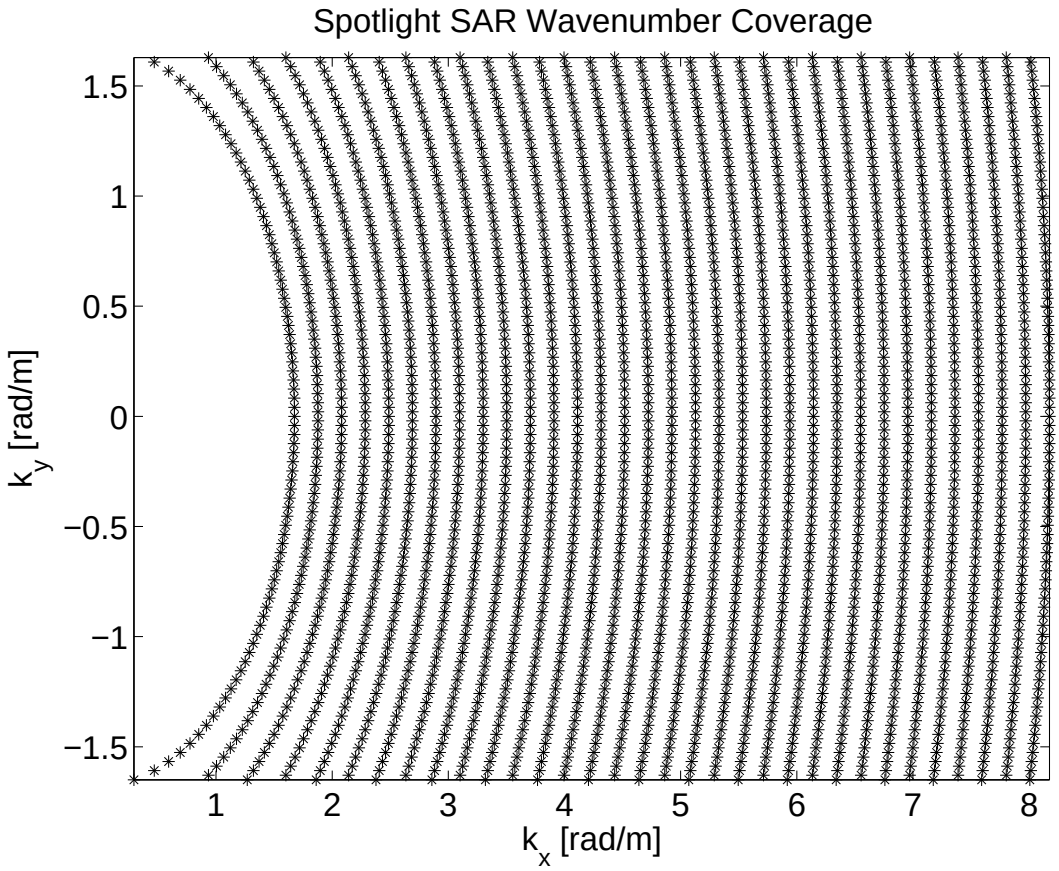

Figure 60: Spotlight SAR wavenumber coverage of a single scatterer at $x = 0\text{m}, y = 0\text{m}$-broadside mode.

Applying the matched filtering operation along t and u axes to the recorded SAR signal in the wavenumber domain one obtains the dechirped spectrum given in the Figure (61).

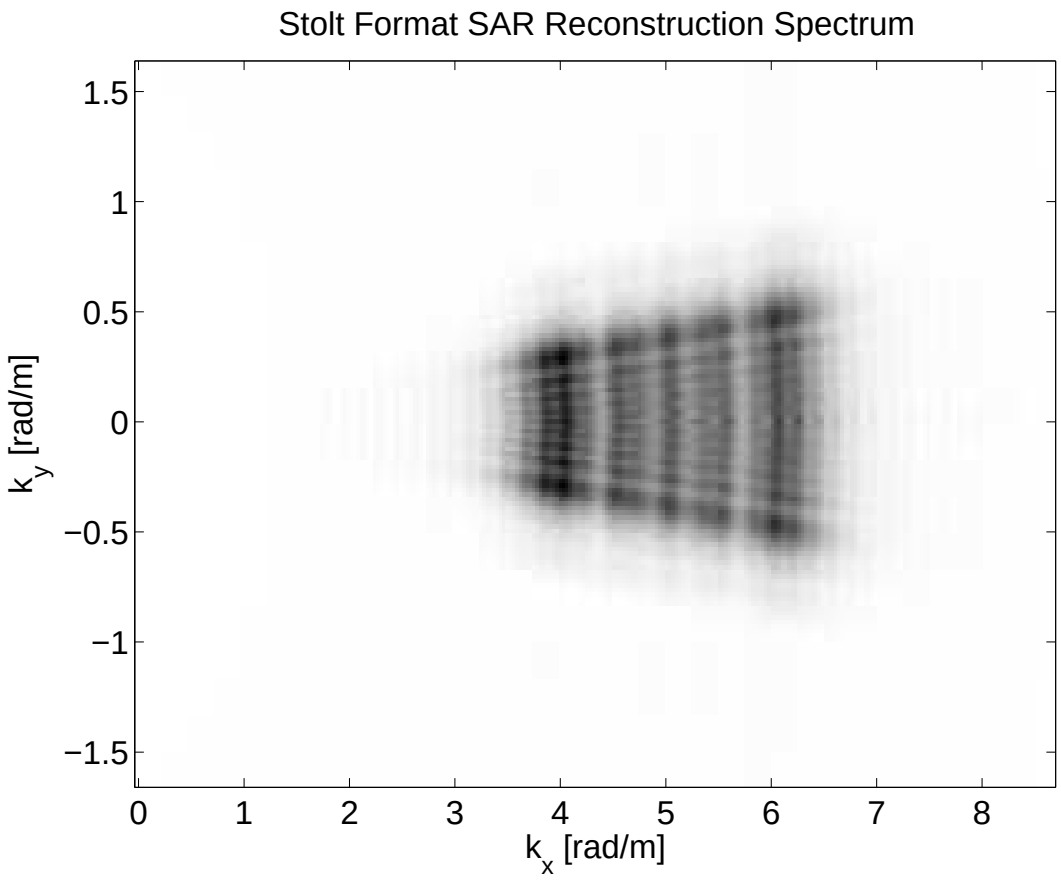

Figure 61: Stolt format SAR reconstruction spectrum of a single scatterer at $x = 0\text{m}, y = 0\text{m}$-broadside mode.

After 2D inverse Fourier transforming one obtains the scene scattering function given in the Figure (62).

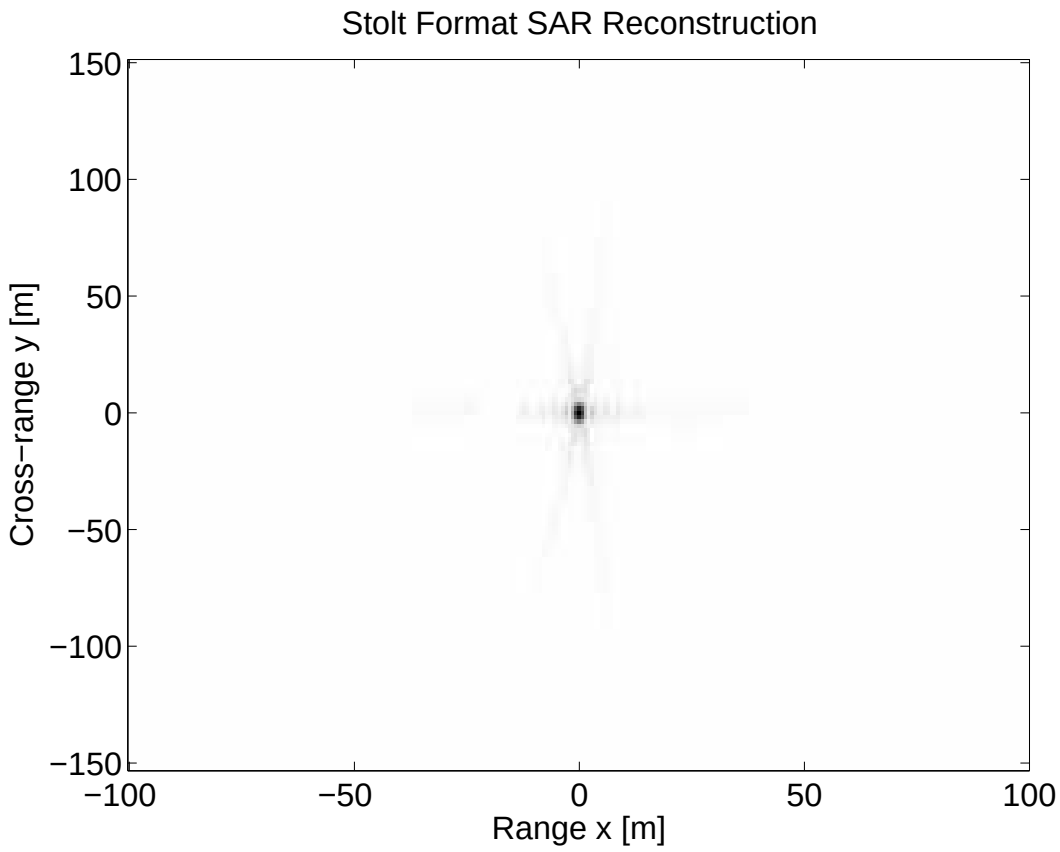

Figure 62: Stolt format SAR reconstruction of a single scatterer at $x = 0\text{m}, y = 0\text{m}$-broadside mode.

The second example is for a single scatterer located at $x = 0\text{m}, y = 0\text{m}$ with the parameters $X_c = 1500\text{m}, Y_c = 500\text{m}, X_o = 100\text{m}, L = 150\text{m}$. This is the same scene illustrated in example 2 of the section 4.2.1. In the Figure (63) the wavenumber coverage for Stolt format processing is presented.

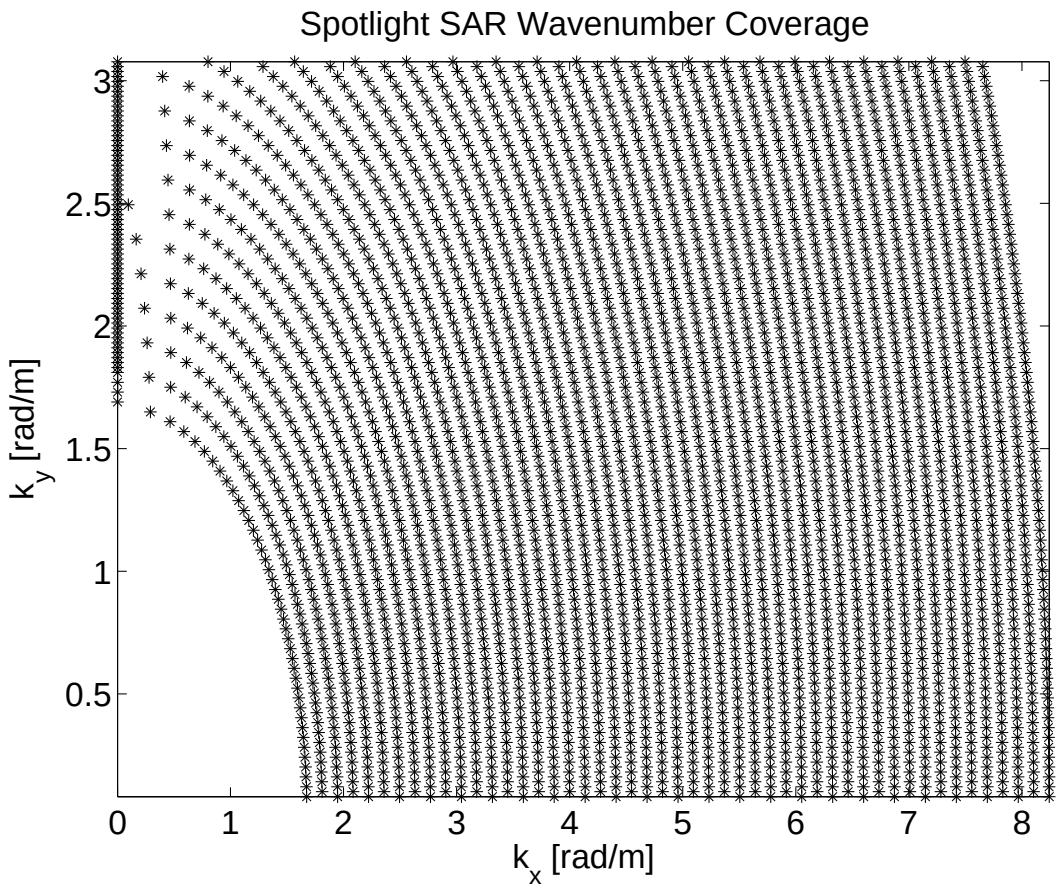

Figure 63: Spotlight SAR wavenumber coverage of a single scatterer at $x = 0\text{m}, y = 0\text{m}$-squinted mode.

Applying the matched filtering operation along t and u axes to the recorded SAR signal in the wavenumber domain one obtains the dechirped spectrum given in the Figure (64).

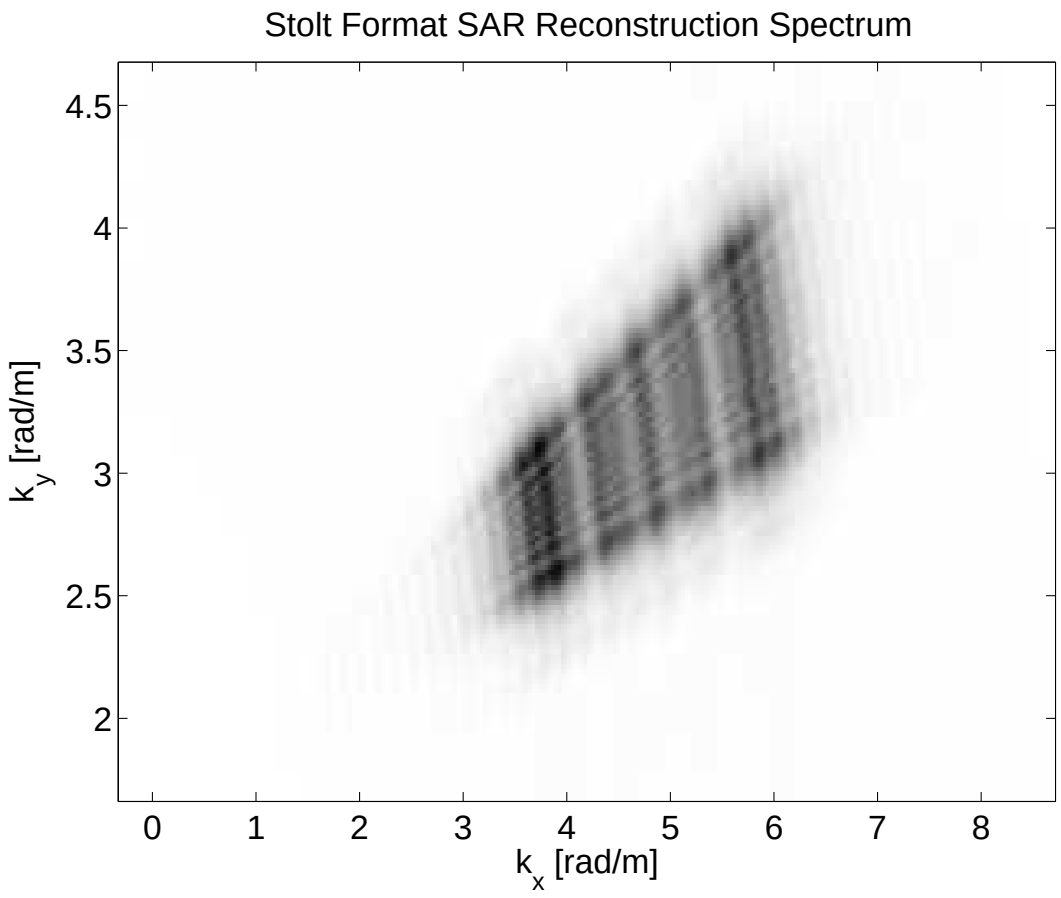

Figure 64: Stolt format SAR reconstruction spectrum of a single scatterer at $x = 0\text{m}, y = 0\text{m}$-squinted mode.

After 2D inverse Fourier transforming one obtains the scene scattering function given in the Figure (65).

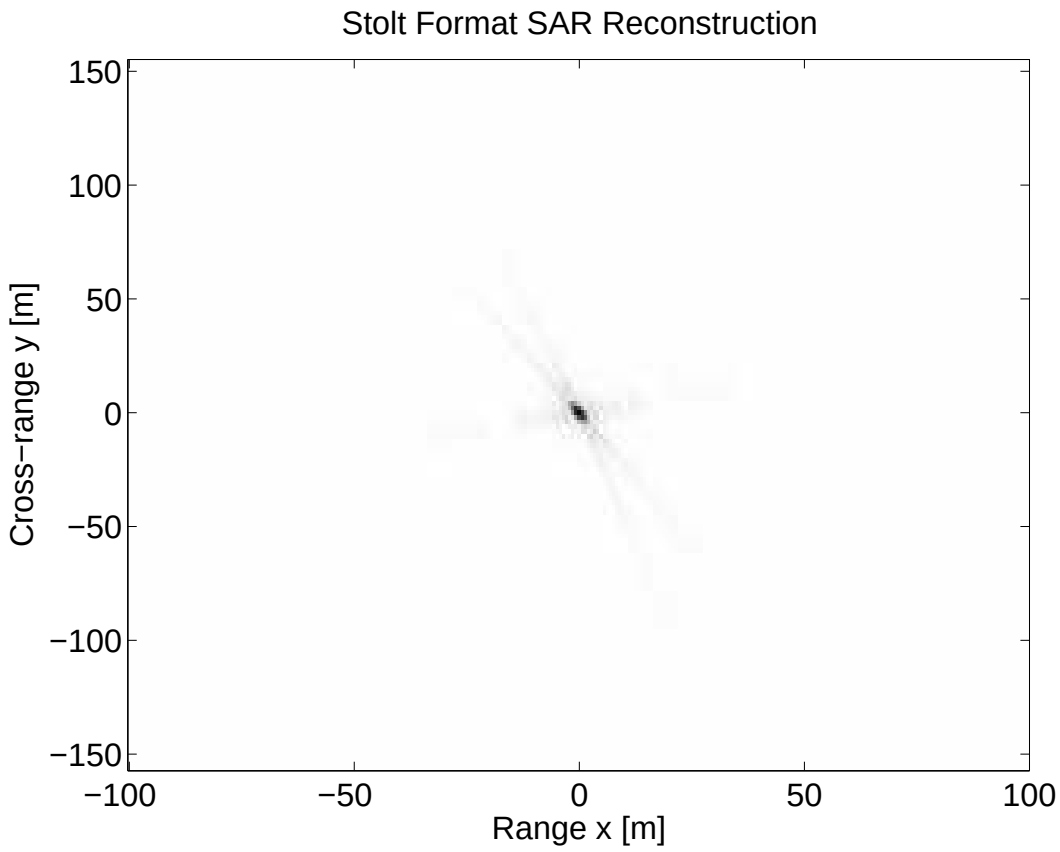

Figure 65: Stolt format SAR reconstruction of a single scatterer at $x = 0\text{m}, y = 0\text{m}$-squinted mode.

The third example is for a single scatterer located at $x = 20\text{m}, y = 20\text{m}$ with the parameters $X_c = 1500\text{m}, Y_c = 0\text{m}, X_o = 100\text{m}, L = 150\text{m}$. This is the same scene illustrated in example 3 of the section 4.2.1. In the Figure (66) the wavenumber coverage for Stolt format processing is presented.

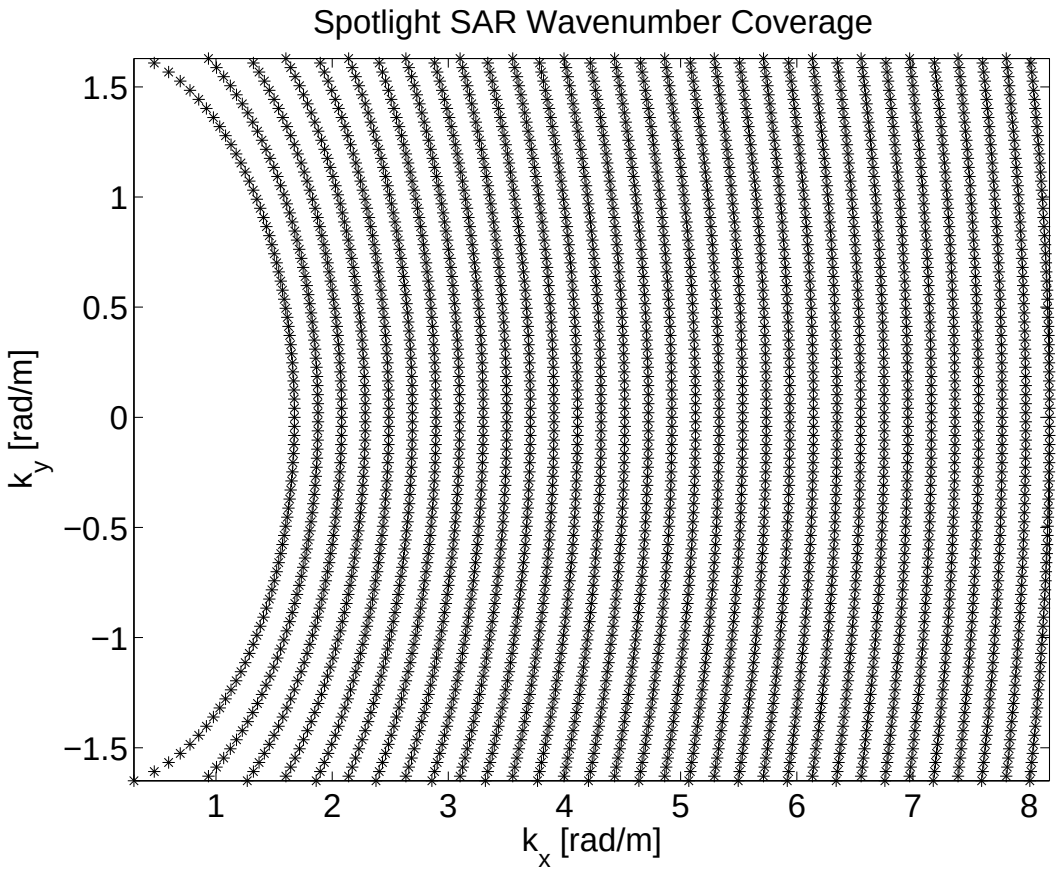

Figure 66: Spotlight SAR wavenumber coverage of a single scatterer at $x = 20\text{m}, y = 20\text{m}$-broadside mode.

Applying the matched filtering operation along t and u axes to the recorded SAR signal in the wavenumber domain one obtains the dechirped spectrum given in the Figure (67).

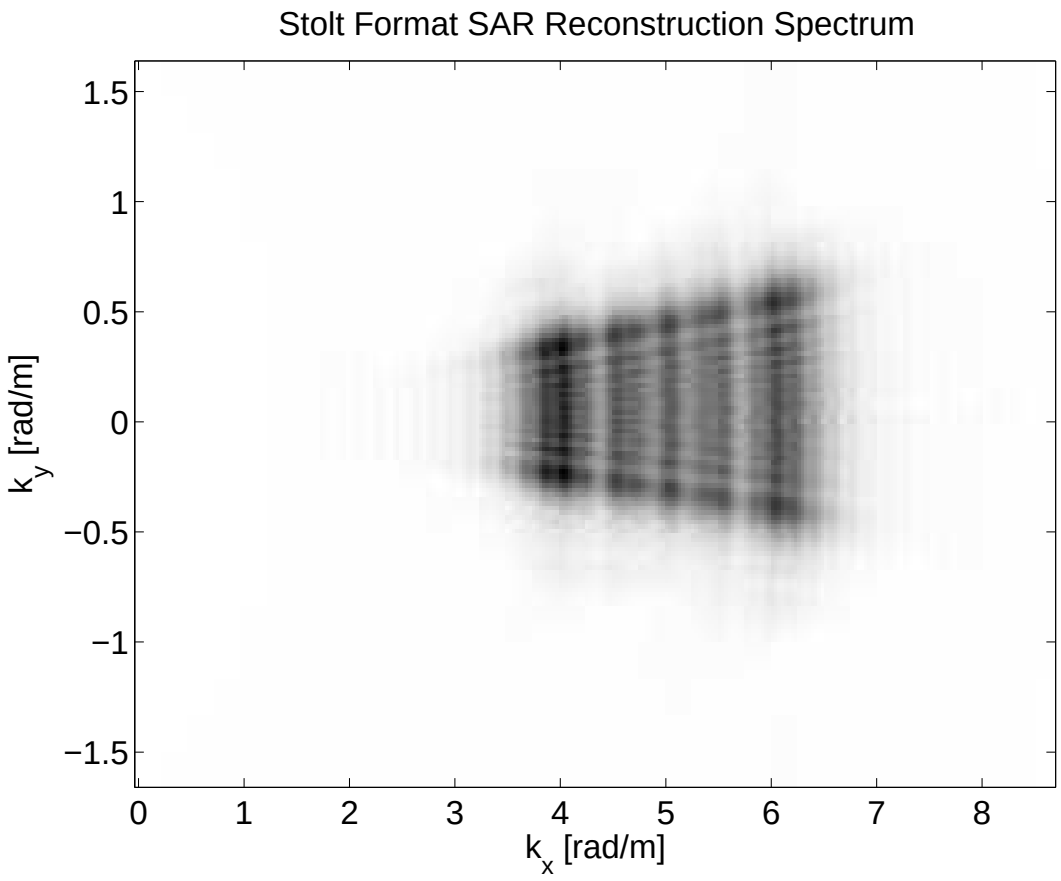

Figure 67: Stolt format SAR reconstruction spectrum of a single scatterer at $x = 20\text{m}, y =$ 20m-broadside mode.

After 2D inverse Fourier transforming one obtain the scene scattering function given in the Figure (68).

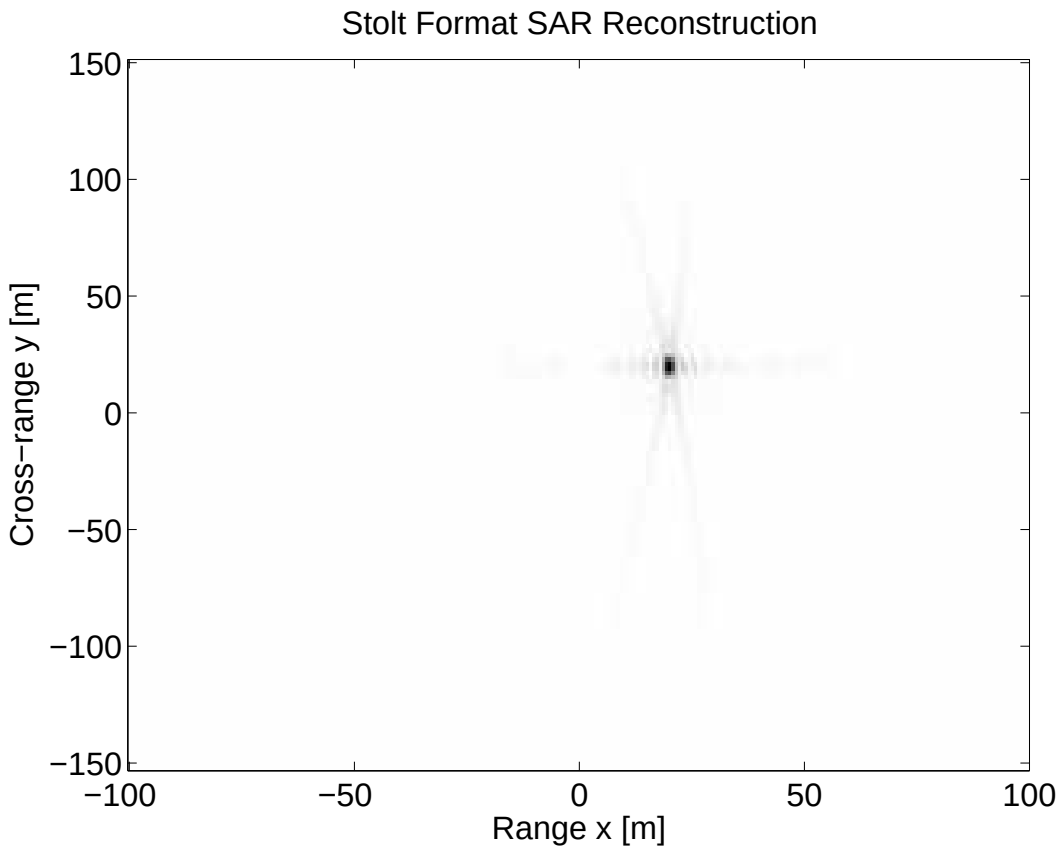

Figure 68: Stolt format SAR reconstruction of a single scatterer at $x = 20\text{m}, y = 20\text{m}$-broadside mode.

The fourth example is for a single scatterer located at $x = 20\text{m}, y = 20\text{m}$ with the parameters $X_c = 1500\text{m}, Y_c = 500\text{m}, X_o = 100\text{m}, L = 150\text{m}$. This is the same scene illustrated in example 4 of the section 4.2.1. In the Figure (69) the wavenumber coverage for Stolt format processing is presented.

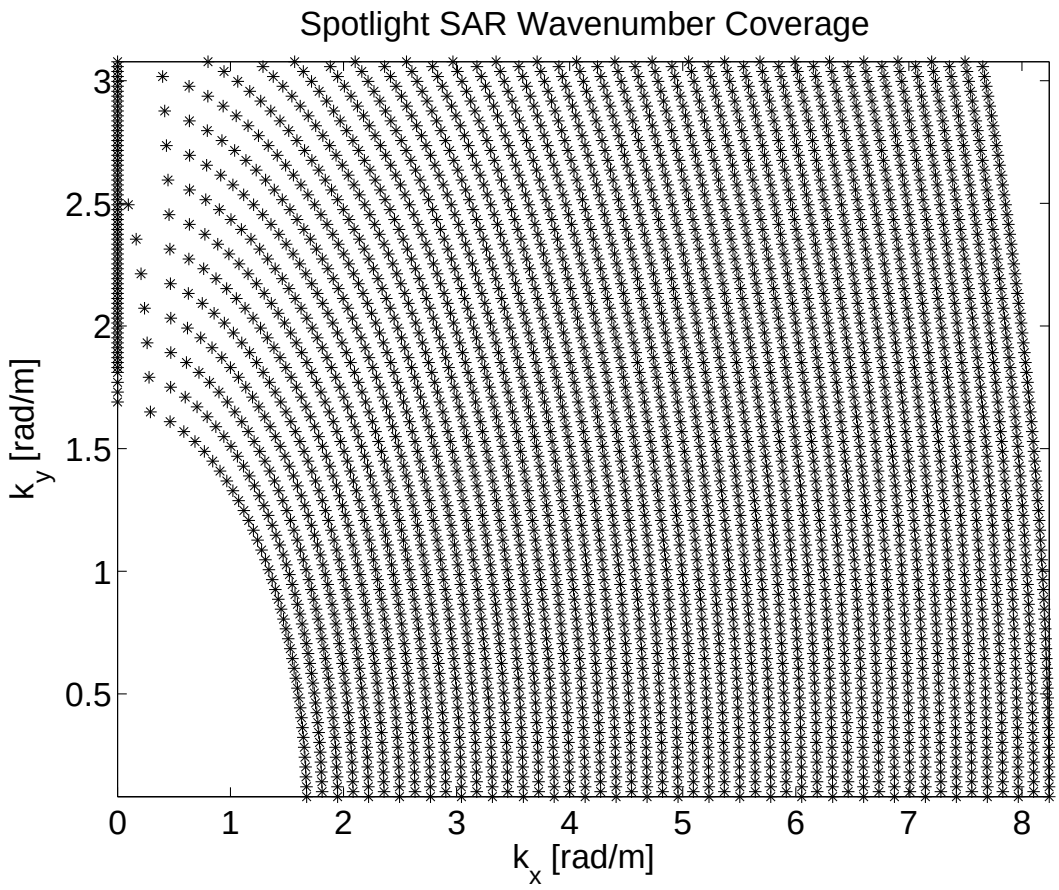

Figure 69: Spotlight SAR wavenumber coverage of a single scatterer at $x = 20\text{m}, y = 20\text{m}$-squinted mode.

Applying the matched filtering operation along t and u axes to the recorded SAR signal in the wavenumber domain one obtains the dechirped spectrum given in the Figure (70).

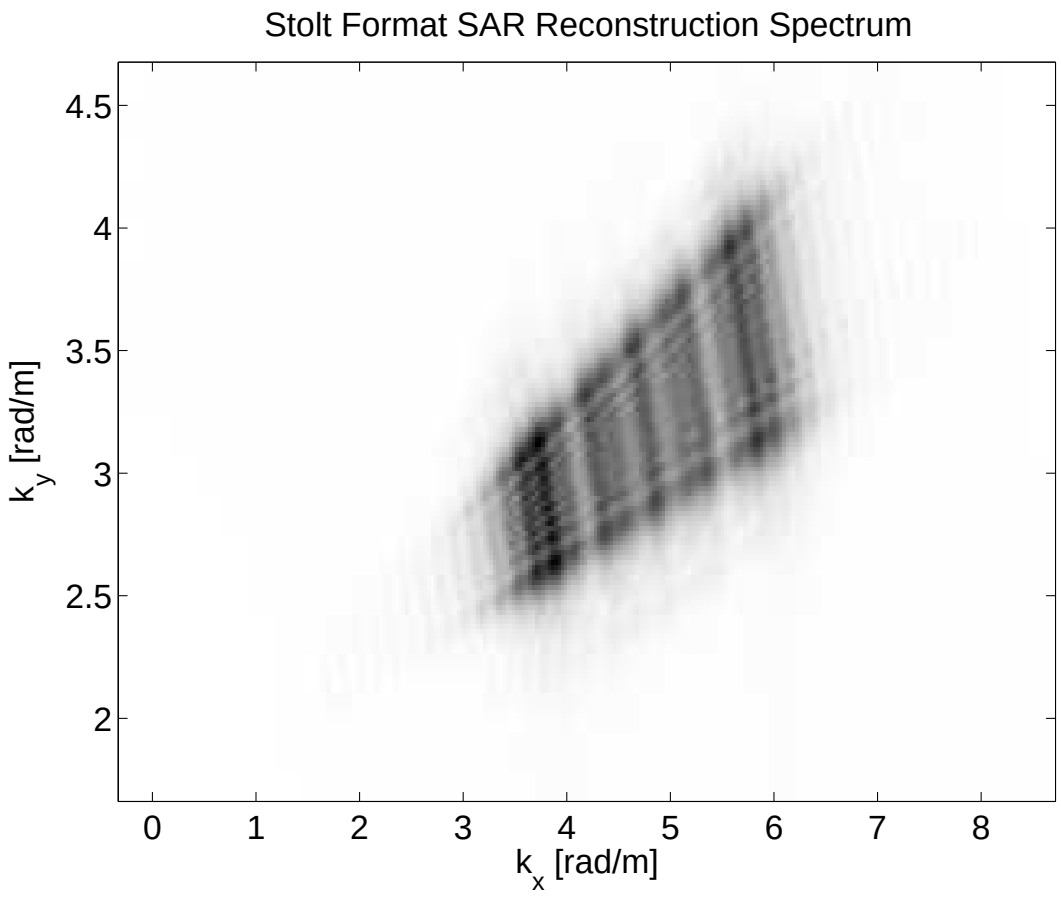

Figure 70: Stolt format SAR reconstruction spectrum of a single scatterer at $x = 20\text{m}, y = 20\text{m}$-squinted mode.

After 2D inverse Fourier transforming one obtains the scene scattering function given in the Figure (71).

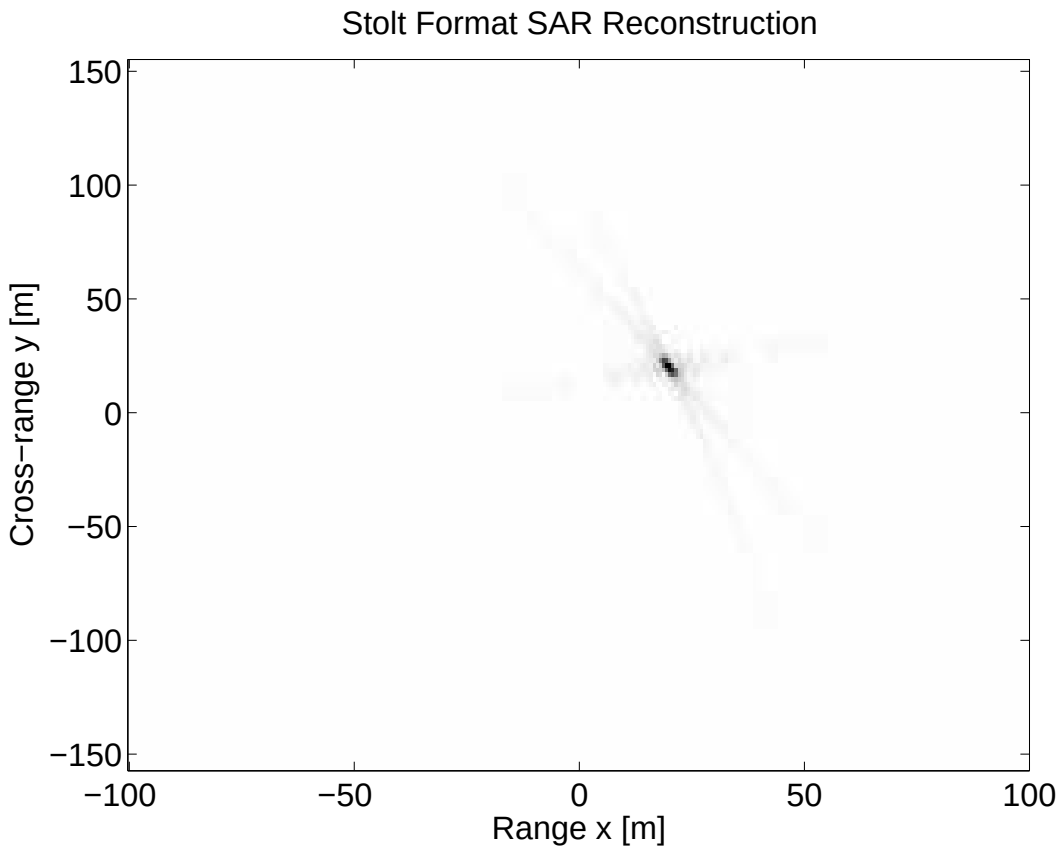

Figure 71: Stolt format SAR reconstruction of a single scatterer at $x = 20\text{m}, y = 20\text{m}$-squinted mode.

The fifth example is for 5 scatterers located at $x_1 = 0\text{m}, y_1 = 0\text{m}$, $x_2 = 70\text{m}, y_2 = -60\text{m}$, $x_3 = -70\text{m}, y_3 = 60\text{m}$, $x_4 = -60\text{m}, y_4 = 75\text{m}$, $x_5 = 60\text{m}, y_5 = -75\text{m}$ with the parameters $X_c = 1500\text{m}, Y_c = 0\text{m}, X_o = 100\text{m}, L = 100\text{m}$. This is the same scene illustrated in example 5 of the section 4.2.1. In the Figure (72) the wavenumber coverage for Stolt format processing is presented.

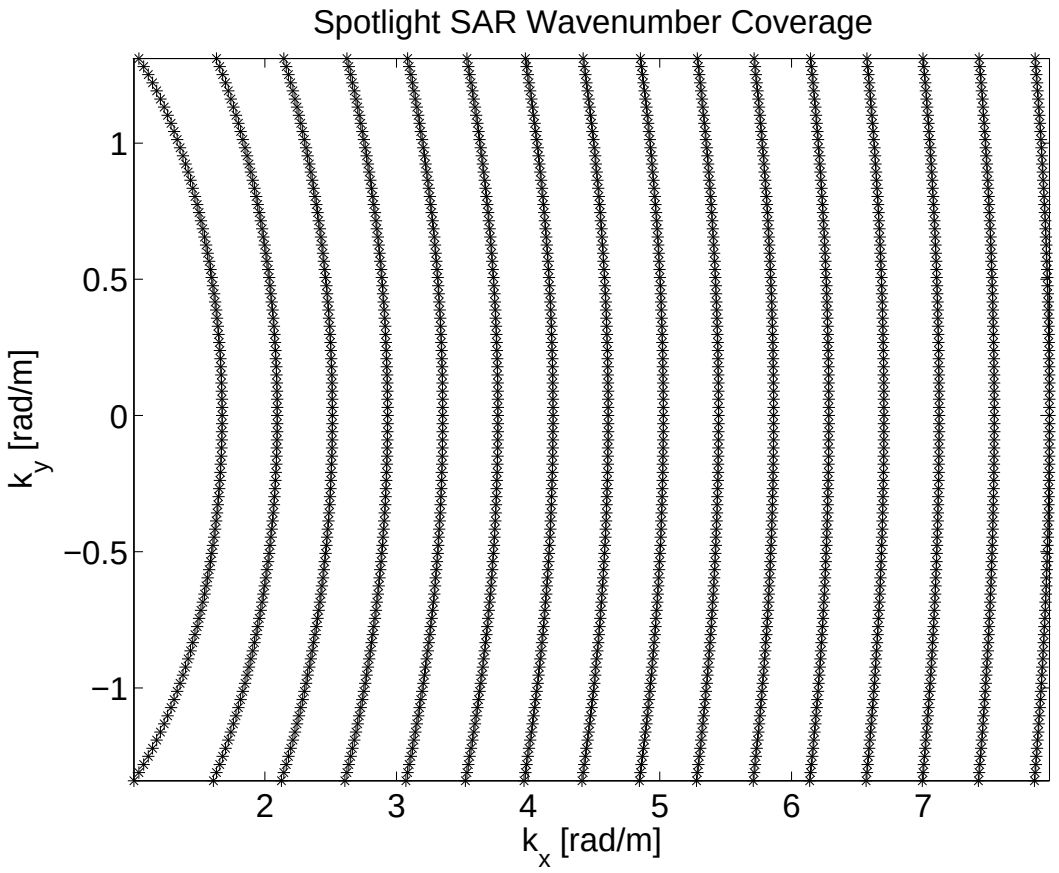

Figure 72: Spotlight SAR wavenumber coverage of 5 scatterers-broadside mode.

Applying the matched filtering operation along t and u axes to the recorded SAR signal in the wavenumber domain one obtains the dechirped spectrum given in the Figure (73).

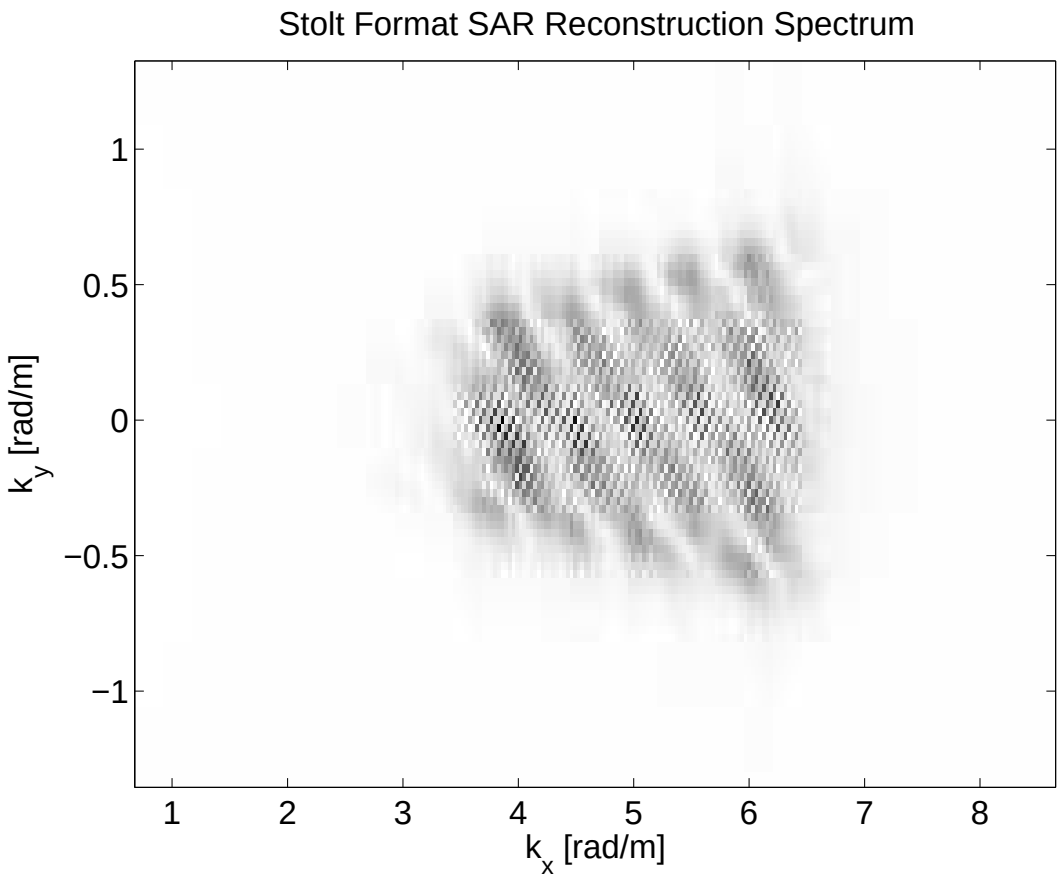

Figure 73: Stolt format SAR reconstruction spectrum of 5 scatterers-broadside mode.

After 2D inverse Fourier transforming one obtains the scene scattering function given in the Figure (74).

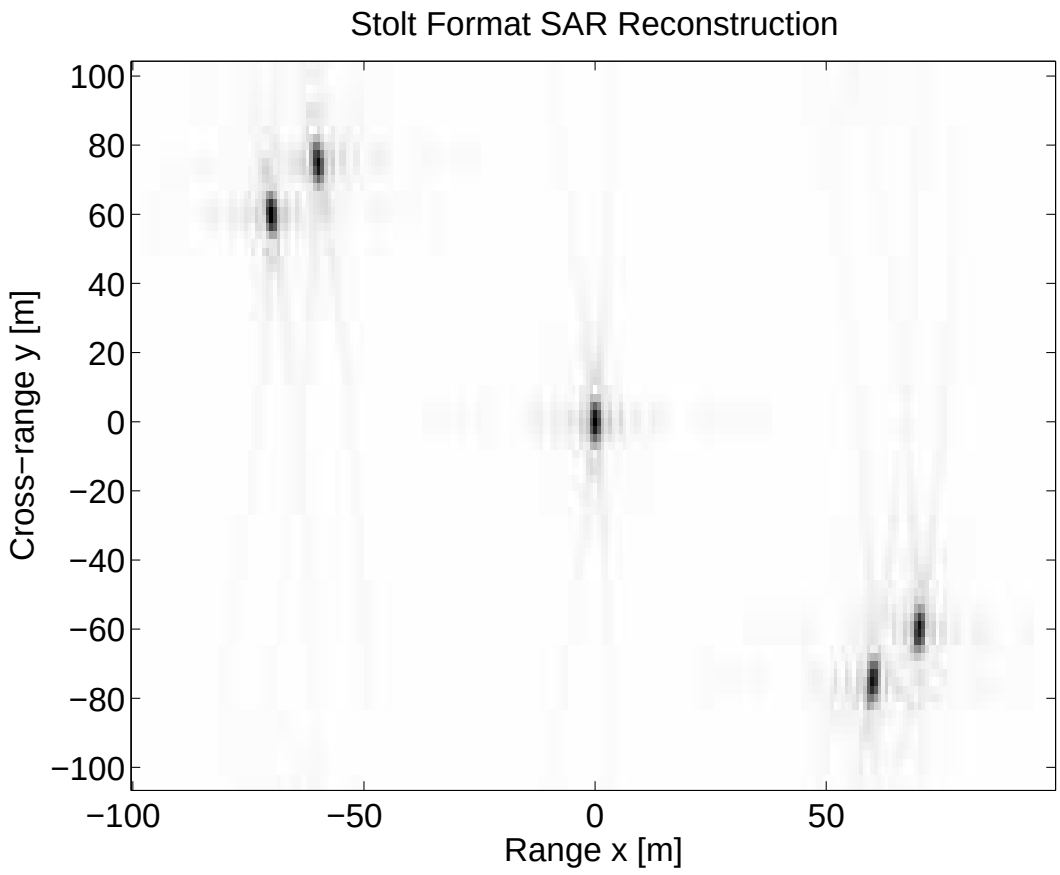

Figure 74: Stolt format SAR reconstruction of 5 scatterers-broadside mode.

The sixth example is for 5 scatterers located at $x_1 = 0\text{m}, y_1 = 0\text{m}$, $x_2 = 70\text{m}, y_2 = -60\text{m}$, $x_3 = -70\text{m}, y_3 = 60\text{m}$, $x_4 = -60\text{m}, y_4 = 75\text{m}$, $x_5 = 60\text{m}, y_5 = -75\text{m}$ with the parameters $X_c = 1500\text{m}, Y_c = 500\text{m}, X_o = 100\text{m}, L = 100\text{m}$. This is the same scene illustrated in example 6 of section 4.2.1 section. In the Figure (75) the wavenumber coverage for Stolt format processing is presented.

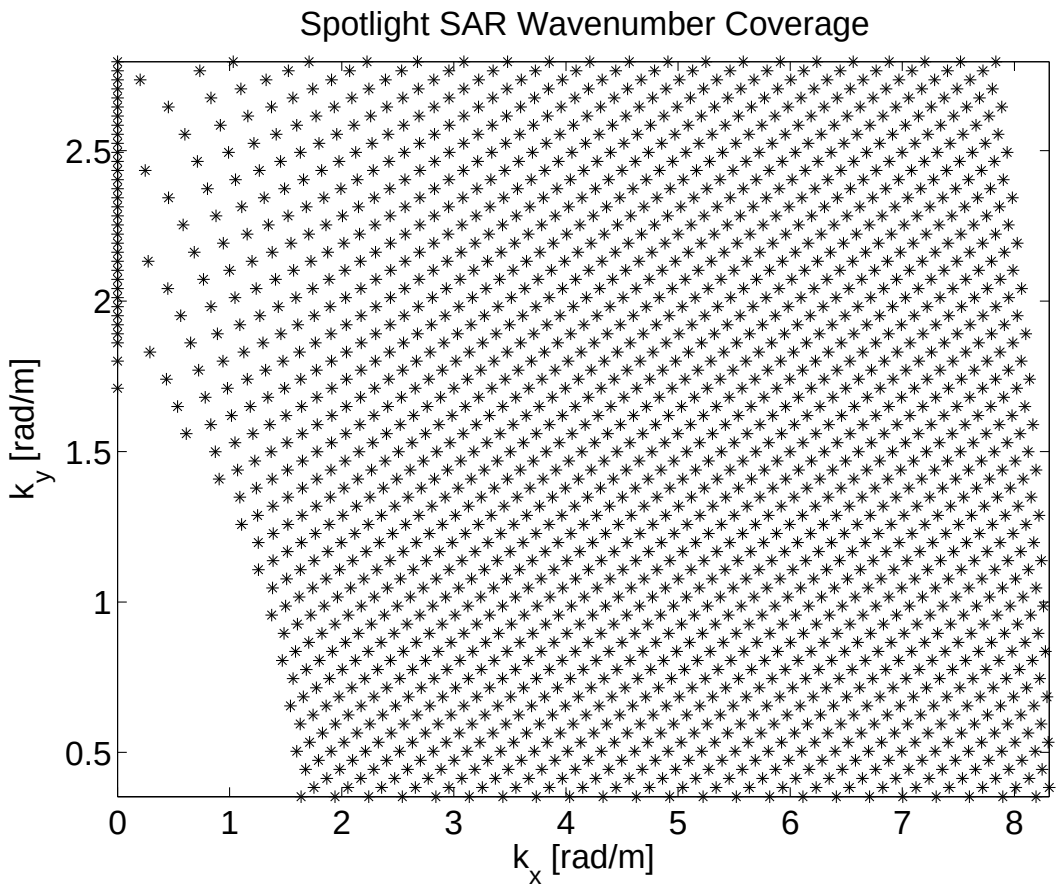

Figure 75: Spotlight SAR wavenumber coverage of 5 scatterers-squinted mode.

Applying the matched filtering operation along t and u axes to the recorded SAR signal in the wavenumber domain one obtains the dechirped spectrum given in the Figure (76).

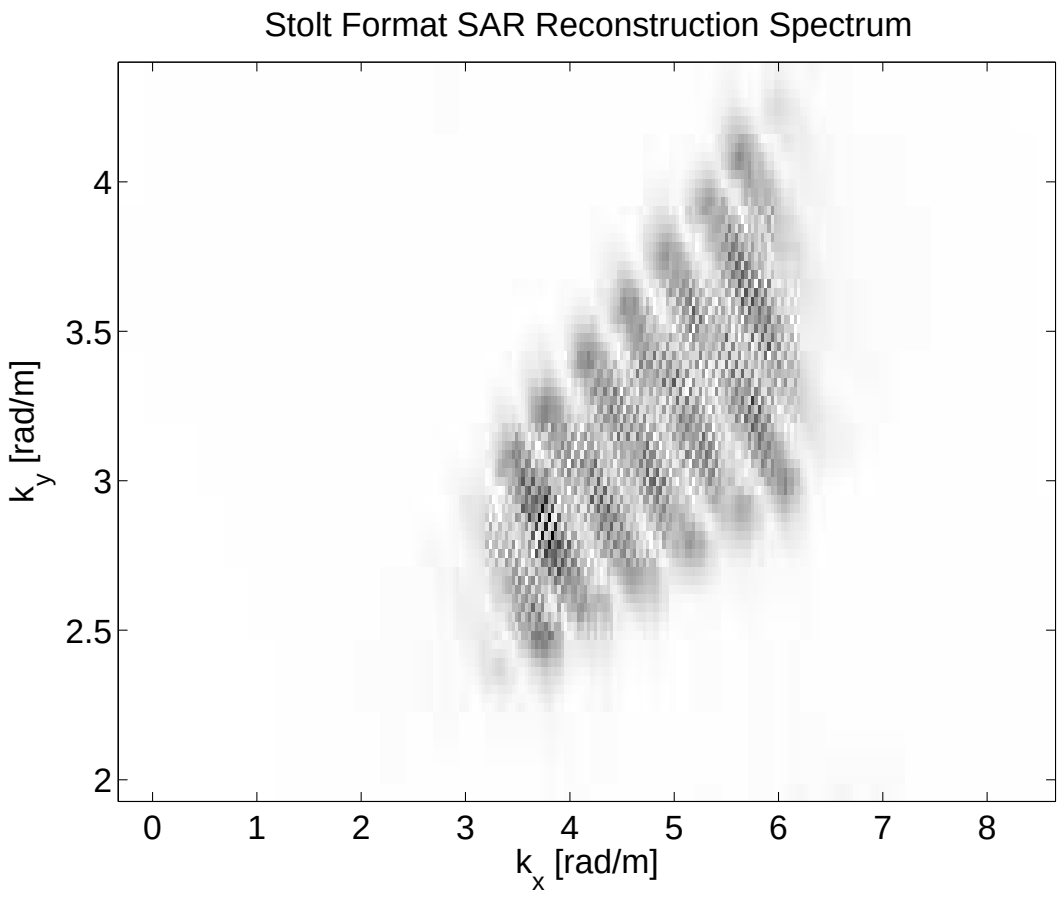

Figure 76: Stolt format SAR reconstruction spectrum of 5 scatterers-squinted mode.

After 2D inverse Fourier transforming one obtains the scene scattering function given in the Figure (77).

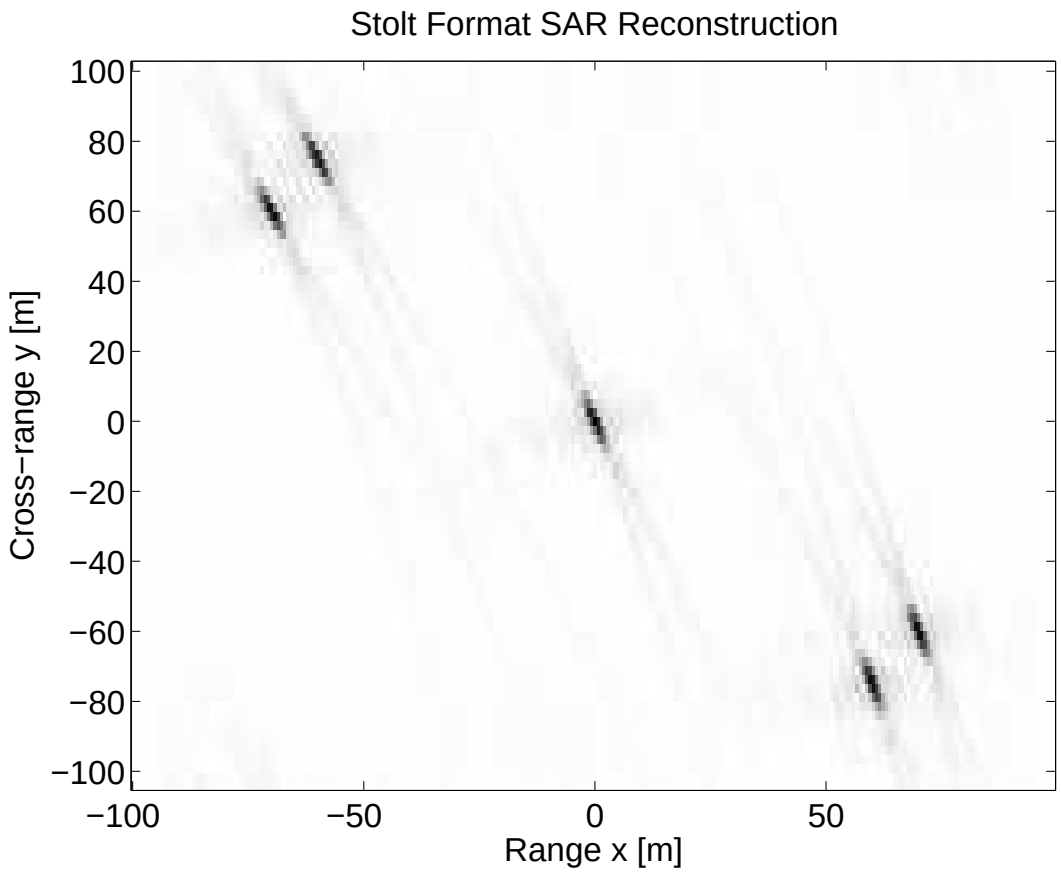

Figure 77: Stolt format SAR reconstruction of 5 scatterers-squinted mode.

The seventh example is for 25 scatterers uniformly distributed inside a square with coordinates $(-50\text{m}, -50\text{m})$, $(-50\text{m}, 50\text{m})$, $(50\text{m}, 50\text{m})$, $(50\text{m}, -50\text{m})$ with the parameters $X_c = 1500\text{m}, Y_c = 0\text{m}, X_o = 100\text{m}, L = 100\text{m}$. This is the same scene illustrated in example 7 of the section 4.2.1. In the Figure (78) the wavenumber coverage for Stolt format processing is presented.

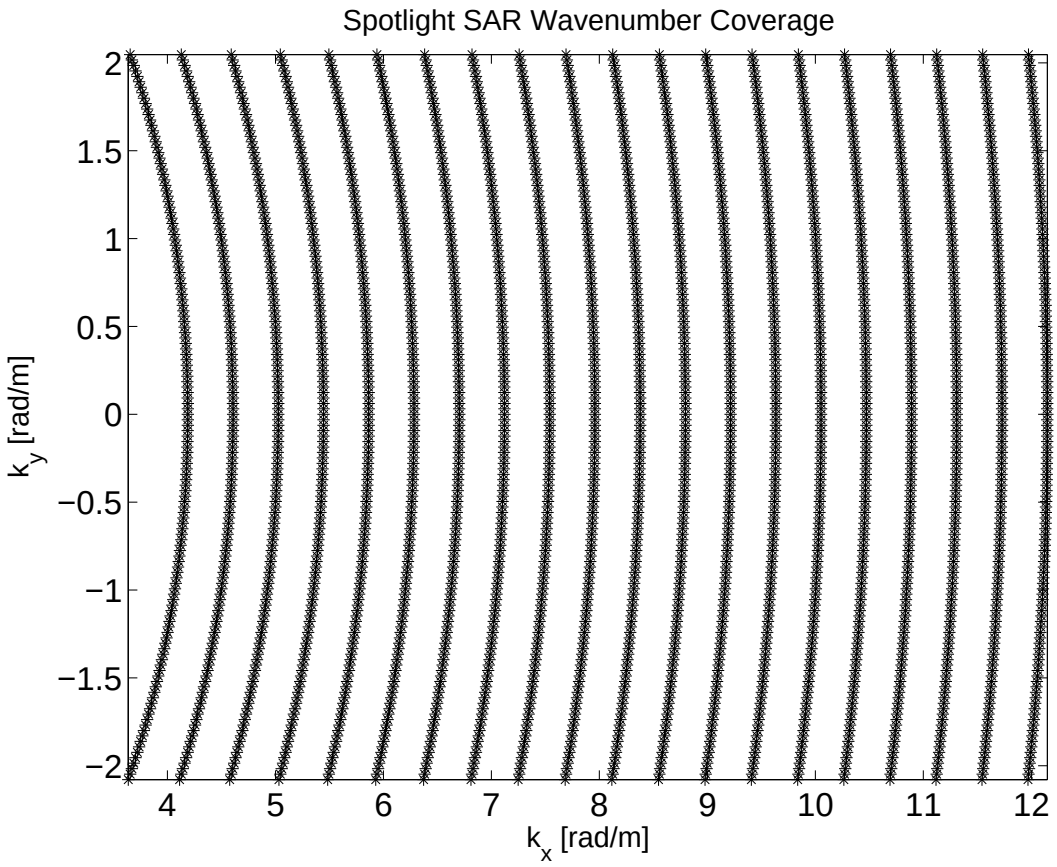

Figure 78: Spotlight SAR wavenumber coverage of 25 scatterers-broadside mode.

Applying the matched filtering operation along t and u axes to the recorded SAR signal in the wavenumber domain one obtains the dechirped spectrum given in the Figure (79).

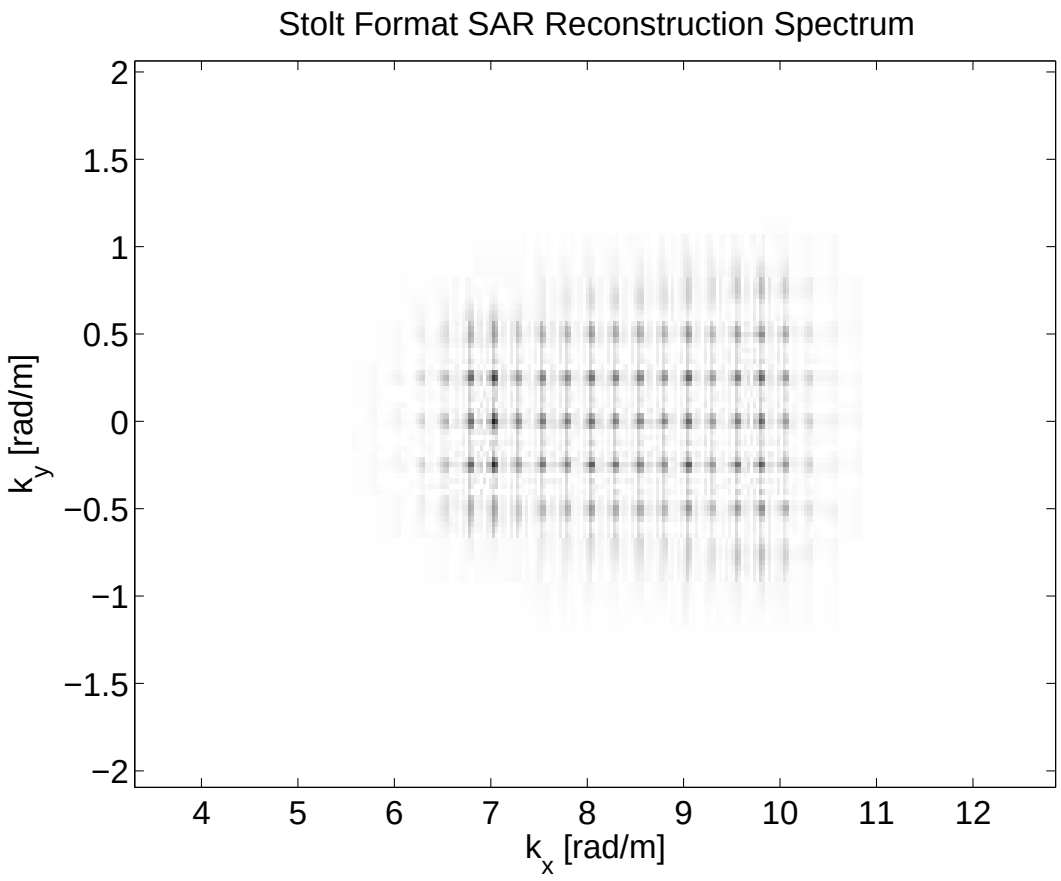

Figure 79: Stolt format SAR reconstruction spectrum of 25 scatterers-broadside mode.

After 2D inverse Fourier transforming one obtains the scene scattering function given in the Figure (80).

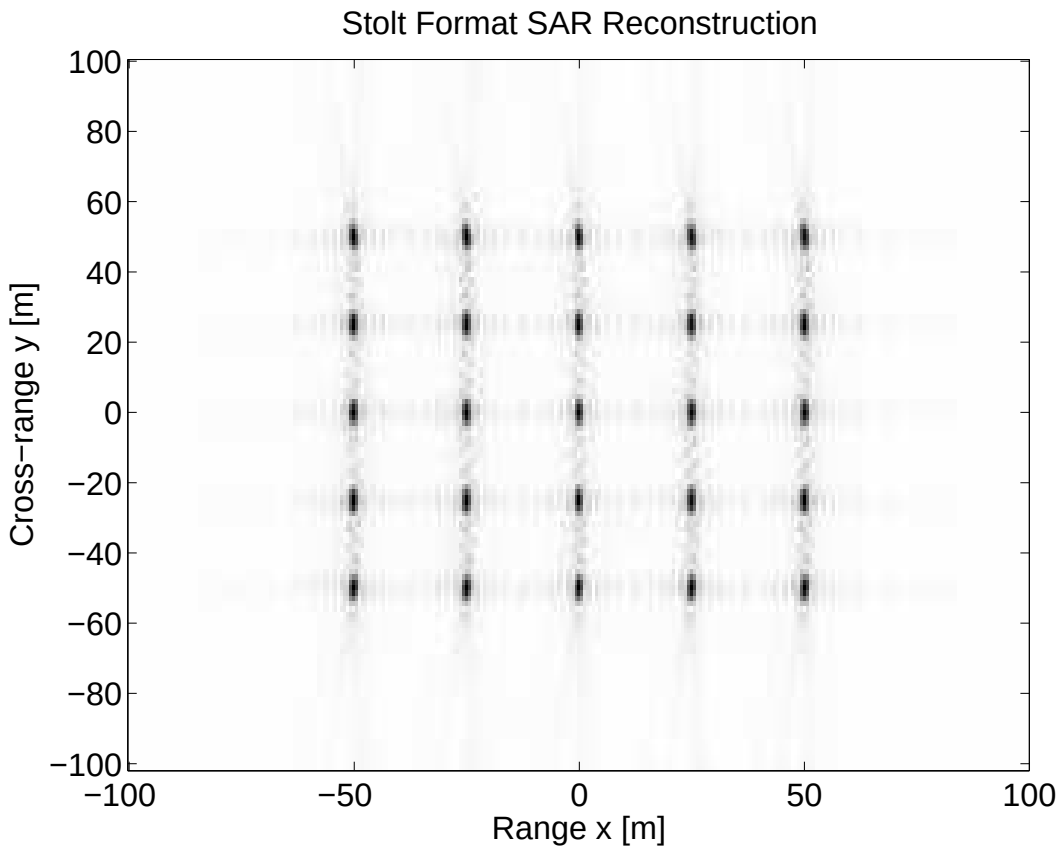

Figure 80: Stolt format SAR reconstruction of 25 scatterers-broadside mode.

The eighth example is for 25 scatterers uniformly distributed inside a square with coordinates $(-50\text{m}, -50\text{m})$, $(-50\text{m}, 50\text{m})$, $(50\text{m}, 50\text{m})$, $(50\text{m}, -50\text{m})$ with the parameters $X_c = 1500\text{m}, Y_c = 500\text{m}, X_o = 100\text{m}, L = 100\text{m}$. This is the same scene illustrated in example 8 of the section 4.2.1. In the Figure (81) the wavenumber coverage for Stolt format processing is presented.

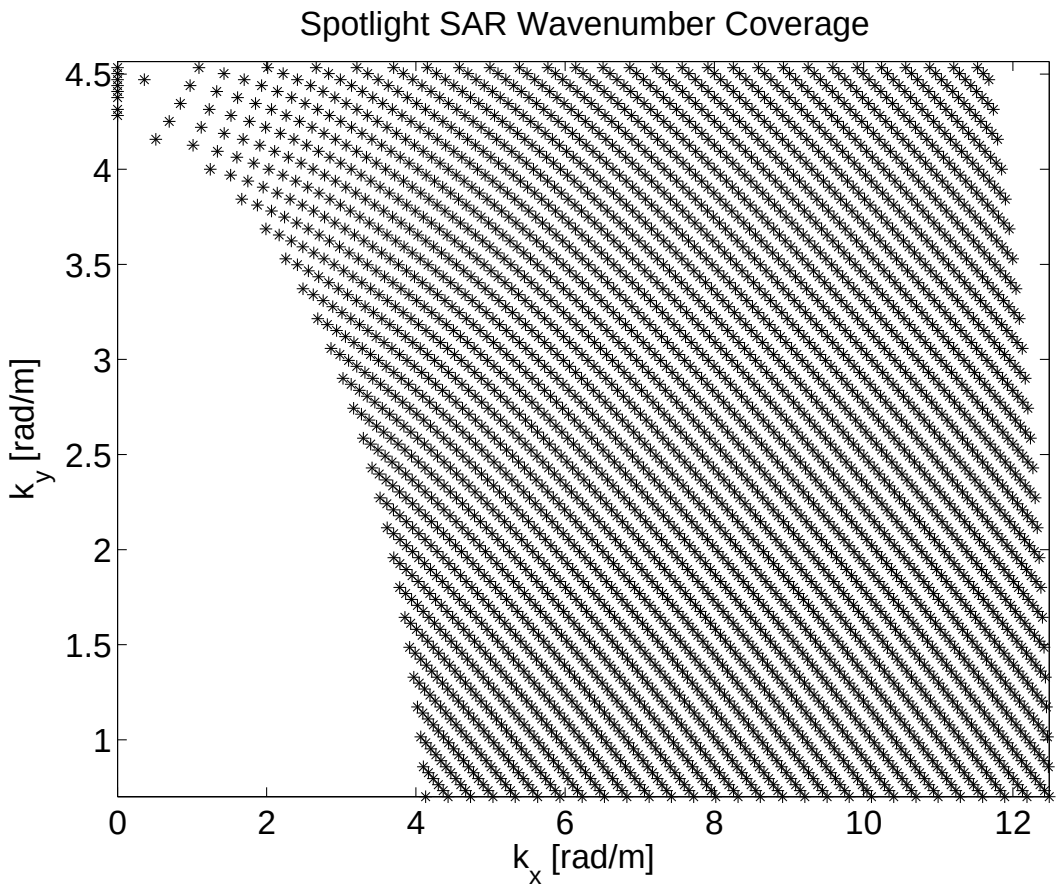

Figure 81: Spotlight SAR wavenumber coverage of 25 scatterers-squinted mode.

Applying the matched filtering operation along t and u axes to the recorded SAR signal in the wavenumber domain one obtains the dechirped spectrum given in the Figure (82).

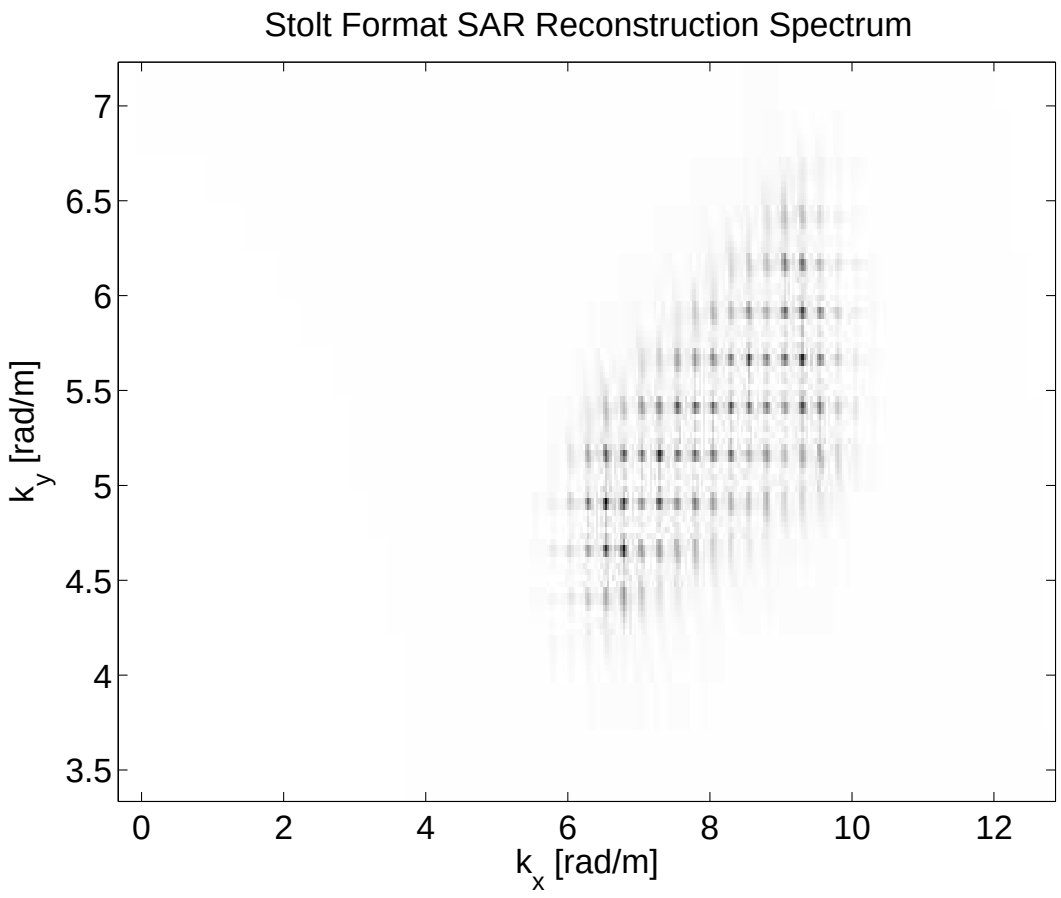

Figure 82: Stolt format SAR reconstruction spectrum of 25 scatterers-squinted mode.

After 2D inverse Fourier transforming one obtains the scene scattering function given in the Figure (83).

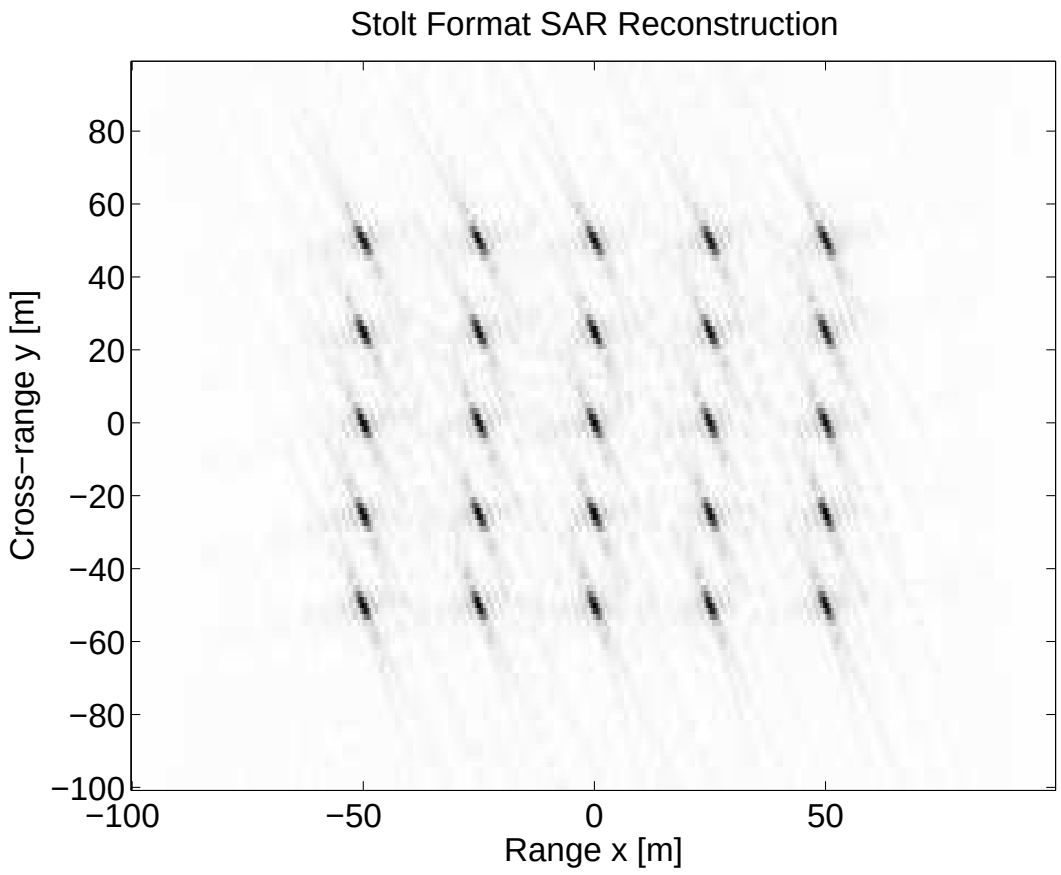

Figure 83: Stolt format SAR reconstruction of 25 scatterers-squinted mode.

The ninth example is for 25 scatterers uniformly distributed inside a square with coordinates $(-50\text{m}, -50\text{m})$, $(-50\text{m}, 50\text{m})$, $(50\text{m}, 50\text{m})$, $(50\text{m}, -50\text{m})$ with the parameters $X_c = 10000\text{m}, Y_c = 0\text{m}, X_o = 100\text{m}, L = 300\text{m}$. This is the same scene illustrated in example 9 of the section 4.2.1. In the Figure (84) the wavenumber coverage for Stolt format processing is presented.

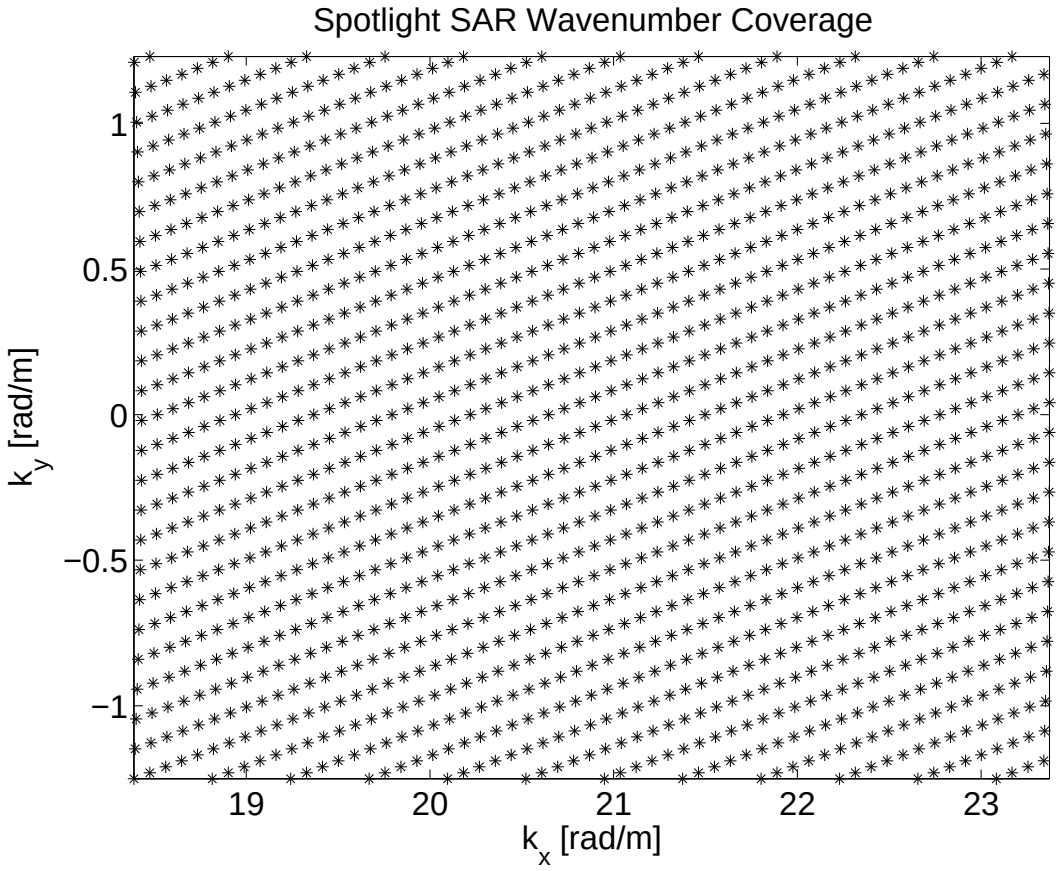

Figure 84: Spotlight SAR wavenumber coverage of 25 scatterers-far field broadside mode.

Applying the matched filtering operation along t and u axes to the recorded SAR signal in the wavenumber domain one obtains the dechirped spectrum given in the Figure (85).

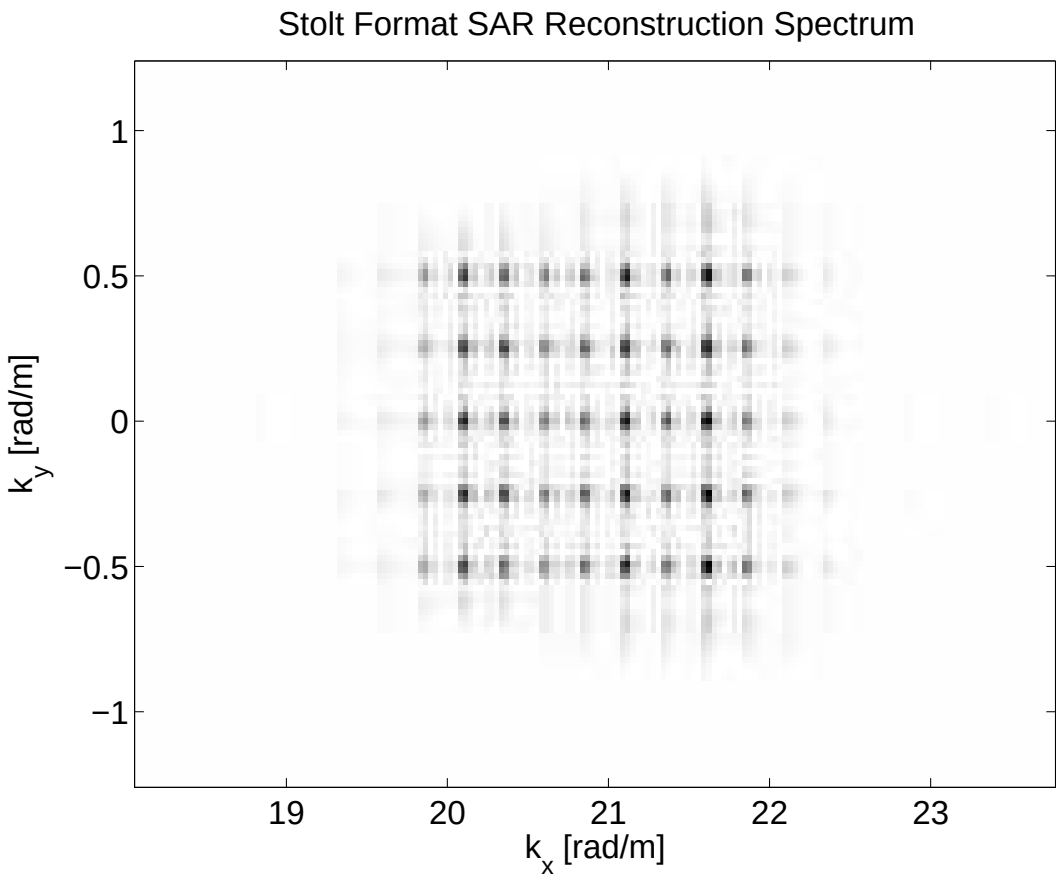

Figure 85: Stolt format SAR reconstruction spectrum of 25 scatterers-far field broadside mode.

After 2D inverse Fourier transforming one obtains the scene scattering function given in the Figure (86).

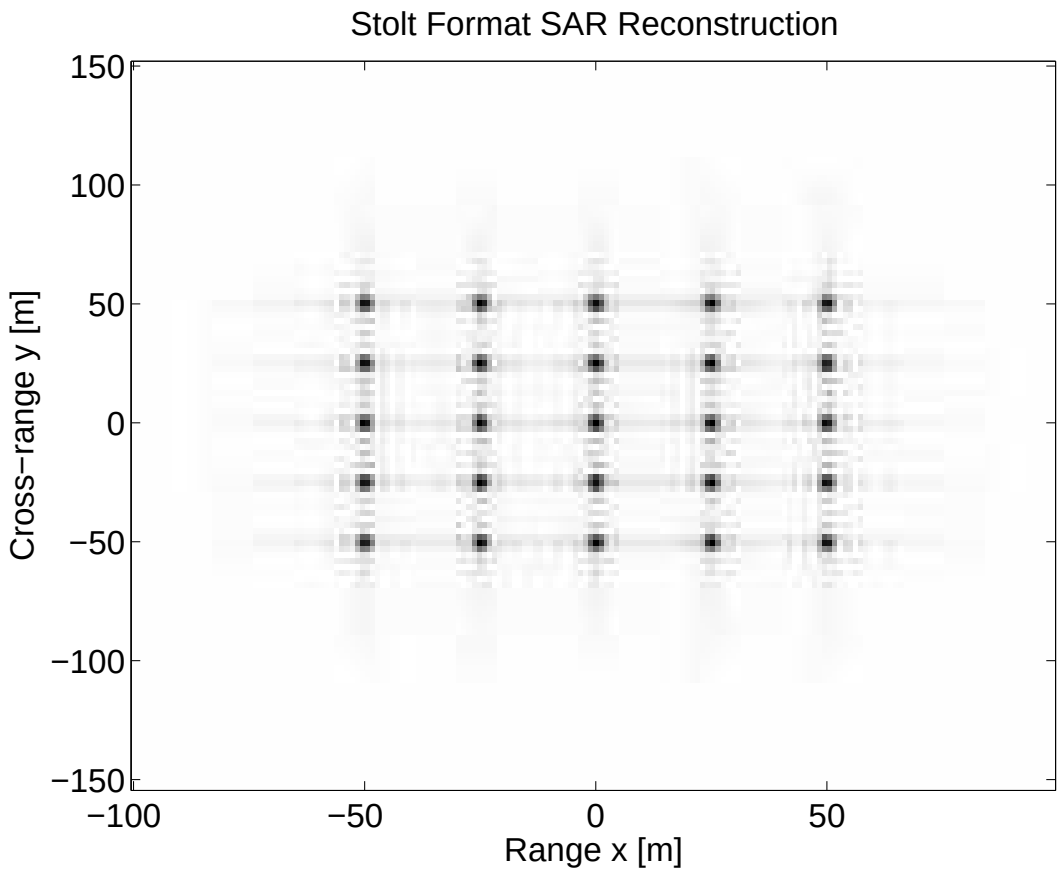

Figure 86: Stolt format SAR reconstruction of 25 scatterers-far field broadside mode.

4.3.2 Stolt Format Processing using $t^{0.75}$FM Signals

In this section the imagery reconstructed by LFM and $t^{0.75}$FM chirps using Stolt format processing are compared. 3 example images which are reconstructed by Stolt format processing for spotlight imaging geometry is presented. Therefore for the $p(t)$ in the equation (114), the expression given in the equation (2) for LFM chirp and the expression given in the equation (36) for $t^{0.75}$FM chirp are used.

The first example is for a single scatterer located at $x = 0\text{m}, y = 0\text{m}$ with the parameters $X_c = 1500\text{m}, Y_c = 500\text{m}, X_o = 100\text{m}, L = 100\text{m}$ with signal parameters $T_p = 1 \times 10^{-6}\text{s}$, $f_c = 200 \times 10^6$ Hz, $f_o = 10 \times 10^6$ Hz. In the Figure (87) the image reconstructed by SFA with LFM chirp signal is presented. The chirp rate for these parameters is $\alpha \approx 6.28 \times 10^{13}$.

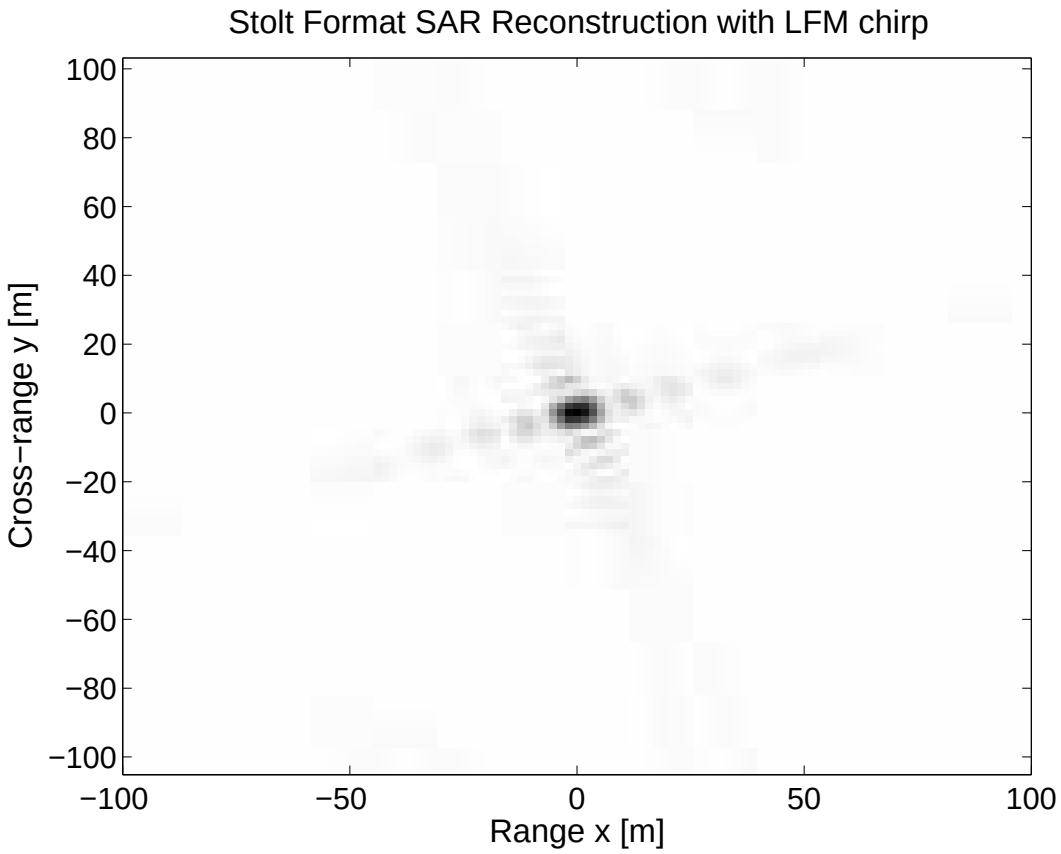

Figure 87: Stolt format SAR reconstruction of a single scatterer at $x = 0\text{m}, y = 0\text{m}$-squinted mode-using LFM chirp.

The image reconstructed by SFA with $t^{0.75}$FM chirp signal, which can be seen in the Figure (88), is almost identical to image reconstructed by LFM chirp with reduced sidelobes, better resolved target and has a lower chirp rate which is $\eta \approx 2.27 \times 10^{12}$.

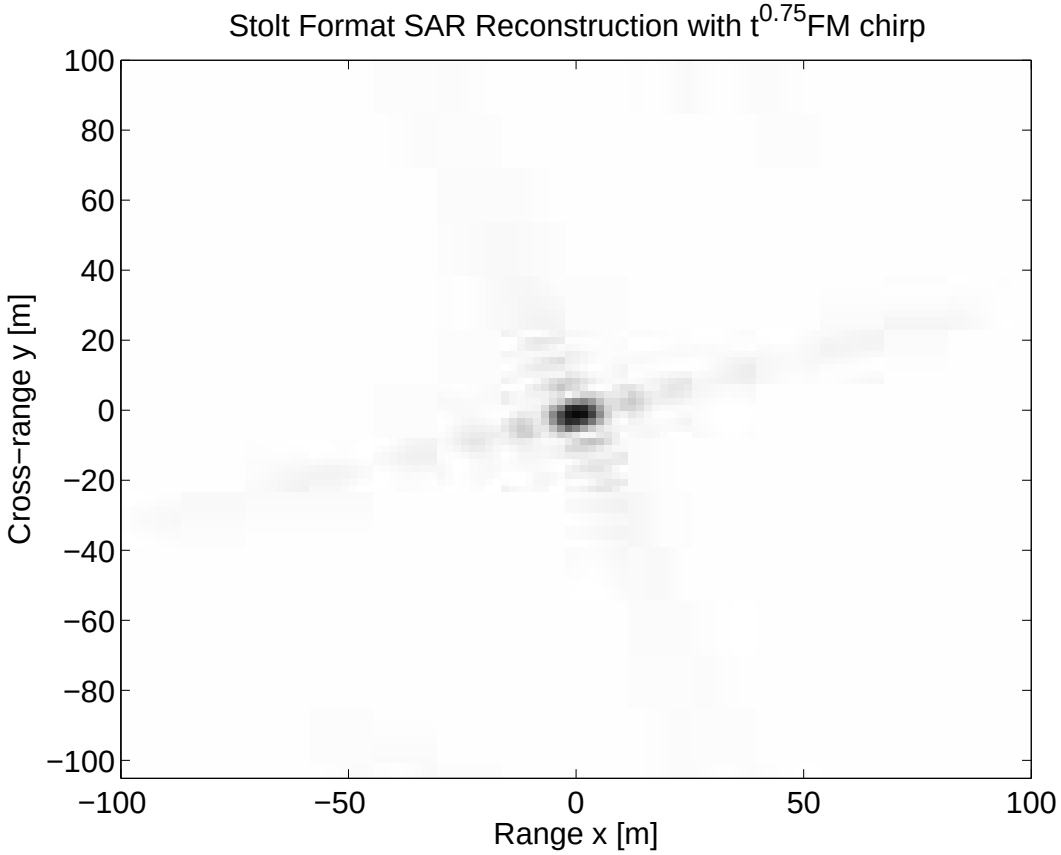

Figure 88: Stolt format SAR reconstruction of a single scatterer at $x = 0\text{m}, y = 0\text{m}$-squinted mode-using $t^{0.75}$FM chirp.

The second example is for 5 scatterers located at $x_1 = 0\text{m}, y_1 = 0\text{m}$, $x_2 = 14\text{m}, y_2 = -12\text{m}$, $x_3 = -14\text{m}, y_3 = 12\text{m}$, $x_4 = -12\text{m}, y_4 = 15\text{m}$, $x_5 = 12\text{m}, y_5 = -15\text{m}$ with the parameters $X_c = 1500\text{m}, Y_c = 0\text{m}, X_o = 100\text{m}, L = 150\text{m}$ with signal parameters $T_p = 10 \times 10^{-6}\text{s}$, $f_c = 200 \times 10^6$ Hz, $f_o = 15 \times 10^6$ Hz. In the Figure (89) the image reconstructed by SFA with LFM chirp signal is presented. The chirp rate for these parameters is $\alpha \approx 9.42 \times 10^{12}$.

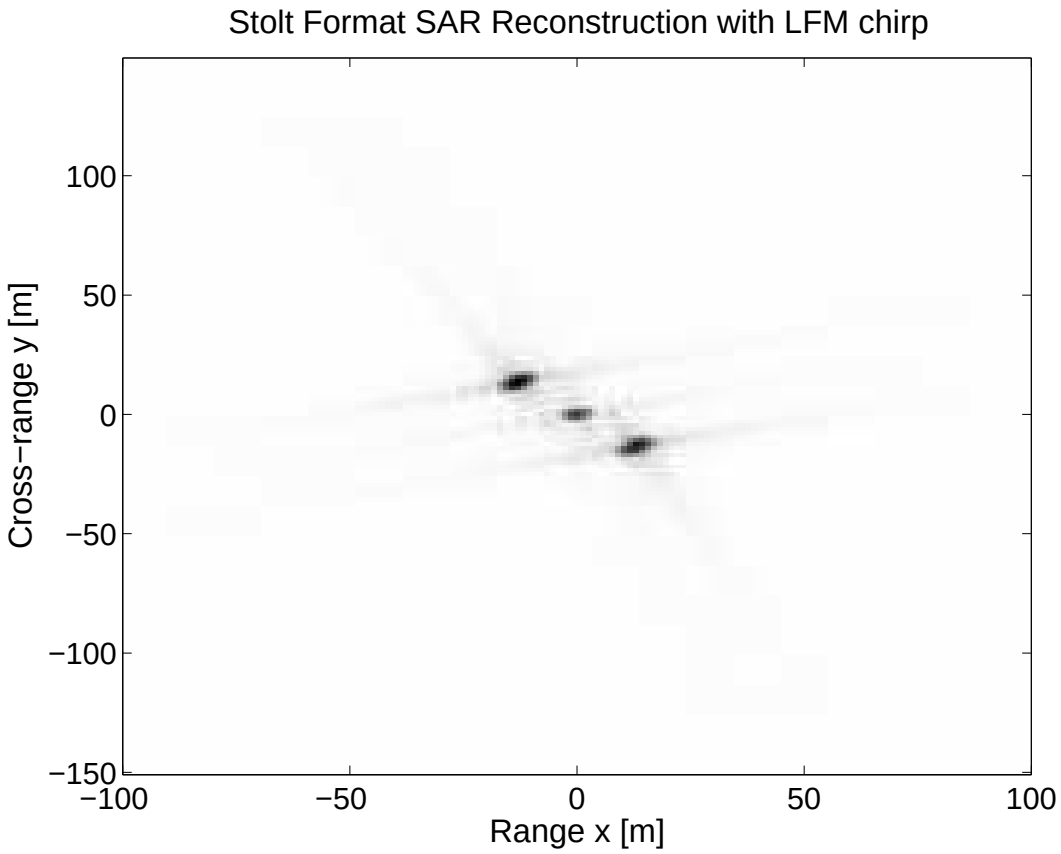

Figure 89: Stolt format SAR reconstruction of 5 scatterers-squinted mode-using LFM chirp.

The image reconstructed by SFA with $t^{0.75}$FM chirp signal, which can be seen in the Figure (90), is almost identical to image reconstructed by LFM chirp with reduced sidelobes and has a lower chirp rate which is $\eta \approx 6.05 \times 10^{11}$.

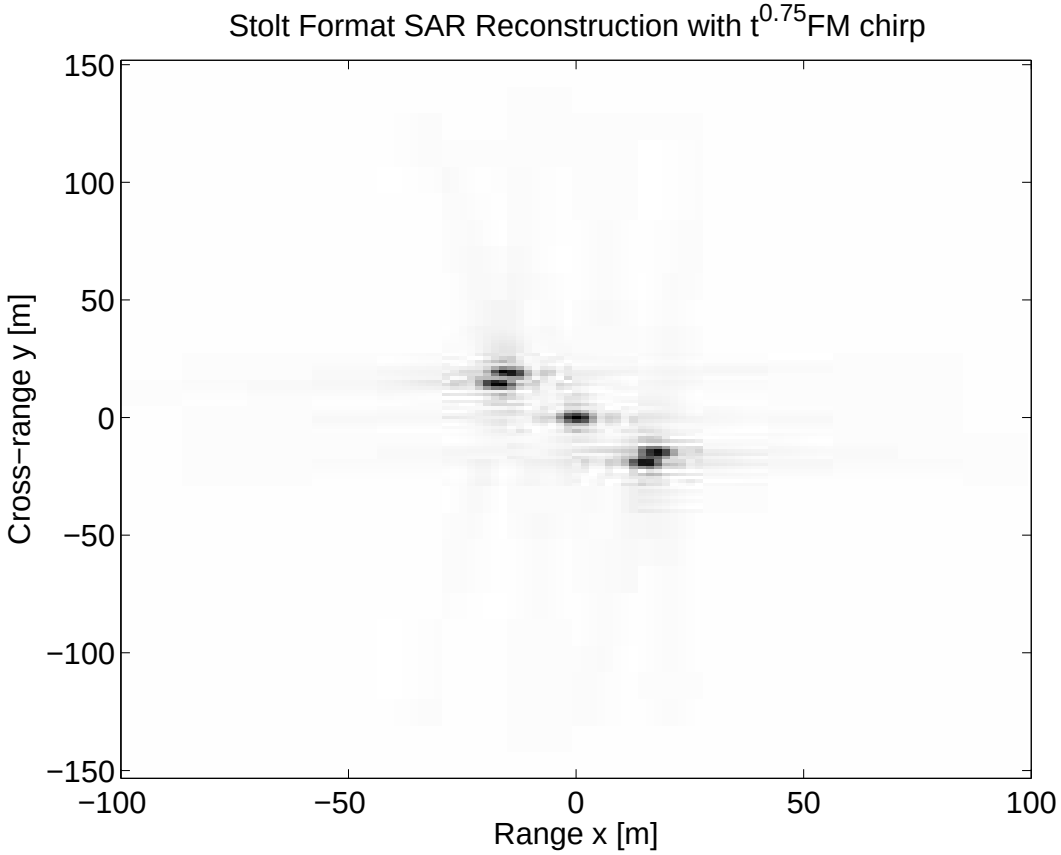

Figure 90: Stolt format SAR reconstruction of 5 scatterers-squinted mode-using $t^{0.75}$FM chirp.

The third example is for 25 scatterers uniformly distributed inside a square with coordinates $(-25\text{m}, -25\text{m})$, $(-25\text{m}, 25\text{m})$, $(25\text{m}, 25\text{m})$, $(25\text{m}, -25\text{m})$ with the parameters $X_c = 1500\text{m}, Y_c = 0\text{m}, X_o = 100\text{m}, L = 100\text{m}$ with signal parameters $T_p = 5 \times 10^{-6}\text{s}$, $f_c = 200 \times 10^6$ Hz, $f_o = 12 \times 10^6$ Hz. In the Figure (91) the image reconstructed by PFA with LFM chirp signal is presented. The chirp rate for these parameters is $\alpha \approx 1.50 \times 10^{13}$.

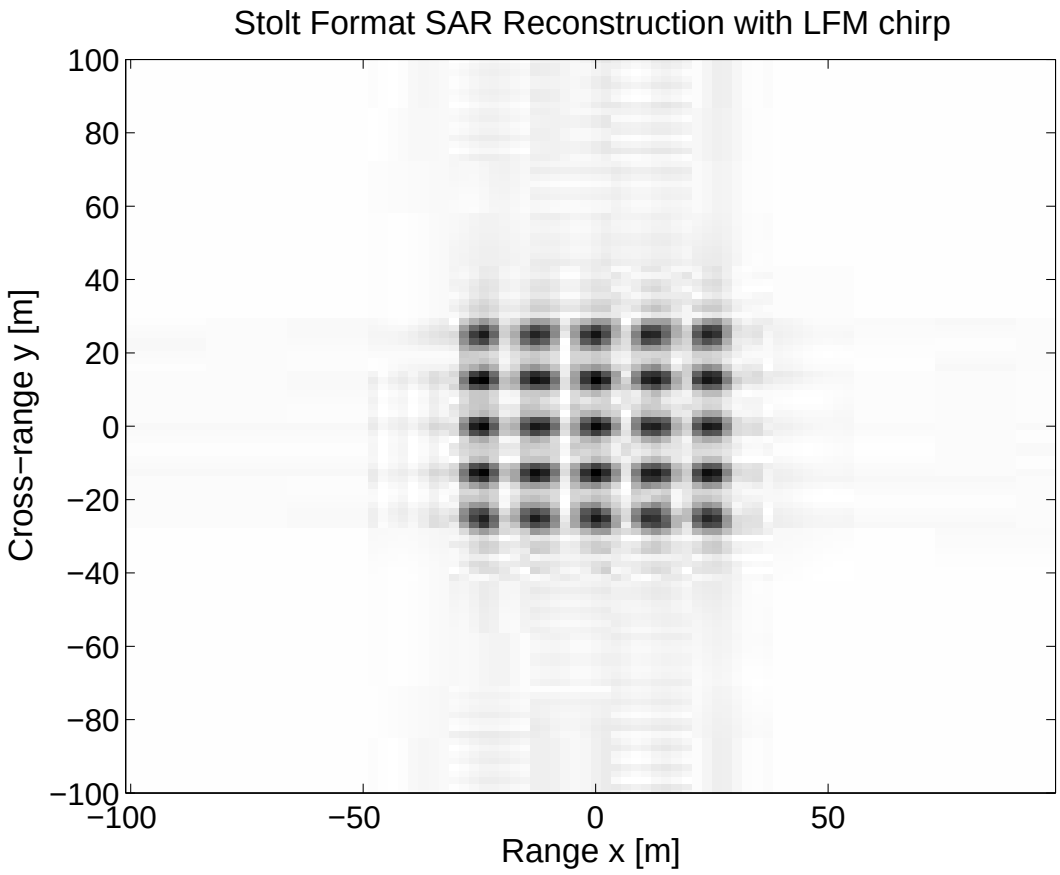

Figure 91: Stolt format SAR reconstruction of 25 scatterers-broadside mode-using LFM chirp.

The image reconstructed by SFA with $t^{0.75}$FM chirp signal, which can be seen in the Figure (92), is almost identical to image reconstructed by LFM chirp with reduced sidelobes and has a lower chirp rate which is $\eta \approx 8.14 \times 10^{11}$.

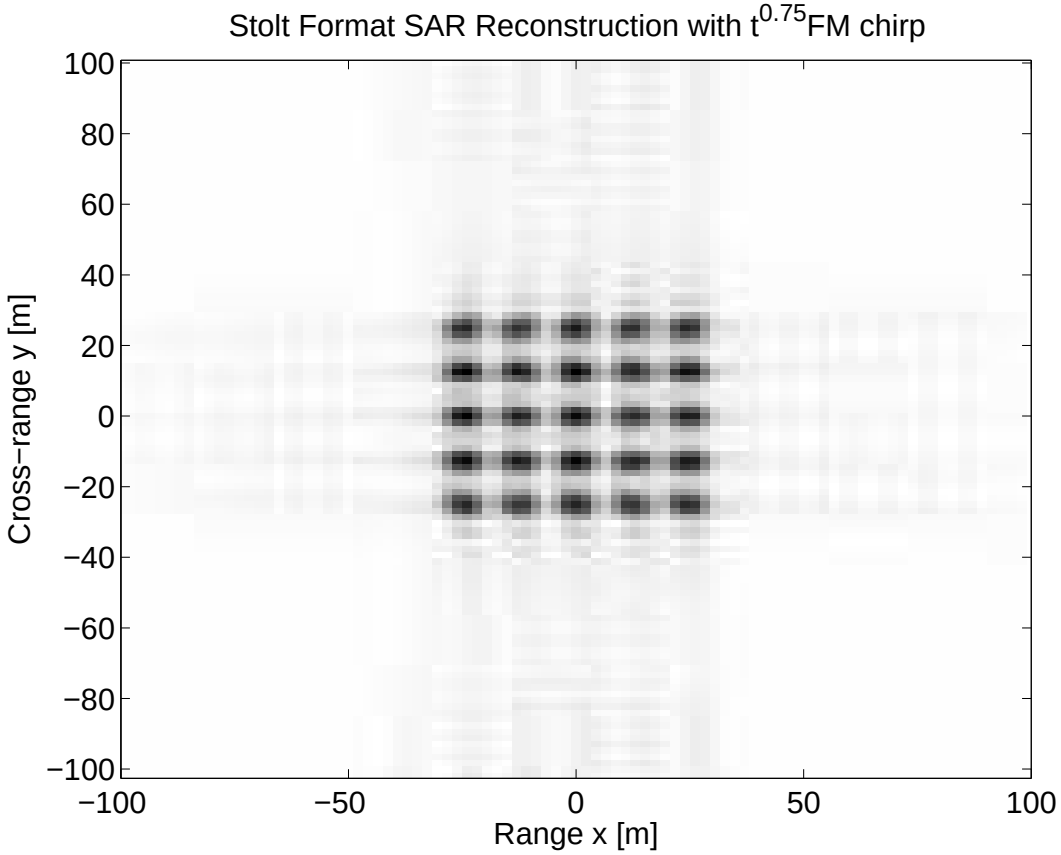

Figure 92: Stolt format SAR reconstruction of 25 scatterers-broadside mode-using $t^{0.75}$FM chirp.

CHAPTER V

CHANGE DETECTION ALGORITHMS

Comparisons between imagery acquired at different times can be performed by mathematical tools known as change detection algorithms. They are used to extract information about the changes occuring in a scene such as the magnitude, location and the direction of the change. Change detection algorithms are widely used in digital image and video processing [51] to detect temporal changes occuring in one or multiple scenes. They have the capability to detect very subtle changes which may seem insignificant to human eye. They may be used to assess not only intensity values but also the phase values which the human eye is not capable of doing.

For ideal change detection mapping, the data should be acquired by the same or at least similar sensor and must be recorded using the same spatial resolution, viewing geometry, spectral bands and time of the day [37]. Depending on the expected changes, the anniversary dates may also have an important effect on the quality of the change detection mapping [37].

Change detection mapping and analysis can be applied to various types of imagery obtained by different sensing systems such as radar, optical, multispectral or lidar and can be applied in diverse disciplines including but not limited to remote sensing, surveillance, medical imaging, civil infrastructure and underwater sensing. In this dissertation the radar imagery obtained by SAR sensors is considered. SAR imagery is widely used for both civilian and military reconnaissance. Earthquake, flood, tsunami, hurricane damage assessment, monitoring oil spills, extreme snow and ice conditions, fires, deforestation, illegal ship traffic, structural damages, military constructions and operations are a few examples to mention where the airborne and satellite SAR imagery is widely used.

Currently there are many change detection algorithms available for use. It is possible to create a classification matrix or tensor of change detection algorithms. One possiblity is to

make a classification based on the dimensions of the imagery, as 2D or 3D change detection algorithms. Depending on if the user selection is required or not, change detection algorithms can be classified into two categories; unsupervised and supervised change detection. Recent studies may also allow us to make a classification depending on whether the change detection is performed in the image domain or in a transformed domain. A comparison of wavelet domain and Fourier domain change detection is given in [52]. The most widely accepted categorization, depending on whether the phase values of the imagery are used or not, is to classify them as coherent or incoherent change detection; therefore, in this dissertation the change detection algorithms are discussed under these headings.

5.1 Incoherent Change Detection

Incoherent change detection identifies changes in the mean backscattered power of the scene by comparing sample estimates of the mean backscatter power taken from the repeat pass image pair. Typically the sample estimates are obtained by spatially averaging the image pixel intensities (gray levels) over local regions in the image pair. The mean backscatter power of a scene is determined by the structural and dielectric properties of the scene and thus may be used to detect changes [41].

As given in [42] the most widely used change detection methods are image differencing and ratioing. In differencing, the intensities (gray levels) of the images taken at two different times are substracted on a pixel-by-pixel basis. In ratioing, the intensities of the images are divided on a pixel-by-pixel basis and often described in decibel scale. Rignot and van Zyl provides a comparison of these methods using a probabilistic model for the thresholds where they assume that image intensities have a gamma distribution [42]. They also test another method known as decorrelation of speckle. It turns out that image differencing and ratioing helps to determine the position as well as the magnitude of the changes occuring whereas decorrelation method only helps detecting the position of the change [42].

A good summary of the existing incoherent change detection methods is given in [39] under subtitles unsupervised and supervised approach.

The unsupervised change detection is performed by separating two multispectral images

into a single band or multiband image in which the change can be detected. In contrast, supervised classification methods requires the selection of a training set to determine the classes [39]. Unsupervised techniques perform change detection algorithms by extracting the change map of the images acquired at two different times. Besides image differencing and ratioing, some other unsupervised change detection methods are offered by researchers. Some of these are normalized difference vegetation index, change vector analysis, principal component analysis, expectation maximization, Markov random field, reduced Parzen estimation, maximum a posteriori probability, object level change detection and maximum autocorrelation factor [39].

The supervised change detection methods require the selection of a region of interest to determine the classes. This approach is more flexible and effective than the unsupervised change detection methods [39]. Among the supervised techniques, the most common category is postclassification comparison. This technique performs change detection by comparing the change maps that were obtained by classifying independently two images of the target obtained at different times [39]. Other methods are based on direct multidata classification, support vector machines, hidden Markov chains and neural networks.

5.2 Coherent Change Detection

Coherent Change Detection (CCD) uses the magnitude of the sample complex cross correlation of an interferometric SAR image pair to quantify changes in the transduced amplitude and phase of the image pixels. Since the transduced pixel amplitude and phase is sensitive to the relative spatial geometry of the scattering contributions within a pixel, CCD has the potential to detect very subtle scene changes when compared to traditional incoherent methods [41]. Additionally the CCD image co-registration step is easier than that of CD [33].

The majority of the CCD methods depend on evaluating the coherence between two images where coherence is generally calculated using correlation coefficient, a statistical tool used in statistics and many engineering branches including digital image processing [24]. For example three different CCD techniques which depends on coherence estimation,

named mean level detector, ordered coherence statistic and censored mean level detector are discussed and an improvement to those techniques is offered in [11]. In some of the literature such as in [33] and [41] a probabilistic method is usually employed for the selection of thresholds along with the coherency calculations.

There are also some deterministic CCD methods recently offered in the literature. A physics based method for coherency calculations for SAR signals reflected from rough soil surfaces is given in [54]. Scattering from soil surface as modeled by Kirchhoff approximation can be seen in [5]. This model is used to calculate the phase values of the scattered radar signal which allows the CCD to be performed.

Additional information about CD and CCD techniques and their potential uses can be seen in [33] or [38].

5.3 Proposed CD Methods and Their Verification against Synthetic Imagery

There is a vast amount of literature on the CD and CCD topics as discussed above. However in the majority of works, the SAR imagery is selected in such a way that it is already possible to discriminate the changed and unchanged regions with naked eye. The main reason behind this fact is that CD suffers from high probability of false alarm rates for given probabilites of detection. It is desirable to reduce the false alarm rate for a given probability of detection or increase the probability of detection for a given false alarm rate.

In this section a new change detection methodology which leads to two final change maps is offered (Figure (93)). Although it is utilized using the CD methods, it can be extended to CCD methods as well. Having a time sequence of n images of the same target area two final change maps are generated.

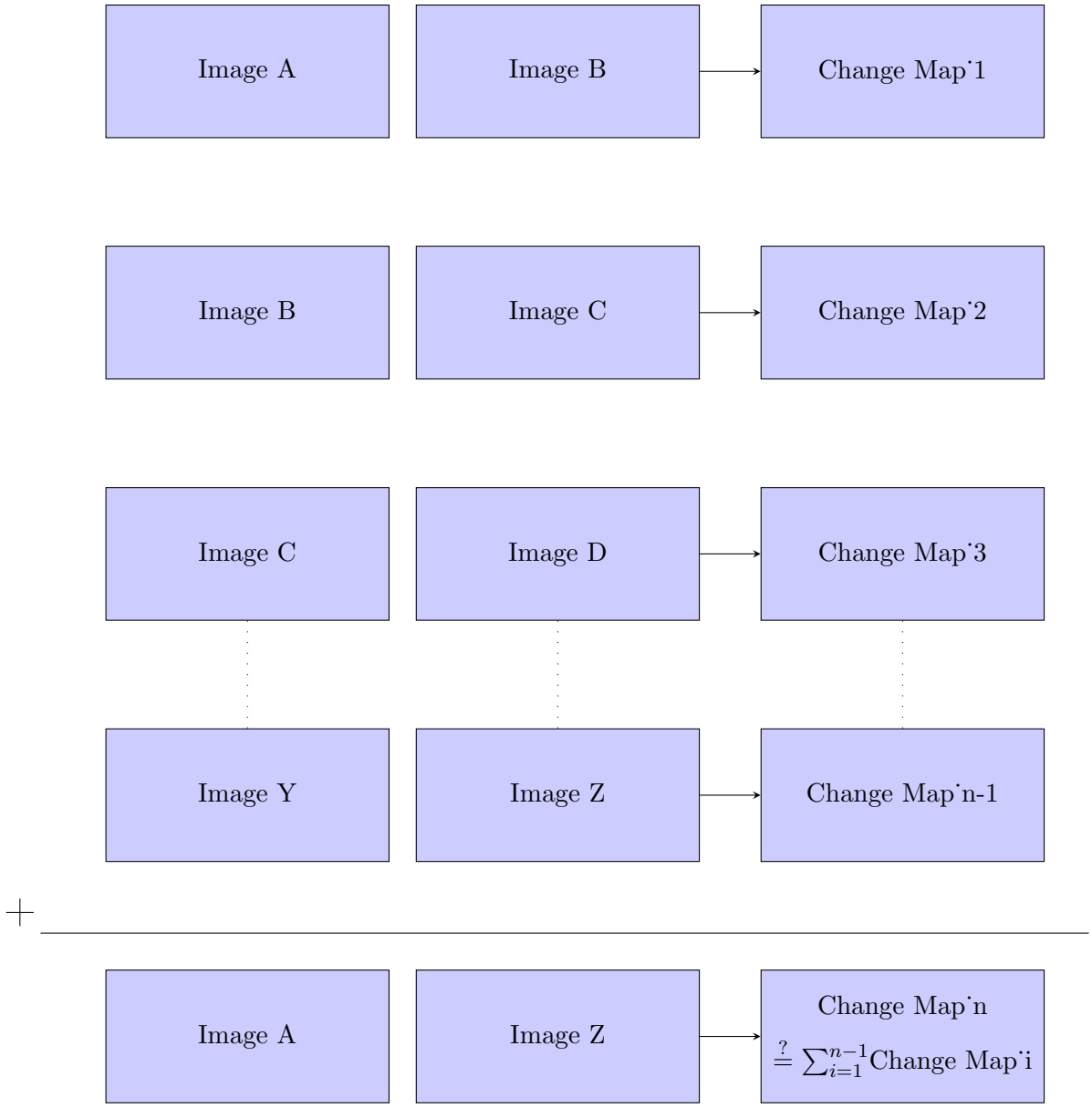

Figure 93: Proposed two final map change detection method.

First change map is obtained by cumulatively adding the successive change maps and the second change map is obtained by comparing the first and the last image in the temporal sequence. Cumulative addition is performed in a manner that common changed areas between the change map sequence is excluded to prevent accounting for a change first appears and then disappears. However uncommon changed areas between the change map sequence is included in an absolute fashion. By adopting this approach two different change

maps between first and the last image can be generated. The changes present in both of the change maps are critical since they are more likely to indicate a detected change, not a false alarm. The changes which are not present in both of the change maps are more likely to be the deficit of the change detection algorithm, thus can be paid less attention or can be ignored. Since more than one change maps are generated using this approach sampling and the accuracy of the change maps increases therefore lower false alarm rates for a given probability of detection can be achieved. This method can provide a double-check mechanism for majority of the CD or CCD algorithms used in the CD literature. This approach is summarized by the flowchart given in Figure (93), in which the addition should be understood as the cumulative addition of changes in the successive change maps. Due to available data this process is applied to the time sequences of n=3 images.

Additionally although some of types disasters, such as earthquakes, are extensively studied and various algorithms are tested on them, other types of disasters, such as oil spills which have an evolving nature as discussed in this dissertation, are not as widely studied. For these purposes the correlation coefficient change statistic and the intensity ratio change statistic algorithms are utilized in this dissertation together with the two change maps method discussed above and they are applied to synthetic as well as the earthquake and the oil spill imagery.

Correlation Coefficient Change Statistic The total correlation coefficient between two images can be expressed by

$$\widehat{\gamma}_{total} = \widehat{\gamma}_{SNR}\widehat{\gamma}_{base}\widehat{\gamma}_{scene}\widehat{\gamma}_{vol}\widehat{\gamma}_{proc} \tag{141}$$

where $\widehat{\gamma_{SNR}}$ denotes the decorrelation due to relative backscatter signal to receiver noise ratio [11], $\widehat{\gamma}_{base}$ denotes the decorrelation that arises due to mismatch in the acquisition geometries between first and repeat-pass data collections [11], $\widehat{\gamma}_{scene}$ denotes the decorrelation in the scene, $\widehat{\gamma}_{vol}$ and $\widehat{\gamma}_{proc}$ denote the decorrelations due to scattering from a volume when a nonzero baseline is used in the acquisition and image processing, respectively [11]. Similar discussions about the partial contributions to the correlation coefficient can be seen in [42], [55]. These parameters is generally taken as $\widehat{\gamma}_{SNR}\widehat{\gamma}_{base}\widehat{\gamma}_{vol}\widehat{\gamma}_{proc} \approx 1$ so that $\widehat{\gamma}_{scene}$ can be

regarded as the primary indicator of the total change in the correlation. From now on for the sake of brevity $\widehat{\gamma}$ is used instead of $\widehat{\gamma}_{scene}$.

The correlation coefficient $\widehat{\gamma}$ between image intensities $f(x,y)$ and $g(x,y)$ is defined as follows [33]

$$\widehat{\gamma}(x,y) = \frac{\left|\sum_{i=1}^{N} f_i g_i\right|}{\sqrt{\sum_{i=1}^{N} |f_i|^2 \sum_{i=1}^{N} |g_i|^2}} \tag{142}$$

where N is the number of pixel points in the neighborhood of the pixel (x,y) and generally taken as $N = 3 \times 3$ or $N = 5 \times 5$ [41]. As given in Appendix C, Cauchy-Schwarz inequality guarantees that $\widehat{\gamma} \in [0,1]$. Since $\widehat{\gamma}$ is the change parameter $\widehat{\gamma} = 1$ refers to no change whereas $\widehat{\gamma} = 0$ refers to a very significant change in the reflectivity of the pixel. Generally a threshold is used to make a decision as to whether there is change or not between two images. Also when the coherent change detecion methods are adopted, the phase values of images become important. In order to have a valid correlation coefficient for CCD, the complex conjugate of either the first or the second image should be taken in the equation (142).

A simple threshold can be applied to the correlation coefficient in order to determine the changed and unchanged regions in a scene. The selection of threshold exhibits a tradeoff between the probabilites of detection (P_d) and false alarm (P_{fa}) therefore related probability density functions (pdf) need to be discussed.

The pdf of the correlation coefficient statistic is derived as [53], [41]

$$p(\widehat{\gamma}|\gamma, N) = 2(N-1)(1-\gamma^2)^N \widehat{\gamma}(1-\widehat{\gamma}^2)^{N-2}\ {}_2F_1(N, N; 1; \gamma^2\widehat{\gamma}^2) \tag{143}$$

where γ is the underlying scene coherence given by

$$\gamma = E\{(m_r)(n_r)\} \quad m_r = f/\sigma_f \quad n_r = g/\sigma_g \tag{144}$$

with m_r and n_r are the unit speckle noise components, $E\{\}$ is the expected value operator and $E\{I_f\} = \sigma_f^2$, $E\{I_g\} = \sigma_g^2$. ${}_1F_2$ denotes for Gauss hypergeometric function which is defined as [3]

$${}_1F_2(a,b;c;z) = F(b,a;c;z) = \frac{\Gamma(c)}{\Gamma(a)\Gamma(b)} \sum_{l=0}^{\infty} \frac{\Gamma(a+l)\Gamma(b+l)}{\Gamma(c+l)} \frac{z^l}{l!} \tag{145}$$

where Γ denotes the gamma function. A plot of this pdf can be seen in the Figure (94) below.

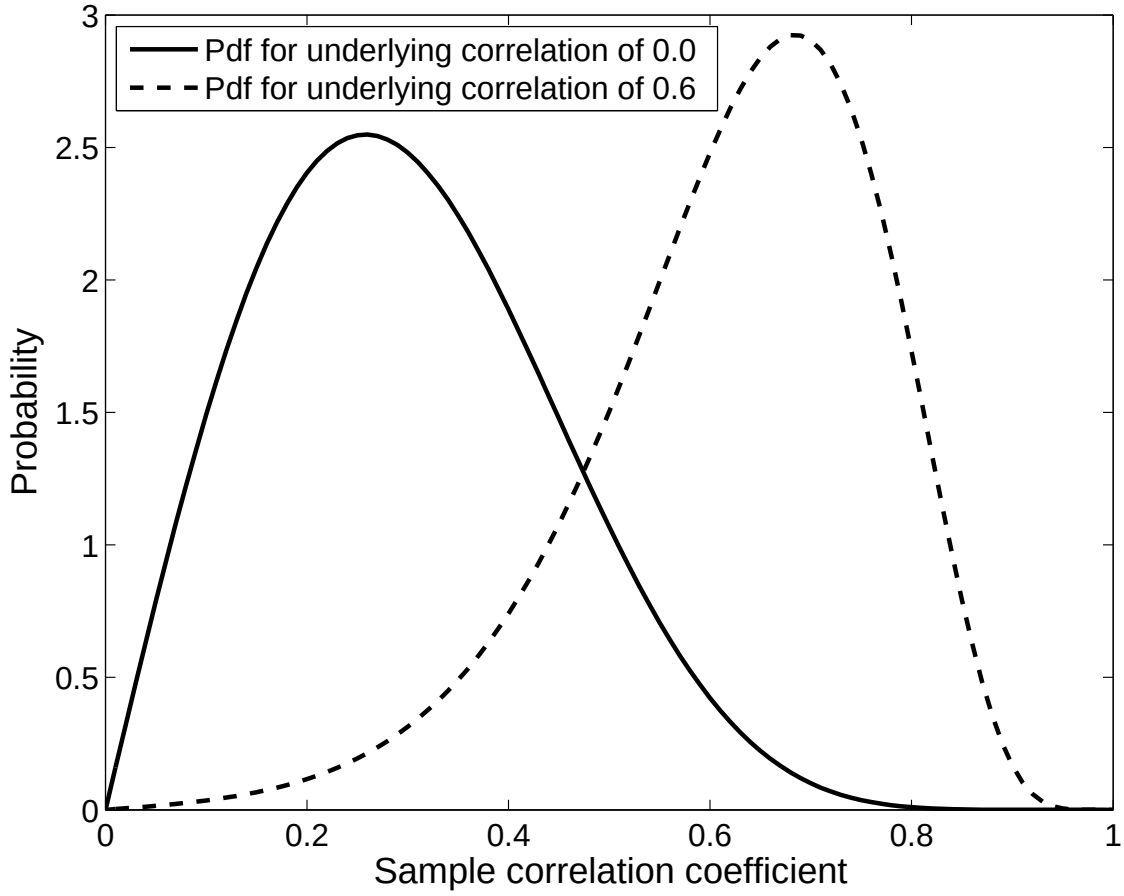

Figure 94: Pdf of correlation coefficient change statistics for an underlying scene coherence of 0.0 and 0.6 for $N = 9$.

This pdf is tested against experimental data and due to its agreement it is widely used in change detection studies such as [53], [41]. Based on this pdf, the P_{fa} and P_d can be calculated using the expressions [41]

$$P_{fa} = \int_0^T p(\widehat{\gamma}|\gamma = \gamma_{unchanged}) d\widehat{\gamma} \quad ; \quad P_d = \int_0^T p(\widehat{\gamma}|\gamma = \gamma_{changed}) d\widehat{\gamma} \tag{146}$$

which is equal to

$$\begin{aligned} P = & \frac{2(N-1)(1-\gamma^2)^N}{\Gamma(N)\Gamma(N-1)} \cdot \\ & \cdot \sum_{k=0}^{N-2} \left[\binom{N-2}{k} (-1)^{N-2-k} \sum_{l=0}^{\infty} \left[\frac{\Gamma(N+l)}{\Gamma(l+1)} \right]^2 \gamma^{2l} \frac{T^{2N+2l-2-2k}}{2N+2l-2-2k} \right] \end{aligned} \tag{147}$$

which defines the P_d and P_{fa} as

$$P = \begin{cases} P_d, & \text{for } \gamma = \gamma_{changed}, \\ P_{fa}, & \text{for } \gamma = \gamma_{unchanged}. \end{cases} \tag{148}$$

For the case $\gamma_{changed} = 0$ then $P = P_d$ becomes [41]

$$P = P_d = 2(N-1)^2 \sum_{k=0}^{N-2} \binom{N-2}{k} (-1)^{N-2-k} \frac{T^{2N-2-2k}}{2N-2-2k} \tag{149}$$

Threshold to be used in the correlation coefficient change statistic method can be decided by making use of P_d vs. P_{fa} graphs. In the Figure (95) P_d vs. P_{fa}, (or sometimes referred to as Receiver Operating Characteristics (ROC)) curves for $\gamma_{changed} = 0$ and $\gamma_{unchanged} = 0.40, 0.60, 0.75, 0.90$ for $N = 9$ is presented. A probability of detection of $P_d = 0.8$ can be achieved for $\gamma_{unchanged} = 0.60$ with a $P_{fa} = 0.1$ as it can be seen in the Figure (95).

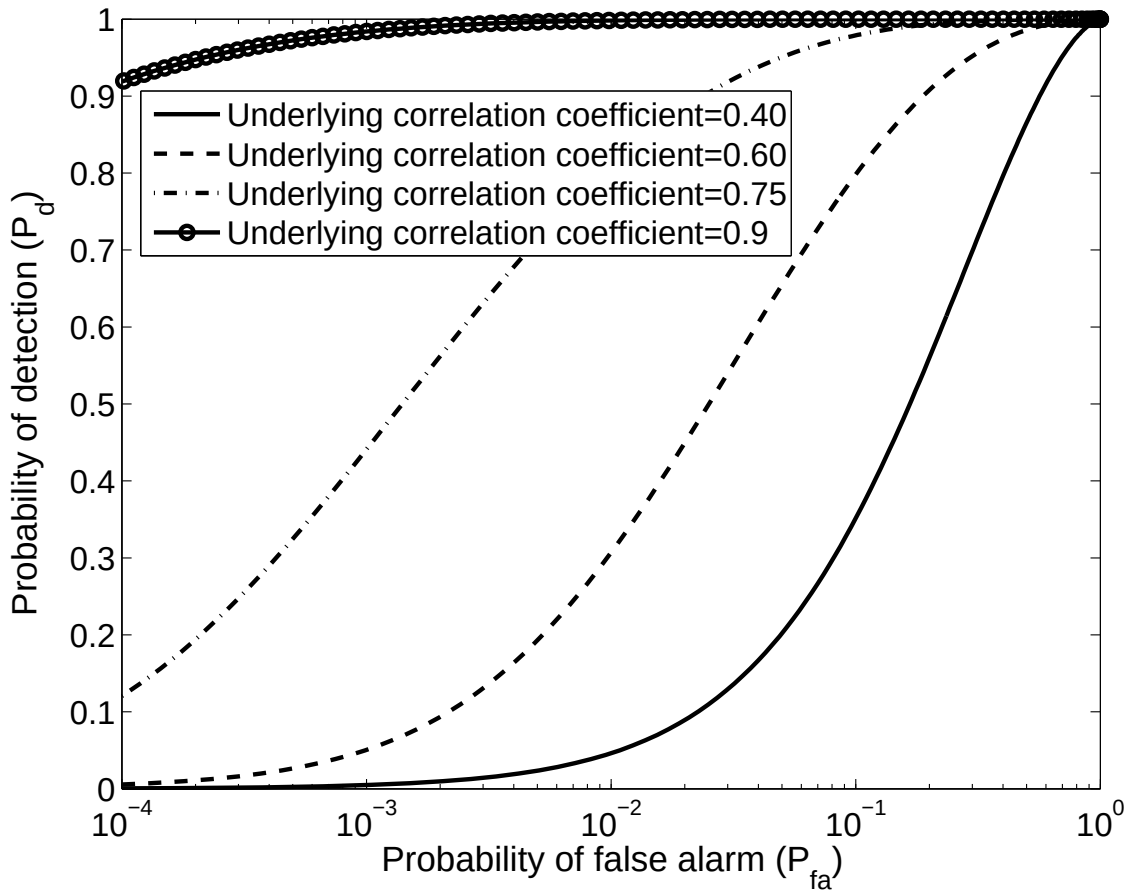

Figure 95: ROC curve for correlation coefficient change statistic obtained with underlying unchanged correlation coefficients of $0.40, 0.60, 0.75, 0.90$ and changed correlation coefficient of 0.0 for $N = 9$.

Generally P_{fa} on the order of 10^{-2} is used in the literature as the acceptable probability of false alarm values [41]. One can reduce the P_{fa} significantly, at least one order of magnitude, by making the sampling window, N, larger [41]. In Figure (96) P_d vs. P_{fa} (ROC) curves for $\gamma_{changed} = 0$ and $\gamma_{unchanged} = 0.60$ for $N = 4, 9, 16, 25$ is presented. As it can be seen on the figure, increasing N, e.g. from 16 to 25 provides, an order of magnitude reduction in the false alarm rate [41].

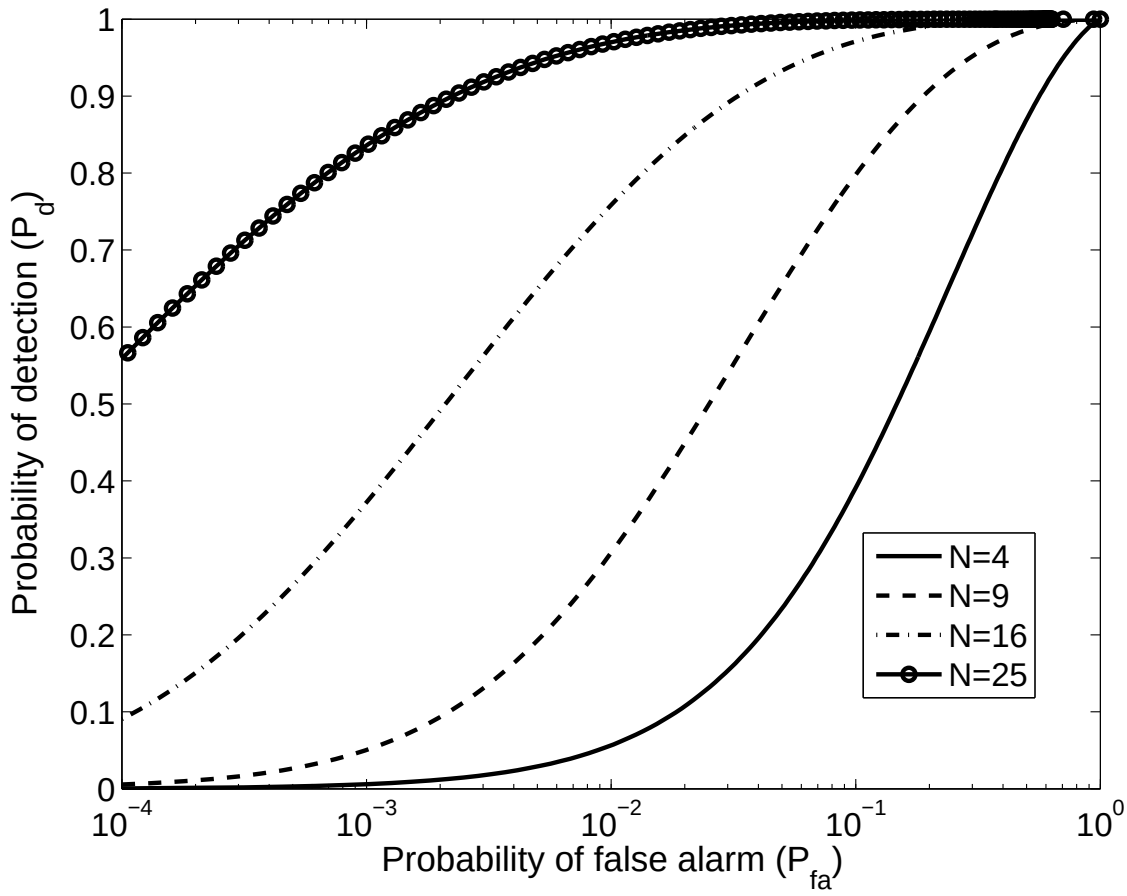

Figure 96: ROC curve for correlation coefficient change statistic obtained with underlying unchanged correlation coefficients of 0.6 for $N = 4, 9, 16, 25$.

However the window size should be commensurate with the disturbance size in the scene in order to prevent contributions from both changed and unchanged pixels [41].

In simulations with the synthetic data, the correlation coefficient change statistic threshold $T = 0.9$ with the window size of $N = 25$ is used. The synthetic data is not a random variable therefore discussing the related P_d and P_{fa} is trivial. However these ROC graphs are utilized to decide on a threshold to be used for the SAR imagery discussed in chapter 6.

Intensity Ratio Change Statistic Another widely used change detection method is the intensity ratio change statistic [41]. Initially one starts with computing the intensity values

using single pixel and averaging as

$$I_f = \frac{1}{N}\sum_{i=1}^{N}|f_i|^2 \qquad I_g = \frac{1}{N}\sum_{i=1}^{N}|g_i|^2 \tag{150}$$

The pdf of these intensities follow a gamma distribution as given in [42], [53], [41]. Detection of changes can be performed by computing the ratio change statistic as

$$\widehat{R} = \frac{I_f}{I_g} \tag{151}$$

which has various forms offered in the literature. A succesful version of this detector was proposed in [53] and is given by

$$\widehat{r} = \begin{cases} \widehat{R}, & \text{if } \widehat{R} \leq 1, \\ \widehat{R}^{-1}, & \text{if } \widehat{R} > 1. \end{cases} \tag{152}$$

The values of $\widehat{r}$ rests between 0 and 1 and a simple threshold can be applied to detect the changed and unchanged areas [41]. The probability density function (pdf) associated with this statistic can be written as [53], [41],

$$p(\widehat{r}|R) = \frac{\Gamma(2N)}{\Gamma^2(N)}\left(\frac{R^N}{(\widehat{r}+R)^{2N}} + \frac{R^{-N}}{(\widehat{r}+R^{-1})^{2N}}\right)\widehat{r}^{N-1} \tag{153}$$

where $R = E\{I_f\}/E\{I_g\}$ and E denotes the expected value. A plot of this pdf can be seen in the Figure (97) below.

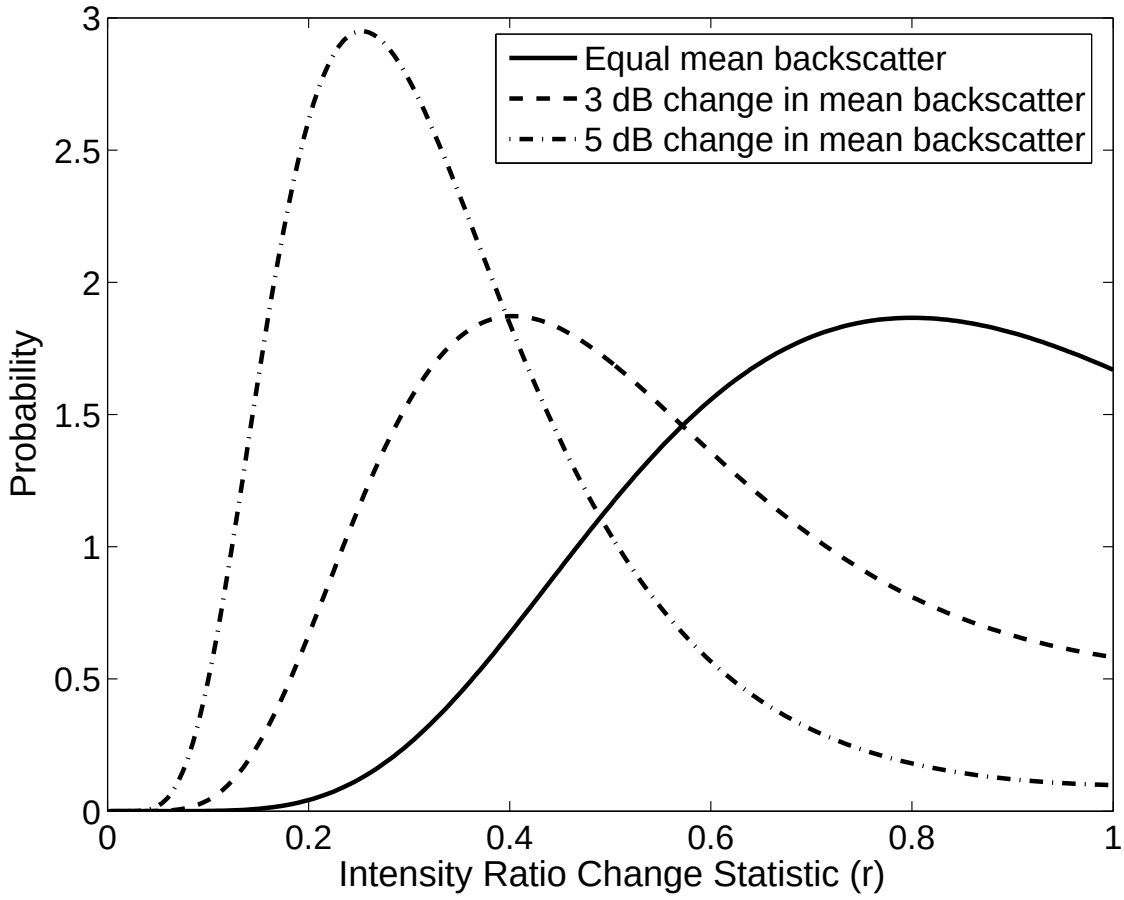

Figure 97: Pdf of intensity ratio change statistics for an unchanged scene (0 dB) and scenes with 3 dB and 5 dB change in the backscatter for $N = 9$.

This pdf is tested against experimental data and due to its agreement it is widely used in change detection studies such as [53], [41]. Based on this pdf one can calculate the P_{fa} and P_d as [41]

$$\begin{aligned} P_{fa} &= \int_0^T p(\widehat{r}|R = R_0)d\widehat{r} \\ &= \frac{\Gamma(2N)}{\Gamma^2(N)} \int_0^T \left(\frac{R_0^N}{(\widehat{r} + R_0)^{2N}} + \frac{R_0^{-N}}{(\widehat{r} + R_0^{-1})^{2N}} \right) \widehat{r}^{N-1} d\widehat{r} \end{aligned} \tag{154}$$

where $R_0 = E\{I_f\}/E\{I_g\}$ with $E\{I_f\}$ and $E\{I_g\}$ are the mean backscattered power in the

unchanged regions of the image [41] and

$$\begin{aligned} P_d &= \int_0^T p(\widehat{r}|R = R_1)d\widehat{r} \\ &= \frac{\Gamma(2N)}{\Gamma^2(N)} \int_0^T \left(\frac{R_1^N}{(\widehat{r} + R_1)^{2N}} + \frac{R_1^{-N}}{(\widehat{r} + R_1^{-1})^{2N}} \right) \widehat{r}^{N-1} d\widehat{r} \end{aligned} \tag{155}$$

where $R_1 = E\{I_f\}/E\{I_g\}$ with $E\{I_f\}$ and $E\{I_g\}$ are the mean backscattered power in the changed regions of the scene [41]. Analytical expressions for these integrals are given in [41]. The evaluation of P_{fa} and P_d leads to the ROC curves given the Figure (98) and Figure (99).

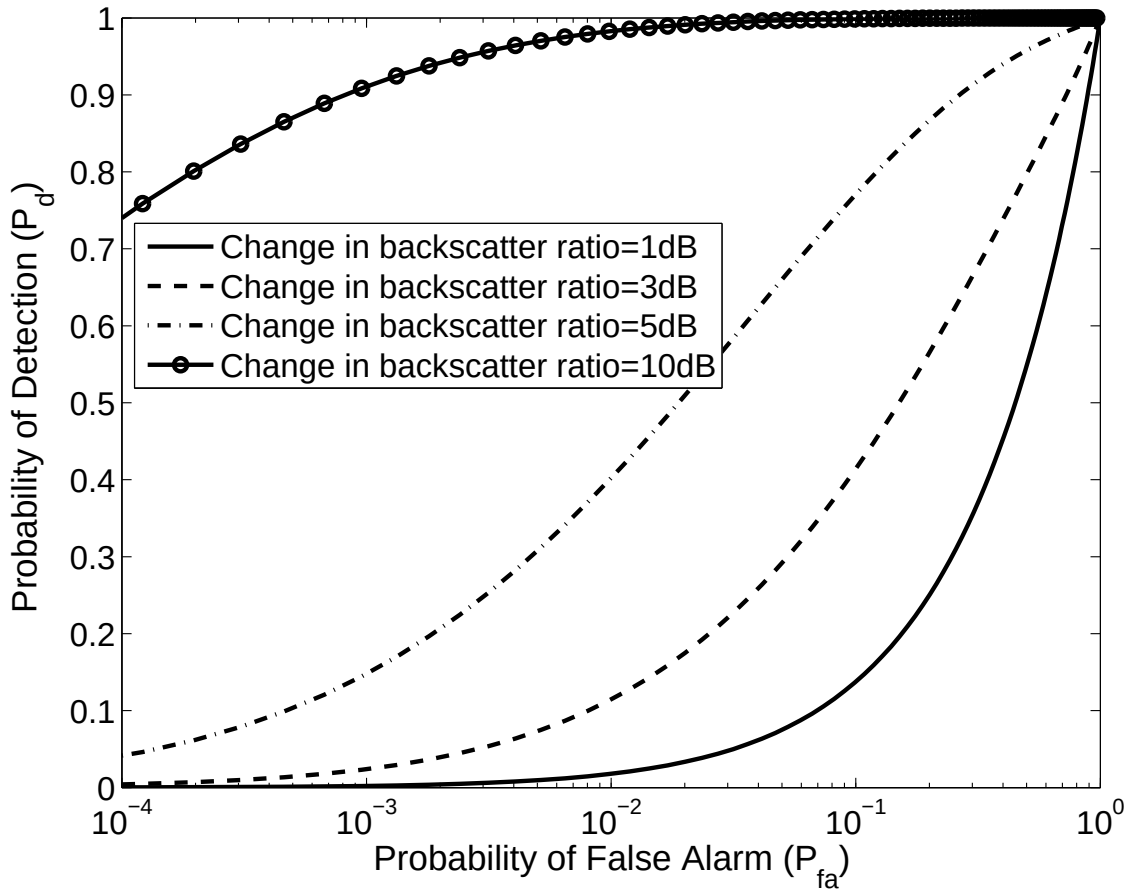

Figure 98: ROC curve for the intensity ratio change statistic obtained with $R_0 = 0$ dB and $R_1 = 1$ dB, 3 dB, 5 dB, 10 dB for $N = 9$.

It is useful to note that for $P_d = 0.7$ and $N = 9$ intensity ratio change statistics with $R_1 = 3$ dB and correlation coefficient change statistic with $\gamma_{unchanged} = 0.60$ shows a

quite similar behavior with both result at $P_{fa} = 0.07$. Additionally, as it can be seen in the Figure (98) above for a backscatter ratio change (R_1) of 3 dB and for $P_d = 0.7$ the probability of false alarm turns out to be $P_{fa} \approx 0.35$ which is an unacceptably high value [41]. One possibility to overcome this high false alarm rate problem is to increase the N.

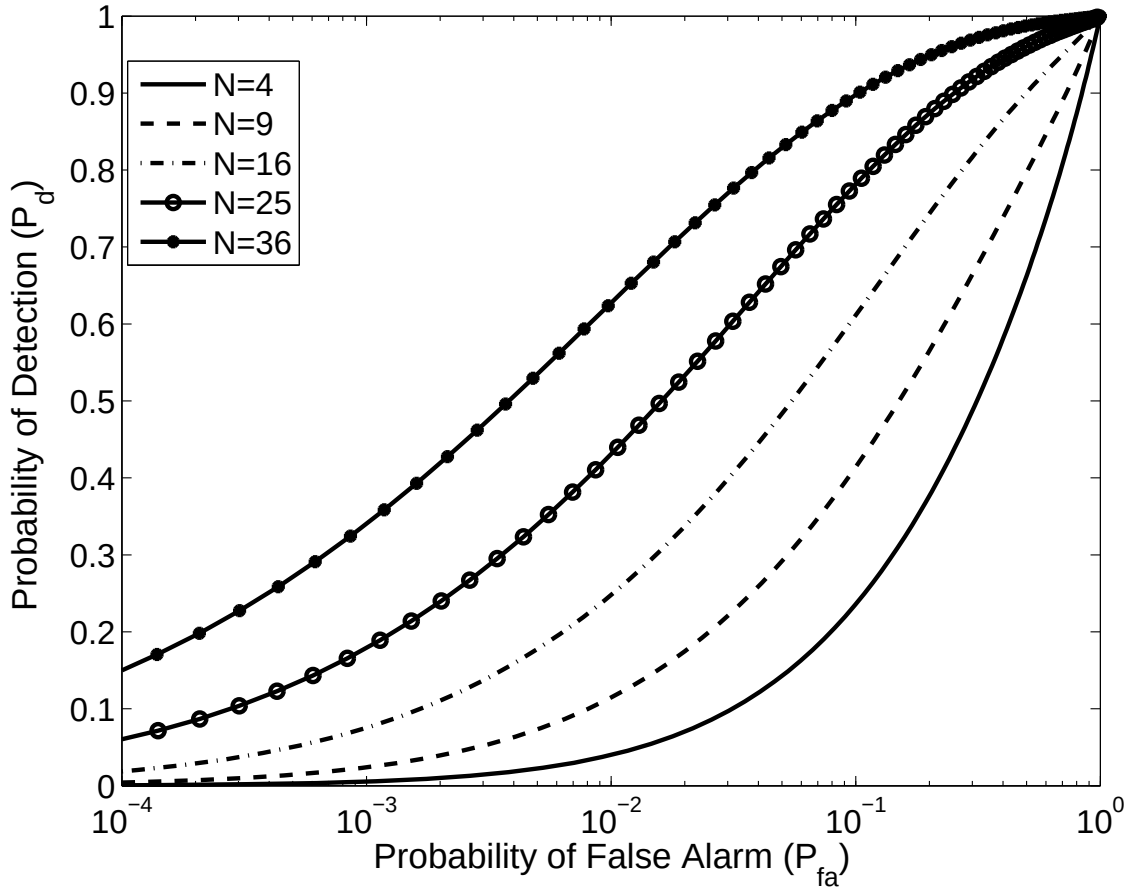

Figure 99: ROC curve for the intensity ratio change statistic obtained with $R_0 = 0$ dB and $R_1 = 3$ dB for $N = 4, 9, 16, 25, 36$.

As it can be seen in Figure (99) above, increasing N from 9 to 25 results decreases the P_{fa} from 0.35 to 0.06, for $P_d = 0.7$ and $R_1 = 3$ dB. However the window size should be commensurate with the disturbance size in the scene in order to prevent contributions from both changed and unchanged pixels [41].

In simulations with the synthetic data the intensity ratio change statistic threshold $T = 0.5$ with the window size of $N = 25$ is used. The synthetic data is not a random

variable therefore discussing the related P_d and P_{fa} is trivial. However these ROC graphs are utilized to decide on a threshold to be used for the SAR imagery discussed in chapter 6.

Verification of the CD Methods using Synthetic Imagery In this section, the two final change map CD method proposed above is tested by applying the specific CD algorithms summarized. For this purpose, synthetic images are reconstructed using Stolt format processing, which provides higher resolution imagery compared to polar format processing, is used.

In simulations with the synthetic data, the correlation coefficient change statistic threshold $T = 0.9$ and the intensity ratio change statistic threshold $T = 0.5$ with the window size of $N = 25$ is used. The synthetic data is not a random variable, therefore discussing the related P_d and P_{fa} is trivial. Two examples can be seen in the Figures (100) and (101) below.

In the first example three successive images with some artifical changes injected are presented. Initially the scene has 3 scatterers located, however one of the scatterers is first relocated and then one other scatterer is removed. Using the correlation coefficient change statistic and the intensity ratio change statistic algorithms the two final change map method offered is tested. Changed regions are indicated as white pixels throughout this dissertation. As can be seen in the Figure (100) below, the change maps between the first and the third image (CM 3) is the same as the change map obtained by cumulatively adding the change maps between the first and the second (CM 1) and the second and the third (CM 2) images. Also joint change areas of the two final change maps are presented. This approach will provide a double-check mechanism when the real data will be discussed in chapter 6.

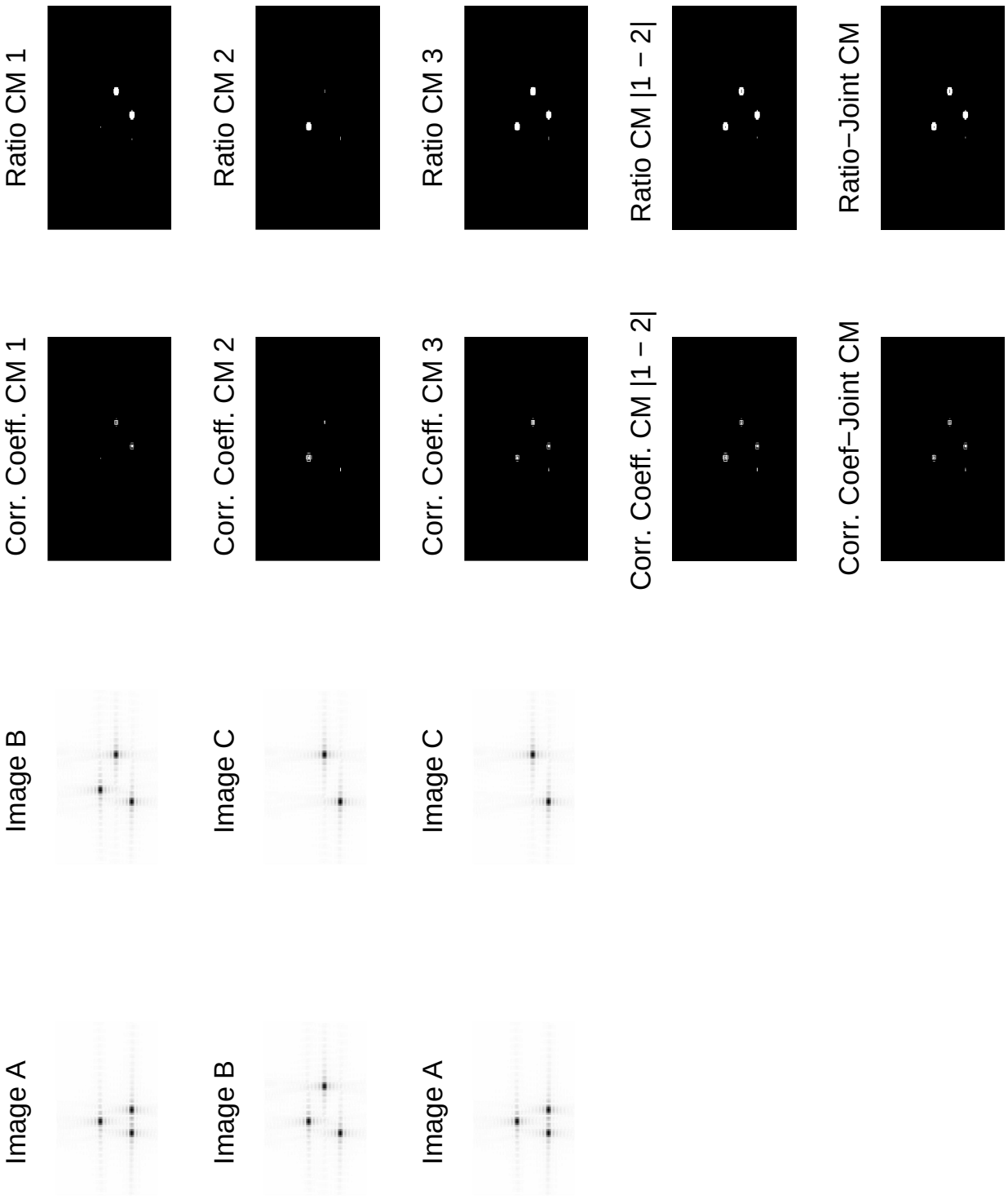

Figure 100: Change maps of synthetic imagery-example 1.

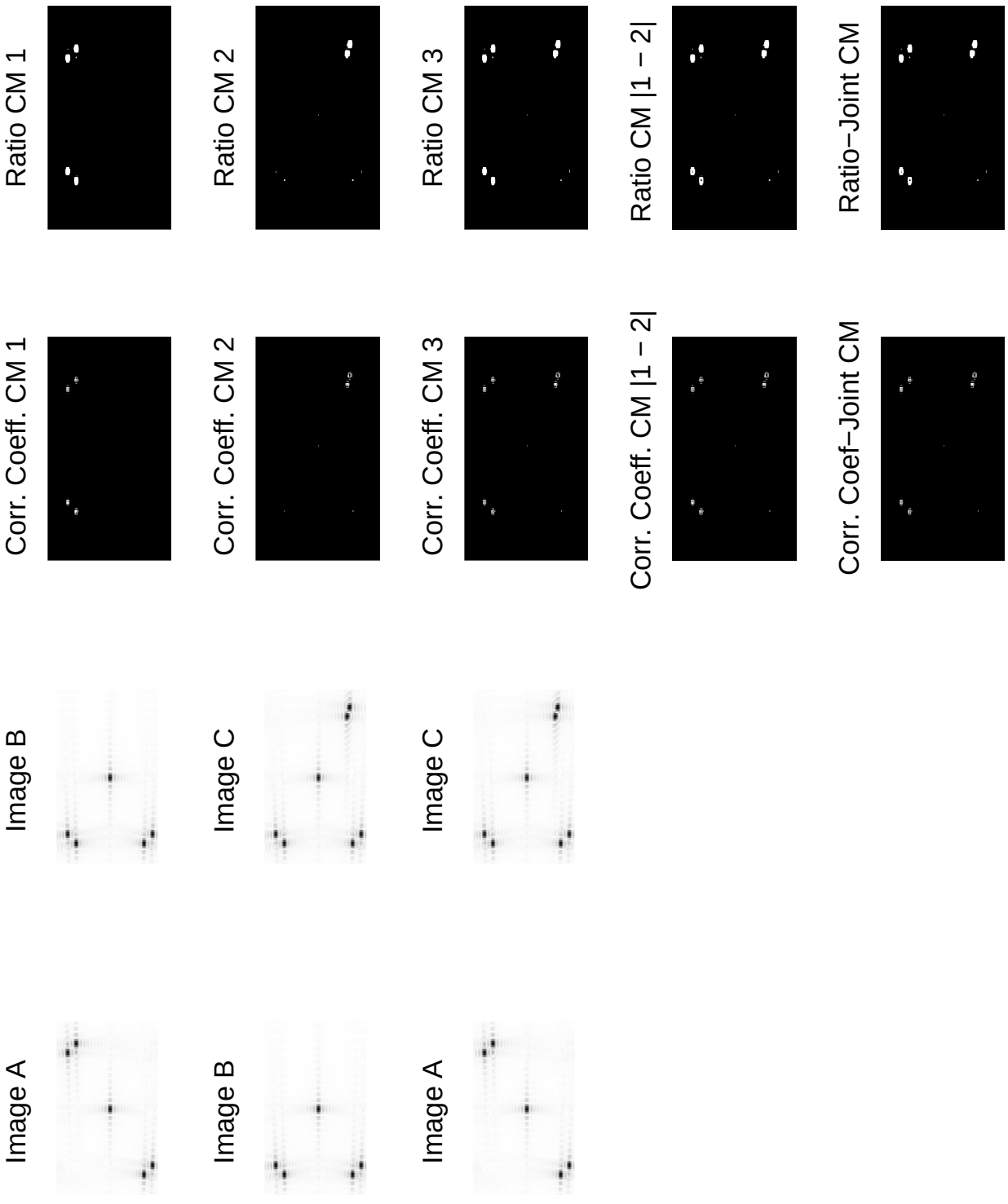

Figure 101: Change maps of synthetic imagery-example 2.

In the second example, three successive images with some artifical changes injected are presented. Initially the scene has 5 scatterers located, however two of the scatterers are first relocated and then two others are added. Using the correlation coefficient change statistic and the intensity ratio change statistic algorithms the two final change map method offered is tested. As it can be seen in the Figure (101) above the change maps between the first and the third image (CM 3) is the same as the change map obtained by cumulatively adding the change maps between the first and the second (CM 1) and the second and the third (CM 2) images. Also joint change areas of the two final change maps are presented. This approach will provide a double-check mechanism when the real data will be discussed in chapter 6.

CHAPTER VI

RESULTS AND DISCUSSION

Besides many uses for nondisaster monitoring purposes, SAR imagery is extensively used for monitoring various types of natural hazards and disasters [34]. They include but are not limited to oil spills, earthquakes and faults, landslides, flooding, volcanic activity, fires, hurricanes and tsunami runups. Satellite systems became indispensible tools for early warning and post disasters assessment studies since they provide a global picture of the disaster area which is critically important to identify the effected areas due to disaster. Compared to some small scale monitoring systems they can also provide information about the extent of the disaster in the inhabited areas. A detailed review of the satellite sensors and image processing techniques used for monitoring the natural hazards and disasters can be seen in [34].

In this dissertation two types of disasters are considered; oil spill and earthquake triggered landslides. Oil spill disaster is an evolving type of disaster wheras earthquake is an impulsive type of disaster. Additionally CD methods are not widely tested against oil spill imagery which is a new contribution, whereas the earthquake imagery help the new offered CD method to be tested against a classical type of disaster imagery. The case studies focused on are the 2010 Gulf of Mexico oil spill and the 2008 China Sichuan earthquake triggered landslides. While there are various satellite systems in operation only a few of them offer pre- and post-disaster imagery of the inspected regions. Among these satellite data, that provided by Advanced Land Observing Satellite of Japan Aerospace Exploration Agency is used in this dissertation.

6.1 Data Acquisition System

The data used in this study is obtained from the Advanced Land Observing Satellite (ALOS) of Japan Aerospace Exploration Agency (JAXA). ALOS has been launched by JAXA on January 24, 2006. With a total weight of 4000 kg, ALOS has an orbital revisit period of 46

days [44]. It is powered with a 7 kW 9-segment solar array paddle which has a dimension of 3 m by 22 m [44].

The mission of ALOS is to contribute to cartography, disaster monitoring and earth resource survey as well as to advance land-observing technology [28]. For disaster monitoring the repeat cycle is the most crucial parameter of a satellite system. The ALOS has a mean repeat cycle of 24 hours and for the worst case its repeat cycle becomes 48 hours [28].

The ALOS is equipped with three sensors. Panchromatic remote sensing instruments for stereo mapping (PRISM) and advanced visible and nearinfrared radiometer type 2 (AVNIR-2) are two optical sensors on ALOS. The third sensor is phased array type L-band synthetic aperture radar (PALSAR) which is an improved version of JERS-1's synthetic aperture radar [28]. In this study, the data provided by the PALSAR sensor of ALOS is used.

The PALSAR's antenna has 4 segments and has 80 T/R modules on them. The size of PALSAR's antenna is 3.1 m by 8.9 m. With this relatively small size, the Doppler bandwidth and the orbit altitude of 691 km, the pulse repetition frequency varies between 1500 Hz and 2500 Hz along the orbit of the ALOS [44]. PALSAR is capable of generating electromagnetic waves with a scattering angle of 8 to 60 degrees from the earth's surface [28]. PALSAR is a fully polarimetric instrument which can operate in fine beam mode with single polarization (HH or VV), dual polarization (HH+HV or VV+VH) or quad polarimetry (HH+HV+VH+VV) [44]. PALSAR can also operate in wide-swath ScanSAR mode with single polarization (HH or VV) [44]. The center frequency of PALSAR is 1270 MHz (23.6 cm). The bandwidth for the single polarization mode of the PALSAR is 28 MHz whereas the bandwidths for dual polarization, quad polarization and ScanSAR modes are 14 MHz [44]. With these parameters, the range and azimuth resolutions at 41.5 degrees are approximately for single polarization 9 m by 10 m, for dual polarization 19 m by 10 m, for quad polarization 30 m by 10 m and for ScanSAR mode 71 m by 157 m [44]. Additional information about the ALOS satellite can be seen in [28] and [44].

6.2 Oil Spill Monitoring using SAR Imagery

SAR imagery is widely used for monitoring the ocean environment. The SEASAT satellite which was launched by USA in 1978 was the first satellite used to monitor the ocean environment and it was the first civilian SAR satellite. After that satellites ERS-1, ERS-2, RADARSAT-1, RADARSAT-2, ENVISAT and ALOS were placed on their orbits for monitoring both the ocean and land surface.

Measurements of sea ice, ocean surface waves and spectra, wave refraction and breaking, upwelling, ocean currents and current gradients, oceanic internal waves and solitons, wind speed and direction, marine atmospheric boundary layers, underwater topography and detection of ships and wakes are just a few examples to mention where SAR imaging is used [32]. SAR imagery is also used to detect oils and surfactants [32].

Oil on the ocean surface can result from seepage from seabottom, can be released from ships or can be spilled from offshore platforms after catastrophic collapses, fires or even under normal operating conditions. Short gravity-capillary waves on the ocean surface are the most responsible components of the ocean wave spectra for the radar backscatter where Bragg scattering is the dominant mechanism [32]. Since mineral oil on the ocean surface damps these gravity-capillary waves, radar backscatter is reduced and therefore oil appears as dark patches in the SAR imagery of the ocean [32]. Unfortunately dark patches on the ocean surface are not only due to mineral oil so that unambiguous identification of the oil becomes extremely hard. Turbulent ship wakes, rain impinging on the ocean surface, grease or ice floating on the ocean surface, wind speed reduction in the wind shadow provided by islands or mountains and ocean temperature differences can cause dark patches in the imagery by reducing the backscatter which is described by Bragg scattering [32]. These processes can lead to false identification of oil patches on the ocean surface. Some algorithms are developed to minimize the risk of false identification such as given in [20] and [21].

In terms of hydrodynamics, oil spill on the ocean surface can be treated as a two layer flow. In order to model oil spill on the ocean surface, realistic ocean wave models such as given in [6] can be extended for two layer flow including the capillary effects which

are characterized by surface tension and curvature of the ocean surface [35]. Using these extended models, scattering of electromagnetic waves from the ocean surface can be modeled by the methods described in [5]. Some similar studies can be seen in [32] where generally approximate ocean models are used. While these studies can provide a better understanding of the physics which governs the scattering of microwaves from the ocean surface they may not be the best way to understand the larger dynamics of oil spill on the ocean surface.

A summary of the existing oil spill detection techniques is given in [13] where they are classified under two categories, manual and automatic inspection. In manual inspection, operator goes over the whole image to determine the dark spots which is a time consuming and open to human errors process [13]. In contrast, the automatic oil spill detection algorithms consists of dark spot detection, feature extraction and classification steps [13].

In section 6.2.2 change detection method and algorithms discussed in chapter 5 are utilized. The focus is on the Gulf of Mexico oil spill which happened in 2010, April 20. Utilizing the change detection techniques given in chapter 5 an assessment of the oil spill and a verification of the change detection techniques using the SAR imagery provided by PALSAR sensor of the ALOS satellite is provided.

6.2.1 2010 Gulf of Mexico Oil Spill

The 2010 Gulf of Mexico oil spill, also referred to as the Deepwater Horizon oil spill, the BP oil spill and the Macondo blowout is an oil spill in the Gulf of Mexico on the coordinates (28.737 N, 88.387 W) which flowed for three months in 2010 between the April, 20th and the July, 15th [2]. It is the largest accidental marine oil spill in the history of the petroleum industry [2]. The spill started with the explosion of the Deepwater Horizon oil rig. The explosion killed 11 workers on the platform and injured 17 others [2]. An estimated 8400 m^3 per day was escaping from the well with a decaying rate. Until the capping of the wellhead on 15 July 2010 an estimated total of 780000 m^3 of crude oil was released to the environment [2].

In the beginning of the spill, oil was spread southerly due to winds [2]. By the April 25th, the oil spill covered 1500 km^2 and was as close as 50 km from the Chandeleur Islands, the

habitat for many species [2]. 5 days later the area over which oil had spread had increased to 10000 km^2 [2]. An image of the early stage of the 2010 Gulf of Mexico oil spill taken on May 2nd by ENVISAT satellite can be seen in the Figure (102) below.

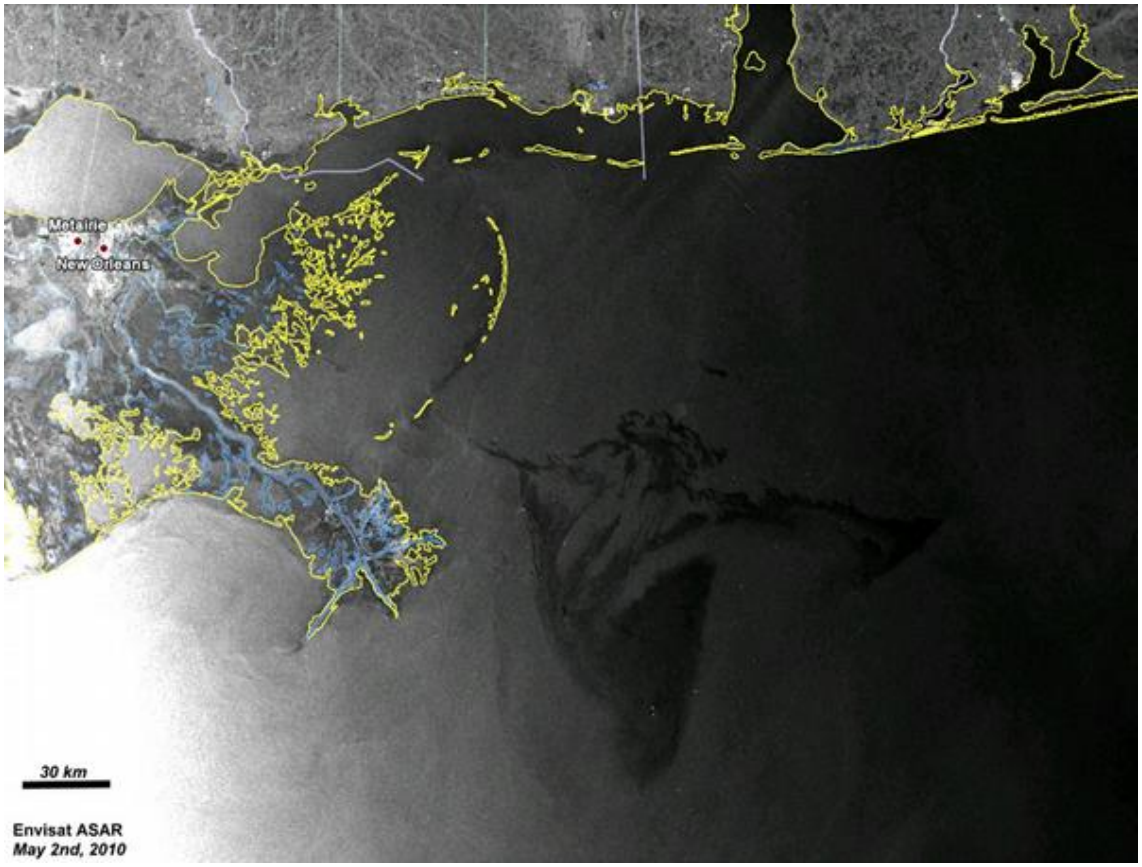

Figure 102: 2010 Gulf of Mexico Oil Spill obtained by ENVISAT on May 2nd.

On May 19th, the National Oceanic and Atmospheric Administration (NOAA) tracking the spill using the ENVISAT data announced that oil had reached the loop current, which is a clockwise current in the Gulf of Mexico flowing towards Florida and then joins the Gulf Stream along the east coast of U.S. [2]. On June 29th, the NOAA decided that the oil slick could no longer reach to the loop current and stopped tracking offshore oil predictions inside the loop current area [2].

The 2010 Gulf of Mexico oil spill caused extensive damage to marine life and to the tourism and fishing industries of the area [2]. Many marine animals died or were disabled or mutated due to spill. The tourism and fishing industries suffered losses as high as several

billions of dollars [2]. In late November 2010 the amount of Louisiana shoreline affected by oil was 510 km and the total area over which oil was spread was as high as 180000 km^2 despite efforts to stop spreading of the spill and forcing it to mix with water by using chemical dispersing agents [2].

It is crucially important to track such an oil spill in order to identify the effected areas and take some precautions to save the areas under threat in a similar future event. The primary way of achieving a global assessment of this kind of big impact disasters is using the satellite data. In section 6.2.2, utilizing the change detection methods discussed in the chapter 5, an example of applying SAR CD methods to the 2010 Gulf of Mexico oil spill imagery is provided.

6.2.2 2010 Gulf of Mexico Oil Spill Assessment Using CD Methods

The oil spill images used in this study are obtained in three different regions in the Gulf of Mexico oil spill area. The locations of the acquired imagery and the location of the 2010

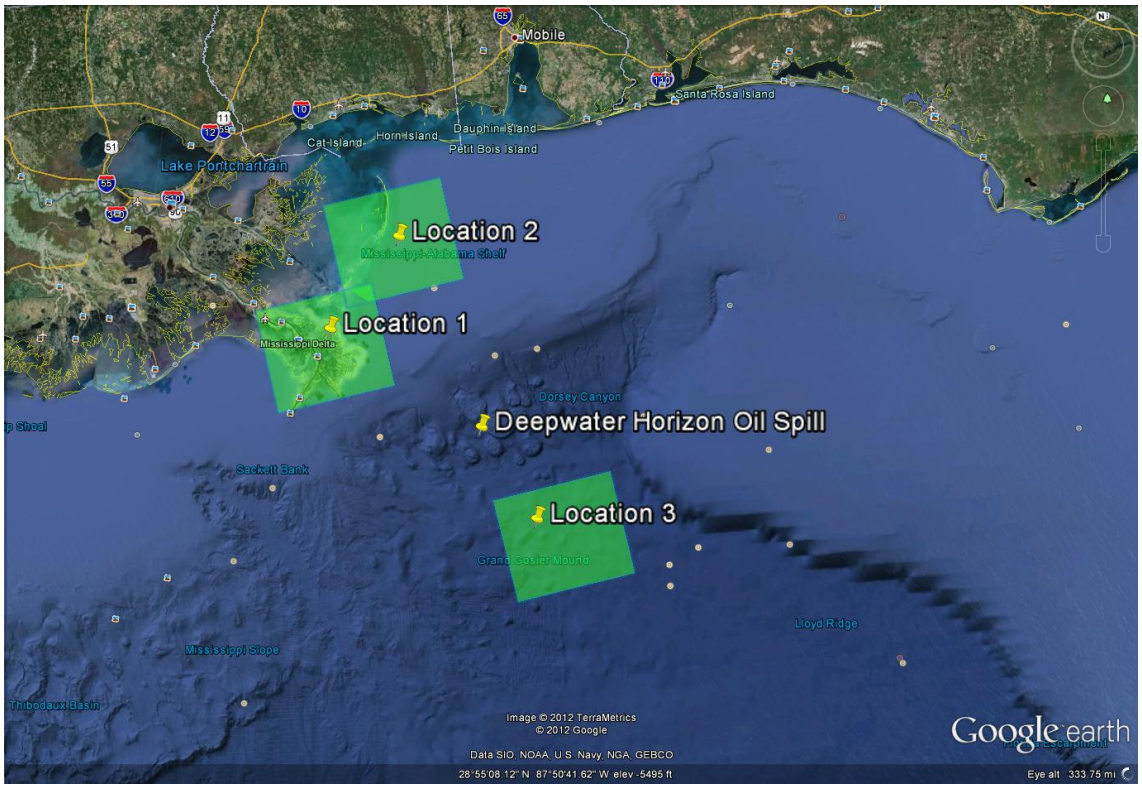

Figure 103: Locations of satellite data for Gulf of Mexico Oil Spill.

Gulf of Mexico oil spill can be seen in the Figure (103) above.

Table 1: Satellite Imagery for the 2010 Gulf of Mexico Oil Spill

	Scene ID	Acquisition Date	Path No.	Frame	Polarization
LOCATION 1	ALPSRP229470570	05/16/2010	164	570	HH+HV or VV+VH
	ALPSRP236180570	07/01/2010	164	570	HH+HV or VV+VH
	ALPSRP242890570	08/16/2010	164	570	HH+HV or VV+VH
LOCATION 2	ALPSRP193440580	09/11/2009	163	580	HH+HV or VV+VH
	ALPSRP200150580	10/27/2009	163	580	HH+HV or VV+VH
	ALPSRP240410580	07/30/2010	163	580	HH+HV or VV+VH
LOCATION 3	ALPSRP231220550	05/28/2010	162	550	HH+HV or VV+VH
	ALPSRP237930550	07/13/2010	162	550	HH+HV or VV+VH
	ALPSRP244640550	08/28/2010	162	550	HH+HV or VV+VH

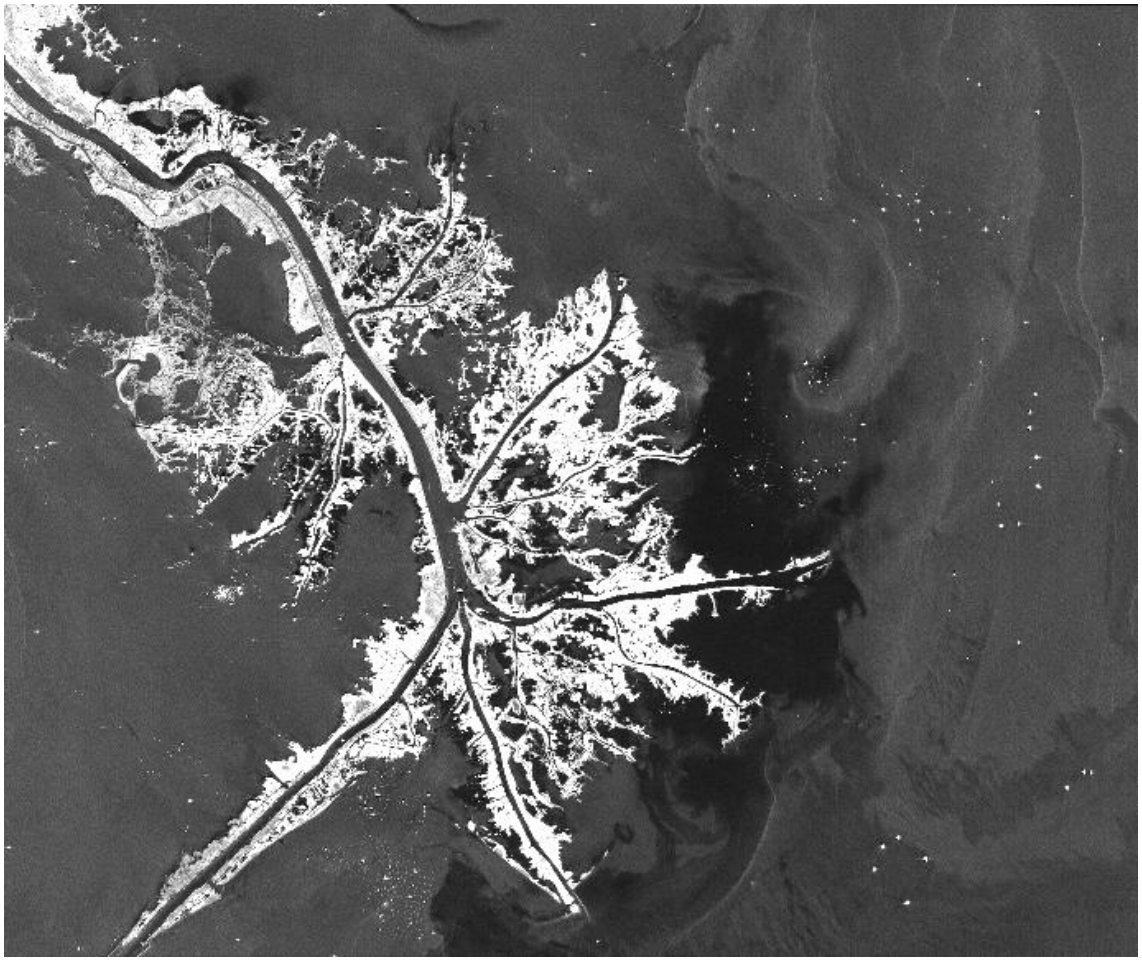

Figure 104: Image ALPSRP229470570-Acquisition Date 05/16/2010.

At each location three different images acquired at different times, thus a total of nine images, are analyzed in this section. The specific names, acquisition dates, path and frame numbers and polarizations of these images are tabulated in the Table (1) above. The co-registered images acquired at location 1 can be seen in the Figures (104), (105) and (106) above and below

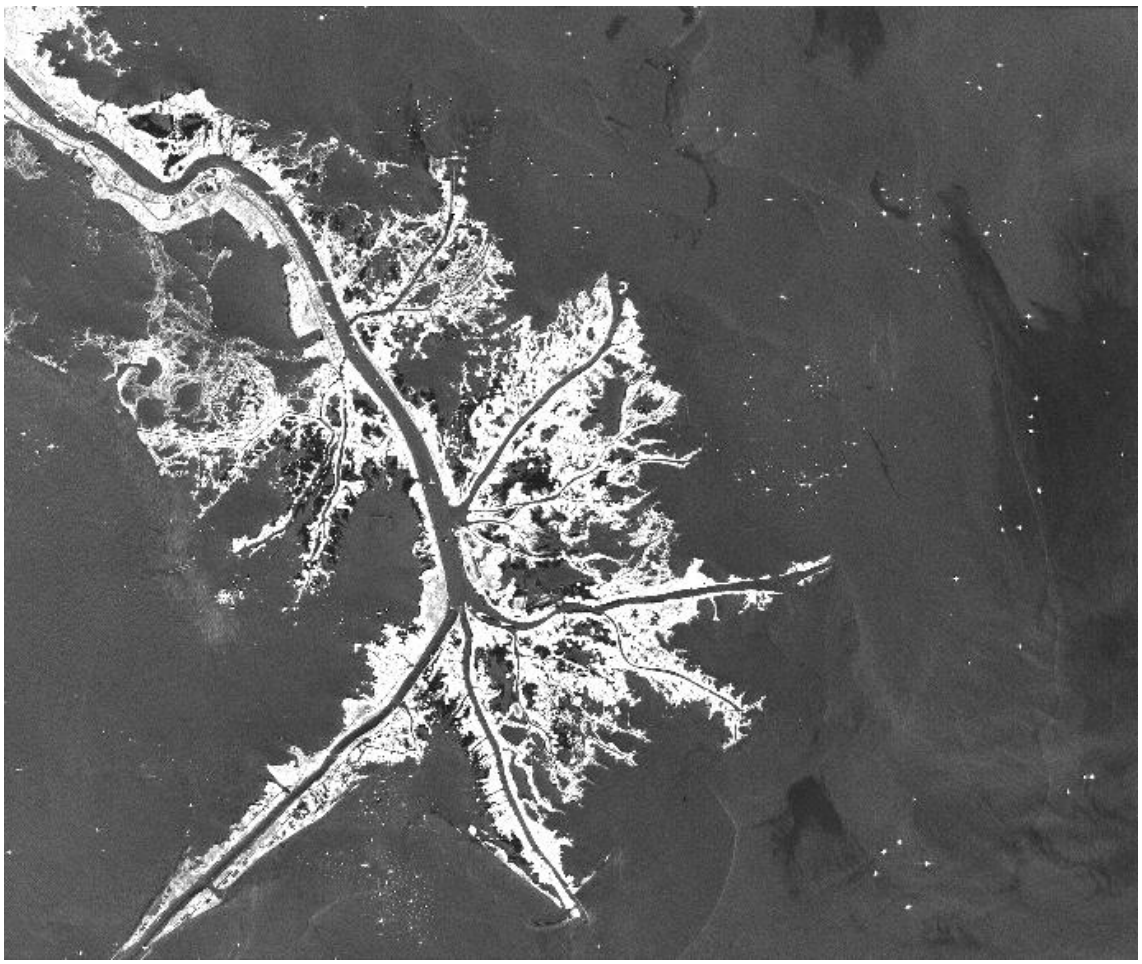

Figure 105: Image ALPSRP236180570-Acquisition Date 07/01/2010.

The oil spill in the vicinity of the peninsula is visible to naked eye as can be seen in the figures. In Figure (107) the histograms of the image pixel values of the imagery acquired at location 1 are presented. It can be seen on the histograms that while the image pixel values follow a normal distribution, the dark patches due to oil spill introduces a spike in the histograms especially in the first histogram. Also due to very high image pixel values on

the peninsula resulting from high reflectivity of the land compared to sea, the histograms show another spike at the high intensities.

Figure 106: Image ALPSRP242890570-Acquisition Date 08/16/2010.

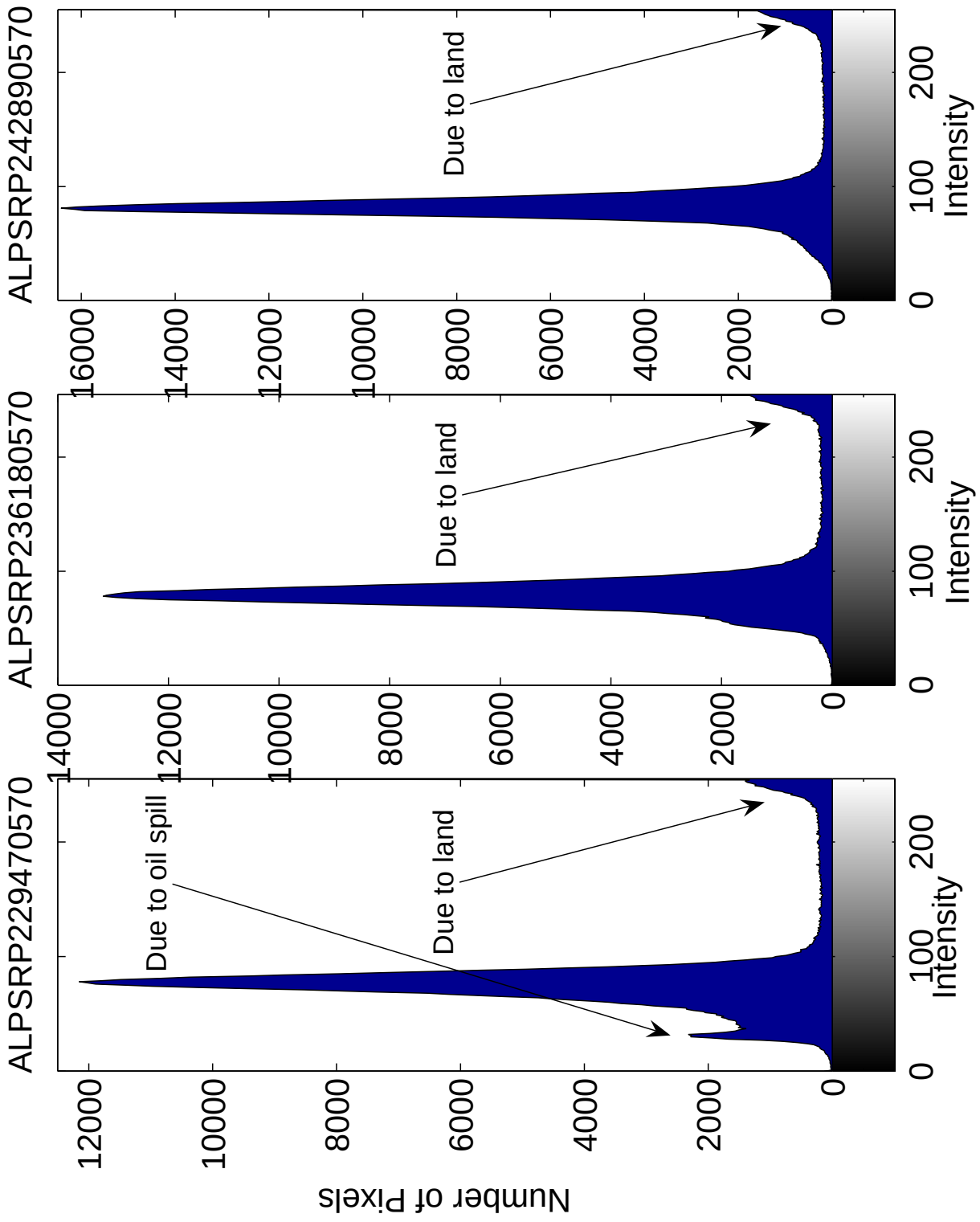

Figure 107: Histograms of oil spill imagery collected on location 1.

For the correlation coefficient change statistics algorithm, the selection of representative changed and unchanged areas lead to $\gamma_{changed} \approx 0.45$ and $\gamma_{unchanged} = 0.92$, respectively. This result confirms that in terms of the correlation coefficient change statistic, the correlation between images are very high even in the totally changed regions therefore the change detection becomes harder. Additionally the correlation coefficient change statistic is more sensitive to the changes in the bright pixel areas than to the changes in the dark pixel areas. Therefore when the oil spill is in the vicinity of land, correlation coefficient change statistics behaves poorly. For a threshold of $T = 0.6$, the change maps can be obtained with the probabilites of $P_d \approx 0.90$ and $P_{fa} \approx 0.35$. Although having this high value of probability of false alarm which is decided at the expense of having a high probability of detection to capture the oil spill changes in the vicinity of the peninsula, the correlation coefficient change statistic algorithm behaves poorly in detecting the changes due to oil spill as it can be seen in the Figures (108) and (109) below.

For the intensity ratio change statistics algorithm, the selection of representative changed and unchanged areas lead to $R_0 \approx 0$ dB and $R_1 \approx 5.05$ dB. With a threshold of $T = 0.5$, the change maps can be obtained with the probabilites of $P_d \approx 0.95$ and $P_{fa} \approx 0.01$ which can be read from the ROC curves presented in chapter 5. The intensity ratio change statistic performs excellent for detecting the oil spill changes which causes the pixels to appear dark, even in the vicinity of the peninsula which has a bright appearance. This is mainly because the intensity ratio measure is more sensitive to the changes in the dark pixels compared to the changes in the bright pixels. The resulting change maps can be seen in the Figures (108) and (109) below.

Figure 108: Change maps of oil spill imagery collected on location 1.

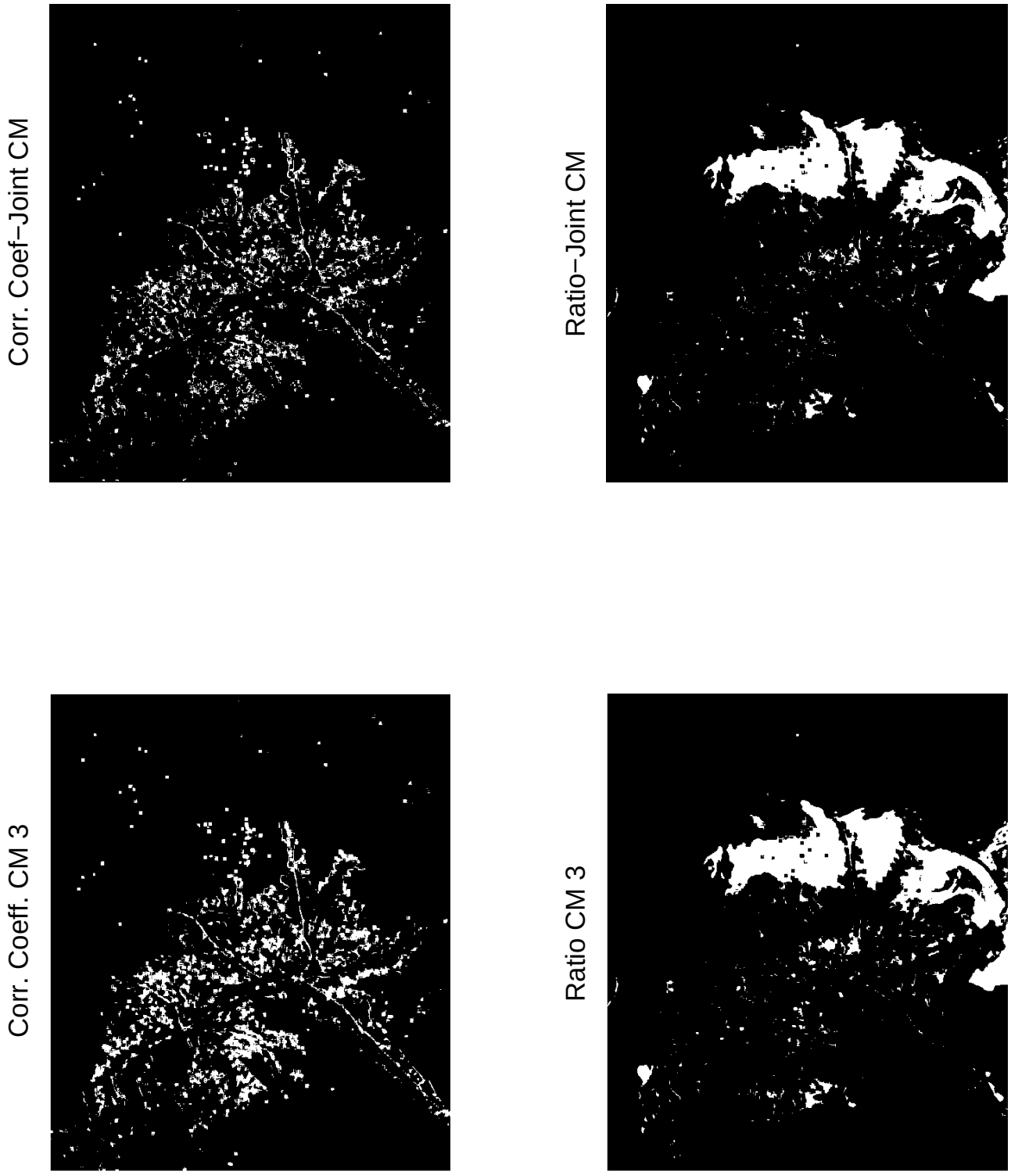

Figure 109: Final change maps of oil spill imagery collected on location 1.

Additionally as it can be seen in the Figures (108) and (109) above, two final change map method proposed can be used as a double-check mechanism and can reduce the probability of false alarm. This method works well both for the correlation coefficient change statistic and the intensity ratio change statistic algorithms. The probabilities of false alarm and detection of the joint change map can be calculated as $P_{fa} \approx 0.35^2 = 0.12$ and $P_d \approx 0.90^2 = 0.81$ for the correlation coefficient change statistic. For the intensity ratio change statistic these probabilities for the joint change map can be calculated as $P_{fa} \approx 0.01^2 = 0.0001$ and $P_d \approx 0.95^2 = 0.90$. Although the joint change maps obtained causes a small amount of reduction in P_d it can be very beneficial for reducing the P_{fa} significantly. When higher values of P_d is used in obtaining the two change maps, the joint change map will suffer less from the loss of P_d, almost to an insignificant level.

The co-registered images acquired at location 2, which shows the Chandeleur Islands, can be seen in the Figures (110), (111) and (112) below

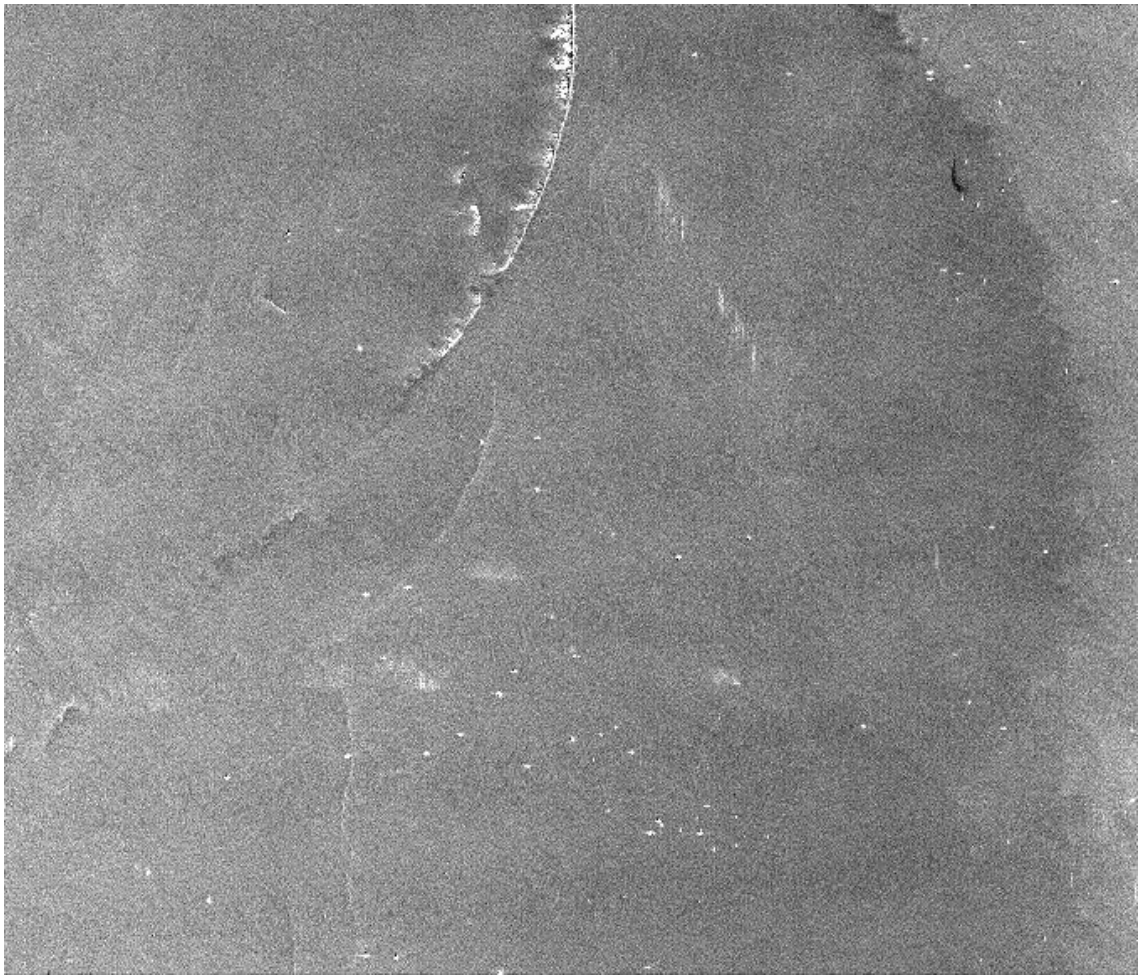

Figure 110: Image ALPSRP193440580-Acquisition Date 09/11/2009.

In the Figure (113) the histograms of the image pixel values of the imagery acquired at location 2 are presented. It can be seen on the histograms that the image pixel values follow a normal distribution due to lack of large dark areas (due to oil spill) or large bright areas (due to land).

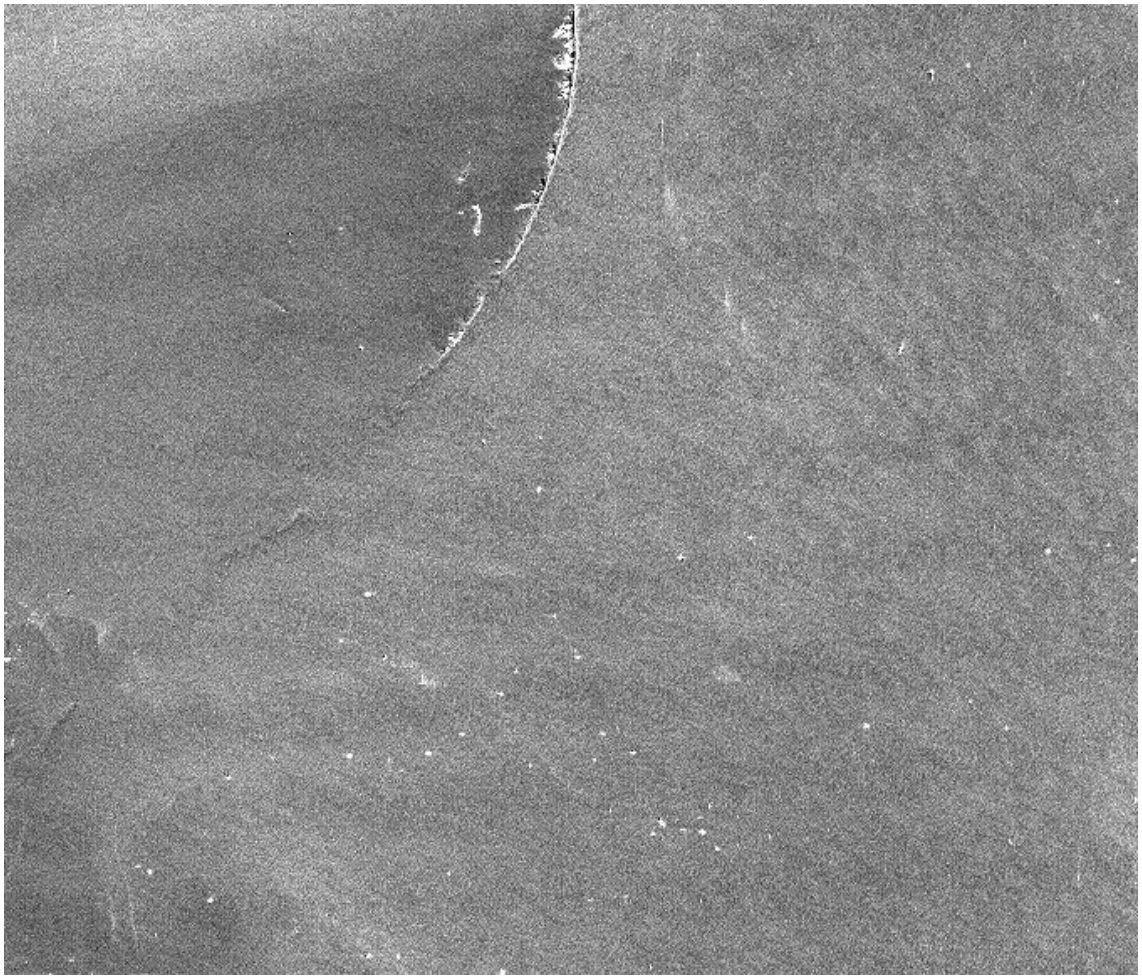

Figure 111: Image ALPSRP200150580-Acquisition Date 10/27/2009.

Figure 112: Image ALPSRP240410580-Acquisition Date 07/30/2010.

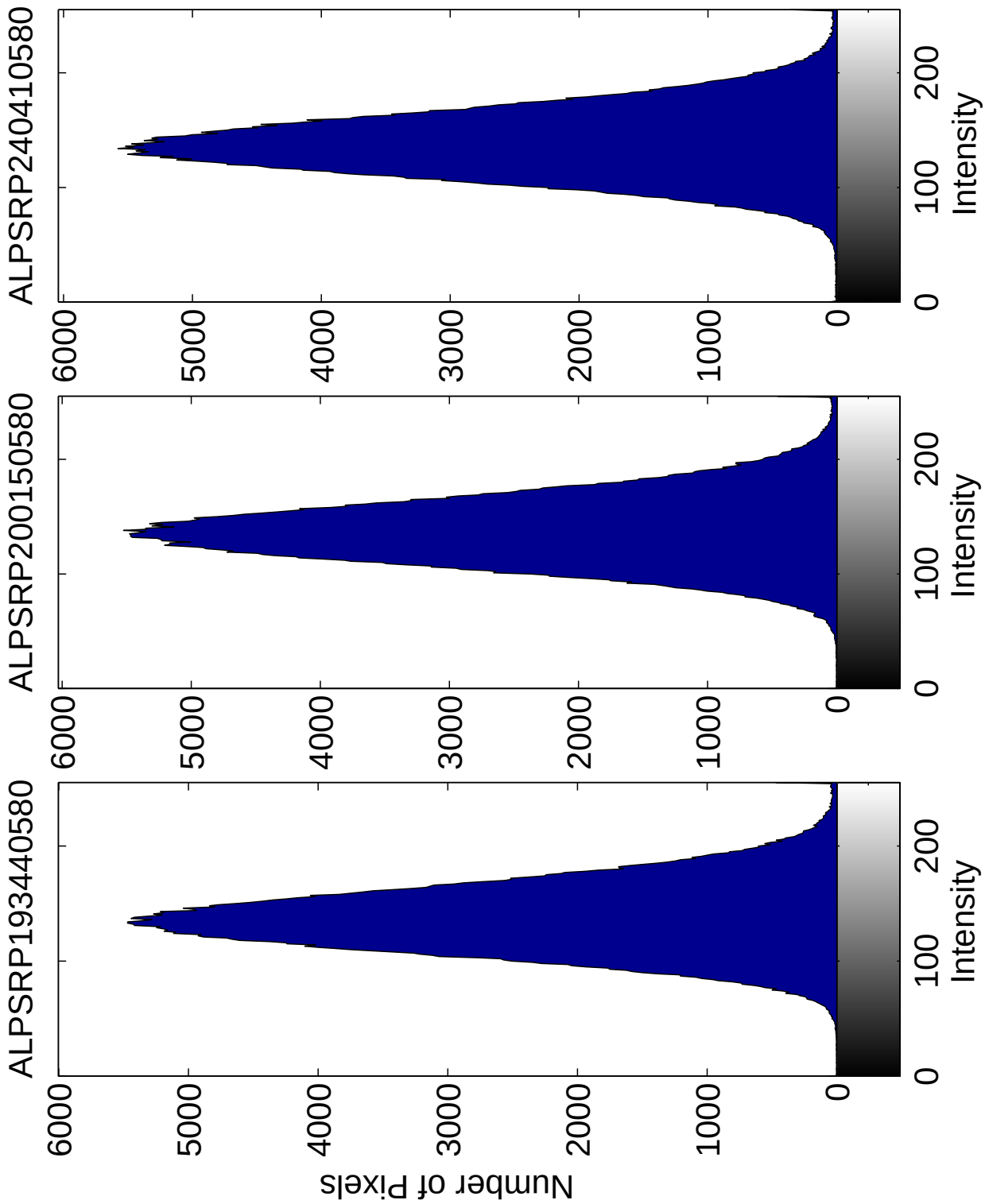

Figure 113: Histograms of oil spill imagery collected on location 2.

As it can be seen in change maps presented in the Figures (114) and (115) below, the

correlation coefficient change statistics algorithm for the imagery acquired at location 2 is again more sensitive to the changes on the bright areas due to land of Chandeleur Islands. However the intensity ratio change statistic is more successful in capturing the oil spill changes which can be seen in the third image in the temporal sequence. Therefore the second and the third change maps obtained by the intensity ratio change statistics (Ratio CM 2, Ratio CM 3) can be used to decide the extent of the oil spill. Additionally it can be realized from the figures that two final change map method increases the number of change map sample therefore can effectively be used to reduce the probability of false alarm, both for correlation coefficient change statistic and intensity ratio change statistic. The probabilities of false alarm and detection of the joint change map can be calculated as $P_{fa} \approx 0.35^2 = 0.12$ and $P_d \approx 0.90^2 = 0.81$ for the correlation coefficient change statistic. For the intensity ratio change statistic these probabilities for the joint change map can be calculated as $P_{fa} \approx 0.01^2 = 0.0001$ and $P_d \approx 0.95^2 = 0.90$. Although the joint change maps obtained causes a small amount of reduction in P_d it can be very beneficial for reducing the P_{fa} significantly. When higher values of P_d is used in obtaining the two change maps, the joint change map will suffer less from the loss of P_d, almost to an insignificant level.

It is useful to mention that Chandeleur Islands is a very dynamics coastal region which is subject to hurricanes, floods, waves and therefore coastal erosion. For this reason they suffer erosion losses. Correlation coefficient change statistic can be used as a critical change measure for monitoring the coastal erosion amounts and rates.

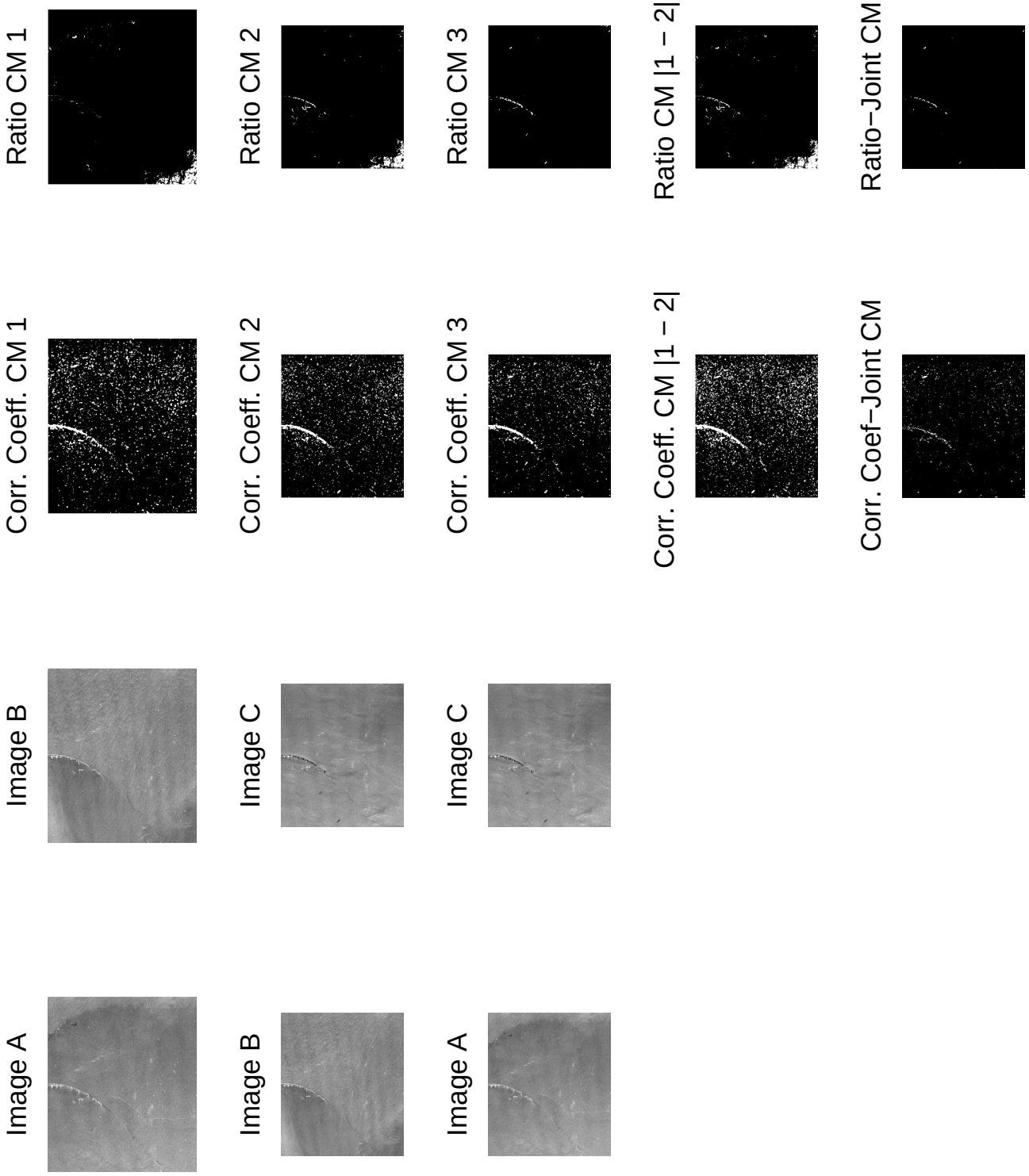

Figure 114: Change maps of oil spill imagery collected on location 2.

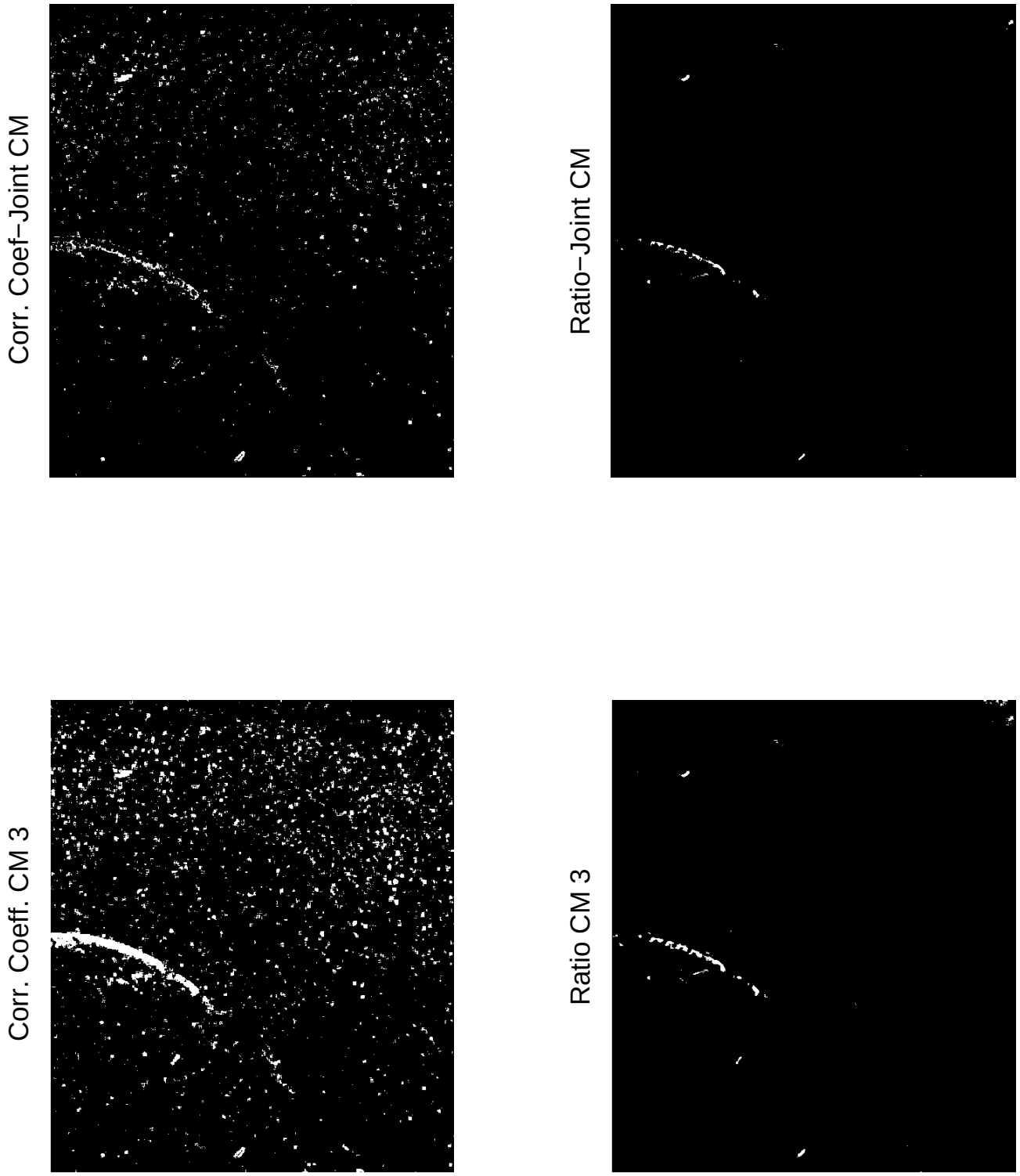

Figure 115: Final change maps of oil spill imagery collected on location 2.

The co-registered images acquired at location 3 can be seen in the Figures (116), (117) and (118) below

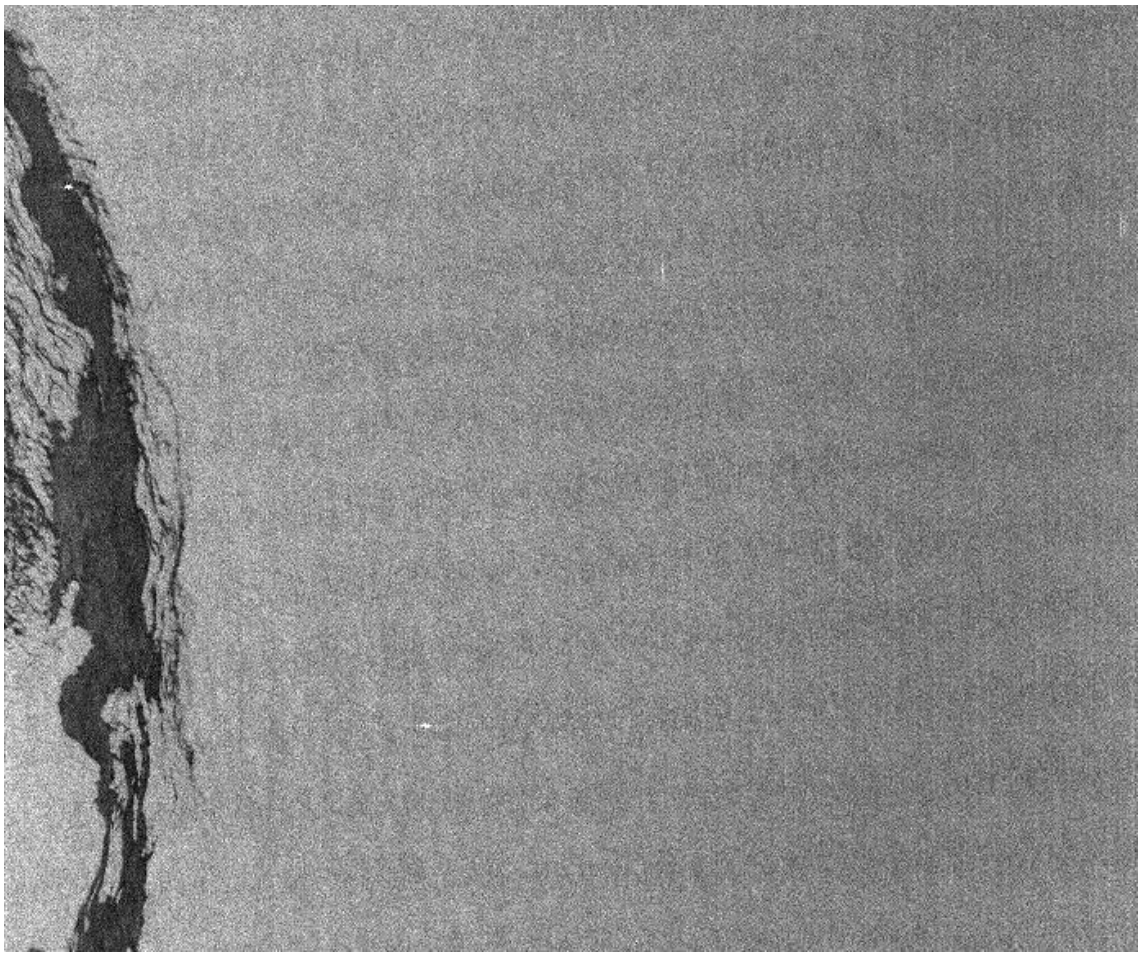

Figure 116: Image ALPSRP231220550-Acquisition Date 05/28/2010.

In the Figure (119) the histograms of the image pixel values of the imagery acquired at location 3 are presented. It can be seen on the histograms that the image pixel values follow a normal distribution, however due to a large area affected by the oil spill in the second image of the sequence, second histogram exhibits a spike around pixel value of 50.

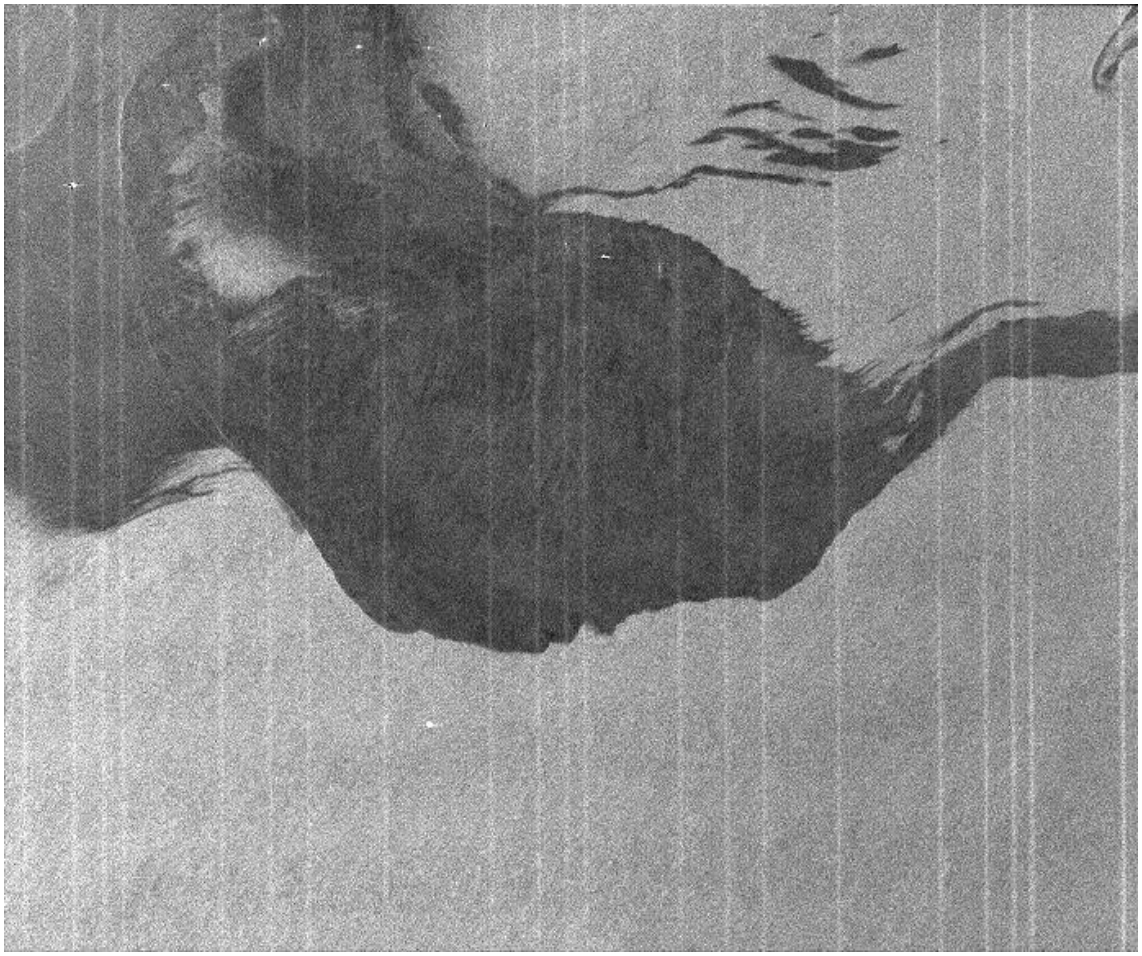

Figure 117: Image ALPSRP237930550-Acquisition Date 07/13/2010.

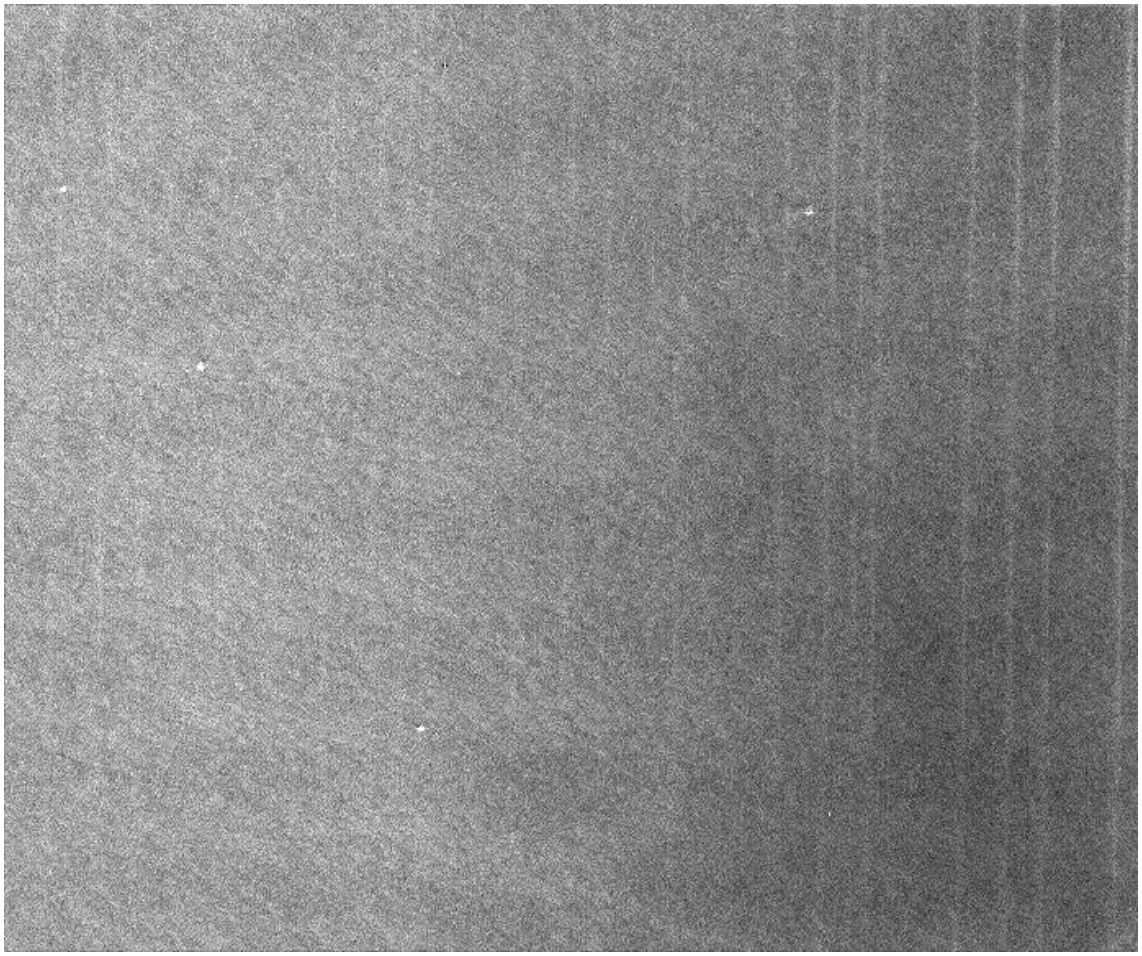

Figure 118: Image ALPSRP244640550-Acquisition Date 08/28/2010.

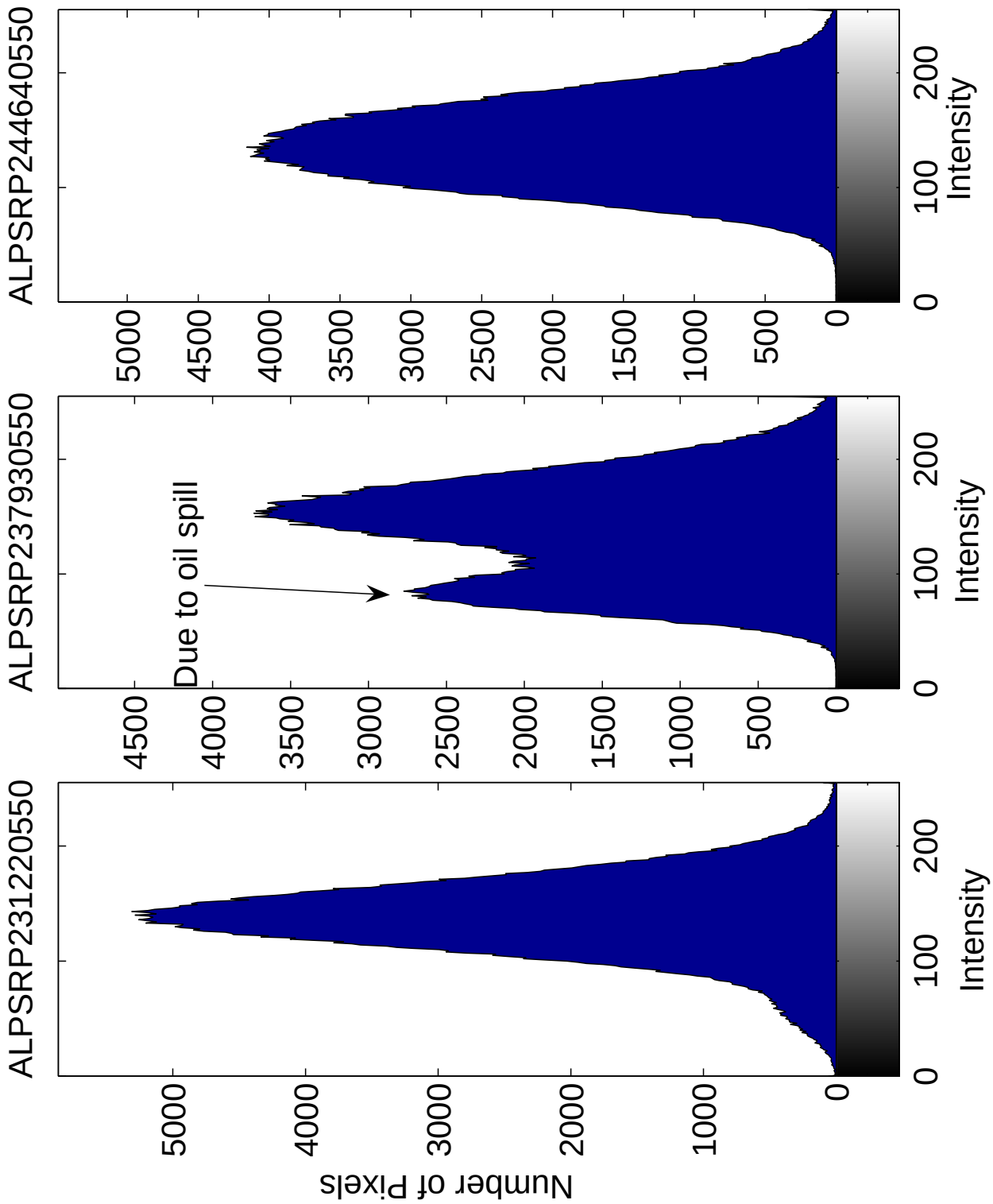

Figure 119: Histograms of oil spill imagery collected on location 3.

For the correlation coefficient change statistics algorithm on this image set, the selection of representative changed and unchanged areas lead to $\gamma_{changed} \approx 0.30$ and $\gamma_{unchanged} = 0.69$, respectively. Using a threshold of $T = 0.5$, we can obtain the change maps for $P_d \approx 0.93$ and $P_{fa} \approx 0.08$. The parameters for the intensity ratio change statistics is the same as before.

As it can be seen in change maps presented in the Figures (120) and (121) below, although the intensity ratio change statistics still performs better, the correlation coefficient change statistics is also successful in determining the extent of the contaminated areas due to the oil spill. This is mainly because there is no land in the scene so that there are only very few bright pixels. Due to this reason, the correlation coefficient change statistics performs better compared to its previous performance. Also the first image in the sequence has a denser oil surfactant compared to the second image, therefore the corresponding pixels are darker. This causes the CD methods to behave better since change measures get more different from the thresholding values.

Additionally the two final change map method helps to reduce the number of false alarms. This can be realized by comparing the change map between the first and the third images (CM 3) and the joint change map (Joint CM) obtained by intersecting the CM 3 and the additions of CM 1 and CM 2, both for the correlation coefficient and the intensity ratio change statistics. The probabilities of false alarm and detection of the joint change map can be calculated as $P_{fa} \approx 0.08^2 = 0.0064$ and $P_d \approx 0.93^2 = 0.87$ for the correlation coefficient change statistic. For the intensity ratio change statistic these probabilities for the joint change map can be calculated as $P_{fa} \approx 0.01^2 = 0.0001$ and $P_d \approx 0.95^2 = 0.90$. Although the joint change maps obtained causes a small amount of reduction in P_d it can be very beneficial for reducing the P_{fa} significantly. When higher values of P_d is used in obtaining the two change maps, the joint change map will suffer less from the loss of P_d, almost to an insignificant level.

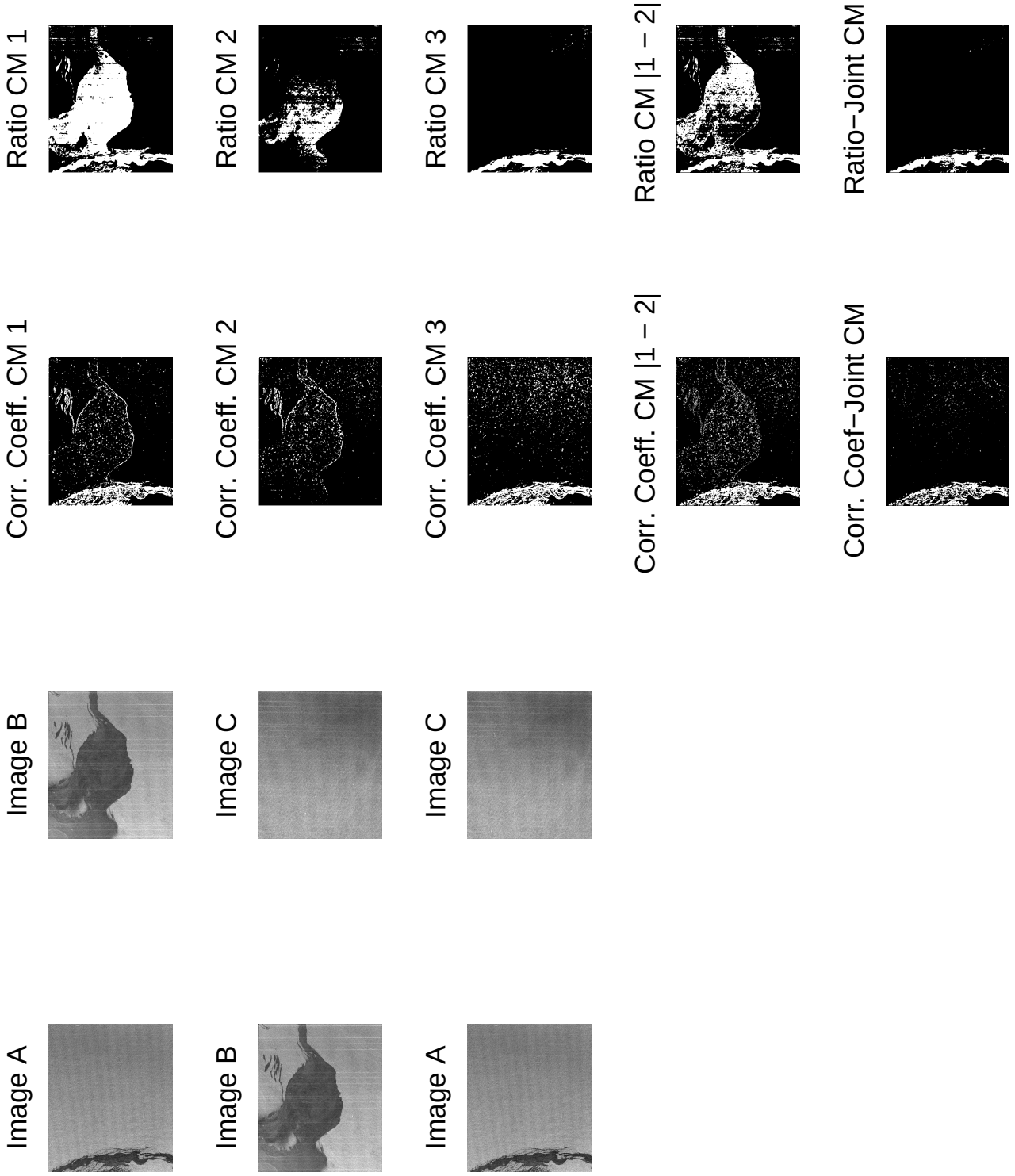

Figure 120: Change maps of oil spill imagery collected on location 3.

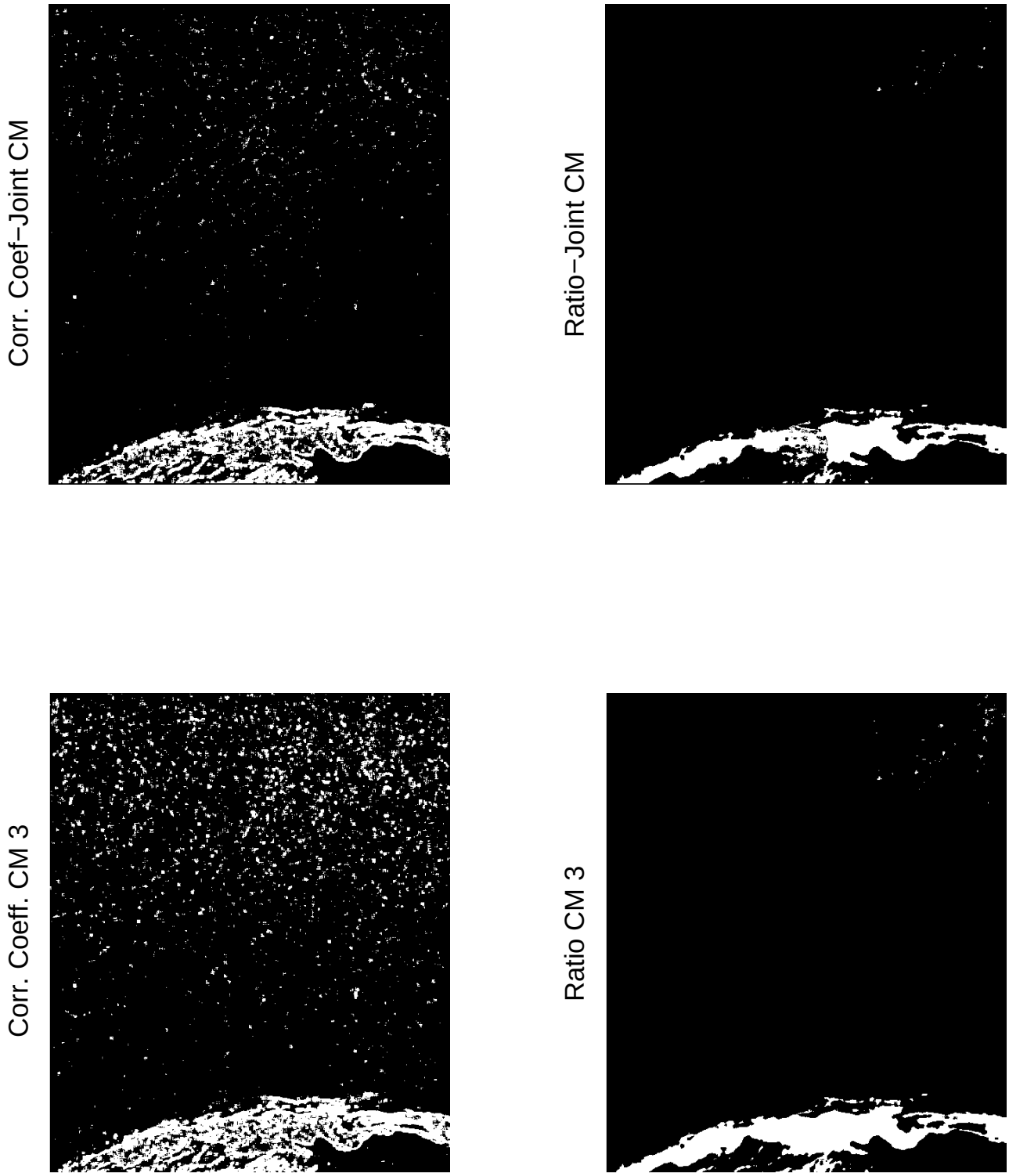

Figure 121: Final change maps of oil spill imagery collected on location 3.

6.3 Landslide Monitoring using SAR Imagery

SAR and other types of imagery are also extensively used for detection and monitoring the landslides [34]. The majority of landslide detection and monitoring is performed by differential synthetic aperture radar interferometry (InSAR) [19]. SAR image processing, image pair registration, coherence measurement, interferogram production, phase unwrapping, phase conversion to deformation and performing deformation analysis are the necessary steps for InSAR processing [19]. Currently InSAR techniques are succesfully employed to measure slowly advancing landslides with a rate of millimeters to centimeters per month [19]. A detailed review of InSAR technique and applications can be seen in [43].

InSAR technique has some drawbacks. First of all, InSAR can only measure the displacements in the slant range direction and the displacements in the along track direction can not be measured [19]. Secondly InSAR techniques require the phase information which can not be applied to the imagery providing intensity information only. Additionally resolution of the InSAR technique is limited by the spatial and temporal resolution of the imaging SAR system [19].

The approach adopted in this dissertation is to use the change detection algorithms to make an assessment of the earthquakes and earthquake triggered landslides. The specific change detection algorithms utilized are discussed in chapter 5. The primary advantage of the proposed approach is that it does not require phase imagery which may be a strict limitation when the existing SAR systems and data are considered. Change maps are generated comparing the pre- and post-earthquake imagery which can be used to determine the extent and the propagation rate of the landslide provided that the temporal and spatial resolution of the data is high enough.

In section 6.3.2 the change detection methods discussed in the chapter 5 are utilized. The focus is on the China Sichuan earthquake triggered landslides which happened on 2008, May 12. Utilizing the change detection techniques given in chapter 5, an assessment the earthquake triggered landslides and a verification of the change detection techniques using the SAR imagery provided by PALSAR sensor of the ALOS satellite was performed.

6.3.1 2008 China Sichuan Earthquake and Landslide

The 2008 China Sichuan earthquake, also known as Wenchuan earthquake hit the Sichuan province of China On May 12 with a surface wave magnitude (M_s) 8.0 and a moment magnitude (M_w) 7.9 [1]. A discussion of these magnitudes can be seen in [45]. The epicenter of the earthquake was the Wenchuan County on the west-northwest of Chengdu with location (30.986N, 103.364E) [1]. The focal depth of the earthquake was 19 km. The estimated number of fatalities and injuries are 69197 and 374176 respectively [1]. It is also felt in the nearby regions as far as 1700 km away [1]. Due to the 2008 China Sichuan earthquake 4.8 million people are left out homeless and as high as 15 million people are affected [1]. It is the 21st deadliest earthquake of all time. A detailed discussion of the 2008 China Sichuan earthquake statistics can be seen in [1] and a detailed discussion of its tectonics can be seen in [31].

Figure 122: Landslide triggered by 2008 China Sichuan earthquake-photo courtesy of Zhu Wei-Xinhua/AP.

Earthquake and strong aftershocks, some above 6 (M_w), triggered many landslides in the affected regions. One of the landslides can be seen in Figure (122).

The primary way of achieving a global assessment of this kind of large disaster is using satellite data. In section 6.3.2, utilizing the change detection methods discussed in the chapter 5, an example of applying SAR CD methods to the 2008 China Sichuan earthquake imagery is provided.

6.3.2 2008 China Sichuan Earthquake and Landslide Assessment Using CD Methods

The earthquake images used in this study are obtained in three different regions in the Sichuan province of China. The locations of the acquired imagery and the epicenter of the 2008 China Sichuan earthquake can be seen in the Figure (123) below

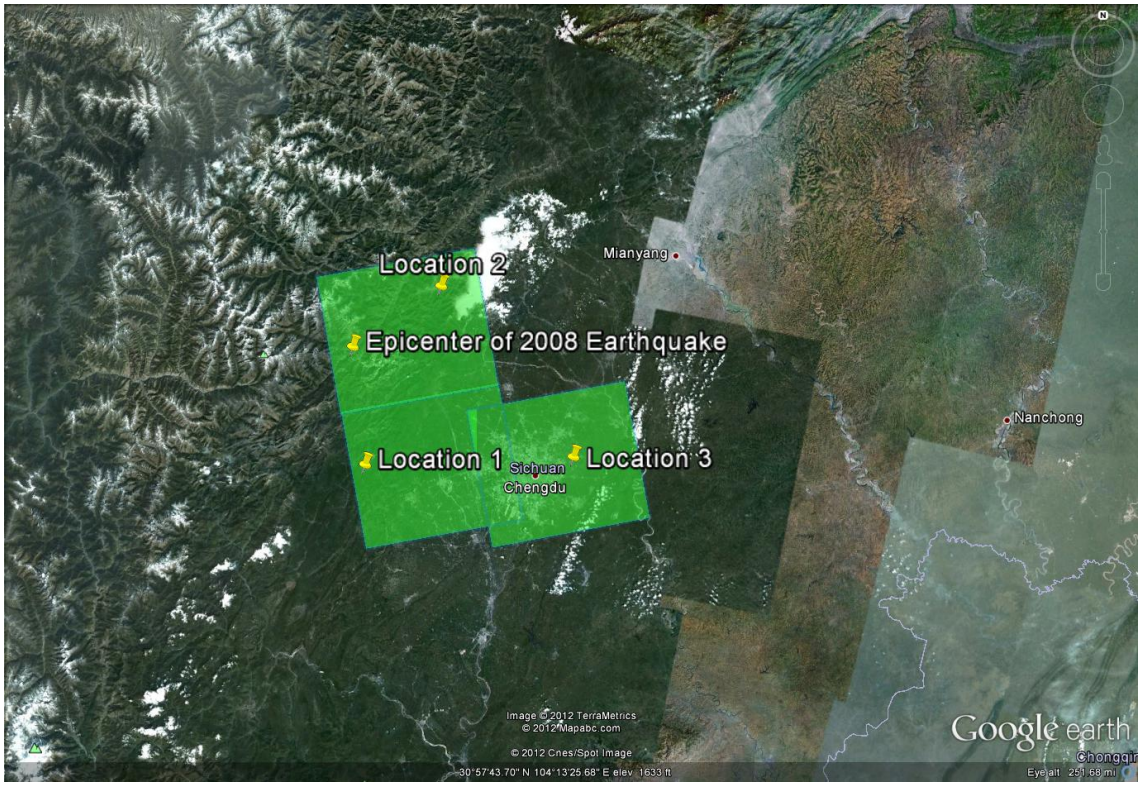

Figure 123: Locations of satellite data for China Sichuan Earthquake.

Table 2: Satellite Imagery for the 2008 China Sichuan Earthquake

	Scene ID	Acquisition Date	Path No.	Frame	Polarization
LOCATION 1	ALPSRP101610600	12/21/2007	475	600	HH or VV
	ALPSRP108320600	02/05/2008	475	600	HH or VV
	ALPSRP128450600	06/22/2008	475	600	HH or VV
LOCATION 2	ALPSRP101610610	12/21/2007	475	610	HH or VV
	ALPSRP108320610	02/05/2008	475	610	HH or VV
	ALPSRP128450610	06/22/2008	475	610	HH or VV
LOCATION 3	ALPSRP105840600	01/19/2008	474	600	HH or VV
	ALPSRP112550600	03/05/2008	474	600	HH or VV
	ALPSRP125970600	06/05/2008	474	600	HH or VV

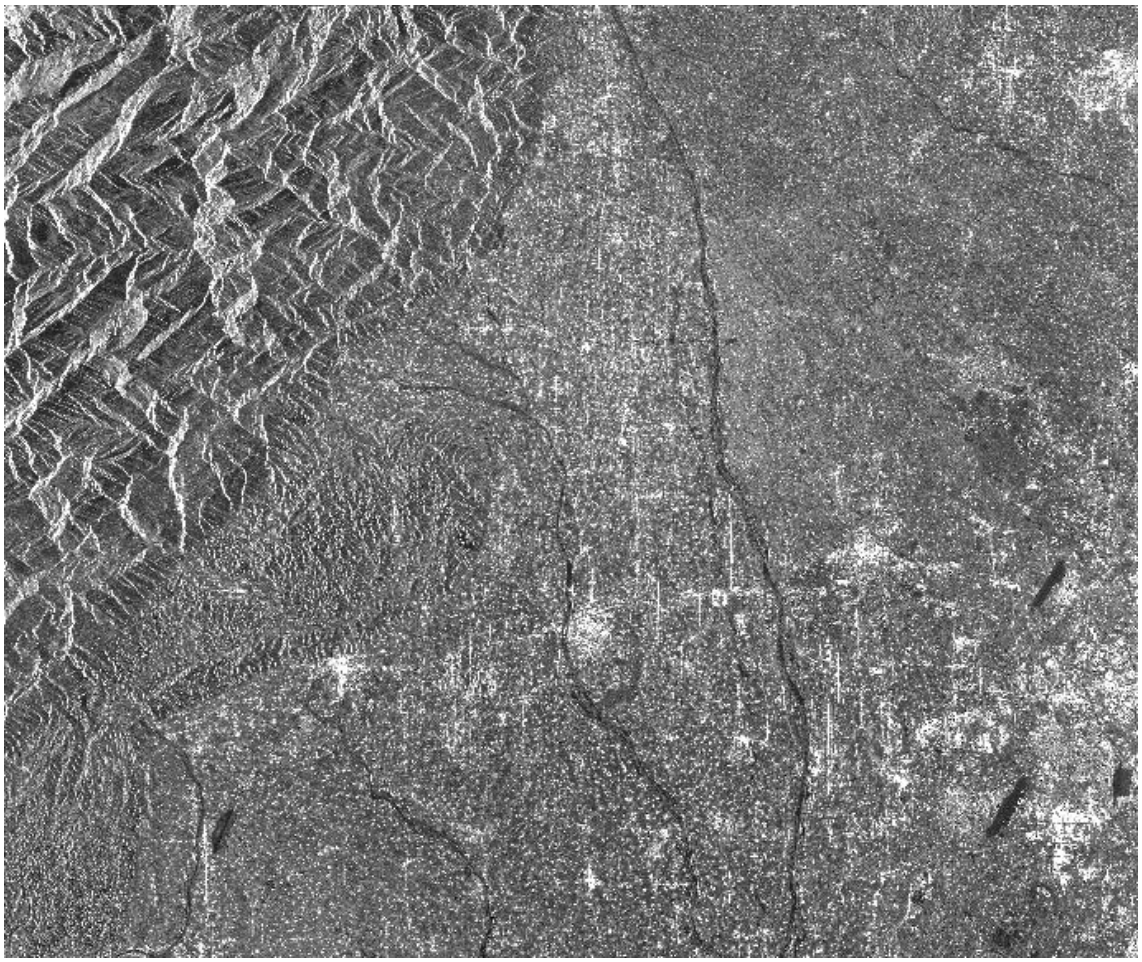

Figure 124: Image ALPSRP101610600-Acquisition Date 12/21/2007.

At each location three different images acquired at different times, thus a total of nine images, are analyzed in this section. The specific names, acquisition dates, path and frame

numbers and polarizations of these images are tabulated in the Table (2) above. The co-registered images acquired at location 1 can be seen in the Figures (124), (125) and (126) above and below

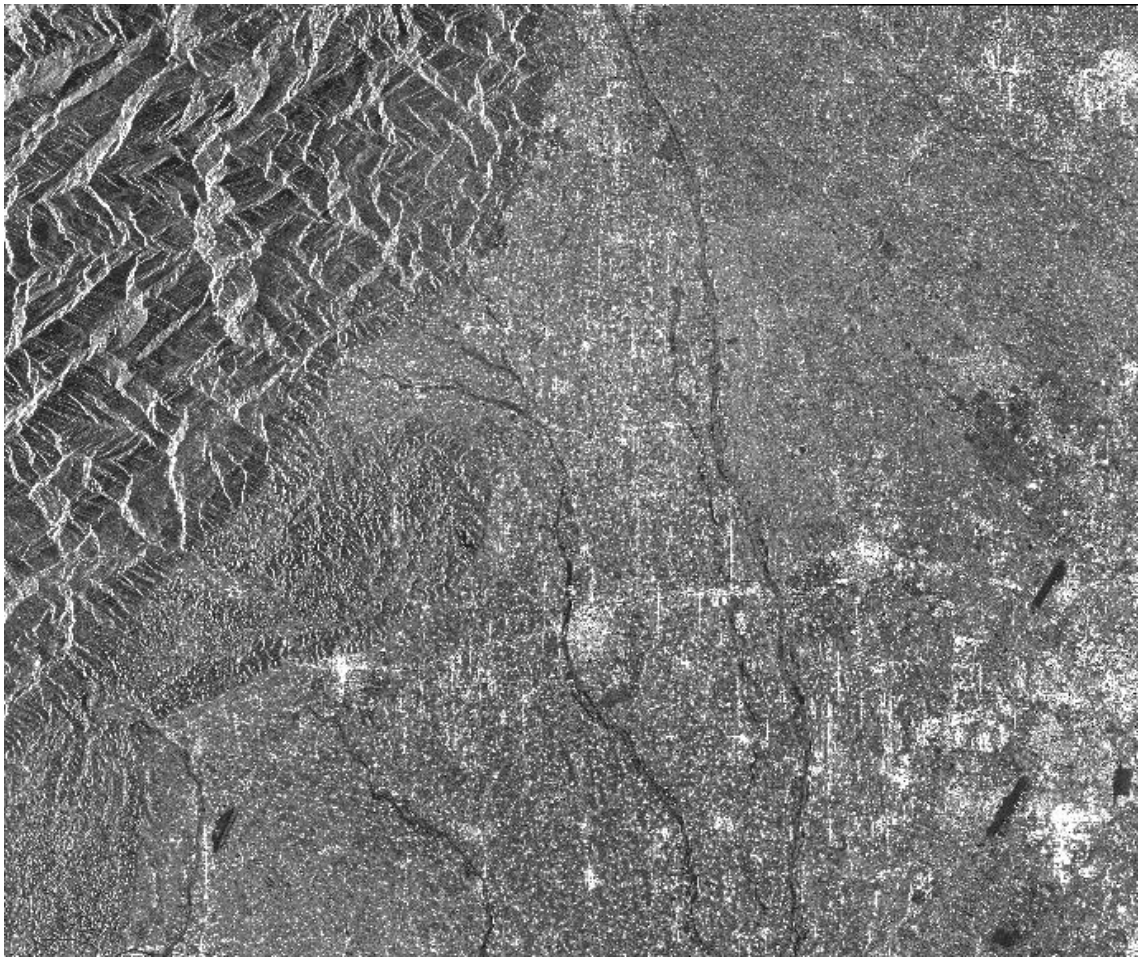

Figure 125: Image ALPSRP108320600-Acquisition Date 02/05/2008.

In the Figure (127) the histograms of the image pixel values of the imagery acquired at location 1 are presented. It can be seen on the histograms that the image pixel values follow a normal distribution, however there is a spike in the bright pixels due to the west side of mountains and residental areas in the scenes, since these areas have to higher reflectivity.

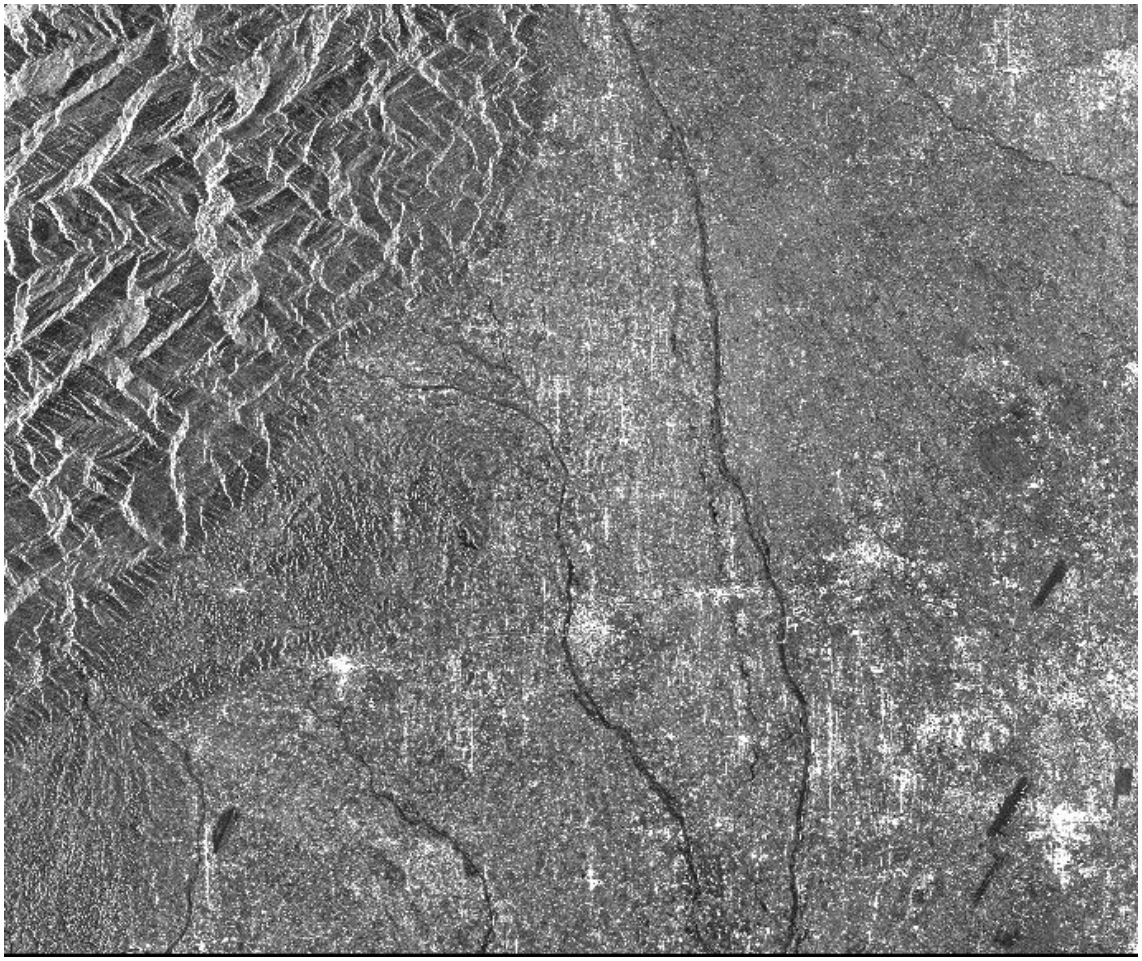

Figure 126: Image ALPSRP128450600-Acquisition Date 06/22/2008.

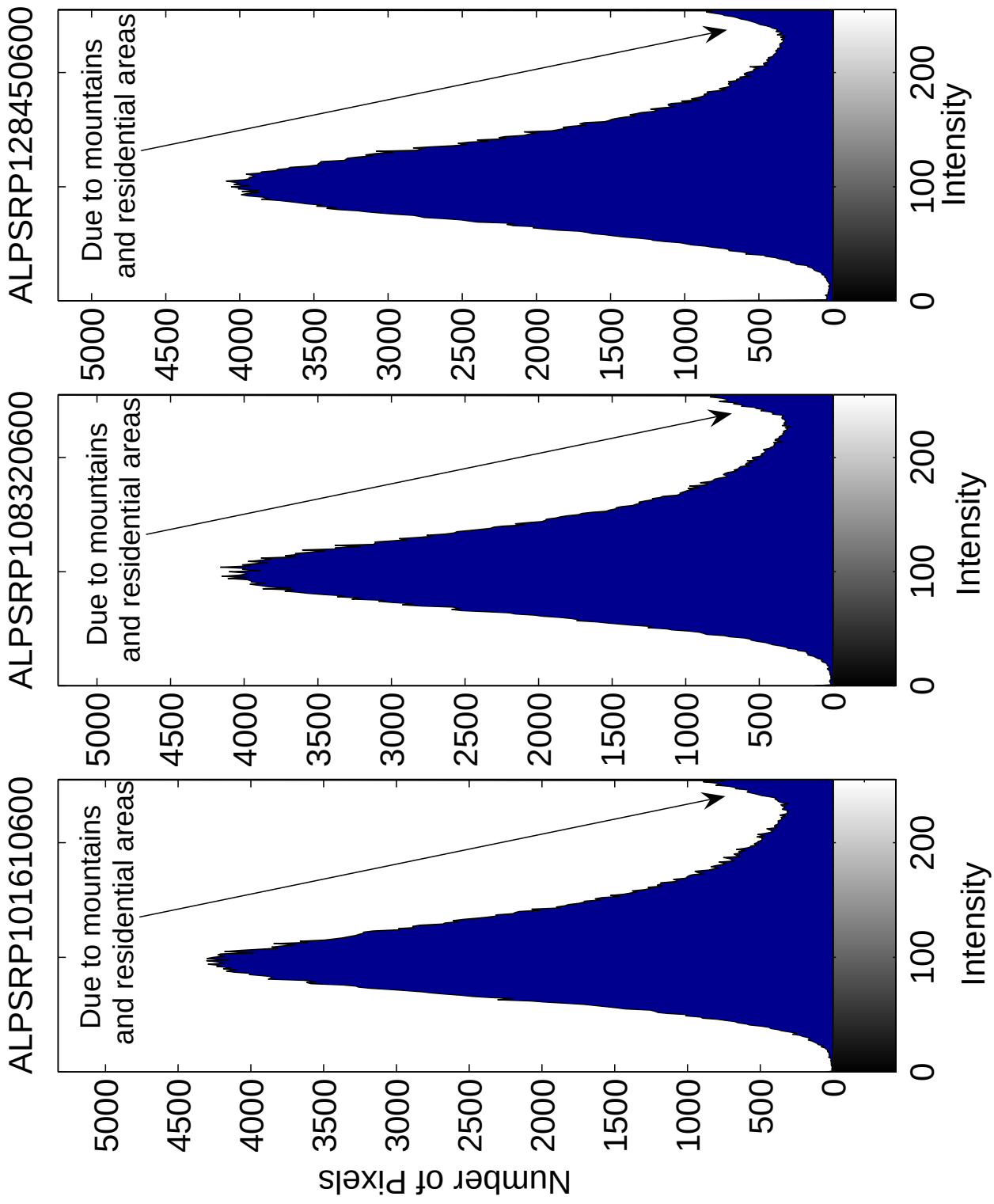

Figure 127: Histograms of earthquake imagery collected on location 1.

From applying the correlation coefficient change statistics algorithm to earthquake images, the selection of representative changed and unchanged areas lead to $\gamma_{changed} \approx 0.32$ and $\gamma_{unchanged} = 0.68$, respectively. Using a threshold of $T = 0.51$, we can obtain the change maps for $P_d \approx 0.92$ and $P_{fa} \approx 0.10$. For the intensity ratio change statistics algorithm, the selection of representative changed and unchanged areas lead to $R_0 \approx 0$ dB and $R_1 \approx 3.01$ dB. With a threshold of $T = 0.6$, the change maps can be obtained with the probabilites of $P_d \approx 0.74$ and $P_{fa} \approx 0.07$ which can be read from the ROC curves presented in the chapter 5. The resulting change maps can be seen in the Figures (128) and (129) below.

Similar to the oil spill case, the correlation coefficient change statistics is more likely to detect the changes in the areas which has brighter pixels since correlation coefficient measure is more sensitive to the changes in these areas rather than dark pixel areas such as lakes, dams, mountains. On the other hand intensity ratio change statistics is more sensitive to the changes in the areas with dark pixels due to the ratioing adopted as a measure. Therefore one can use both of the methods jointly when a reconnaissance is necessary.

Figure 128: Change maps of earthquake imagery collected on location 1.

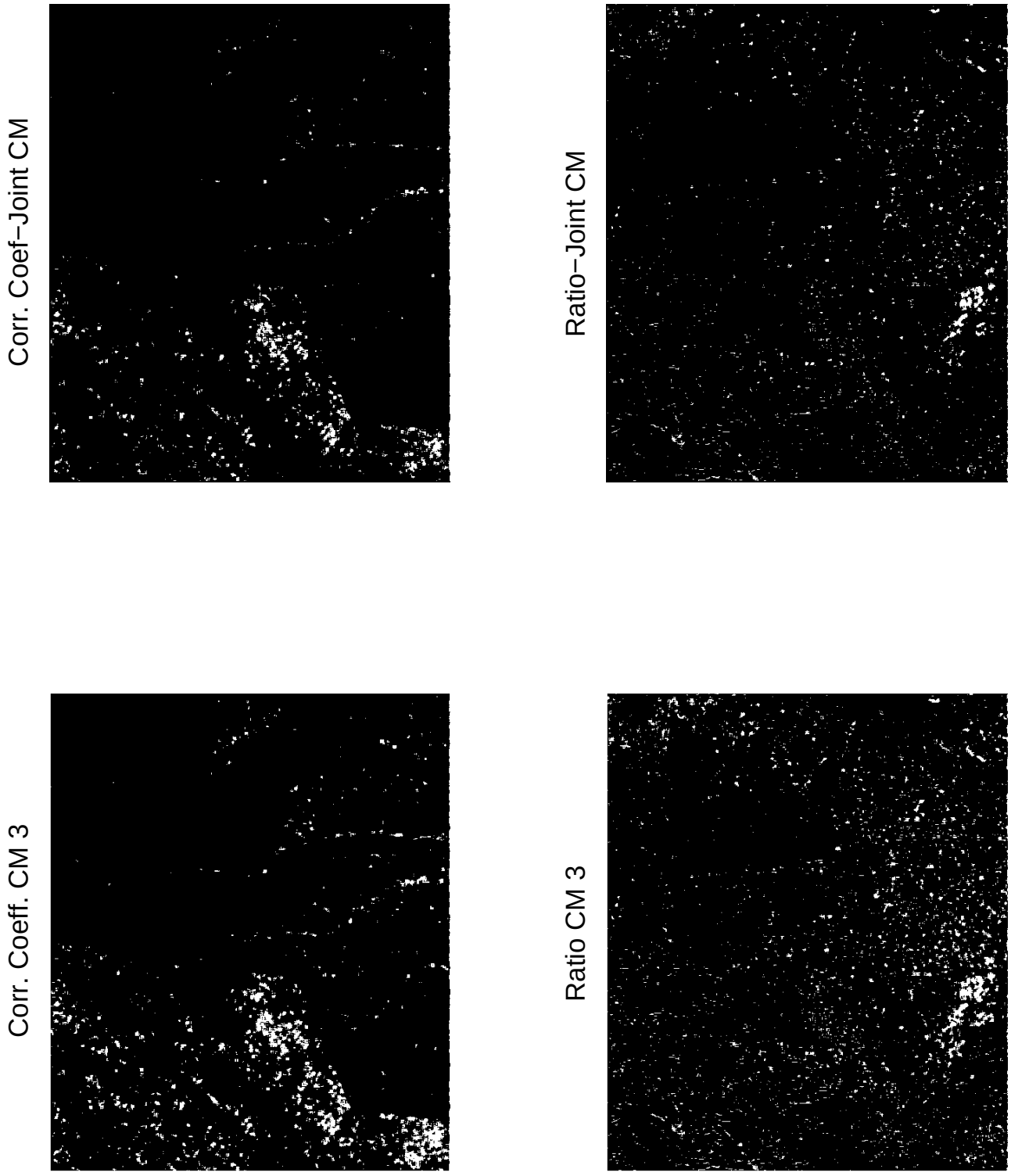

Figure 129: Final change maps of earthquake imagery collected on location 1.

Additionally as it can be seen in the Figures (128) and (129) above, two final change map method proposed can be used as a double-check mechanism and can reduce the number of false alarms significantly. This method works well both for the correlation coefficient change statistic and the intensity ratio change statistic algorithms. The probabilities of false alarm and detection of the joint change map can be calculated as $P_{fa} \approx 0.1^2 = 0.01$ and $P_d \approx 0.92^2 = 0.85$ for the correlation coefficient change statistic. For the intensity ratio change statistic these probabilities for the joint change map can be calculated as $P_{fa} \approx 0.07^2 = 0.005$ and $P_d \approx 0.74^2 = 0.55$. Although the joint change maps obtained causes a small amount of reduction in P_d it can be very beneficial for reducing the P_{fa} significantly. When higher values of P_d is used in obtaining the two change maps, the joint change map will suffer less from the loss of P_d, almost to an insignificant level.

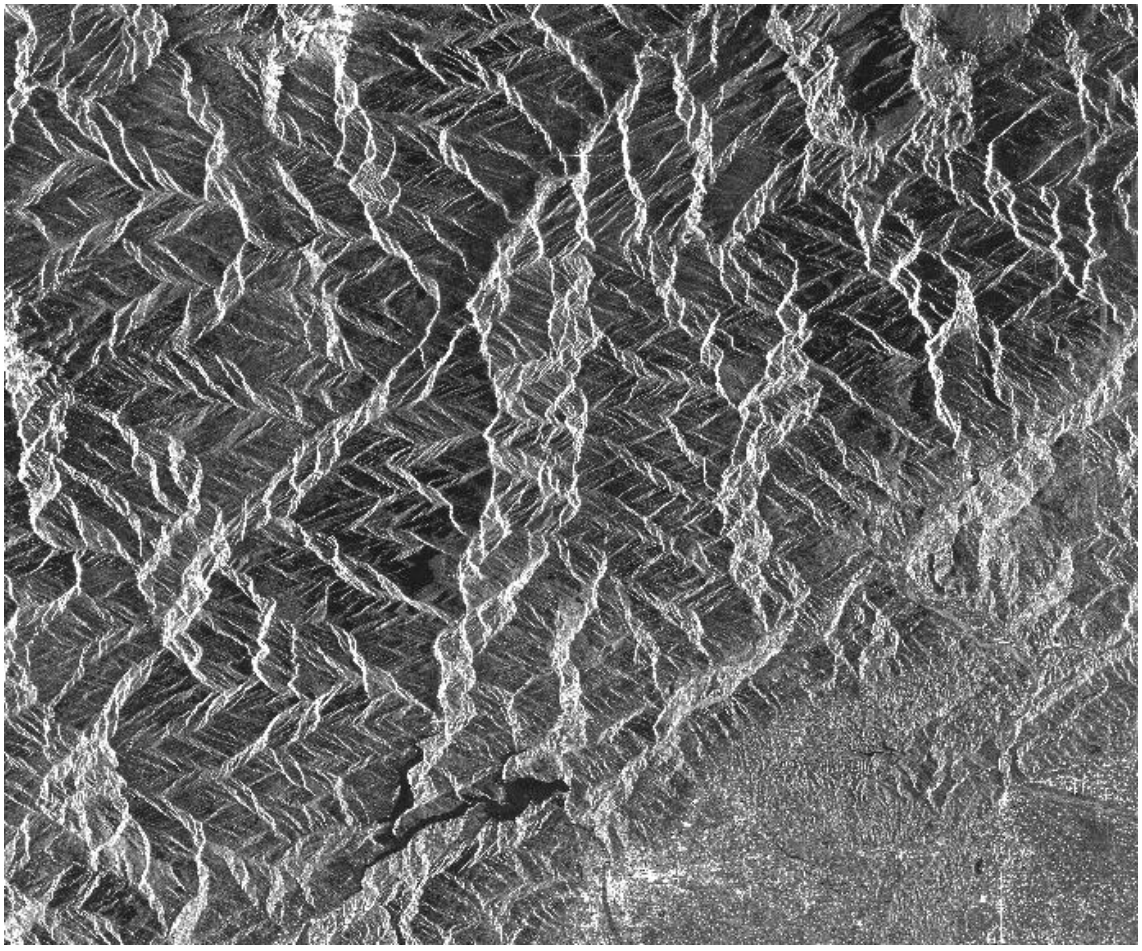

Figure 130: Image ALPSRP101610610-Acquisition Date 12/21/2007.

The co-registered images acquired at location 2 can be seen in the Figures (130), (131) and (132) above and below

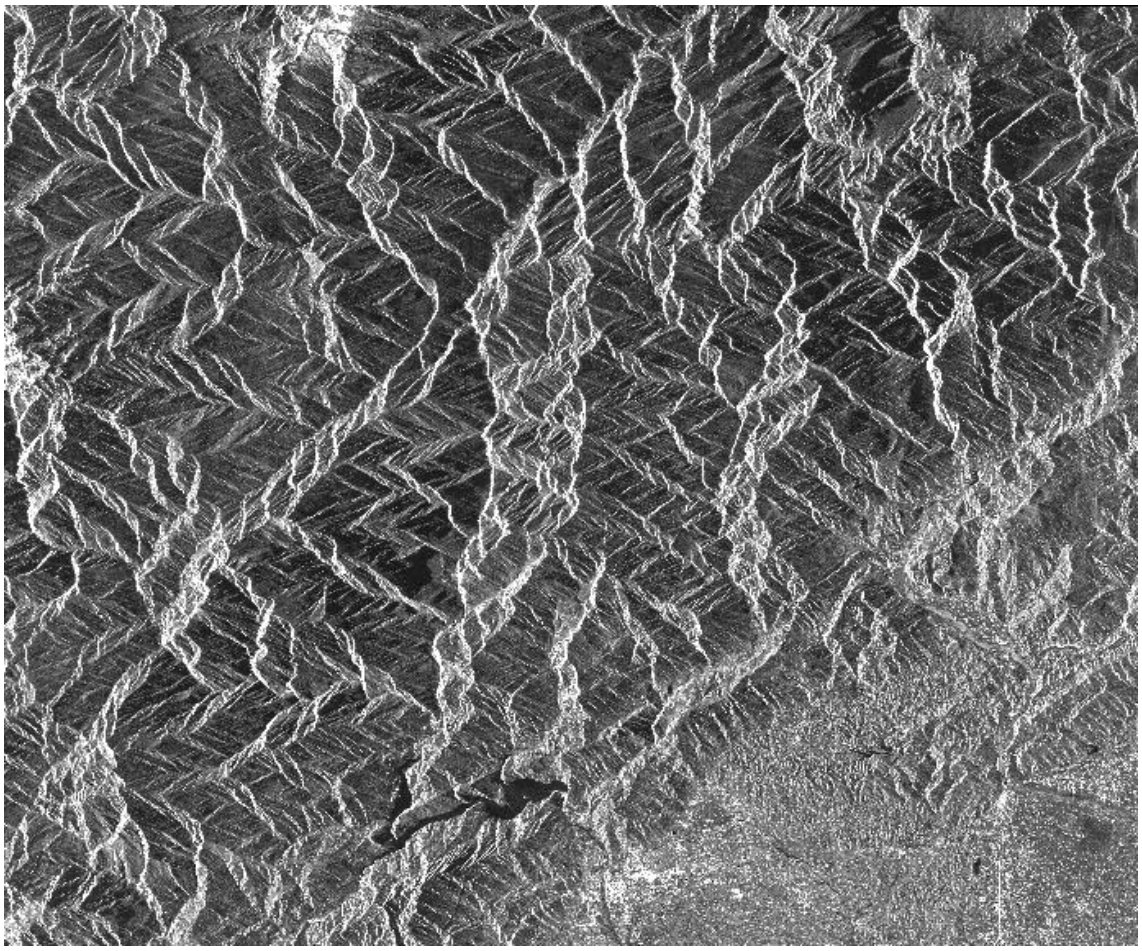

Figure 131: Image ALPSRP108320610-Acquisition Date 02/05/2008.

In the Figure (133) the histograms of the image pixel values of the imagery acquired at location 2 are presented. It can be seen on the histograms that the image pixel values follow a normal distribution, however there is a spike in the bright pixels due to the west side of mountains and residental areas in the scenes.

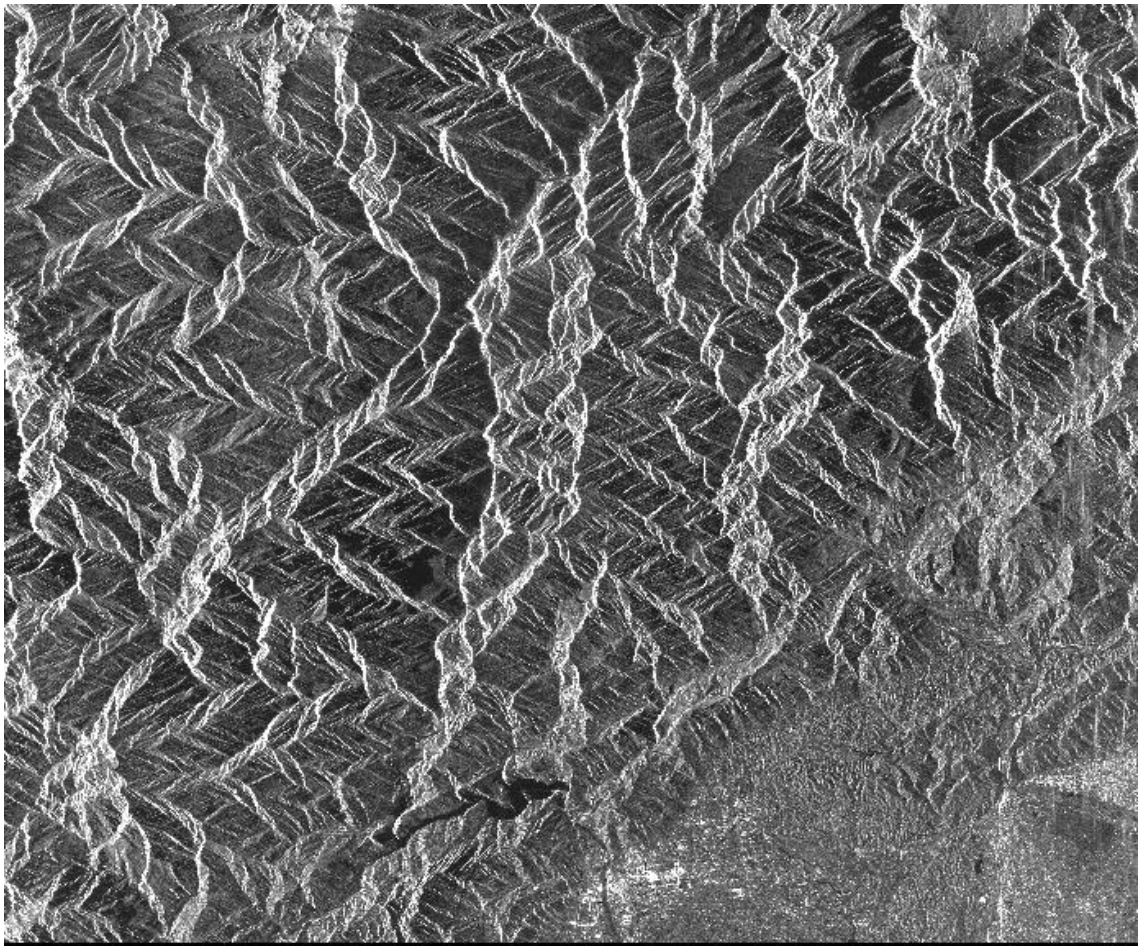

Figure 132: Image ALPSRP128450610-Acquisition Date 06/22/2008.

The resulting change maps can be seen in the Figures (134) and (135) below. Similar to the oil spill case, the correlation coefficient change statistics is more likely to detect the changes in the areas which has brighter pixels since correlation coefficient measure is more sensitive to the changes in these areas rather than dark pixel areas such as lakes, dams, mountains. On the other hand intensity ratio change statistics is more sensitive to the changes in the areas with dark pixels due to the ratioing adopted as a measure. Therefore one can use both of the methods jointly when a reconnaissance is necessary.

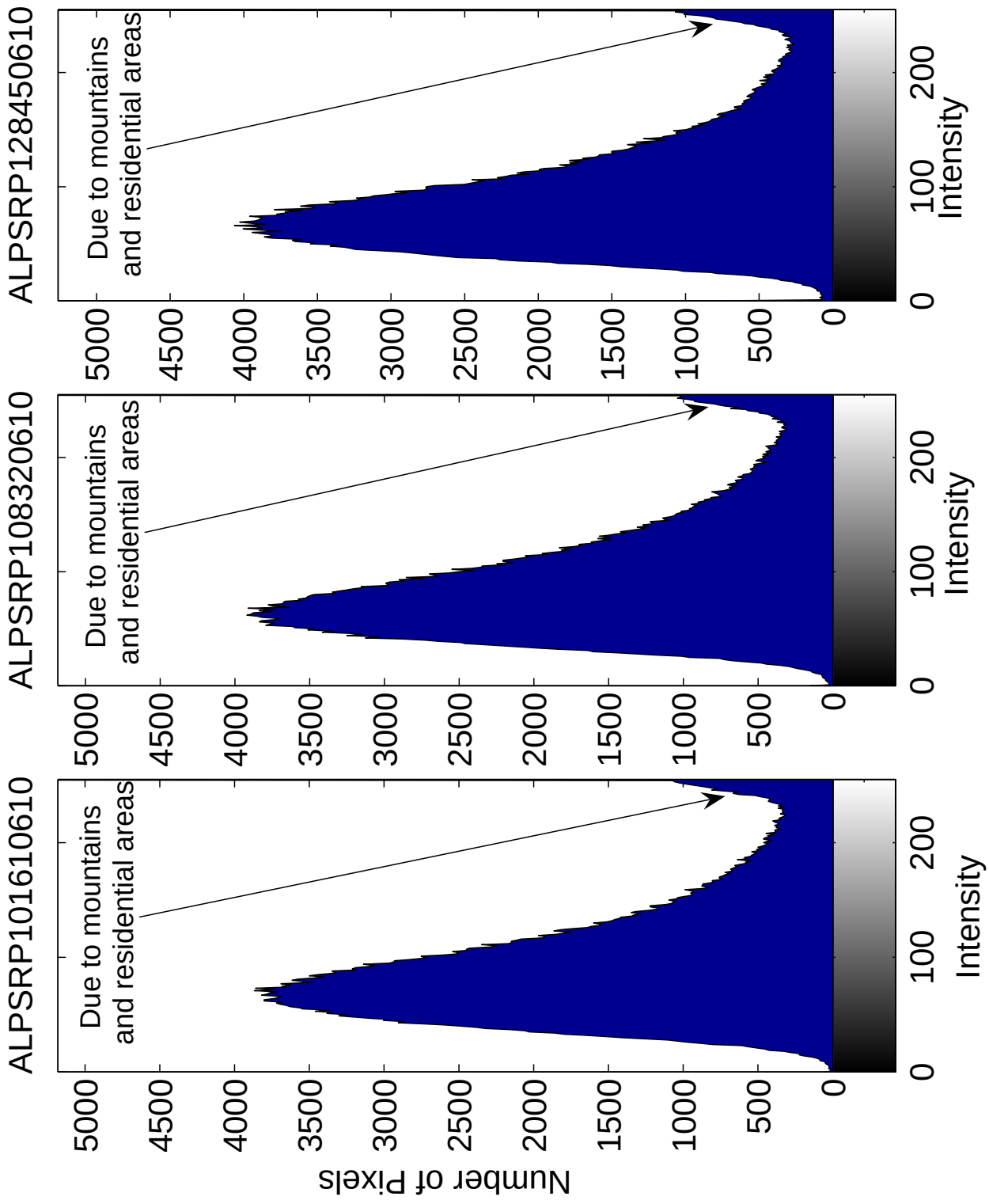

Figure 133: Histograms of earthquake imagery collected on location 2.

Figure 134: Change maps of earthquake imagery collected on location 2.

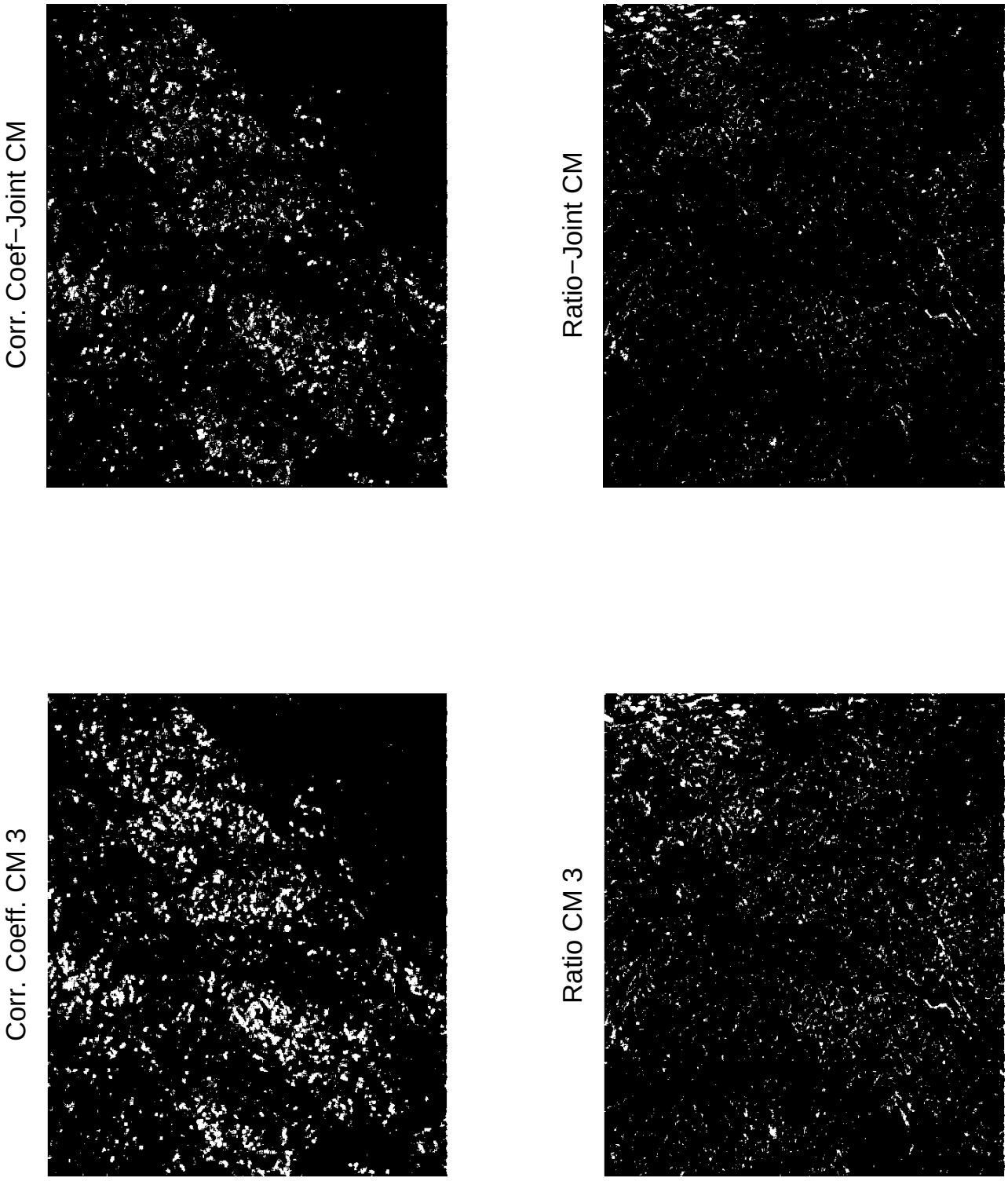

Figure 135: Final change maps of earthquake imagery collected on location 2.

Additionally as it can be seen in the Figures (134) and (135) above, two final change map method proposed can be used as a double-check mechanism and can reduce the number of false detections. This method works well both for the correlation coefficient change statistic and the intensity ratio change statistic algorithms. The probabilities of false alarm and detection of the joint change map can be calculated as $P_{fa} \approx 0.1^2 = 0.01$ and $P_d \approx 0.92^2 = 0.85$ for the correlation coefficient change statistic. For the intensity ratio change statistic these probabilities for the joint change map can be calculated as $P_{fa} \approx 0.07^2 = 0.005$ and $P_d \approx 0.74^2 = 0.55$. Although the joint change maps obtained causes a small amount of reduction in P_d it can be very beneficial for reducing the P_{fa} significantly. When higher values of P_d is used in obtaining the two change maps, the joint change map will suffer less from the loss of P_d, almost to an insignificant level.

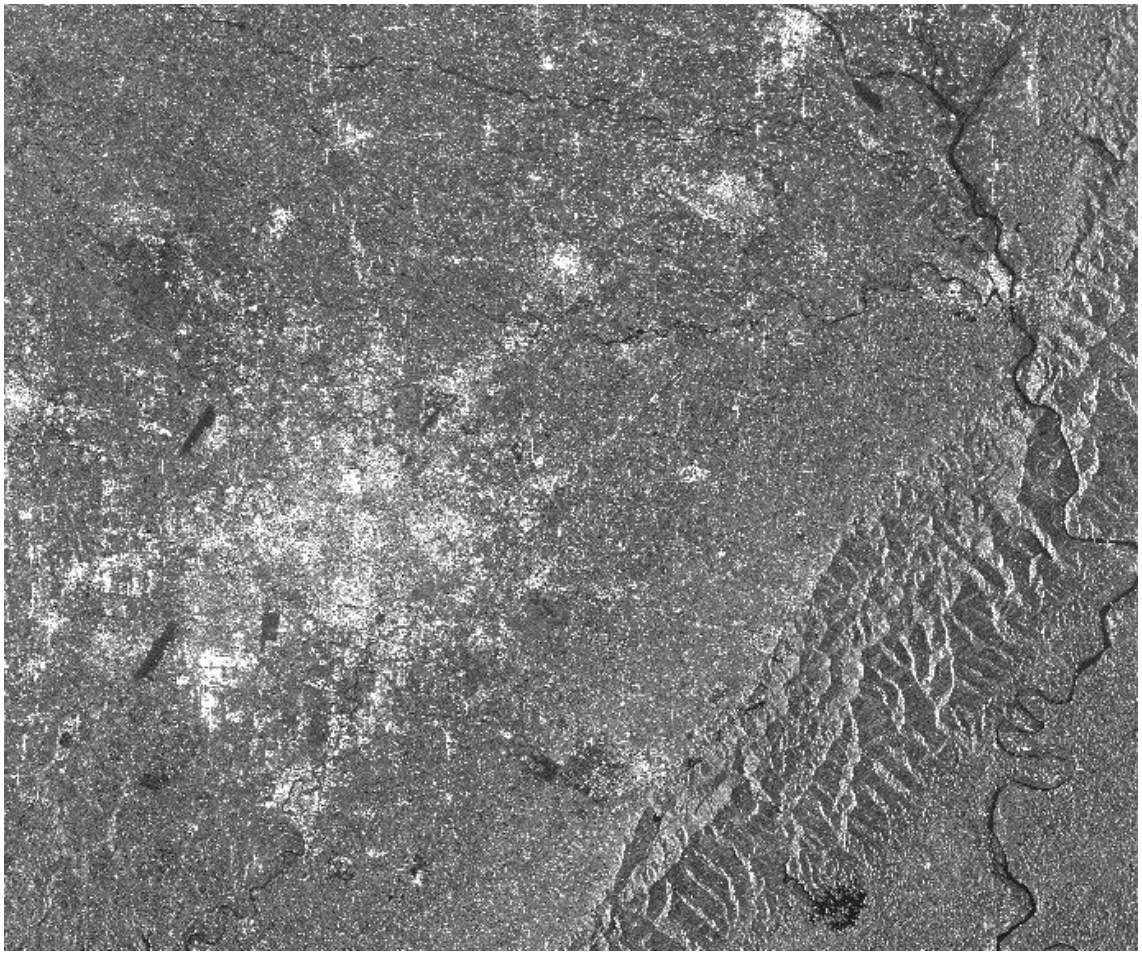

Figure 136: Image ALPSRP105840600-Acquisition Date 01/19/2008.

The co-registered images acquired at location 3 can be seen in the Figures (136), (137) and (138) above and below

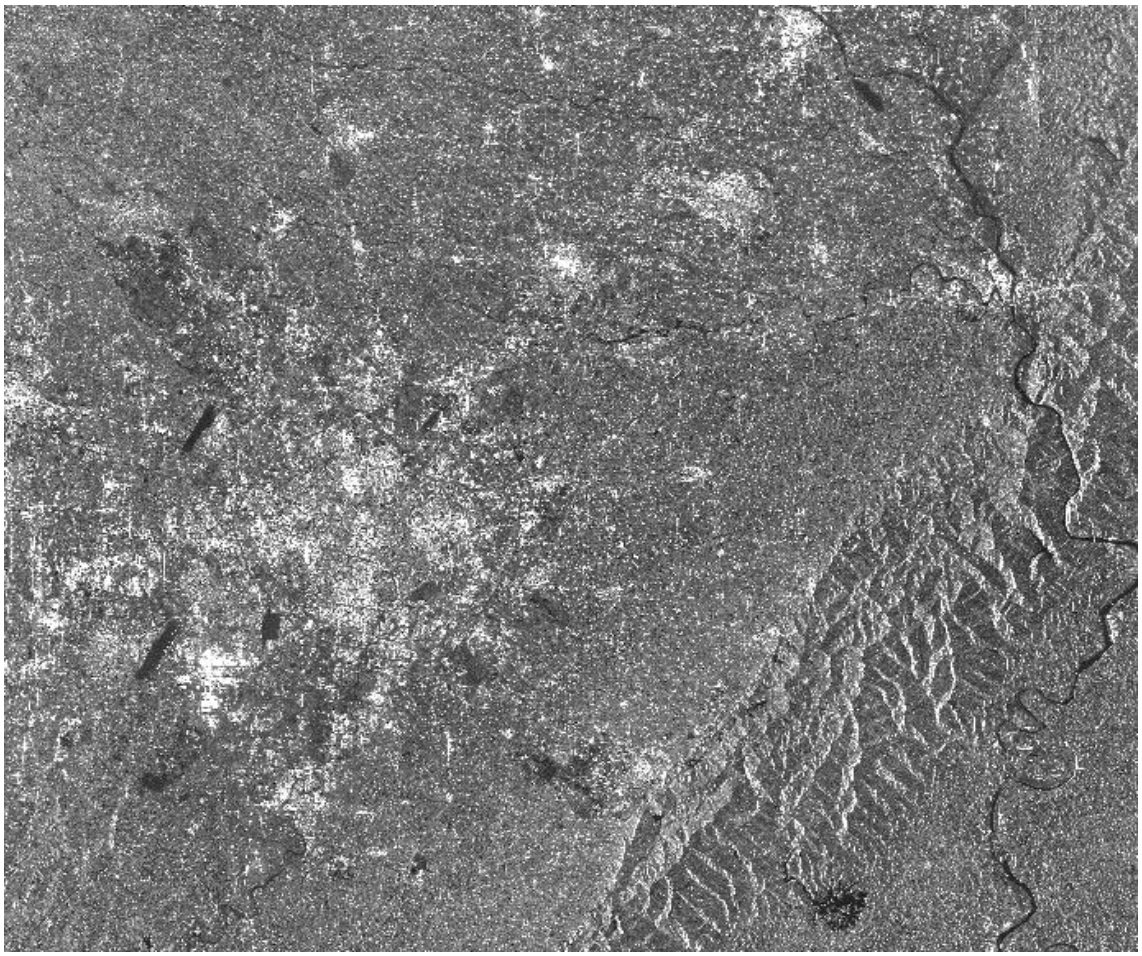

Figure 137: Image ALPSRP112550600-Acquisition Date 03/05/2008.

In the Figure (139) the histograms of the image pixel values of the imagery acquired at location 3 are presented. It can be seen on the histograms that the image pixel values follow a normal distribution, however there is a spike in the bright pixels due to residental areas in the scenes.

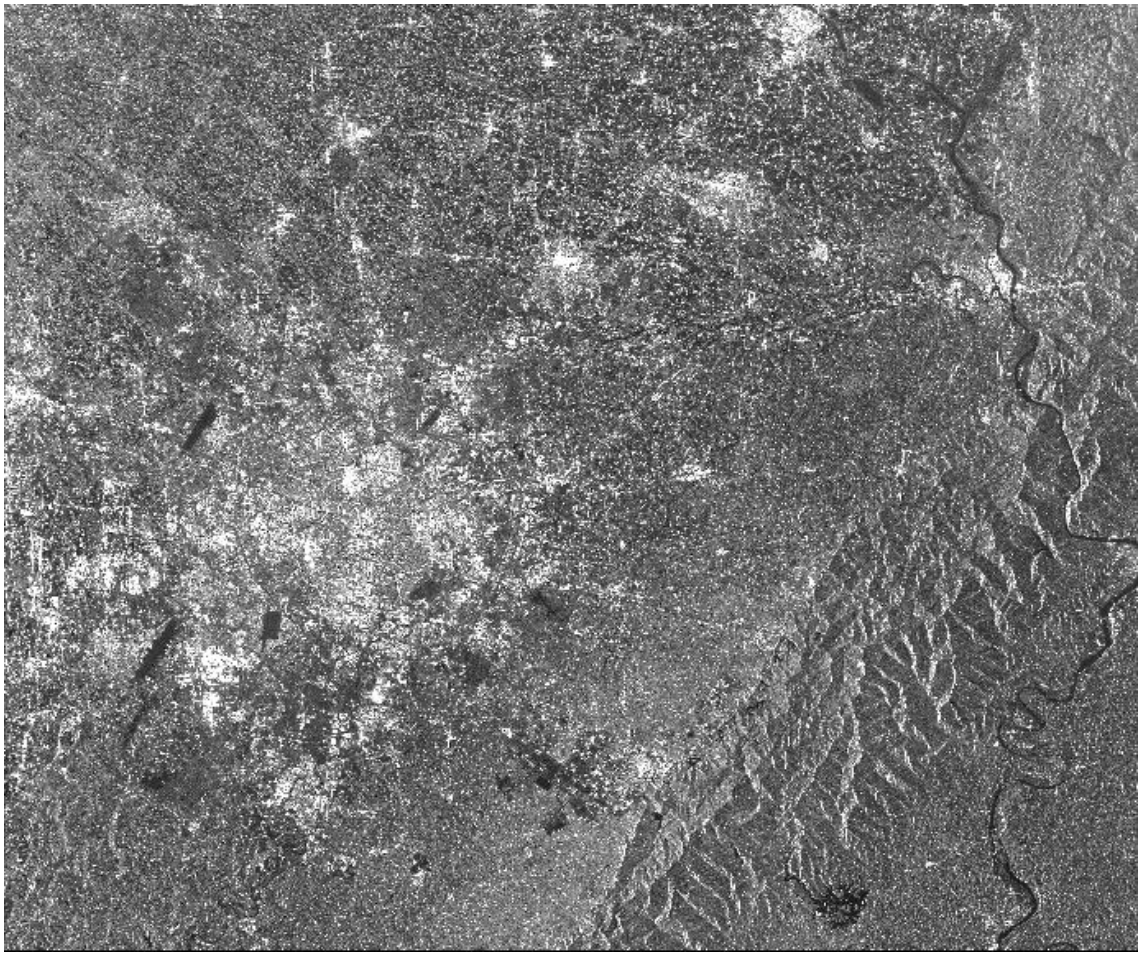

Figure 138: Image ALPSRP125970600-Acquisition Date 06/05/2008.

The resulting change maps can be seen in the Figures (140) and (141) below. Similary to the oil spill case, the correlation coefficient change statistics is more likely to detect the changes in the areas which has brighter pixels since correlation coefficient measure is more sensitive to the changes in these areas rather than dark pixel areas such as lakes, dams, mountains. On the other hand intensity ratio change statistics is more sensitive to the changes in the areas with dark pixels due to the ratioing adopted as a measure. Therefore one can use both of the methods jointly when a reconnaissance is necessary.

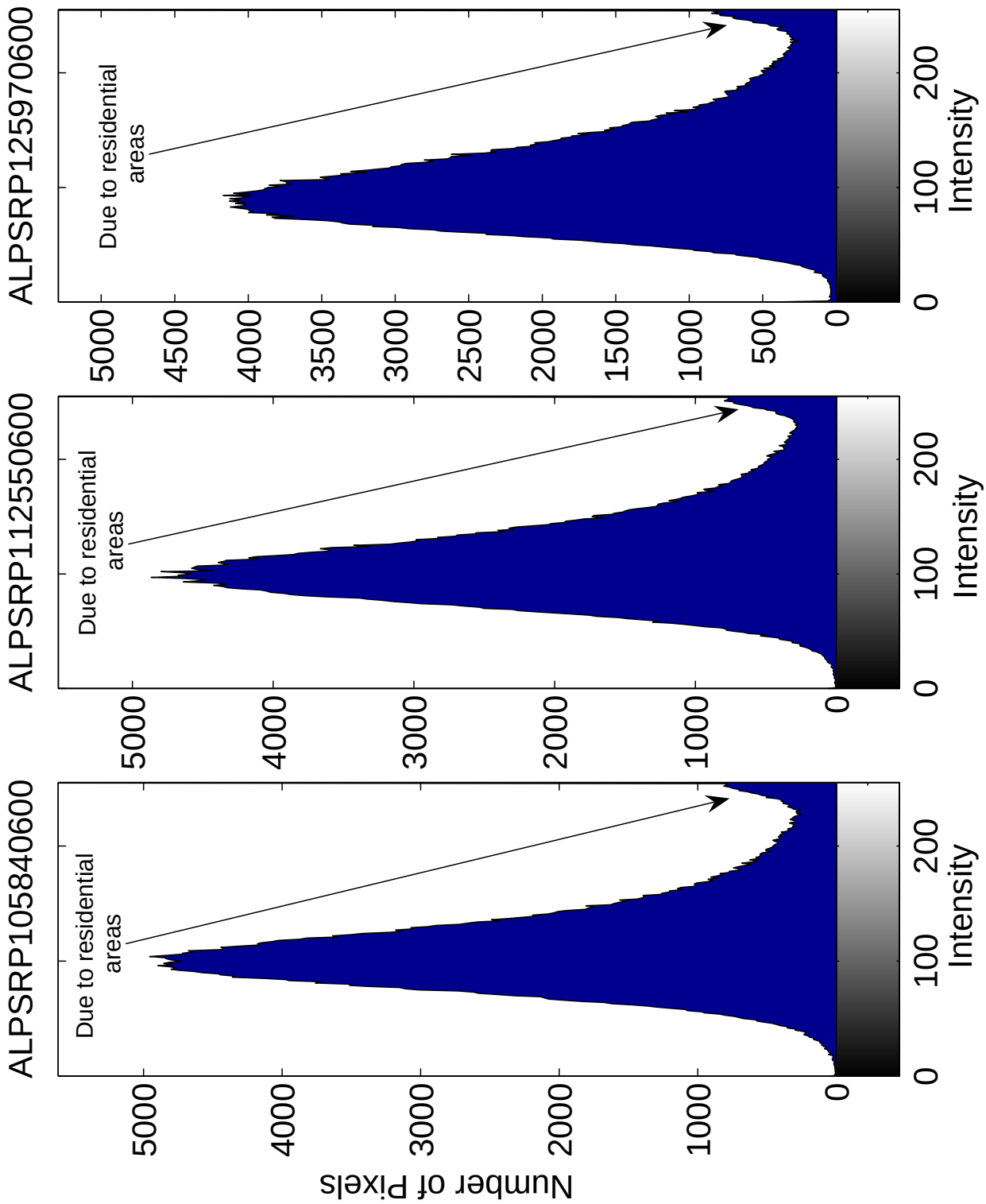

Figure 139: Histograms of earthquake imagery collected on location 3.

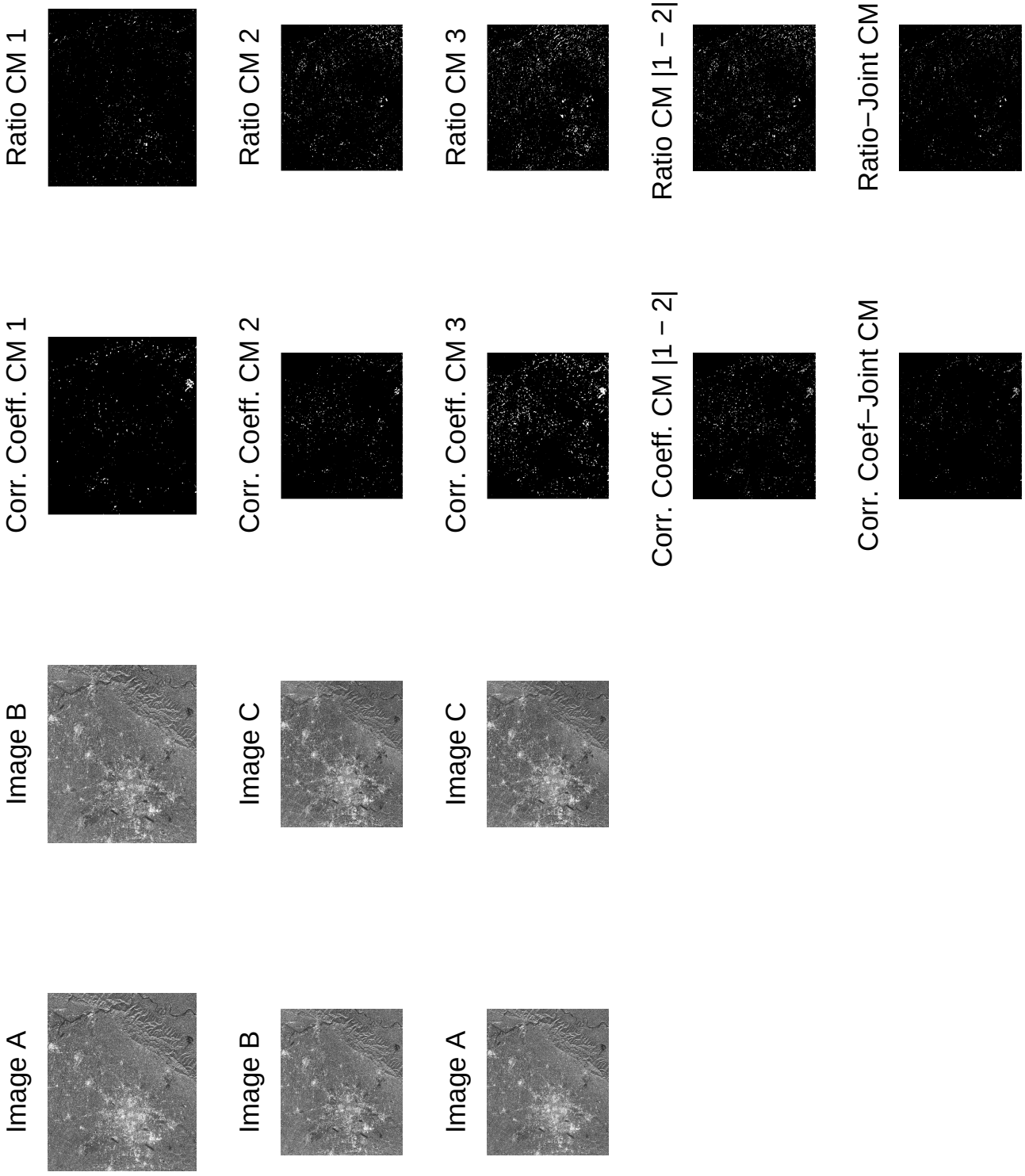

Figure 140: Change maps of earthquake imagery collected on location 3.

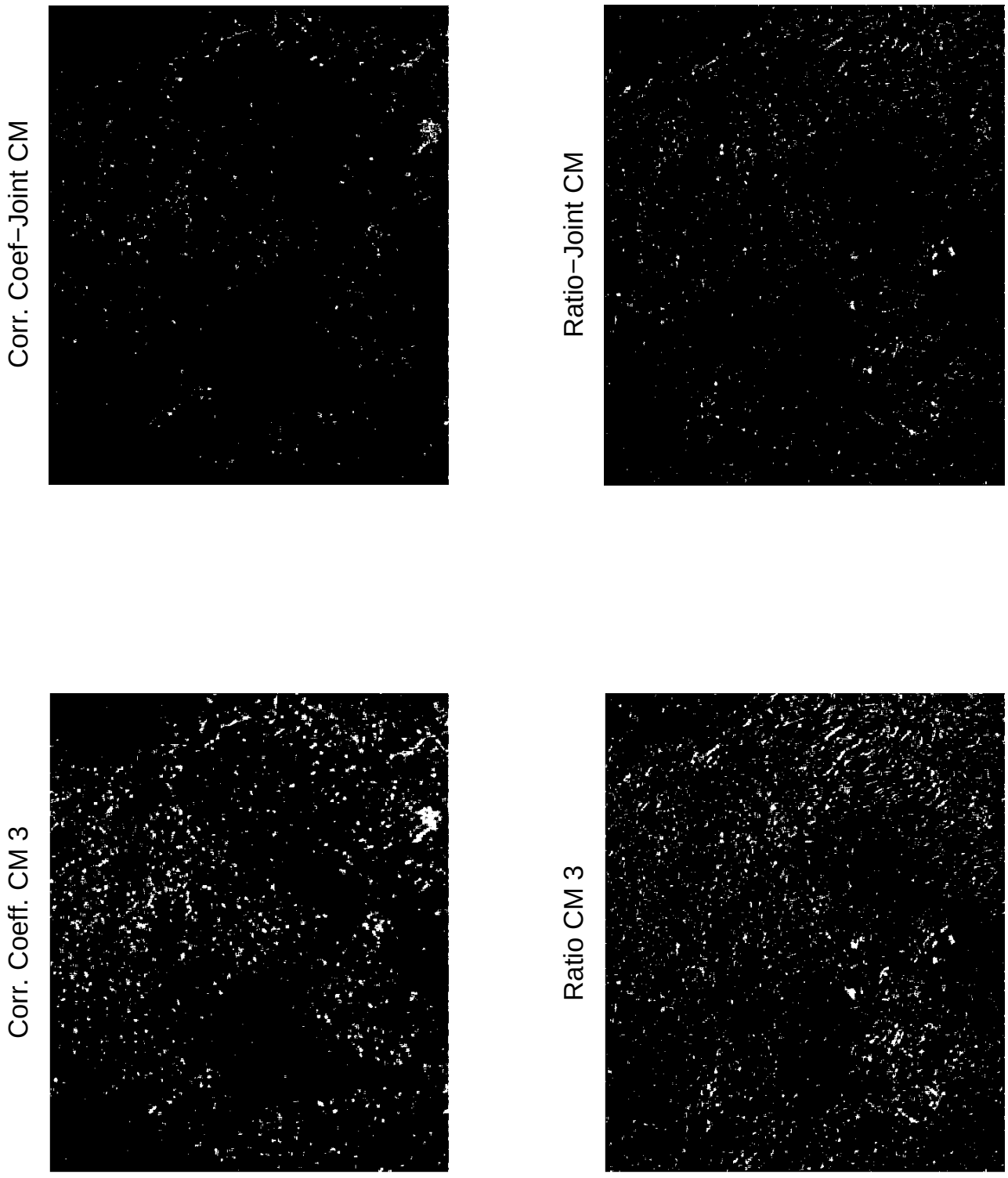

Figure 141: Final change maps of earthquake imagery collected on location 3.

Additionally as it can be seen in the Figures (140) and (141) above, two final change map method proposed can be used as a double-check mechanism and can reduce the probability of false alarm. This method works well both for the correlation coefficient change statistic and the intensity ratio change statistic algorithms. The probabilities of false alarm and detection of the joint change map can be calculated as $P_{fa} \approx 0.1^2 = 0.01$ and $P_d \approx 0.92^2 = 0.85$ for the correlation coefficient change statistic. For the intensity ratio change statistic these probabilities for the joint change map can be calculated as $P_{fa} \approx 0.07^2 = 0.005$ and $P_d \approx 0.74^2 = 0.55$. Although the joint change maps obtained causes a small amount of reduction in P_d it can be very beneficial for reducing the P_{fa} significantly. When higher values of P_d is used in obtaining the two change maps, the joint change map will suffer less from the loss of P_d, almost to an insignificant level.

CHAPTER VII

CONCLUSION & RECOMMENDATIONS FOR FUTURE WORK

In this dissertation both the linear and nonlinear frequency modulated chirp signals are discussed. The most widely used frequency modulated chirp signal, linear frequency modulated chirp signal, and some of its properties such as spectrum, point spread function and matched filter are summarized. A new nonlinear frequency modulated chirp signal which has the form of $\exp(j\eta t^{1.75})$ and named as $t^{0.75}$ frequency modulated ($t^{0.75}$FM) chirp signal is introduced. Compared to the generally used linear frequency modulated chirps, this chirp is shown to be capable of reducing the sidelobes of the point spread function without having an adverse effect on signal-to-noise ratio and mainlobe width of the point spread function. It is also shown that adopting a same bandwidth same slew rate approach, $t^{0.75}$FM chirp has a shorter pulse duration compared to linear frequency modulated chirp therefore is more efficient. It is also discussed that $t^{0.75}$FM can have some other potential uses such as when used in hybrid chirps it can help to improve the resolution.

In order to validate the new offered chirp signal, spotlight SAR imaging geometry together with polar and Stolt format reconstruction algorithms are considered. The synthetic examples are generated using both chirps with polar and Stolt format processing. Reconstructed imagery provides a synthetic data basis for testing the change detection methodology and algorithms.

A new change detection method which depends on the idea of generating two different final change maps of the initial and final images, is offered. First final change map is obtained by cumulatively adding the sequences of change maps in such a manner that common change areas are excluded and uncommon change areas are included in the successive change maps. The second final change map is obtained by comparing the first and the last images in the temporal sequence. This method requires at least three image sequence to be employed and can be generalized to longer temporal image sequences. The purpose of this approach is

to provide a double check mechanism to the conventional approach and thus to reduce the probability of false alarm. The specific algorithms utilized for testing this method are the widely used correlation coefficient change statistic and the intensity ratio change statistic algorithms. Therefore these algorithms and the probabilistic selection of the threshold criteria is discussed as well.

This method together with the algorithms mentioned are first applied to synthetic data generated by Stolt format processing which provides higher resolution imagery compared to polar format processing and obeys the real imaging scenarios better. It is shown that the method works on synthetic data. The method together with the algorithms mentioned are also applied to real disaster data which is acquired by Japanese Aerospace Agency's Advanced Land Observing Satellite (ALOS). The two disasters considered are the 2010 Gulf of Mexico oil spill and the 2008 China Sichuan earthquake. While oil spill is an evolving type of disaster, the earthquake is an impulsive type. The correlation coefficient change statistic and the intensity ratio change statistic algorithms as well as the two final change map method are tested on these disaster imagery. It is shown that correlation coefficient change statistic has a higher performance on assessing the changes occured in bright pixel areas whereas the intensity ratio change statistic is a better choice for the oil spill detection, especially in the vicinity of lands. The use of both statistics can be necessary to detect the changes in the bright or dark pixel regions. It is also shown that the number of false alarms can be significantly reduced using the double check mechanism introduced by two final change map method.

As a future work in the signal processing part, SAR imaging is always open for new imaging geometries and reconstruction methods. Also development of new waveforms used in the imaging which can provide reduced sidelobes of the point spread functions while keeping the changes mainlobe widths of the point spread functions acceptably low, as well as preserves the signal-to-noise ratio of the waveform and can more easily and efficiently be generated in the hardware is always desired.

As a future work on change detection, the two final change map method offered in this dissertation can be tested with other change detection algorithms both for 2D and

3D, except with those which give identically the same result of the direct comparison of the first and the last image in the sequence, such as simple differencing or log-ratioing. Additionally the two final change map method can also be implemented together with coherent change detection techniques, again except for the trivial cases. Also the change detection method proposed can be tested on other types of disaster such as floods, tsunamis, hurricanes. Another possible direction is defining a correlation coefficient based on Hölders inequality. Correlation coefficient based on the Hölders inequality can be adopted as a general tool of statistics and can also be applied for change detection purposes. Since Hölders inequality gives equal or unequal weights to image pixel values, it can be used to put unequal weight to the repeat-pass imagery pixels. This may give researchers a flexibility with the threshold values used for testing the changed or unchanged hypothesis. Also since the resolutions in the range and azimuth direction of a SAR system may differ, a correlation coefficient based on Hölders inequality can be used to overcome this difficulty. A correlation coefficient with two or more input vectors can be adopted between two or more images. There is also a tendency towards performing the change detection not in the image but in a transformed domain. Some of the transforms which can be used for this purpose are the Walsh, Hadamard, Hotelling, Hough and discrete cosine transforms in addition to widely adopted Fourier transforms.

Another possible contribution would be using the change detection methods to assess the quality of synthetically generated images. For example comparisons between different image modalities or different image reconstruction methods can be perfomed using change detection methods.

APPENDIX A

METHOD OF STATIONARY PHASES

Integrals which can not be evaluated in terms of elementary functions can be approximated by asymptotic methods. One of the most commonly used asymptotic methods is the method of stationary phases. Most commonly used form of the method of stationary phases is summarized below which can be found in [40]. Considering an integral of the form

$$I = \int_{-\infty}^{\infty} f(t) e^{j\Lambda(t)} dt \tag{156}$$

If the first derivative of phase function is zero at a point that point is called stationary point. Denoting the stationary point as x_s it can be concluded that $\dot{\Lambda}(t_s) = 0$. The Taylor series expansion of the phase function around stationary point can is given by

$$\Lambda(t) \approx \Lambda(t_s) + \frac{1}{2}\ddot{\Lambda}(t_s)(t - t_s)^2 \tag{157}$$

Pluging this expression into equation (156) we obtain

$$I \approx f(t_s) e^{j\Lambda(t_s)} \int_{-\infty}^{\infty} e^{j\ddot{\Lambda}(t_s)(t-t_s)^2/2} dt \tag{158}$$

Making the substitutions $t = \sqrt{\frac{2}{\ddot{\Lambda}(t_s)}}x + t_s$ and $dt = \sqrt{\frac{2}{\ddot{\Lambda}(t_s)}}dx$ and using Fresnel integrals given by equation (7) this expression reduces to

$$I \approx \sqrt{\frac{2\pi j}{\ddot{\Lambda}(t_s)}} f(t_s) e^{j\Lambda(t_s)} \tag{159}$$

which provides an asymptotic approximation to the expression given by equation (156). A more general discussion of the method of stationary phases can be found in [7],[40] and [10]. In this section the derivation given in [7], which is not restricted to the second order in Taylor series expansion, is closely followed.

Considering a generalized Fourier integral given by

$$I(\omega) = \int_a^b f(t) e^{j\omega\Lambda(t)} dt \tag{160}$$

Riemann-Lebesgue lemma states that

$$\int_a^b f(t)e^{j\omega t}dt \to 0, \text{ as } \omega \to +\infty, \tag{161}$$

provided that $\int_a^b |f(t)|\,dt$ exists. Riemann-Lebesgue lemma is also valid for the generalized Fourier integrals in the form of $I(\omega)$ given in the equation (160). For $I(\omega) \to 0$ as $\omega \to +\infty$, $|f(t)|$ has to be integrable, $\Lambda(t)$ has to be continuously differentiable on $[a, b]$ and $\Lambda(t)$ has to be nonconstant on any subinterval of $[a, b]$ [7].

Generalized Fourier integrals of the form given in equation (160) can be written as a sum of integrals in which $\Lambda^{'}(t)$ vanishes only at one integral limit. Such a point is called a stationary point. Selecting a as the stationary point, that is $\Lambda^{'}(a) = 0$, and for $\Lambda^{'}(t) \neq 0$ on $a < t \leq b$ we can rewrite equation (160) as follows

$$I(\omega) = \int_a^{a+\epsilon} f(t)e^{j\omega\Lambda(t)}dt + \int_{a+\epsilon}^b f(t)e^{j\omega\Lambda(t)}dt \tag{162}$$

where ϵ is a small positive number. The second integral in the equation (162) decays like $1/\omega$ as $\omega \to \infty$ since there are no stationary points in the interval $a + \epsilon \leq t \leq b$. Leading behavior of the first integral in the equation (162) can be obtained by replacing $f(t)$ by $f(a)$ and $\Lambda(t)$ by $\Lambda(a) + \Lambda^{(p)}(a)(t-a)^p/p!$ where $\Lambda^{(p)}(a) \neq 0$ but $\Lambda^{'}(a) = ... = \Lambda^{(p-1)}(a) = 0$. By making these changes one obtains

$$I(\omega) \sim \int_a^{a+\epsilon} f(a) \exp\left\{j\omega\left[\Lambda(a) + \frac{1}{p!}\Lambda^{(p)}(a)(t-a)^p\right]\right\} dt, \quad \text{as} \quad \omega \to +\infty, \tag{163}$$

Letting $z = t - a$ and replacing ϵ by ∞, which introduces negligible vanishing errors like $1/\omega$ as $\omega \to +\infty$, one obtains

$$I(\omega) \sim f(a)e^{j\omega\Lambda(a)} \int_{-\infty}^{\infty} \exp\left[\frac{j\omega}{p!}\Lambda^{(p)}(a)z^p\right] dz, \quad \text{as} \quad \omega \to +\infty, \tag{164}$$

For $\Lambda^{(p)}(a) > 0$ the integration contour can be rotated from real-z axis by an angle $\pi/2p$ and make the following substitution

$$z = e^{j\pi/2p}\left[\frac{p!\,y}{\omega\Lambda^{(p)}(a)}\right]^{1/p} \tag{165}$$

For $\Lambda^{(p)}(a) < 0$ the integration contour can be rotated from real-z axis by an angle $-\pi/2p$ and make the following substitution

$$z = e^{-j\pi/2p}\left[\frac{p!\,y}{\omega\left|\Lambda^{(p)}(a)\right|}\right]^{1/p} \tag{166}$$

which leads to

$$I(\omega) \sim 2f(a)e^{j\omega\Lambda(a)\pm j\pi/2p}\left[\frac{p!}{\omega\left|\Lambda^{(p)}(a)\right|}\right]^{1/p}\frac{\Gamma(1/p)}{p}, \quad \text{as} \quad \omega \to +\infty, \tag{167}$$

where the factor $e^{j\pi/2p}$ needs to be used if $\Lambda^{(p)}(a) > 0$ or the $e^{-j\pi/2p}$ needs to be used if $\Lambda^{(p)}(a) < 0$. Γ is the gamma function is given by

$$\Gamma(m) = \int_0^\infty t^{m-1}e^{-t}dt \qquad (Re(m) > 0) \tag{168}$$

Equation (167) is an asymptotic approximation of the generalized Fourier integral given by equation (160). It is useful to note that for $p = 2$ and $\omega = 1$ expression given by equation (167) reduces to expression given by equation (159).

APPENDIX B

ROTATIONS OF FOURIER TRANSFORMS

In this appendix it is shown that Fourier transform of a rotated function is equal to the rotated Fourier transform of the original function. A similar analysis can be seen in [48] or [33]. Let

$$f'(x', y') = f(x, y) \tag{169}$$

where

$$\begin{bmatrix} x' \\ y' \end{bmatrix} = \begin{bmatrix} \cos(\theta_c) & \sin(\theta_c) \\ -\sin(\theta_c) & \cos(\theta_c) \end{bmatrix} \begin{bmatrix} x \\ y \end{bmatrix} \tag{170}$$

A discussion of the matrix algebra can be seen in [27]. Denoting the rotation matrix with Ψ as

$$\Psi = \begin{bmatrix} \cos(\theta_c) & \sin(\theta_c) \\ -\sin(\theta_c) & \cos(\theta_c) \end{bmatrix} \tag{171}$$

the equation (170) can be rewritten as follows

$$\mathbf{x}' = \begin{bmatrix} x' \\ y' \end{bmatrix} = \Psi \begin{bmatrix} x \\ y \end{bmatrix} = \Psi \mathbf{x} \tag{172}$$

The Jacobian of the transformation is

$$|J| = \cos^2(\theta_c) + \sin^2(\theta_c) = 1 \tag{173}$$

Taking the Fourier transform of the equation (169) and using the Jacobian of the rotation given in equation (173) one obtains

$$F'(\mathbf{k}_{\mathbf{x}'}) = \int_{\mathbf{x}'} f'(\mathbf{x}') \exp\left[-j\mathbf{k}_{\mathbf{x}'}^T \mathbf{x}'\right] |J| \, d\mathbf{x}' = \int_{\mathbf{x}} f(\mathbf{x}) \exp\left[-j\mathbf{k}_{\mathbf{x}'}^T \Psi \mathbf{x}\right] d\mathbf{x} \tag{174}$$

The relation, which can be verified by using the orthogonality of the rotation matrix,

$$\mathbf{k}_{\mathbf{x}}^T = \mathbf{k}_{\mathbf{x}'}^T \Psi \tag{175}$$

allows one to rewrite equation (174) as

$$F'(\mathbf{k}_{\mathbf{x}'}) = \int_{\mathbf{x}} f(\mathbf{x}) \exp\left[-j\mathbf{k}_{\mathbf{x}}^T\mathbf{x}\right] d\mathbf{x} = F(\mathbf{k}_{\mathbf{x}}) \tag{176}$$

which leads to the property

$$F'(k_{x'}, k_{y'}) = F(k_x, k_y) \tag{177}$$

where

$$\mathbf{k}_{\mathbf{x}'} = \begin{bmatrix} k_{x'} \\ k_{y'} \end{bmatrix} = \begin{bmatrix} \cos(\theta_c) & \sin(\theta_c) \\ -\sin(\theta_c) & \cos(\theta_c) \end{bmatrix} \begin{bmatrix} k_x \\ k_y \end{bmatrix} = \Psi\mathbf{k}_{\mathbf{x}} \tag{178}$$

Therefore it can be concluded that Fourier transform of a rotated function is equal to the rotated Fourier transform of the original function.

APPENDIX C

INEQUALITIES

In this appendix the derivation of well known Cauchy-Bunyakovsky-Schwars inequality of mathematics is presented. The correlation coefficient is defined based on this inequality in chapter 5.

Cauchy-Bunyakovsky-Schwarz Inequality Cauchy-Bunyakovsky-Schwarz inequality is given by

$$|f \cdot g| \leq \|f\|_2 \|g\|_2 \tag{179}$$

where f and g are any vectors. While a different derivation can be seen in [29], the derivation given in [27] is closely followed. One starts with the inequality

$$(f + \beta g) \cdot (f + \beta g) \geq 0 \tag{180}$$

where β is a scalar. This inequality is guaranteed by the definition of a dot product [27]. Noting that $f \cdot f = \|f\|_2^2$ and $g \cdot g = \|g\|_2^2$ we can rewrite the equation (180) as

$$\|f\|_2^2 + 2\beta f \cdot g + \beta^2 \|g\|_2^2 \geq 0 \tag{181}$$

Regarding β as a variable and f and g fixed parameters the left hand side of the equation (181) is minimized when $\partial(\text{L.H.S})/\partial\beta = 0$ which leads to

$$2f \cdot g + 2\beta \|g\|_2^2 = 0 \tag{182}$$

therefore

$$\beta = -\frac{f \cdot g}{\|g\|_2^2} \tag{183}$$

Using this optimal value of β in the equation (181) one obtains

$$\|f\|_2^2 - 2\frac{(f \cdot g)^2}{\|g\|_2^2} + \frac{(f \cdot g)^2}{\|g\|_2^2} \geq 0 \tag{184}$$

which can be simplified as

$$\|f\|_2^2 \|g\|_2^2 \geq (f \cdot g)^2 \tag{185}$$

Taking the square root of the expression in the equation (185) one can obtain the Cauchy-Bunyakovsky-Schwarz inequality given by the equation (179). If the vectors f and g are N dimensional real valued vectors then using the definition of the norm the equation (179) can be rewritten as

$$\left| \sum_{i=1}^{N} f_i g_i \right| \leq \sqrt{\sum_{i=1}^{N} |f_i|^2} \sqrt{\sum_{i=1}^{N} |g_i|^2} \tag{186}$$

If the f and g are N dimensional complex valued vectors then using the definiton of the norm the equation (179) can be rewritten as

$$\left| \sum_{i=1}^{N} f_i g_i^* \right| \leq \sqrt{\sum_{i=1}^{N} |f_i|^2} \sqrt{\sum_{i=1}^{N} |g_i|^2} \tag{187}$$

REFERENCES

[1] "2008 Sichuan Earthquake." http://en.wikipedia.org/wiki/2008-Sichuan-earthquake. Accessed: 07/09/2012.

[2] "Deepwater Horizon Oil Spill." http://en.wikipedia.org/wiki/Deepwater-Horizon-oil-spill. Accessed: 07/06/2012.

[3] Abramowitz, M. and Stegun, I. A., *Handbook of Mathematical Functions with Formulas, Graphs and Mathematical Tables*. New York: Dover Publications, 1972.

[4] Barnes, C. F., *Synthetic Aperture Radar Image Formation Processing*. 2012. In preparation.

[5] Bass, F. G. and Fuks, I. M., *Wave Scattering from Statistically Rough Surfaces*. New York: Pergamon Press, 1979.

[6] Bayindir, C., "Implementation of a computational model for random directional seas and underwater acoustics," Master's thesis, University of Delaware, October 2009.

[7] Bender, C. M. and Orszag, S. A., *Advanced Mathematical Methods for Scientists and Engineers I*. New York: Springer-Verlag, 1999.

[8] Blahut, R., *Theory of Remote Image Formation*. Cambridge, UK: Cambridge University Press, 2004.

[9] Bleistein, N., Cohen, J. K., and Stockwell, J. W., *Mathematics of Multidimensional Seismic Imaging, Migration and Inversion*. New York: Springer-Verlag, 2001.

[10] Bleistein, N. and Handelsman, R., *Asymptotic Expansions of Integrals*. New York: Holt, Rinehart and Winston, 1975.

[11] Bouaraba, A., Younsi, A., Belhadj-Aissa, A., Acheroy, M., Milisavljevic, N., and Closson, D., "Robust techniques for coherent change detection using Cosmo-Skymed SAR images," *Progress in Electromagnetics Research M*, vol. 22, no. 1, pp. 219–232, 2012.

[12] Bracewell, R., *The Fourier Transform and Its Applications*. New York: McGraw-Hill, third ed., 1999.

[13] Brekke, C. and Solberg, A. H. S., "Oil spill detection by satellite remote sensing," *Remote Sensing of Environment*, vol. 95, no. 1, pp. 1–13, 2005.

[14] Carrara, W., Goodman, R., and Majewski, R., *Spotlight Synthetic Aperture Radar Signal Processing Algorithms*. Norwood, Massachusetts: Artech House, 1995.

[15] Çadalli, N. and Munson, J., "A comparison of $\omega - k$ and generalized SAR inversion for runway imaging," *Proceedings of IEEE International Conference on Image Processing*, vol. 1, 2000.

[16] Collins, T. and Atkins, P., "Nonlinear frequency modulation chirps for active sonar," *IEEE Proceedings on Radar, Sonar and Navigation*, vol. 146, no. 6, pp. 312–316, 1999.

[17] Curlander, J. C. and McDonough, R. N., *Synthetic Aperture Radar Systems and Signal Processing*. Wiley Series in Remote Sensing, New York: John Wiley and Sons, 1991.

[18] Doerry, A. W., "Generating precision nonlinear FM chirp waveforms," *Radar Sensor Technology XI*, vol. 6547, pp. 65470D1–65470D12, 2007.

[19] Eberhardt, E., Froese, C., Turner, A. K., and Leroueil, S., *Landslides and Engineered Slopes: Protecting Society through Improved Understanding*, vol. 1-2. Lillington, North Carolina: CRC Press, 2012.

[20] Espedal, H. A., Johannessen, J. A., Dano, E., Lyzenga, D. R., and Knulst, J. C., "ERS-1/2 SAR detection of natural film on the ocean surface," *Journal of Geophysical Research*, vol. 10, pp. 24969–24982, 1998.

[21] Fiscella, B., Giancaspro, A., Nirchio, F., Pavese, P., and Trivero, P., "Oil spill detection using marine SAR images," *International Journal of Remote Sensing*, vol. 21, no. 18, pp. 3561–3566, 2000.

[22] Flores-Tapia, D., Thomas, G., and Pistorius, S., "Wavefront reconstruction of elevation circular synthetic aperture radar imagery using a cylindrical Green's function," *Eurasip Journal on Advances in Signal Processing*, vol. 2010, no. 657323, pp. 1–12, 2009.

[23] Franceschetti, G. and Lanari, R., *Synthetic Aperture Radar Processing*. New York: CRC Press, 1999.

[24] Gonzalez, R. C. and Woods, R. E., *Digital Image Processing*. Upper Saddle River, New Jersey: Prentice-Hall, 2002.

[25] Goodman, J. W., *Introduction to Fourier Optics*. Englewood, Colorado: Roberts and Company Publishers, third ed., 2004.

[26] Gough, P. T. and Hawkins, D. W., "Imaging algorithms for strip-map synthetic aperture sonar: Minimizing the effects of aperture errors and aperture undersampling.," *IEEE Journal of Oceanic Engineering*, vol. 22, no. 1, pp. 27–39, 1997.

[27] Greenberg, M. D., *Advanced Engineering Mathematics*. Upper Saddle River, New Jersey: Prentice-Hall, 1998.

[28] Hamazaki, T., "Overview of the advanced land observing satellite (ALOS): Its mission requirements, sensors, and a satellite system.," *ISPRS Joint Workshop 'Sensors and Mappings from Space'*, 1999.

[29] Hardy, G. H., Littlewood, J. E., and Polya, G., *Inequalities*. Cambridge, Great Britain: Cambridge University Press, 1952.

[30] Hein, A., *Processing of SAR Data: Fundamentals, Signal Processing, Interferometry*. Berlin, Germany: Springer-Verlag, 2004.

[31] Hubbard, J. and Shaw, J. H., "Uplift of the Longmen Shan and Tibetan plateau, and the 2008 Wenchuan (M=7.9) earthquake," *Nature*, vol. 458, no. doi:10.1038, pp. 194–197, 2009.

[32] Jackson, C. R. and Apel, J. R., "Synthetic aperture radar marine users manual," tech. rep., US Department of Commerce, Washington, District of Columbia, 2004.

[33] Jakowatz, C. V., Wahl, D. E., Eichel, P. H., Ghiglia, D. C., and Thompson, P. A., *Spotlight-Mode Synthetic Aperture Radar: A Signal Processing Approach.* Norwell, Massachusetts: Kluwer Academic Publishers, 1996.

[34] Joyce, K. E., Belliss, S. E., Smasonov, S. V., McNeill, S. J., and Glassey, P. J., "A review of the status of satellite remote sensing and image processing techniques for mapping natural hazards and disasters," *Progress in Physical Geography*, vol. 33, no. 2, pp. 183–207, 1999.

[35] Lamb, H., *Hydrodynamics.* New York: Cambridge University Press, 1997.

[36] Levanon, N. and Mozeson, E., *Radar Signals.* Hoboken, New Jersey: John Wiley and Sons, 2004.

[37] Lillesand, T. M. and Kiefer, R. W., *Remote Sensing and Image Interpretation.* New York: John Wiley and Sons, 1994.

[38] Oliver, C. and Quegan, S., *Understanding Synthetic Aperture Radar Images.* Raleigh, North Carolina: Scitech, 2004.

[39] Pacifici, F., Frate, F. D., Solimini, C., and Emery, W. J., "An innovative neural-net method to detect temporal changes in high-resolution optical satellite imagery," *IEEE Transactions on Geoscience and Remote Sensing*, vol. 45, no. 9, pp. 2940–2952, 2007.

[40] Papoulis, A., *Systems and Transforms with Applications in Optics.* New York: McGraw-Hill, 1968.

[41] Preiss, M. and Stacy, N. J. S., "Coherent change detection: Theoretical description and experimental results," Tech. Rep. DSTOTR1851, Intelligence, Surveillance and Reconnaissance Division of Defence Science and Technology Organization, Edinburgh, Australia, 2006.

[42] Rignot, E. J. M. and van Zyl, J. J., "Change detection techniques for ERS-1 SAR data," *IEEE Transactions on Geoscience and Remote Sensing*, vol. 31, no. 4, pp. 896–906, 1993.

[43] Rocca, F., Prati, C., Guarnieri, A. M., and Ferretti, A., "SAR interferometry and its applications," *Surveys in Geophysics*, vol. 21, pp. 159–176, 2000.

[44] Rosenqvist, A., Shimada, M., and Watanabe, M., "ALOS PALSAR: Technical outline and mission concepts.," *4th International Symposium on Retrieval of Bio- and Geophysical Parameters from SAR Data for Land Applications*, 2004.

[45] Scholz, C. H., *The Mechanics of Earthquakes and Faulting.* Cambridge, UK: Cambridge University Press, second ed., 2002.

[46] Soumekh, M., *Fourier Array Imaging.* Englewood Cliffs, New Jersey: Prentice Hall, 1994.

[47] Soumekh, M., "Reconnaissance with slant plane circular SAR imaging," *IEEE Transactions Image Processing*, vol. 5, no. 8, pp. 1252–1265, 1996.

[48] Soumekh, M., *Synthetic Aperture Radar Signal Processing with MATLAB Algorithms.* New York: John Wiley and Sons, 1999.

[49] Stolt, R. H., "Migration by Fourier Transform," *Geophysics*, vol. 43, no. 1, pp. 23–48, 1978.

[50] Stolt, R. H. and Benson, A. K., *Seismic Migration: Theory and Practice.* London, UK: Geophysical Press, 1986.

[51] Tekalp, A. M., *Digital Video Processing.* Upper Saddle River, New Jersey: Prentice Hall, 1995.

[52] Tong, H. and He, G., "A comparison of wavelet and fourier analysis for image change detection," *IEEE International Geoscience and Remote Sensing Symposium*, vol. 4, pp. 2270–2272, 2005.

[53] Touzi, R., Lopes, A., and Bousquet, P., "A statistical and geometrical edge detector for SAR images," *IEEE Transcations on Geoscience and Remote Sensing*, vol. 26, pp. 764–773, 1988.

[54] Williams, M. L. and Preiss, M., "Physics-based predictions for coherent change detection using X-band synthetic aperture radar," *EURASIP Journal on Applied Signal Processing*, vol. 20, no. 1, pp. 3243–3258, 2004.

[55] Zebker, H. A. and Villasenor, J., "Decorrelation in interferometric radar echoes," *IEEE Transcations on Geoscience and Remote Processing*, vol. 30, no. 5, pp. 950–959, 1992.

VITA

Cihan Bayındır received the B.S. degree, with honors rank, in civil engineering from the Boğaziçi University, İstanbul, Turkey, in 2007, the M.S. degree in coastal and ocean engineering with a minor in mathematics from the University of Delaware, Newark, in 2009, and the M.S. degree in electrical and computer engineering with minors in mathematics and mechanical engineering from the Georgia Institute of Technology, Atlanta, in 2011, where he is currently working towards the Ph.D. degree at the department of civil and environmental engineering. He completed his Ph.D. minor studies in electrical and computer engineering with an emphasis on synthetic aperture radar imaging. He was a research assistant for an underwater acoustics project supported by the Office of Naval Research at the University of Delaware and currently a research assistant for a disaster reconnaissance using satellite imagery project supported by the Georgia Institute of Technology.

Mr. Bayındır is a member of the IEEE and IEEE Oceanic Engineering Society. His research interests are synthetic aperture radar and sonar imaging, disaster reconnaissance using satellite imagery, underwater acoustics, fluid mechanics, computational mathematics, ocean wave energy conversion and parallel programming in general.